Understanding Geochemical Tracers in Deep-Sea Corals from a Biomineralization Perspective

Thesis by

Sang Chen

In Partial Fulfillment of the Requirements for

the degree of

Doctor of Philosophy

CALIFORNIA INSTITUTE OF TECHNOLOGY

Pasadena, California

2019

(Defended 05/30/2019)

Sang Chen
ORCID: 0000-0001-8941-0791

ACKNOWLEDGEMENTS

Reflecting on my seven-year long journey for a Ph.D. degree in a country seven thousand miles away from home, especially on the past five years of wonderful life in Southern California, I cannot believe how quickly time has gone by to put me on the verge of my thirties. In traditional Chinese culture, Confucius called the age of thirty the time of true independence for a man. My pursuit of a Ph.D. degree feels no less than a search for the grounds of true independence both intellectually and practically.

This journey toward intellectual independence would not have been possible without the support of many. First and foremost, my advisor Jess has been the central part of my gradual development into an oceanographer and a scientist in general. I not only learned so much fascinating knowledge and so many useful skills from a mind as deep as the abyssal ocean in Jess, but also enjoyed his encouragement and support to pursue my best interests both in science and life. I will not forget the hospitality of Jess and his family to someone who often spends holidays alone, as well as the little things we honestly shared about our life experiences. I hope I can repay what I learned with more good work in the future.

During my stay at Caltech, I have also benefited tremendously from listening and talking to other great minds, which substantially extended my perspective on geochemistry and earth science in general. Among them are John Eiler, George Rossman, Alex Sessions, Woody Fischer and Paul Asimow, each of whom seems to know everything in the field and always has an elegant answer to your random questions and a solution to your practical needs in the lab. I have also enjoyed the many field trips enthusiastically led by Joe Kirschvink despite still being an amateur geologist. I am also indebted to David Lea for his pioneering work and joining my thesis committee to provide sound career advice.

I could not have got through my Ph.D. without the care and support of current and previous lab mates, including John, Dan, Sophie, Adam, Ted, Guillaume, Jared, Grace, Yoni and Preston. The trio of Sophie, Adam and Ted has inspired John, Dan and me to try to be the best of ourselves and pass on the torch of scientific grit and perseverance in the group. Dan has an incredible ability to manage an always-full schedule while maintaining good work-life balance, which I hope to learn more about in the coming months. John is my role model for a rock-solid reliable lab mate as well as a devoted husband. Jared patiently helped me work my way into a cleaner chemist in the lab, which will benefit me so much in the long run. It is my honor to have worked with all of you in the Adkins lab.

All scientific work builds on previous experience, and a lot of my work at Caltech relies heavily on knowledge and experience accumulated by previous and current students as well as postdocs in the division. Among them are Alex Gagnon, Uri Ryb, Tony Wang, Nithya Thiagarajan, David Case, Max Lloyd and Alison Piasecki. Your work and advice have sparked light along my tortuous exploration in the darkness of unknown territories in oceanography and geochemistry.

I have enjoyed incredible technical and administrative support at Caltech. Yunbin Guan, Nami Kitchen, Mike Baker and Chi Ma are all amazingly capable technicians and scientists without whom I would not have survived my Ph.D. Nora, Julie, Liz, Kathy of GPS and Claudia, Daniel, Laura of Caltech (and many others) have taken extremely good care of me and helped relieve a lot of annoyance from daily trivial matters. I would also like to acknowledge generous financial support from the China Scholarship Council, Caltech, JPL and NSF during my Ph.D. studies, without which none of my work would be possible.

I am also fortunate enough to have a group of great collaborators and mentors at an early stage of my career that greatly extended my horizon in the field. Among them are Jonathan Erez, James Rae, Andrea Burke, Kim Cobb, Rob Sherrell, Chris Charles, Will Berelson, Richard Zeebe and Joji Uchikawa. In particular, James and Kim are my role models as oceanographers and climate scientists. I have gained so much valuable first-hand experience from both of you, from the unfathomable caves in Borneo to the tranquil seaside of St. Andrews. I also owe many thanks to your teams that include Jessica Moerman, Stacy Carolin, Eloise Littley, Jess Crumpton-Banks and many others. In addition, it was my pleasure to share my first oceanic cruise with the CDisK-IV scientific team led by Jess A. and Will B. into the deep North Pacific that solidified my identity as an oceanographer.

Life at Caltech would be much less fun without the company of friends. I really enjoyed being among a group of young scientists with incessant curiosity and desire for new knowledge and life experience. Among them are Yuanlong, Peter, Ellen, Alistair, Kyle, Austin, Voon, Elle, Leah, Nancy, Elizabeth, Alex P., Hao and Guannan. You have both inspired me to work as hard as you do and entertained me to embrace the bittersweet life associated with a difficult scientific mission. I will also not forget the care and support from my old Michigan friends in my early days in the United States, including Yi, Peng, Ke, Chenghuan, Tao, Xiaofei and Tiffany, as well as instructors and mentors such as Kacey Lohmann, Brian Arbic and Ingrid Hendy.

My journey toward a Ph.D. in the United States would not have started had it not been someone who identified my potential as a scientist among hundreds of almost identical applications. Back in 2012, Dave Lund gave me what was then the only chance to come overseas to pursue a degree and a scientific career with full financial support, and well prepared me in the next two years at Michigan for future challenges at Caltech. I cannot thank you enough for finding and trusting me, and I hope to reward your choice with a decent career in the future.

Last but not least, I will be nowhere near who I am today without the loving support of my family. I owe all my good nature and habits to my parents and grandparents, which were, are and will be some of the greatest treasures in my life. I can never repay what you have done for me, and I only hope to make you proud with future achievements in my life and career. Finally, I cannot be more blessed to have Ting as my partner for what has been the best one third of my life. Nothing makes me more fulfilled than marrying you, and I hope to share and shoulder everything good or bad in life with you in the upcoming decades.

ABSTRACT

Deep-sea corals have been developed as a useful archive of the chemistry and circulation of intermediate and deep waters in past oceans over the last three decades. However, applications of traditional paleoceanographic tracers in deep-sea corals remain a challenge due to our incomplete understanding of the biomineralization mechanisms underlying the incorporation of these tracers and their variabilities in the coral skeletons (a.k.a. the "vital effects"). In this thesis, an effort was made to understand the vital effects associated with the stable isotope as well as minor and trace element compositions of the aragonitic skeletons of the deep-sea coral species *Desmophyllum dianthus*, through a combination of empirical observations and a numerical model of coral calcification. Observations of the chemical and isotopic compositions of the coral skeletons were performed on four different spatial scales in a suite of modern *D.dianthus* specimens: bulk samples, micromilled samples, SIMS and nanoSIMS. These observations reveal tracer correlations in deep-sea corals that are coherent over different spatial scales and point toward a universal mechanism of the incorporation of these tracers through the biomineralization process. A few tracers emerge as promising proxies for the temperature (Li/Mg, Sr/Ca) and carbonate chemistry (U/Ca, B/Ca, Ba/Ca) of the oceans. The numerical model for coral calcification explains the strong $\delta^{18}O$ and $\delta^{13}C$ vital effects in individual deep-sea corals with an updated physicochemical basis, and carbonic anhydrase is found to play a key role in setting the slopes of the strong $\delta^{18}O$-$\delta^{13}C$ correlations in different biogenic carbonates. The model also constrains the key physical parameters in the biomineralization process and is extended to explain the observed minor and trace element variabilities and correlations in deep-sea corals. The model can qualitatively explain the observed correlation patterns between Mg/Ca, Li/Ca, B/Ca and Sr/Ca in the coral skeletons, but quantitative data-model comparison is limited by both deficiencies in high-quality data and a lack of a well-constrained inorganic reference frame for aragonite. Future improvements in the geochemical tracers in biogenic carbonates will benefit from more extended empirical calibrations as well as a more complete mechanistic understanding of the key physicochemical and biological processes underlying the incorporation of tracers.

PUBLISHED CONTENT AND CONTRIBUTIONS

Chen, S., Gagnon, A.C., & Adkins, J.F. (2018). "Carbonic anhydrase, coral calcification and a new model of stable isotope vital effects". In: *Geochimica et Cosmochimica Acta* 236, pp. 179–197. doi: 10.1016/j.gca.2018.02.032.

S.C. participated in the design of the model, wrote an updated version of the model, analyzed the model results, and wrote the manuscript.

Chen, S., Ryb, U., Piasecki, A.M., Lloyd, M.K., Baker, M.B., & Eiler, J.M. (2019). "Mechanism of solid-state clumped isotope reordering from aragonite heating experiments". In: *Geochimica et Cosmochimica Acta*. doi: 10.1016/j.gca.2019.05.018.

S.C. participated in the conception of the project, performed the aragonite reordering experiments, and did the mineralogy and clumped isotope analyses. S.C. contributed to the interpretation of the data and participated in the writing of the manuscript.

Chen, S., Hoffmann, S.S., Lund, D.C., Cobb, K.M., Emile-Geay, J., & Adkins, J.F. (2016). "A high-resolution speleothem record of western Pacific rainfall: implications for Holocene ENSO evolution". In: *Earth and Planetary Science Letters*. 442, pp. 61-71. doi: 10.1016/j.epsl.2016.02.050

S.C. contributed to the stable isotope data collection while at the University of Michigan. S.C. contributed to the data interpretation and the writing of the manuscript at Caltech.

TABLE OF CONTENTS

LIST OF ILLUSTRATIONS AND/OR TABLES

Number *Page*

Chapter 1

INTRODUCTION

1.1 Deep-sea Corals as an Oceanic Archive

The deep ocean has been found to play a key role in modulating climate change and the earth's carbon cycle during the Pleistocene glacial-interglacial cycles. Numerous studies have suggested that the deep ocean is the major contributor to a drawdown of atmospheric CO_2 concentration by 80–100 ppm during glacial times, through a combination of physical, chemical and biological processes (Broecker, 1982; Knox & McElroy, 1984; Sarmiento & Toggweiler, 1984; Siegenthaler & Wenk, 1984; Broecker & Peng, 1987; Lea, 1993; Toggweiler, 1999; Sigman & Boyle, 2000; Sigman et al., 2010; Hain et al., 2010; Adkins, 2013). Despite significant progress in our understanding of these processes, the relative contribution of different processes to the glacial CO_2 drawdown remains a question of ongoing debate. A key component of uncertainty in our understanding of the glacial CO_2 problem is the reconstruction of the state of the deep ocean through glacial-interglacial cycles. Fully characterizing the role of the deep ocean would require information about its physical properties (temperature and salinity), carbonate chemistry, nutrient status as well as the rate of the overturning circulation.

Deep-sea corals are a useful archive of the chemistry and circulation of intermediate and deep waters in past oceans (Adkins, 1998). Their uranium-rich aragonitic skeletons can be dated with both radiocarbon and U-Th techniques to provide unbioturbated records of climate change (Cheng et al., 2000). Vertical growth rates of ~1 mm/yr of the skeletons (Adkins et al., 2004) offer the potential for records of sub-decadal resolution with microsampling techniques. Over the past two decades, multiple paleoceanographic tracers have been developed in deep-sea corals (especially in the species *Desmophyllum dianthus*). These tracers include radiocarbon (Adkins et al. 2002), Cd/Ca (Adkins et al., 1998), clumped isotopes (Thiagarajan et al., 2011), nitrogen isotopes (Wang et al., 2014), B/Ca and boron isotopes (Anagnostou et al., 2012; Stewart et al., 2016), Ba/Ca and Ba isotopes (Anagnostou et al., 2011; Spooner et al., 2018; Hemsing et al., 2018), U/Ca (Anagnostou et al., 2011; Raddatz et al., 2014), P/Ca (Anagnostou et al., 2011), Nd isotopes (van de Flierdt et al., 2010) and Pb isotopes (Wilson et al., 2017). These tracers have been

used to reveal the coupling between ocean dynamics, biogeochemistry and carbon cycle over the last glacial cycle (Adkins et al., 1998; Robinson et al., 2005; Eltgroth et al., 2006; Thiagarajan et al., 2014; Wilson et al., 2014; Hines et al., 2015; Wang et al., 2017; Rae et al., 2018).

1.2 Vital Effects in Deep-sea Corals

Despite the substantial progress that has been made with paleo-proxy development in deep-sea corals, applications of traditional paleoceanographic tracers such as oxygen and carbon isotopes and the Sr/Ca thermometer remain a challenge due to our incomplete understanding of these tracers in terms of both empirical calibrations and the underlying biomineralization mechanisms. Not only do these tracers deviate from expected thermodynamic equilibrium, but they also show a wide range of variability within individual corals (Adkins et al., 2003; Rollion-Bard et al., 2003; Gagnon et al., 2007; Case et al., 2010; Robinson et al., 2014). These non-equilibrium effects in biogenic carbonates are generally termed "vital effects" due to the involvement of biological activity in setting the values of the tracers (Weber & Woodhead, 1972).

Vital effects have been observed in a wide variety of marine calcifying organisms (McConnaughey, 1989a). For example, different foraminifera species are offset in their absolute $\delta^{18}O$ values at the same temperature and $\delta^{18}O$ of water, despite having similar temperature sensitivity (Shackleton & Opdyke, 1973; Bemis et al., 1998; Marchitto et al., 2014). Thus robust marine $\delta^{18}O$ records are generally based on species-specific calibrations and the assumption of constant "vital effects." These species-specific vital effects have also been observed in other widely used proxies such as the Mg/Ca thermometer in foraminifera (Lea et al., 1999; Anand et al., 2003; Bentov & Erez, 2006; Bryan & Marchitto, 2008) and the Sr/Ca thermometer in corals (Cohen et al., 2002; Correge, 2006).

While substantial effort has been put into empirical species-specific tracer calibrations through both natural and cultured samples, until recently relatively little effort has been focused on the mechanism of these vital effects on a physicochemical and quantitative basis. A key process of the mechanism of vital effects in marine calcifying organisms is the biological manipulation of the chemistry of their calcifying fluid relative to seawater. It has been observed that both foraminifera

and corals elevate the pH and $CaCO_3$ saturation state of their calcifying fluid relative to seawater through membrane-bound Ca^{2+} and proton transporters (Al Horani et al., 2003; Zoccola et al., 2004; Venn et al., 2011; Toyofuku et al., 2017). This process is perhaps best represented in pH sensitive tracers such as boron isotopes. Most coral species and many foraminifera species have higher $\delta^{11}B$ values in their carbonate shells/skeletons than the borate ions ($B(OH)_4^-$, which is considered the dominant species that is incorporated) in the ambient seawater (Hönisch et al, 2004; Foster, 2008; Krief et al., 2010; Rollion-Bard & Erez, 2010; Henehan et al., 2013; Anagnostou et al., 2012; McCulloch et al., 2012; Stewart et al., 2016), suggesting a pH elevation of up to 1 pH unit. This pH up-regulation has been suggested to explain vital effects in other tracers such as oxygen and carbon isotopes (McConnaughey, 1989b; Adkins et al., 2003; Marchitto et al., 2014) and minor and trace element concentrations (Me/Ca ratios) (Sinclair & Risk, 2006; Gagnon et al., 2007; Gaetani et al., 2011; Gagnon et al., 2012). Understanding the pH up-regulation process and the associated biological calcification dynamics is not only important for deconvolving vital effects from environmental imprints on paleo-proxies, but it can also shed light on the fate of marine calcification under future climate change and ocean acidification.

Deep-sea corals are ideal test organisms to study vital effects, due to a lack of complication of the calcification process from photosymbionts, as well as large tracer gradients in individual corals growing under relatively constant environments. A single deep-sea coral can have a 5‰ range in $\delta^{18}O$, a 10‰ range in $\delta^{13}C$ (Emiliani et al., 1978; Adkins et al., 2003; Blamart et al., 2005; Rollion-Bard et al., 2010), a factor of 2–3 change in Mg/Ca and Li/Ca (Gagnon et al., 2007; Case et al., 2010), a 10% change in Sr/Ca (Gagnon et al., 2007), and a factor of 2 change in B/Ca (Blamart et al., 2007) and U/Ca (Robinson et al., 2006; Stewart et al., 2016). The vital effects are maximized in the optically dense bands called centers of calcification (COCs). Despite being identified as aragonite with Raman spectroscopy, the COCs are organic rich crystal nodules with random orientations compared to the c-axis aligned secondary aragonite (Gladfelter, 1982; Gagnon et al., 2007). They are thought of as the initial nucleation sites for the calcification to be triggered, and are sometimes referred to as early mineralization zones (Cuif & Dauphin, 2005; Rollion-Bard et al., 2010). They are depleted in $\delta^{18}O$ and $\delta^{13}C$ (Adkins et al., 2003; Blamart et al., 2005), enriched in Mg/Ca and Li/Ca (Gagnon et al., 2007; Case et al., 2010), and depleted in B/Ca, $\delta^{11}B$ (Blamart et al., 2007) and U/Ca (Robinson et al., 2006), compared to the secondary aragonite.

Outside the extreme composition of the COCs, the secondary aragonite of the corals displays large variability, with strong correlations between tracers such as $\delta^{18}O$ and $\delta^{13}C$, Mg/Ca and Li/Ca, and Mg/Ca and Sr/Ca (Figure 1-1). It should be noted that the composition of COCs falls off the tracer-tracer correlation trend in the secondary aragonite, and the range in the data could not be explained by a simple mixture of two components. The correlations between the tracers instead suggest that they respond to a common process during biomineralization. The goal of this thesis is to explore this underlying biomineralization process and its effect on the geochemical tracers in deep-sea corals, with a combination of tracer data collection in a suite of modern deep-sea corals and a numerical model of coral calcification.

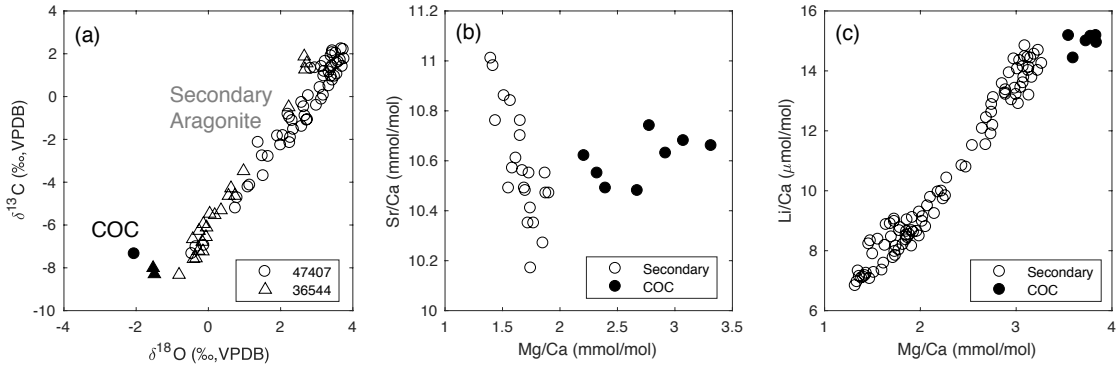

Figure 1-1 Observed tracer variability and correlations in individual *D.dianthus*. Open symbols represent secondary aragonite and filled symbols represent COCs. (a) Cross plot of $\delta^{18}O$ and $\delta^{13}C$ in two individual *D.dianthus* specimens 47407 (circles) and 36544 (triangles) from Adkins et al. (2003). (b) Cross plot of Mg/Ca and Sr/Ca in 47407 from Gagnon et al. (2007). (c) Cross plot of Mg/Ca and Li/Ca in DMC08 from Case et al. (2010).

1.3 Strategy and Thesis Structure

Development of paleoceanographic tracers has generally taken two approaches: the theoretical/physicochemical approach and the empirical approach. They are not mutually exclusive, and application of a tracer with a physicochemical basis to its variability requires validation by empirical calibrations. For tracers in biogenic carbonates, there are two major ways of calibrations: laboratory culture experiments and "core top" calibrations. Although they provide the basis for the application of the tracers, they do not always follow theoretical/physicochemical expectations. As discussed in the previous section, vital effects play a major role in these differences, and a

quantitative and mechanistic understanding of the biomineralization process helps to bridge the gaps between theoretical predictions and empirical observations.

The strategy of studying vital effects in this thesis is a combination of empirical observations and a numerical model of coral calcification. To best bridge the gaps between the two, the data collection on stable isotopes and trace elements in the deep-sea coral species *D.dianthus* was carried out on four different scales for individual corals: bulk powder (samples of millimeter to centimeter size drilled from a single specimen), micromilled growth bands (tens to hundreds of microns wide, a few millimeters long), spots within growth bands from secondary ion mass spectrometry (SIMS) (tens of microns in size), and element maps of even finer spatial scales with nanoSIMS (tens of nanometers to a few microns). The observations on fine spatial scales in individual corals are used to inform the numerical model and constrain key parameters in the calcification process. They can also be used to quantify the magnitude of vital effects that is present in the bulk samples. The bulk powder measurements were performed on a selection of modern *D.dianthus* specimens that span a wide range of environmental conditions to serve as the "core top" calibration of tracers for this species. The *D.dianthus* individuals selected from the Caltech collection for this thesis are listed in Table 1-1 with a map showing their spatial distributions in Figure 1-2. The ultimate goal is to explore how a better understanding of the biomineralization processes can help improve the empirical tracer calibrations.

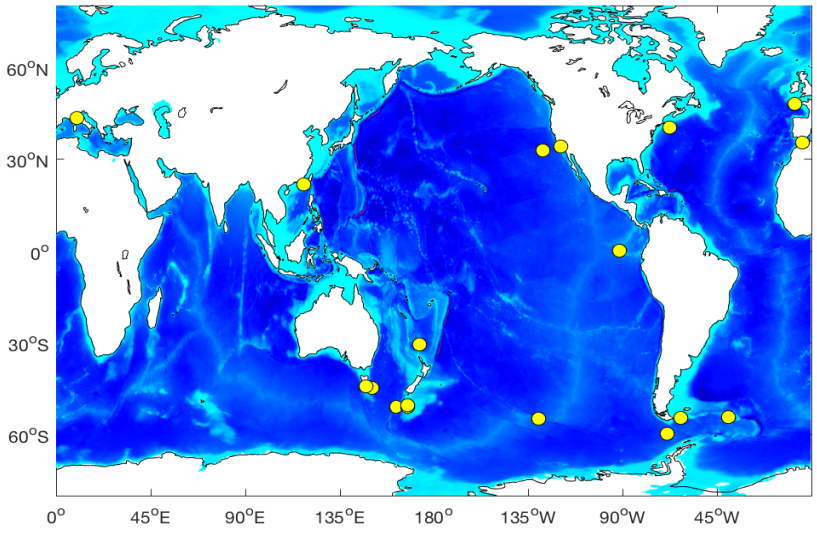

Figure 1-2 Distribution of *D.dianthus* specimens in this thesis study. Note that the locations of some corals overlap on the map.

Table 1-1 *D.dianthus* individuals selected for this thesis study

Ocean	Coral Name	Lon (°E)	Lat (°N)	Depth (m)	Bulk	Micromill	SIMS	Nano SIMS
Atlantic	62309	–67.7	40.4	430–613	x	x	x	x
	80358	–7.8	48.0	358	x		x	
Pacific	19249	–119.5	34.0	274	x			
	83583	–127.8	32.9	440–488	x		x	
	84820	–91.6	0.2	806	x	x	x	x
	94071	173.3	–30.7	590–640	x		x	
Southern Ocean	Big Beauty	–62.2	–54.7	816	x	x	x	
	47396	–68.8	–59.7	1042–1207	x		x	
	47409	–39.4	–54.5	659–686	x			
	47407	–129.8	–54.8	549	x	x	x	x
	82065	–129.8	–54.8	567–604	x		x	
	47413	167.6	–50.6	421	x	x	x	
	53377	167.8	–51.1	210	x			
	47394	162.0	–51.0	333–371	x			
	Gaia	150.3	–44.8	2395	x		x	
	Leda	147.3	–44.3	1460	x			
	Titan	147.3	–44.4	2066	x	x		
Mediterranean	48744	9.8	43.3	595–660	x			
	80404	–4.2	35.4	395	x			
South China Sea	97275	117.6	21.7	412–430	x			

In Chapter 2 of the thesis, a numerical model of coral calcification is developed to describe the strong stable isotope vital effects observed in deep-sea corals. In particular, the strongly correlated $\delta^{18}O$ and $\delta^{13}C$ that are depleted from thermodynamic equilibrium in deep-sea corals, as well as many other marine calcifying organisms, is explained by the coupling of internal pH-elevation and changes in the relative contributions of two inorganic carbon sources. A relatively narrow range of slopes of the $\delta^{18}O$ and $\delta^{13}C$ in different calcifying organisms can be explained by the activity of the enzyme carbonic anhydrase in the calcifying space. We also find that the isotope

composition of the deep-sea coral skeletons at the enriched end is consistent with recent inorganic precipitation experiments and an ion-by-ion growth model (Watkins et al., 2013; Watkins et al., 2014; Watkins & Hunt, 2015). This biomineralization model establishes the quantitative basis for the use of the oxygen and carbon isotopes as indicators of the magnitude of vital effects in deep-sea corals, which is later used to understand the minor and trace element distributions.

In Chapter 3 of the thesis, I report the minor and trace element distributions together with stable isotopes in individual *D.dianthus* measured on micromilled growth bands. Some patterns of tracer correlations are observed for individual corals, and these correlations show potential responses to different environmental factors. The numerical model developed in Chapter 2 for stable isotopes is extended to minor and trace elements to explore the important biomineralization processes that are responsible for the observed changes in tracer correlations. A combination of the tracer correlations and the model also provides clues to possible ways of improving the tracers on a mechanistic basis.

In Chapter 4 of the thesis, the observed Me/Ca correlations in Chapter 3 are refined by SIMS and nanoSIMS measurements, and more robust correlation patterns are established with the SIMS data. With nanoSIMS imaging, we observed quasi-rhythmic growth bands in Mg/Ca in *D.dianthus* on micron scales that are similar to surface corals. These bands are less clear for other Me/Ca ratios. By comparing the observed Me/Ca correlations with the numerical model, I further discuss the biomineralization processes relevant for the observed correlation patterns and possible environmental impacts on these patterns. Two appendix sections are added to Chapter 4 on two related projects that involved significant time investment with high-quality data generated. One of them is X-ray absorption spectra of Ca and Sr in *D.dianthus* skeletons that were collected at the Stanford Synchrontron Radiation Lightsource (SSRL). The other is nanoSIMS mapping of organic associated elements in *D.dianthus* with the Cs^+ source. These two pieces of work are good complements to the tracer development effort in deep-sea corals in helping us visualize the vital effects and understand its basis on the atomic scale.

In Chapter 5 of the thesis, I report the empirical correlations of Me/Ca ratios in bulk *D.dianthus* samples to environmental factors. Some relatively strong correlations were found despite significant scatter in the data. Li/Mg in *D.dianthus* is strongly temperature dependent and

shares the same relation with temperature as other coral species. Sr/Ca in *D.dianthus* is also strongly correlated with temperature with the same temperature sensitivity as inorganic aragonite. Both B/Ca and U/Ca are correlated with [CO_3^{2-}] of the ambient seawater, while Ba/Ca shows potential as an alkalinity proxy. The biomineralization mechanisms constrained by the fine scale observations and the numerical model are used to explain the potential vital effects behind the scatter in the tracer calibrations, and attempts are made to use tracer-tracer correlations to improve the paleo-proxies in deep-sea corals.

Chapter 6 of the thesis is on a separate topic: solid-state clumped isotope reordering in aragonite heating experiments. I started this project in the Eiler lab as a first year research requirement of the GPS Division, and was fortunate to learn the clumped isotope measurement techniques and continue to expand the dataset and improve the interpretations with new experiments. This has resulted in a manuscript that has been published in *Geochimica et Cosmochimica Acta*. It is included in the thesis due to the significant amount of work invested, and its relevance for the preservation of clumped isotope records in fossil aragonites. This project also shares the spirit of previous chapters in deep-sea corals in trying to understand the atomic scale mechanisms behind geochemical proxies in natural carbonate minerals.

Chapter 2

A Numerical Model of Stable Isotope Vital Effects in Deep-sea Corals with the Role of Carbonic Anhydrase

The content of this chapter has been published with the citation below. The title and the text are slightly modified in the chapter to make better connections with other chapters.

Chen, S., Gagnon, A.C., & Adkins, J.F. (2018). "Carbonic anhydrase, coral calcification and a new model of stable isotope vital effects". In: *Geochimica et Cosmochimica Acta 236*, pp. 179–197. doi: 10.1016/j.gca.2018.02.032.

Abstract

The stable isotope compositions of biogenic carbonates have been used for paleoceanographic and paleoclimatic reconstructions for decades, and produced some of the most iconic records in the field. However, we still lack a fully mechanistic understanding of the stable isotope proxies, especially the biological overprint on the environmental signals termed "vital effects." A ubiquitous feature of stable isotope vital effects in marine calcifying organisms is a strong correlation between $\delta^{18}O$ and $\delta^{13}C$ in a range of values that are depleted from inorganic calcite/aragonite. Two mechanisms have been proposed to explain this correlation, one based on kinetic isotope effects during $CO_2(aq)$-HCO_3^- inter-conversion, the other based on equilibrium isotope exchange during pH dependent speciation of the dissolved inorganic carbon (DIC) pool. Neither mechanism explains all the stable isotope features observed in biogenic carbonates. Here we present a fully kinetic model of biomineralization and its isotope effects using deep-sea corals as a test organism. A key component of our model is the consideration of the enzyme carbonic anhydrase in catalyzing the $CO_2(aq)$-HCO_3^- inter-conversion reactions in the extracellular calcifying fluid (ECF). We find that the amount of carbonic anhydrase not only modulates the carbonate chemistry of the calcifying fluid, but also helps explain the slope of the $\delta^{18}O$-$\delta^{13}C$ correlation. Differences in CA activity in the biomineralization process can possibly explain the observed range of $\delta^{18}O$-$\delta^{13}C$ slopes in different calcifying organisms. A mechanistic understanding of stable isotope vital effects with numerical models can help us develop better paleoceanographic tracers.

2.1 Introduction

The oxygen isotope composition of biogenic carbonates has been established as a proxy for past climate change for decades, since Urey (1947) first worked out the theoretical bases of the ^{18}O thermometer. The proxy is based on the temperature-dependent equilibrium isotope fractionation between carbonates and the fluid from which they precipitated. The successful application of the ^{18}O thermometer in biogenic carbonates relies on the assumption of equilibrium isotope fractionation, or at least a constant offset from equilibrium for the same category of organisms. However, disequilibrium isotope effects between carbonate and water have been widely observed in both laboratory experiments and natural samples. In the first experimental demonstration of the applicability of the ^{18}O thermometer in carbonates, McCrea (1950) noticed the dependence of the isotopic composition of the precipitated calcite on the percentage of carbonate ion in the solution at a constant temperature and $\delta^{18}O$ of water. This carbonate ion effect on the oxygen isotope composition of carbonates was later explained by oxygen isotope partitioning between the dissolved inorganic carbon (DIC) species (Usdowski & Hoefs, 1993; Beck et al., 2005), and was suggested by Zeebe (1999) to cause the non-equilibrium oxygen isotope fractionation observed in inorganic experiments (Kim & O'Neil, 1997) as well as cultured foraminifera (Spero et al., 1997). An insight from the interpretation of Zeebe (1999) is a necessity to incorporate all the DIC species into the solid phase to explain its isotopic composition, making the carbonate-water fractionation ($\alpha_{c\text{-}w}$) a function of pH of the solution in addition to temperature. Follow-up work on this subject also observed a decrease of $\alpha_{c\text{-}w}$ with increasing growth rate of calcite (Gabitov et al., 2012; Watkins et al., 2013) and aragonite (Gabitov, 2013), suggesting kinetic isotope effects (KIE) from ion adsorption and desorption at the solution-solid interface during carbonate precipitation. This growth rate effect can cause an offset of the isotopic composition of the solid from the DIC pool (Watkins et al., 2014).

In addition to the temperature and pH dependent thermodynamic fractionation and growth rate dependent kinetic fractionation, the isotope exchange between the DIC species and water brings another source of disequilibrium, due to the relatively slow rate of $CO_2(aq)$-HCO_3^- inter-conversion. Although the timescale for one $CO_2(aq)$-HCO_3^- inter-conversion cycle is on the order of a minute at seawater pH, many cycles are required to achieve a complete exchange of oxygen atoms between the DIC species and water to reach isotope equilibrium (McConnaughey, 1989b).

As a result, the equilibration timescale for oxygen isotopes in the DIC pool (hours to days) is significantly longer than for carbon isotopes (seconds to minutes), especially at high pH when the CO_2(aq)-HCO_3^- inter-conversion approaches an irreversible reaction (McConnaughey, 1989b; Zeebe & Wolf-Gladrow, 2001). The oxygen isotope equilibration timescale is longer than most natural calcification processes, as well as many laboratory experiments, which could lead to a significant expression of KIEs during hydration and hydroxylation of CO_2 and subsequently in the resulting carbonates. Carbon isotopes also experience KIEs during DIC speciation, but to a smaller extent than oxygen. The KIEs of hydration/hydroxylation were proposed by McConnaughey (1989a,b) to explain the strong correlation between $\delta^{18}O$ and $\delta^{13}C$ observed in a variety of marine calcifying organisms growing under the same environmental conditions (Figure 2-1). McConnaughey (1989a) also pointed out the role of photosymbionts on the carbon isotope composition of coral skeletons, making the $\delta^{13}C$ more enriched compared to non-symbiotic corals.

The KIE mechanism by McConnaughey (1989a,b) predicts a simple linear relation between $\delta^{18}O$ and $\delta^{13}C$ in biogenic carbonates with a particular slope. A challenge to this mechanism was raised from a study of deep-sea corals (*Desmophyllum dianthus*), which observed a break in the $\delta^{18}O$-$\delta^{13}C$ linear relation at the most isotopically depleted end (Adkins et al., 2003). The optically dense central bands in these deep-sea corals, called centers of calcification (COCs), have similar $\delta^{13}C$ to the most depleted values in the surrounding aragonite fibers, but are more depleted in $\delta^{18}O$ than the secondary aragonite. The unique composition of the COCs causes a kink in the $\delta^{18}O$-$\delta^{13}C$ relation (Figure 2-1a), which led Adkins et al. (2003) to propose a different mechanism for the stable isotope vital effects (Figure 2-2). This mechanism was based on the observed pH up-regulation in corals within their ECF by the enzyme Ca-ATPase (Al-Horani et al., 2003; Venn et al., 2011). As Ca-ATPase pumps Ca^{2+} into the ECF in exchange for two protons, the pH of the ECF is raised, which shifts the DIC speciation towards the ^{18}O-depleted carbonate ion. Simultaneously, decreasing CO_2(aq) concentration in the ECF causes a larger ^{13}C-depleted CO_2 flux from the calicoblastic cells into the ECF, as opposed to ^{13}C-enriched DIC from the seawater leak. The simultaneous depletion of $\delta^{18}O$ and $\delta^{13}C$ during pH up-regulation stops when the pH of ECF reaches a threshold (pK_{a2}). After pK_{a2}, CO_2(aq) in the ECF is so low that the cell CO_2 flux is maximized, while the DIC speciation keeps moving from bicarbonate to carbonate ion, promoting further depletion of $\delta^{18}O$ in the $CaCO_3$. This is hypothesized to explain the $\delta^{18}O$-$\delta^{13}C$ kink

produced by the COCs. In this model, however, Adkins et al. (2003) assumed equilibrium isotope fractionation between the DIC species. The neglect of KIEs during oxygen isotope exchange caused their numerical model to have a steeper $\delta^{18}O$-$\delta^{13}C$ slope than the observed range in deep-sea corals (1.9-2.6). In addition, the isotopic composition of the skeleton predicted by the composition of the DIC pool is offset from the expected inorganic aragonite values. This begs a new model of biomineralization to explain the observed $\delta^{18}O$-$\delta^{13}C$ data that takes into account the KIEs during DIC speciation, and applies the correct fractionation between the carbonate, DIC species and water.

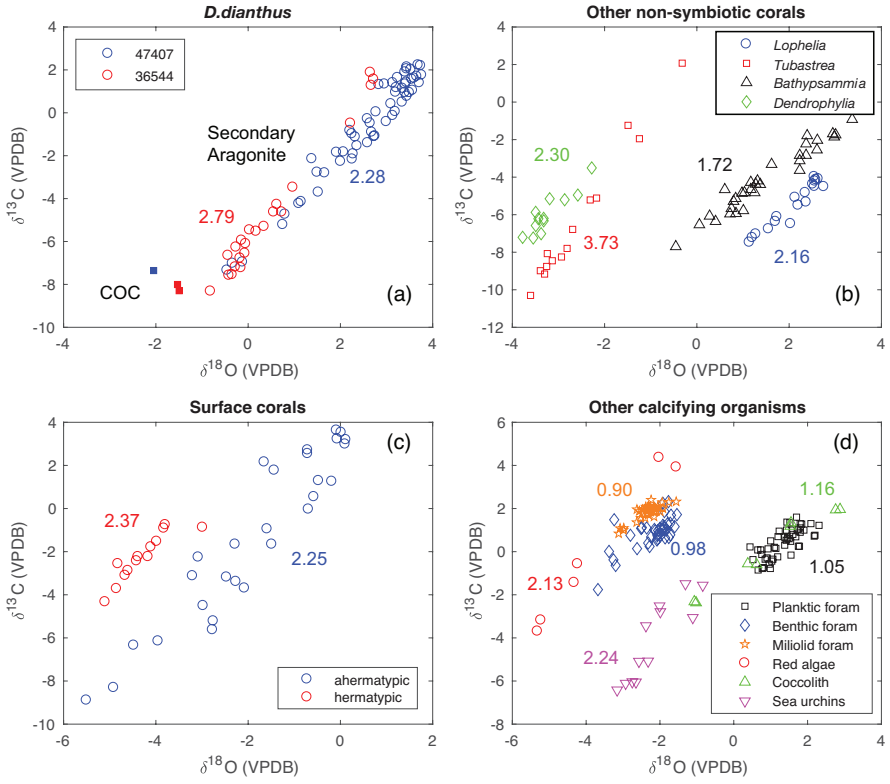

Figure 2-1 A compilation of stable isotope data in marine biogenic carbonates updated from McConnaughey (1989a). The labeled numbers are $\delta^{18}O$-$\delta^{13}C$ slopes of the dataset of the same color. (a) Two deep-sea coral *D.dianthus* specimens (Adkins et al., 2003). The squares are from COCs and are not included in the slope calculation. (b) Other non-symbiotic corals (Weber & Woodhead, 1970; Emiliani et al., 1978; McConnaughey, 1989a; Adkins et al., 2003). (c) Surface corals (Keith & Weber, 1965; Land & Lang, 1977). (d) Other calcifying organisms including planktic foraminifera *Globorotalia truncatulinoides* (Vergnaud-Grazzini, 1976), benthic perforated foraminifera *Amphistegina radiata* and benthic miliolid foraminifera *Sorites marginalis* (Vinot-Bertouille & Duplessy, 1973), red algae (Keith & Weber, 1965), coccolithophores (Hermoso et al., 2014) and sea urchins (Weber & Raup, 1966). The difference in the intercepts of these datasets may result from temperature and metabolic CO_2 effects, and are not the focus of this study.

Here we present a numerical model of coral calcification modified from Adkins et al. (2003). The fundamental components of the model are based on biological and geochemical observations of the coral calcification process, most of which were also considered in McConnaughey's seminal work (McConnaughey, 1989a, b). As observed in calcein and trace metal labeling experiments, seawater is directly involved in the coral calcification process (Tambutte et al., 2012; Gagnon et al., 2012). In our model, we treat ambient seawater as the starting material of the ECF, the composition of which the corals constantly modify. Corals actively up-regulate the pH of their ECF relative to ambient seawater, to locally increase saturation state and calcification rate, as suggested by direct pH measurements (e.g. Al Horani et al., 2003; Venn et a., 2011) and boron isotopes (e.g. McCulloch et al., 2012; Wall et al., 2015). Ca-ATPase, an enzyme that exchanges protons for calcium ions, plays an important role in the pH up-regulation, and has been localized in the calicoblastic cells (Zoccola et al., 2004). In addition, our model considers the role of the enzyme carbonic anhydrase (CA) in the coral calcification process. CA is a ubiquitous enzyme found in almost all living organisms that catalyze the CO_2-HCO_3^- inter-conversion (Bertucci et al., 2013). The role of CA in the calcification process of corals has been suggested from CA-inhibition experiments for decades (Goreau, 1959), but it was only in the last decade that CA has been immunolocalized in the coral ECF and skeleton (Tambutte et al., 2007; Moya et al., 2008; Mass et al., 2014). Although these studies have only been performed on a few coral species, the presence of CA in the calcifying space of both symbiotic (*Stylophora pistillata*) and azooxanthellate (*Tubastrea aurea*) corals, as well as evidence for its influence on the calcification of other species, suggest that it is directly involved in the biomineralization of many scleractinian corals (Tambutte et al., 2007; Moya et al., 2008; Bertucci et al., 2013; Mass et al., 2014). Consideration of carbonic anhydrase in the model represents an important difference from both the McConnaughey (1989a,b) model and the Adkins et al. (2003) model. The two previous models can be regarded as two limits of CA activity in the ECF, with the McConnaughey model corresponding to zero CA activity, and the Adkins model corresponding to infinite CA activity. The effect of CA activity on the carbonate chemistry of the ECF is detailed in the model results section. Finally, debates remain about the relative importance of paracellular seawater transport versus transcellular ion pumping during coral biomineralization (Tambutte et al., 2011; Tambutte et al., 2012; Gagnon et al., 2012), and the degree to which the calcification process is physicochemically or biologically controlled (Cuif & Dauphin, 2005; Venn et al., 2011; Allison et

al., 2014; Mass et al., 2014; Von Euw et al., 2017). Instead of considering the complicated biological processes at a molecular level, our quantitative model treats the major biological processes as fluxes associated with carbonate chemistry, to test the applicability of simple physicochemical rules to tracers in biogenic carbonates.

Deep-sea corals are good test organisms of a stable isotope model given their relative lack of environmental variability and the full range of $\delta^{18}O$ and $\delta^{13}C$ disequilibria observed in their skeletons. Our biomineralization model takes into account different processes during coral calcification that fractionate carbon and oxygen isotopes. In particular, the model tracks the kinetics of CO_2 hydration and hydroxylation in the ECF and its isotope effects under different alkalinity pump rates and ECF pH values. By comparing model results to stable isotope data, the model provides a test of the McConnaughey and Adkins ideas. In addition, the presence of CA in the ECF can facilitate oxygen isotope equilibrium among the DIC species, as has been demonstrated in inorganic precipitation experiments (Uchikawa & Zeebe, 2012; Watkins et al., 2014). As discussed in the model results, accounting for CA activity in the ECF is important in explaining the stable isotope vital effects in deep-sea corals and potentially other calcifying organisms. Finally, the model also applies an offset in the isotopic composition of the carbonate skeleton from the DIC pool for both carbon and oxygen isotopes based on inorganic precipitation experiments and the ion-by-ion growth model (Romanek et al., 1992; Watkins et al., 2014; Watkins & Hunt, 2015). By applying the isotope fractionation factors determined in inorganic experiments to biogenic carbonates, we intend to explore the extent to which vital effects can be explained with fundamental physical chemistry rules. With the major fractionation processes considered above, the model is not only expected to better simulate the deep-sea coral data, but also to explain the range of $\delta^{18}O$-$\delta^{13}C$ slopes observed in different marine calcifying organisms (Figure 2-1).

2.2 The Numerical Model

A schematic diagram of the deep-sea coral based ECF model is shown in Figure 2-2. The model is modified from the McConnaughey and Adkins models, based on the ubiquitous observation that corals up-regulate their ECF pH relative to ambient seawater (e.g. Al Horani et al.,

2003; Venn et al., 2011; McCulloch et al., 2012; Wall et al., 2015). There are two sources of carbon that end up in the coral skeleton, one from seawater DIC and the other from CO_2(aq) diffusing across the ECF membrane. With an increase in the saturation state and calcification rate, corals can be limited by the conversion of CO_2(aq) to bicarbonate and carbonate ions, which is a kinetically slow step due to the reorganization of covalent bonds. There are two ways the rate of this conversion can be biologically enhanced. The first is to increase the pH of the ECF by Ca^{2+}-proton exchange through Ca-ATPase, which lowers CO_2(aq) in the ECF and drives cross-membrane CO_2(aq) fluxes and promotes the faster hydroxylation of CO_2(aq). The second is to synthesize carbonic anhydrase, which directly catalyzes the CO_2(aq) hydration reaction. In our model, we write out the equations of CO_2(aq)-HCO_3^- inter-conversion through both hydration and hydroxylation pathways, and track the time evolution of the chemical species in the ECF as calcification takes place. In particular, we specify an alkalinity pumping rate, and track how alkalinity, different DIC species and [Ca^{2+}] change due to fluxes from hydration/ hydroxylation, seawater transport, cell membrane crossing, and calcification. For the DIC species, we assume that the HCO_3^--CO_3^{2-} conversion is instantaneous (10^{-7} s) compared to the slow CO_2(aq)-HCO_3^- conversion (10^2 s) (Zeebe & Wolf-Gladrow, 2001), and combine [HCO_3^-] and [CO_3^{2-}] in the equations as equilibrated inorganic carbon (EIC) pool. In addition, we treat CA activity as a rate enhancement factor (k_{cat}) in the CO_2(aq) hydration reaction. Given the low CO_2(aq) concentration in seawater, the CA-catalyzed hydration can be approximated with first-order kinetics (Uchikawa & Zeebe, 2012). The seawater and cell fluxes are treated as a concentration gradient driven diffusion process as in Adkins et al. (2003). The calcification rate law is obtained from inorganic aragonite precipitation experiments (Romanek et al., 2011). The differential equations in the model are listed in the chapter appendix (Section 2.6). For a given alkalinity pump rate, the forward model is run toward steady state with Matlab's ode15s solver, with seawater composition as the initial condition. The carbonate chemistry of the ECF is updated at each time step with CO2SYS. In our fully kinetic model, the carbonate system of the ECF may not reach equilibrium, due to the kinetic barrier of CO_2(aq)-EIC conversion. However, in the range of pH simulated (pH>8), CO_2(aq) constitutes less than 1% of DIC at equilibrium, and the maximum CO_2(aq) excess we get from the kinetic barrier is 1.6%. This non-equilibrium effect corresponds to a maximum pH offset of 0.03 units in our CO2SYS calculations, or 7% in H^+ activity, which does not significantly influence our model results.

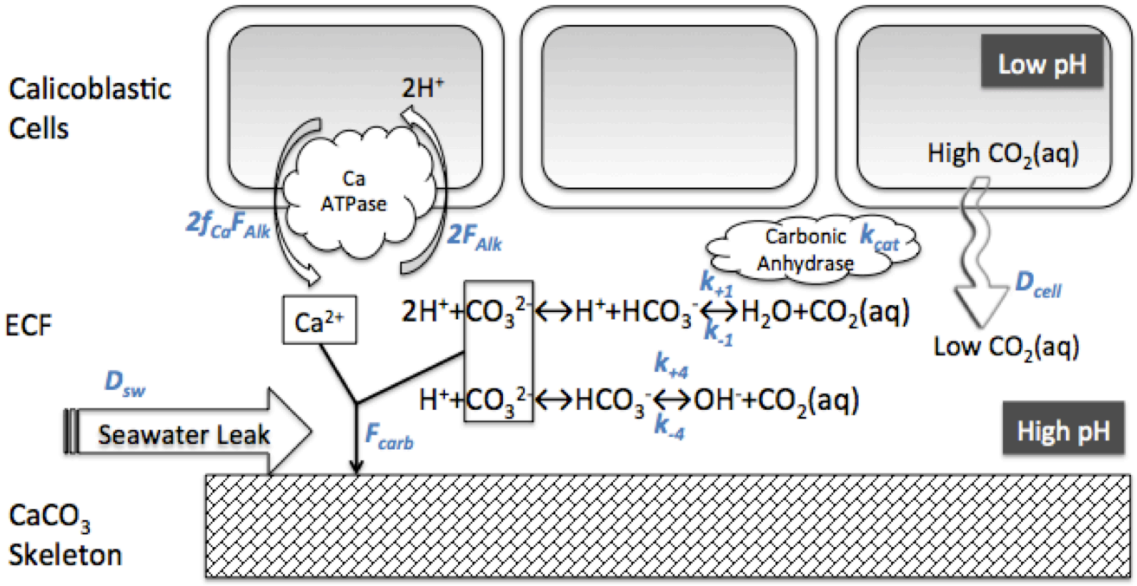

Figure 2-2 Schematic diagram of coral calcification. Black text shows the chemical species in the model, while blue text represents fluxes or reaction rate constants. The effect of carbonic anhydrase is represented by a rate enhancement factor k_{cat}. With carbonic anhydrase the rate constant for $CO_2(aq)$ hydration is $k_{cat} \cdot k_{+1}$ and HCO_3^- dehydration is $k_{cat} \cdot k_{-1}$. Conversion between HCO_3^- and CO_3^{2-} is considered instantaneous and the two are written together in the differential equations as equilibrated inorganic carbon (EIC) pool. The effect of Ca-ATPase is represented by an exchange of Ca^{2+} into the ECF for two protons, which adds two units of alkalinity. The only DIC species that can passively move across the ECF membrane is $CO_2(aq)$, driven by the difference between $[CO_2(aq)]$ in the calicoblastic cells and $[CO_2(aq)]$ in the ECF.

In order to track the isotope processes with the model, we also write out equations for the ^{13}C and ^{18}O substituted species, with the fractionation factors incorporated in the rate constants. The processes that fractionate isotopes in the model are: $CO_2(aq)$-HCO_3^- inter-conversion through hydration/dehydration and hydroxylation/dehydroxylation, precipitation of the skeleton from the EIC pool, and $CO_2(aq)$ diffusion across the cell membranes. Both carbon and oxygen isotopes can be fractionated through these processes. There have been relatively reliable constraints on the carbon isotope fractionation factors associated with the related processes (Marlier & O'Leary, 1984; O'Leary et al., 1984; O'Leary et al., 1992; Zeebe & Wolf-Gladrow, 2001), although inconsistencies remain between experimental data and theoretical calculations (Zeebe, 2014). However, the kinetic fractionation factors for oxygen isotopes are not as well constrained, especially for the $CO_2(aq)$ hydration and hydroxylation reactions. As a result, we started with the

range of values calculated based on transition state theory (Zeebe, 2014) and tested the model's sensitivity to the fractionation factors. We find that a range of fractionation factors can fit the data, and the exact values needed to fit the data depend strongly on the CA rate enhancement factor. In addition, we incorporate the pH and growth rate dependence of the carbonate-water oxygen isotope fractionation (Watkins et al., 2014) and carbonate-DIC carbon isotope fractionation (Watkins & Hunt, 2015) to account for the isotope effects of fluid-solid interaction. A fluid-solid ^{13}C and ^{18}O fractionation factor based on pH and $CaCO_3$ precipitation rate is assigned following the ion-by-ion model (Watkins et al., 2014; Watkins & Hunt, 2015) at each time step as the forward model is run toward steady state. In the isotope-enabled fully kinetic model, every given alkalinity pump rate also corresponds to a steady state carbon and oxygen isotope composition of the coral skeleton. A summary of the model parameters and fractionation factors is given in Table 2.1 in the chapter appendix (Section 2.6).

2.3 Model Results

2.3.1 Carbonate chemistry in the ECF

Figure 2-3 shows the steady state solutions of the carbonate chemistry species in the ECF at different alkalinity pump rates as a function of Alk-DIC space. The three cases examined are associated with different CA activities in the ECF. The slow kinetics case corresponds to no CA, and the $CO_2(aq)$-HCO_3^- inter-conversion follows inorganic seawater rate constants (Johnson, 1982; Zeebe & Wolf-Gladrow, 2001), as proposed by McConnaughey (1989a,b). In the other extreme, the $CO_2(aq)$-HCO_3^- inter-conversion through hydration/dehydration is instantaneous, as has been examined in the model by Adkins et al. (2003). Between the two extremes, a finite amount of CA activity in the ECF is shown as a 2000 times enhancement of the hydration/dehydration rates. As the alkalinity pump rate is increased, the pH of the ECF is elevated, and the steady state solutions of DIC and alkalinity in the ECF moves from the lower right to the upper left corner in the Alk-DIC space (Figure 2-3a). However, the pathways of pH elevation are different in the presence or absence of CA. In the absence of CA, the DIC of ECF first decreases significantly relative to the seawater source while the pH is rapidly elevated, after which there is a small change in DIC as alkalinity is further pumped in. In the presence of CA, however, DIC first starts to increase with a

relatively small increase in pH, and then decreases rapidly with rapid pH elevation like the slow kinetics case. In all cases, there is a maximum carbonate ion concentration as the alkalinity pump is turned up (Figure 2-3b). However, the reasons for the [CO_3^{2-}] increase towards a maximum are different for the different cases. While the CA-absent case gets to a [CO_3^{2-}] maximum solely by increasing pH (and thus the fraction of CO_3^{2-} in DIC), the CA-present cases approaches a [CO_3^{2-}] maximum by the combined effects of DIC and pH increase. The contrast between these cases demonstrates the fundamental role CA plays in the carbon budget and calcification dynamics of the ECF.

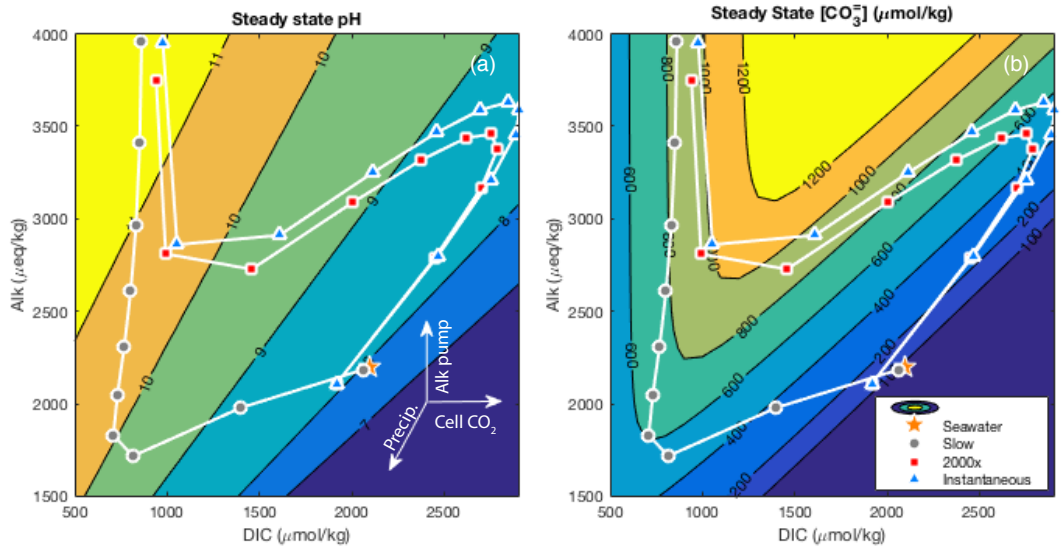

Figure 2-3 Steady state model solutions of DIC and alkalinity on pH and [CO_3^{2-}] contour plots for the slow kinetics (grey circles), instantaneous kinetics (blue triangles) and 2000× CA rate enhancement (red squares) cases. Each point represents a steady state solution to a given alkalinity pump rate. The pump rate increases along each path from the lower right corner to the upper left corner. The evolution paths are different for the slow kinetics case and the CA-enhanced case. The vectors represent the three major processes controlling the carbonate chemistry of the ECF in the model. The presence of CA increases the cell CO_2(aq) flux that generates higher DIC and buffers pH compared to the slow kinetics case.

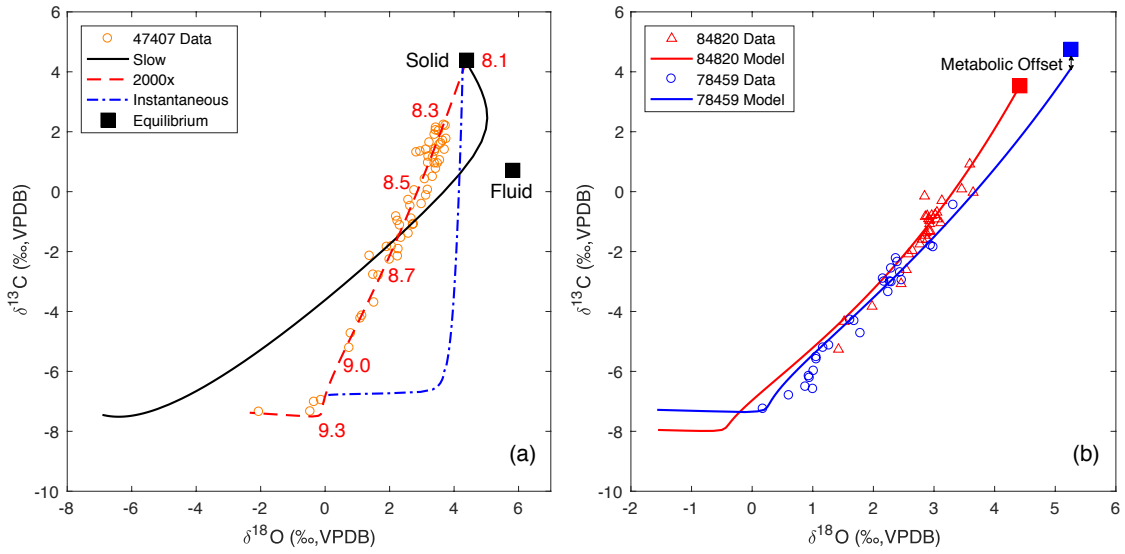

Figure 2-4 Model output of stable isotope compositions of coral skeletons. (a) Stable isotope composition of the coral skeleton from model output for the slow kinetics (black), instantaneous (blue) and 2000× CA rate enhancement (red) cases, compared to a deep-sea coral dataset (orange circles, Adkins et al., 2003). There is a systematic change in the slope of the $\delta^{18}O$-$\delta^{13}C$ trend with different CA activity. A 2000× CA rate enhancement generates a line that goes through the data. The model lines represent a series of steady state solutions with different alkalinity pump rates. An increase in pump rate drives the stable isotopes from the upper right corner (enriched values) to the lower left corner (depleted values). The black squares represent the steady state composition of the EIC and corresponding solid at zero pump rate. Isotope fractionation factors between the EIC and the solid carbonate based on inorganic experiments (Wang et al., 2013; Watkins et al., 2014; Watkins & Hunt, 2015) needs to be applied to make the model line go through the data. The red numbers mark the pH corresponding to the stable isotope compositions for the 2000× case. (b) Model fit to two other deep-sea corals (Adkins et al., 2003). The model lines are generated with all biological parameters the same as panel (a), including a 2000× CA rate enhancement, and varying only the ambient seawater conditions at each coral's collection site. A metabolic offset of 1‰ in $\delta^{13}C$ is applied to cross-membrane $CO_2(aq)$ (black arrow) to make the model line go through the data for coral 78459.

2.3.2 Stable Isotopes

Figure 2-4 shows the steady state isotope compositions of the skeleton as the alkalinity pump is turned up for the three cases presented in Figure 2-3. As the pH is elevated with the alkalinity pump, both $\delta^{18}O$ and $\delta^{13}C$ get more depleted. In all cases, there is a kink in the $\delta^{18}O$-$\delta^{13}C$ relation, but the kink shows up more clearly with the presence of CA. In addition, there is a systematic change in slope of the $\delta^{18}O$-$\delta^{13}C$ relationship, with a higher CA activity corresponding to a steeper slope. In the instantaneous kinetics case, the $\delta^{18}O$-$\delta^{13}C$ linear trend is close to being vertical. Data from deep-sea coral 47407 (Adkins et al., 2003) is best fit by a CA rate enhancement

of 2000× (Figure 2-4a). To test the robustness of the model, we also tried to fit different deep-sea coral datasets by only changing the ambient seawater conditions while holding the other parameters constant (Figure 2-4b). With the same set of parameters, our model also fits the stable isotope data of two other deep-sea corals. It should be noted that a $\delta^{13}C$ offset of 1‰ was applied to cross-membrane $CO_2(aq)$ for coral 78459 to make the model line go through the data. We suspect this reflects different fractions of ^{13}C-depleted metabolic CO_2 used for calcification. The fraction of metabolic carbon corresponding to a 1‰ $\delta^{13}C$ offset is estimated to be 6-7% of all $CO_2(aq)$, consistent with radiocarbon constraints of a maximum of 6-8% metabolic carbon contribution to the skeleton in *D.dianthus* (Adkins et al., 2002) . The effect of CA on the model fit to the stable isotope data again suggests its important role in the calcification process, and points towards a new mechanism for stable isotope vital effects.

2.4 Discussion of Model Results and Implications

2.4.1 CA and ECF carbonate chemistry

As shown above, the steady state DIC and alkalinity responses to increasing alkalinity pump diverge by adding CA to the model. Figure 2-5 shows the steady state carbonate chemistry variables of the ECF corresponding to different alkalinity pump rates (a different view of Figure 2-3), and further demonstrates this difference. In the slow kinetics case, the pH of the ECF rises rapidly from the seawater value to a pH of 10 at a very small increase in the pump rate, after which the pH rises more gradually (Figure 2-5a). These high pH values are dangerous to the corals as they would promote saponification of the lipid membranes. During the rapid pH rise, there is also a sharp decrease in DIC, but the pH effect dominates to drive a $[CO_3^{2-}]$ increase (Figure 2-5c). When CA is present, however, the pH of the ECF is much more strongly buffered with the alkalinity pump increase. There is a slow pH rise as the pump is turned up from zero until a pH around 9.3, the value of pK_{a2} at deep-sea coral growth conditions (5°C, 500 m), after which there is a sharp pH rise (Figure 2-5a). Between seawater pH and pK_{a2}, $[CO_3^{2-}]$ increases until a maximum value at the sharp pH jump (Figure 2-5c). Corresponding to this maximum $[CO_3^{2-}]$, there is also a dramatic decrease in the slope of the precipitation rate with pump rate (Figure 2-5f). In the model, $[CO_3^{2-}]$ is the dominant factor controlling the saturation state, and precipitation rate, in the ECF with a factor

of 5-6 change, as opposed to [Ca^{2+}] which changes by less than a factor of 2 (Figure 2-5d). Similar observations have been made in laboratory simulations of the biomineralization process (Zeebe & Sanyal, 2002). It has been previously suggested that pK_{a2} represents an energetic limit of biological pH elevation (Adkins et al., 2003). After pK_{a2}, the additional precipitation rate obtained from the ATP-driven alkalinity pump is minimal, as observed in our model. ECF pH measurements in surface corals have found few cases of pH above pK_{a2} (Al-Horani et al., 2003; Venn et al., 2011; Cai et al., 2016), consistent with this idea. The [CO_3^{2-}] maximum of ~1000 μmol/kg in our model (Figure 2-5c) also agrees with microelectrode measurements of ECF composition in surface corals (Cai et al., 2016). In addition, there is a range of pump rates in which the DIC of the ECF is elevated relative to seawater (Figure 2-5e). This biologically controlled DIC elevation in the ECF has been experimentally observed in some surface corals (Allison et al., 2014), but not in others (Cai et al., 2016). The difference in DIC concentrations in the ECF may reflect different alkalinity pump rates or CA activity among the coral species (Figure 2-5e).

The change in the ECF carbon budget with the presence of CA indicates a larger carbon flux from somewhere. Figure 2-6 shows the steady state fluxes controlling alkalinity, DIC, and EIC at different pump rates. As expected, the presence of CA drives large hydration and dehydration fluxes (Figure 2-6f), and an increasing imbalance of the two as the alkalinity pump is turned up. This imbalance keeps [CO_2(aq)] low in the ECF (Figure 2-5b), and creates a large [CO_2(aq)] gradient between the cell and ECF. As a result, the CO_2(aq) flux across the cell membrane is higher at low pump rates in the presence of CA (Figure 2-6e vs. 2-6b). As CO_2(aq) is rapidly converted to EIC, the cell flux helps concentrate DIC in the ECF, and maintains a relatively high DIC:Alk ratio so that the pH change is much more gradual. This cross-membrane CO_2(aq) flux also explains the DIC elevation in the ECF relative to seawater (Figure 2-5e), when precipitation is not fast enough to remove all the additional carbon. As the pump rate is further increased, precipitation starts to outcompete the cross-membrane flux to drive DIC down, but [CO_3^{2-}] can keep increasing due to pH elevation (Figure 2-5c, d). In contrast, CO_2(aq) cannot be effectively converted to EIC without CA at low pump rates, causing the ECF to be less buffered and the pH to be very sensitive to small increases in the alkalinity pump. The rapid pH rise in the slow kinetics case then shifts the CO_2(aq)-EIC conversion to the more efficient hydroxylation pathway, causing the cell flux to catch up and the pH to increase more gradually (Figure 2-6b, c). In both the slow

kinetics and CA-enhanced cases, there is a maximum cell CO_2(aq) flux, when CO_2(aq) in the ECF cannot be any lower (Figure 2-5b). After the threshold, the change in the ECF carbon budget can only be modulated by the seawater and precipitation fluxes, which has implications for the stable isotopes in the following discussions. This pH threshold is at pK_{a2} for the CA-enhanced case, as CO_2(aq) can be rapidly converted to EIC. The pH threshold is higher for the slow kinetics case, when there is a kinetic barrier to the CO_2(aq)-EIC conversion.

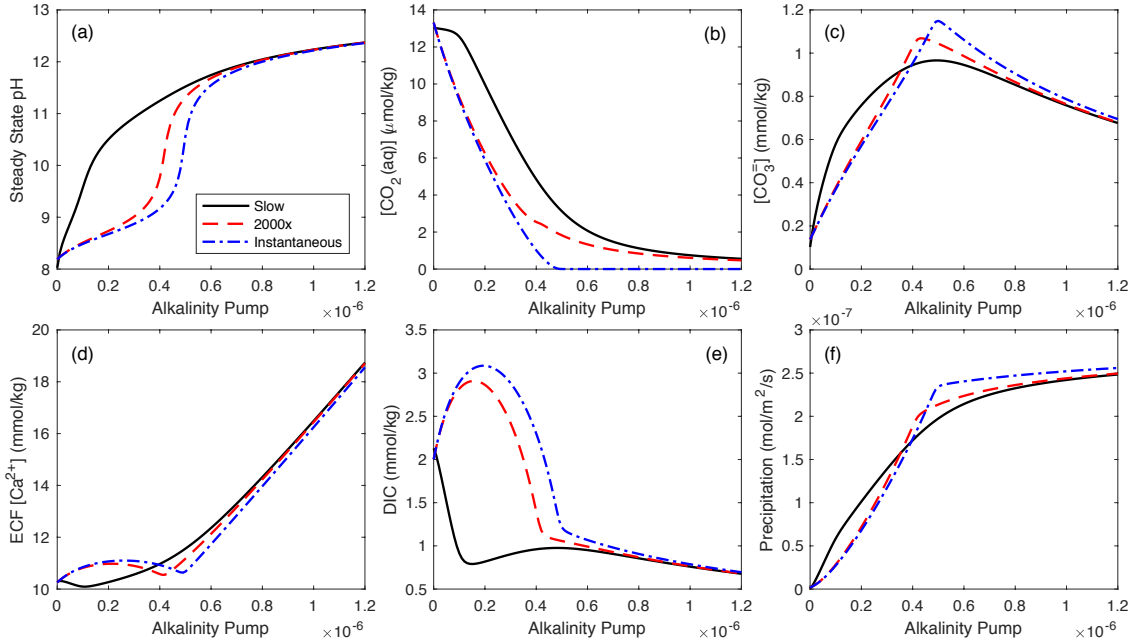

Figure 2-5 Steady state ECF carbonate chemistry as a function of the alkalinity pump strength (mol/m^2/s) for the slow kinetics (black), instantaneous kinetics (blue) and 2000× CA rate enhancement (red) cases. (a) The pH of the ECF is strongly buffered against the alkalinity pump with the presence of CA, up to a pH value of seawater pK_{a2} at 5°C (9.3). The pH of the slow kinetics case rises sharply at low pump rates. The model cases all converge when the pH is high enough for hydroxylation to be the dominant process in CO_2(aq)-EIC conversion. (b) With a kinetic barrier of CO_2(aq) hydration, the CO_2(aq) of the slow kinetics case pool in the ECF at low pump rates, and its rapid decrease lags the CA enhanced cases, until hydroxylation can convert it to EIC. (c) There is a maximum in [CO_3^{2-}] for all three cases, but the reasons for [CO_3^{2-}] increase are different. For the slow kinetics case, the [CO_3^{2-}] increase is caused by a sharp pH rise, while for the CA enhanced cases, the [CO_3^{2-}] increase is a combined result of DIC increase and pH rise. (d) The Ca^{2+} pumped into the ECF by Ca-ATPase is balanced by precipitation at low pump rates. At high pump rates, precipitation can no longer catch up with the pump, and [Ca^{2+}] increases rapidly. (e) CA concentrates DIC in the ECF relative to seawater over a range of alkalinity pump rates. (f) The precipitation rate increases with the pump rate, but there is a sharp change in the slope at the maximum [CO_3^{2-}] in (c) in all cases. Pumping alkalinity beyond the [CO_3^{2-}]$_{max}$ is energetically inefficient. Also the precipitation rate is more dependent on [CO_3^{2-}] than [Ca^{2+}], as has been previously suggested in laboratory simulation of biological calcification (Zeebe & Sanyal, 2002).

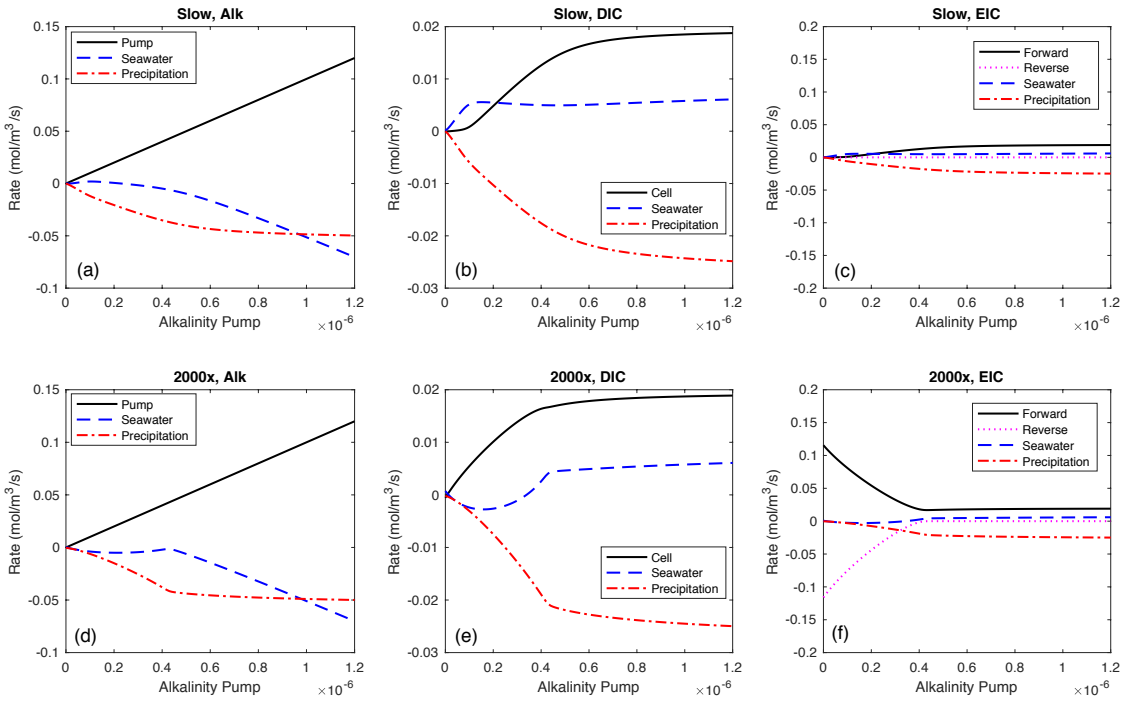

Figure 2-6 Flux balance at steady state for alkalinity, DIC and EIC at different pump rates. Panels (a)-(c) represent the slow kinetics case. Panels (d)-(f) represent the 2000× CA rate enhancement case. Seawater (blue dashed) and precipitation (red dot dashed) represent the tendency for ECF alkalinity, DIC and EIC to change with seawater transport and $CaCO_3$ precipitation. There is a source of alkalinity to the ECF by the Ca-ATPase pump (black solid in a and d), and a source of DIC from cross-membrane CO_2(aq) (black solid in b and e). EIC also feels the relative rates of the forward (hydration/hydroxylation, black solid in c and f) and reverse (dehydration/dehydroxylation, purple dotted in c and f) reactions of CO_2(aq)-EIC inter-conversion. The most apparent difference is the higher forward and reverse reaction rates for the 2000× case in the EIC fluxes. There is a larger imbalance between the forward and reverse reactions in the 2000× case that causes a low CO_2(aq) in the ECF. As a result, the gradient-driven cell CO_2(aq) flux increases more rapidly at low pump rates. This explains the DIC increase in Figure 2-5.

To summarize, our model has found two important roles CA plays in the biological calcification process as compared to slow kinetics: to concentrate DIC in the ECF for calcification, and to buffer the carbonate system of the ECF against unfavorably high pH as the alkalinity pump increases. CA releases the kinetic barrier to EIC production from CO_2(aq) that would otherwise pool in the ECF. By synthesizing CA for use in the calcification process, the calcifying organism can get a steady increase in ECF [CO_3^{2-}] and precipitation rate, in a chemical environment that does not saponify membrane lipids.

2.4.2 Isotope composition of coral skeleton

Figure 2-4 shows that a finite amount of CA activity generates a stable isotope model line that goes through the deep-sea coral data. A fit to the data requires three features to be correctly simulated: (1) the isotope composition at the $\delta^{18}O$ and $\delta^{13}C$ enriched end (equilibrium limit) of the dataset; (2) the slope of the $\delta^{18}O$-$\delta^{13}C$ linear correlation part; and (3) a kink in the $\delta^{18}O$-$\delta^{13}C$ relation that represents the COCs. The three parts are discussed separately below.

2.4.2.1 Biogenic vs. inorganic carbonates at the equilibrium limit

While the $\delta^{18}O$ and $\delta^{13}C$ proxies are based on equilibrium isotope effects, several processes can cause disequilibrium isotope effects in both inorganic precipitation experiments and biological calcification. Since the solid carbonate inherits its isotope composition from the DIC pool, the disequilibrium isotope effects can take place either in the DIC speciation process or in the solid formation process. Isotope exchange during DIC speciation is kinetically limited due to the slow CO_2(aq)-HCO_3^- inter-conversion, especially for oxygen isotopes because water is involved in the exchange (McConnaughey, 1989b; Zeebe & Wolf-Gladrow, 2001; Uchikawa & Zeebe, 2012). In the solid formation process, there is additional isotope fractionation due to ions attaching to and detaching from the solid surface, the net effect of which is reflected by the growth rate of the solid (Watkins et al., 2013). As a result, true carbonate-water isotope equilibrium can only be achieved when all the DIC species are in isotope equilibrium, and the growth of the solid is slow enough to prevent KIEs during precipitation. In a comprehensive survey of this problem, Watkins et al. (2014) used CA to facilitate the DIC species equilibrium, and did inorganic calcite precipitation experiments across a range of temperatures, pH and growth rates, to establish the full dependence of the calcite-water oxygen isotope fractionation on these factors. From the Watkins model, isotope fractionation factors can be obtained between the solid and the two EIC species, bicarbonate and carbonate ions. Similar inorganic precipitation experiments have also been performed for aragonite in seawater, and a new temperature dependent aragonite-water $\delta^{18}O$ fractionation equation was proposed at the equilibrium limit (Wang et al., 2013). Given our assumption that the isotope composition of the coral skeleton is determined by the EIC pool, we applied these fractionation factors to calculate the composition of the skeleton for all pump rates, and their associated $CaCO_3$ precipitation rates. Similar to oxygen isotopes, there is also a carbon isotope fractionation between the EIC species and the resulting solid (Romanek et al., 1992; Watkins & Hunt, 2015). For a pump

rate of zero, we expect the model to predict the inorganic $CaCO_3$ isotope composition at the corresponding growth rate, which is within the equilibrium limit in the Watkins model. The solid squares in Figure 2-4a show the solid-EIC fractionations at the equilibrium limit, with the oxygen isotope fractionation factors from Wang et al. (2013) for aragonite. Applying these offsets between the solid and fluid is necessary to generate a line that goes through the data. Without these fractionation factors, the modeled EIC composition is too depleted in $\delta^{13}C$ and too enriched in $\delta^{18}O$. As a result, the biogenic carbonates provide a confirmation to the fractionation factors derived in inorganic experiments and the ion-by-ion growth model (Wang et al., 2013; Watkins et al., 2014).

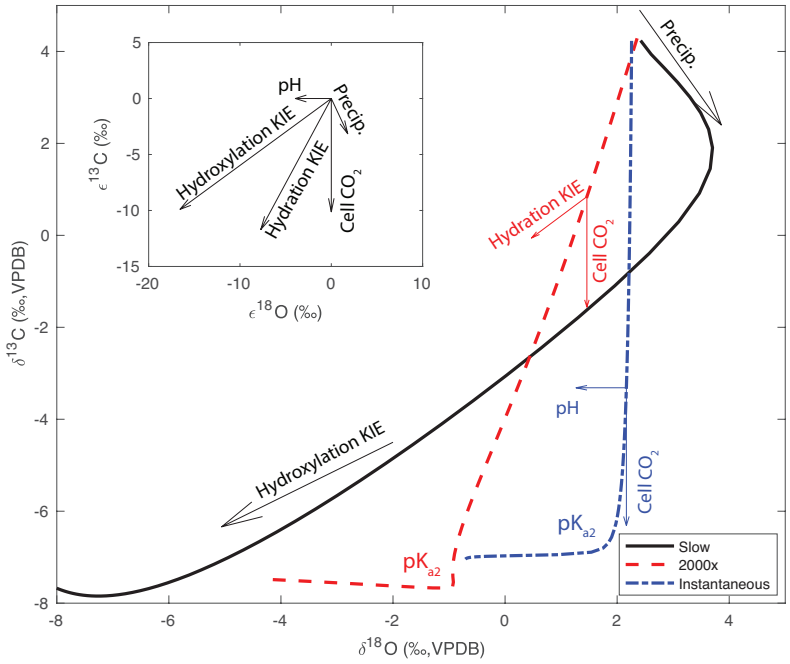

Figure 2-7 Decomposition of different isotope fractionation processes in the model results. The inset vector plot shows the isotope effects of five important processes in the model: pH-driven DIC speciation, input of cross-membrane CO_2(aq), hydration, hydroxylation and the Rayleigh effect by precipitation. The slow kinetics case shows two dominant processes at different ranges of pump rates. At low pump rates, a limited carbon supply from membrane crossing CO_2 creates the Rayleigh effect by precipitation. At high pump rates, high pH converts CO_2(aq) to HCO_3^- via the hydroxylation pathway and expresses the associated KIE. The presence of CA takes away the Rayleigh process by efficiently converting CO_2(aq) to HCO_3^- and providing a second source of carbon besides seawater. For instantaneous kinetics, the oxygen isotopes follow equilibrium DIC speciation, while the carbon fractionation is determined by the relative contribution of cell CO_2(aq) and seawater DIC. A maximum cell CO_2(aq) flux at pK_{a2} causes a kink in the correlation, and makes the slope too steep compared to the data. For a finite amount of CA such as the 2000× case, the hydration KIE is partly expressed. The amount of CA changes the timescale of DIC oxygen isotope equilibration, and determines how much hydration KIE is preserved in the skeleton, thus influencing the $\delta^{18}O$-$\delta^{13}C$ slope.

2.4.2.2 CA and the $\delta^{18}O$-$\delta^{13}C$ slope

As observed by McConnaughey (1989a), a wide variety of marine calcifying organisms show a linear correlation between $\delta^{18}O$ and $\delta^{13}C$ with a relatively narrow range of slopes (Figure 2-1). In our model, we tested a range of CA activities, and observed a systematic change in the $\delta^{18}O$-$\delta^{13}C$ slope, with higher CA activity corresponding to steeper slopes (Figure 2-4). In our flux balance model, it is possible to disentangle what roles different isotope fractionation processes play in setting the slope. The inset vector plot in Figure 2-7 shows the five important processes that fractionate carbon and oxygen isotopes from the seawater EIC composition. Two of these processes represent equilibrium isotope effects. The horizontal arrow to the left represents the equilibrium oxygen isotope effect from pH driven DIC speciation. Although the equilibrium carbon isotope compositions of DIC species are different, it is a closed system in terms of isotope exchange, and significant changes in EIC $\delta^{13}C$ can only be caused by a change in total $\delta^{13}C$ of the DIC pool. The $\delta^{13}C$ of the DIC in the ECF is set by the mixing of two carbon pools with distinct $\delta^{13}C$ values: membrane-crossing CO_2(aq) and seawater DIC. With a pH increase in the ECF, a larger contribution from membrane-crossing ^{13}C-depleted CO_2(aq) lowers the $\delta^{13}C$ of DIC, as represented by the vertical downward arrow. The Adkins model for stable isotope vital effects is a coupling of these two equilibrium processes through pH elevation, with a kink in the correlation as the carbon isotope mixing effect is maximized at pK_{a2}.

The other three processes shown in Figure 2-7 that fractionate isotopes are kinetic processes. Both hydration and hydroxylation of CO_2(aq) create $\delta^{18}O$ and $\delta^{13}C$ depleted EIC, which represent the McConnaughey mechanism of stable isotope vital effects. McConnaughey (1989b) attributed the range of $\delta^{18}O$ and $\delta^{13}C$ observed in biogenic carbonates to different degrees of equilibrium exchange of CO_2(aq) across the ECF membrane. However, since the timescale for carbon isotope exchange (10-100 s) is much shorter than for oxygen isotopes (10^3-10^4 s) (Zeebe & Wolf-Gladrow, 2001; Uchikawa & Zeebe, 2012), the magnitude of carbon isotope hydration/hydroxylation KIE expressed in the resulting solid is expected to be smaller than the oxygen isotopes, given a DIC residence time of 10^2~10^3 s with respect to precipitation. This changes both the magnitude and angle of the hydration/hydroxylation fractionation vectors. An additional kinetic fractionation process happens during precipitation of the skeleton. According to the ion-by-ion growth model (Watkins et al., 2014; Watkins & Hunt, 2015), the precipitating

$CaCO_3$ is enriched in ^{13}C and depleted in ^{18}O relative to the EIC pool in the range of growth rates in our model. This could create a residual EIC that is more depleted in ^{13}C and enriched in ^{18}O through a Rayleigh distillation process by precipitation when carbon supply is limited to seawater at low pump rates and no CA. This process could cause a negative slope in the $\delta^{18}O$-$\delta^{13}C$ correlation, which has not received much consideration in previous models of biomineralization. The Rayleigh process can also give rise to more enriched $\delta^{18}O$ values in biogenic carbonates than inorganic precipitation experiments in the equilibrium limit, although other mechanisms such as rapid incorporation of ^{18}O enriched $CO_2(aq)$ have been suggested to explain observed $\delta^{18}O$ enrichments in organisms like coccolithophore (Hermoso et al., 2014; Hermoso et al., 2016).

The $\delta^{18}O$-$\delta^{13}C$ patterns simulated in our model can be decomposed into the different fractionation processes discussed above (Figure 2-7). For the slow kinetics case, the coral derives most of its carbon for precipitation from seawater DIC at low pump rates, due to the kinetic barrier of $CO_2(aq)$ hydration and low membrane-crossing $CO_2(aq)$ flux. As a result, the precipitation from seawater DIC causes the Rayleigh effect to be expressed in the $CaCO_3$. The Rayleigh effect dominates the $\delta^{18}O$-$\delta^{13}C$ slope until the pH is high enough for hydroxylation to efficiently convert $CO_2(aq)$ to HCO_3^-, after which the hydroxylation KIE is expressed. For the instantaneous kinetics case, CA can catalyze rapid $CO_2(aq)$-HCO_3^- inter-conversion and isotope exchange through hydration/dehydration, so that no hydration KIE is expressed. As a result, what ends up being expressed in the skeleton is the equilibrium isotope effects through pH-driven DIC speciation and carbon source mixing. In the presence of abundant CA, the coral can also take full advantage of the cross-membrane carbon source, so that the Rayleigh effect from precipitation is largely reduced. However, the kink in the $\delta^{18}O$-$\delta^{13}C$ correlation at pK_{a2} makes the slope too steep compared to the deep-sea coral data. The 2000× rate enhancement model case that fits the data in Figure 2-4 is an intermediate case with a finite amount of CA. In this case, the $CO_2(aq)$ hydration KIE is partly expressed for oxygen isotopes (4‰), and to a lesser extent for carbon isotopes (2‰) due to faster isotope equilibration. The observed 10‰ range in deep-sea coral $\delta^{13}C$ is mostly a result of the mixing of cross-membrane $CO_2(aq)$ and seawater DIC, which accounts for 8‰ of the signal. In our model this data-fitting case suggests that the McConnaughey KIE mechanism dominates the observed $\delta^{18}O$ signal, while the Adkins mechanism explains most of the range in $\delta^{13}C$ and the COC kink in deep-sea corals.

The analysis of the fractionation processes for the data-fitting case also provides clues to the role of CA activity in setting the $\delta^{18}O$-$\delta^{13}C$ slope. CA can enhance the CO_2-EIC inter-conversion and shorten the timescale of DIC oxygen isotope equilibration (Uchikawa & Zeebe, 2012). In laboratory experiments, 0.25 μM of CA can shorten the oxygen isotope equilibration timescale by 2-3 orders of magnitude (Uchikawa & Zeebe, 2012; Watkins et al., 2013). As a result, it is expected that the presence of CA in the coral ECF can reduce the magnitude of the oxygen isotope KIE. However, since synthesis of CA costs the coral energy, it is reasonable to assume a finite amount of CA in the ECF, so that the KIE signal of CO_2-EIC conversion is not totally erased. The forward reactions of hydration/hydroxylation make isotopically depleted EIC, and the backward reactions drive the isotope exchange to equilibrium. A metric for the completeness of oxygen isotope exchange is the ratio of the rate of the reverse reactions to the forward reactions. A ratio of one represents equilibrium exchange, while a small ratio represents significant KIE that makes isotopically depleted EIC. This ratio decreases with pH, because higher pH favors the forward reactions as opposed to the backward reactions. Figure 2-8b shows how this metric changes with alkalinity pump rate for both the slow kinetics and CA-enhanced cases, and the associated change in oxygen isotopes. We can see that the presence of CA makes the reverse to forward reaction ratio decrease much more gradually with an increasing alkalinity pump, thus reducing the KIEs expressed in the resulting skeleton. In the slow kinetics case, the ratio drops rapidly with increasing pump rate, and the KIEs are much more significant. As a consequence, the magnitude of the KIE driven $\delta^{18}O$ depletion in the slow kinetics case is much larger, and the $\delta^{18}O$-$\delta^{13}C$ slope is shallower for the same range in $\delta^{13}C$. The rate enhancement factor of 2000 that fits the deep-sea coral dataset may represent an optimal amount of CA the organism decided to synthesize for its growth needs and energy budget. At 5°C, the $CO_2(aq)$ hydration rate constant in seawater is 4×10^{-3} s^{-1} (Johnson, 1982), and a 2000 rate enhancement factor would correspond to a rate constant of 8 s^{-1}. Measurements of CA activity in symbiotic corals constrain a Michealis-Menten constant (k_{cat}/K_M) of 4.6-8.3$\times10^7$ $M^{-1}\cdot s^{-1}$, (Moya et al., 2008; Bertucci et al., 2011). The 2000 times rate enhancement requires sub-micromolar CA concentration in the ECF. However, *in vivo* experiments have shown that certain amino acids and amines act as CA activators and increase CA activity (Bertucci et al., 2010). In surface coral tissue homogenate, the measured CA-catalyzed hydration rate constant is ~50 s^{-1}, although it was unclear how CA activity is distributed

between photosynthesis and calcification (Hopkinson et al., 2015). An in-situ measurement of CA activity in deep-sea corals may help test our model.

Given that CA activity changes the slope of the $\delta^{18}O$-$\delta^{13}C$ linear correlation, we can explain the range of $\delta^{18}O$-$\delta^{13}C$ slopes observed in marine calcifying organisms with the natural variability of CA activities. Figure 2-9 shows a range of CA-induced CO_2 hydration rate enhancements with their associated $\delta^{18}O$-$\delta^{13}C$ slopes in our model. The range of slopes observed in deep-sea corals (1.9-2.6) correspond to a wide range of CA catalyzed rate enhancement (200-2000×). When the environment is changed to surface ocean conditions (T=25°), the CA rate enhancement required for a similar observed $\delta^{18}O$-$\delta^{13}C$ slope range still spans an order of magnitude, between 20 and 200×. With higher temperatures and saturation states in the surface ocean, the precipitation rate is an order of magnitude higher in our model. As a result, it is expected that surface ocean calcifying organisms do not need as much CA, and its associated higher DIC concentration in the ECF. In addition, a temperature rise also facilitates the DIC speciation and oxygen isotope exchange kinetics (Beck et al., 2005; Watkins et al., 2013), which compensates for a lower amount of CA in setting the $\delta^{18}O$-$\delta^{13}C$ slope. Although CA has been shown to influence calcification of many marine calcifying organisms (Hentunen et al., 2000), not every species in Figure 2-1 has been analyzed for CA in its calcifying region. So caution should be applied in applying our model before the enzyme activity is confirmed or denied. In addition, our model does not account for the effect of photosynthesis on the carbon budget. Photosynthetic organisms, or those with photo-symbionts, can have an additional enrichment in $\delta^{13}C$ due to preferential uptake of ^{12}C in photosynthesis, leading to a shallower $\delta^{18}O$-$\delta^{13}C$ slope (McConnaughey, 1989a), or generally more scattered data.

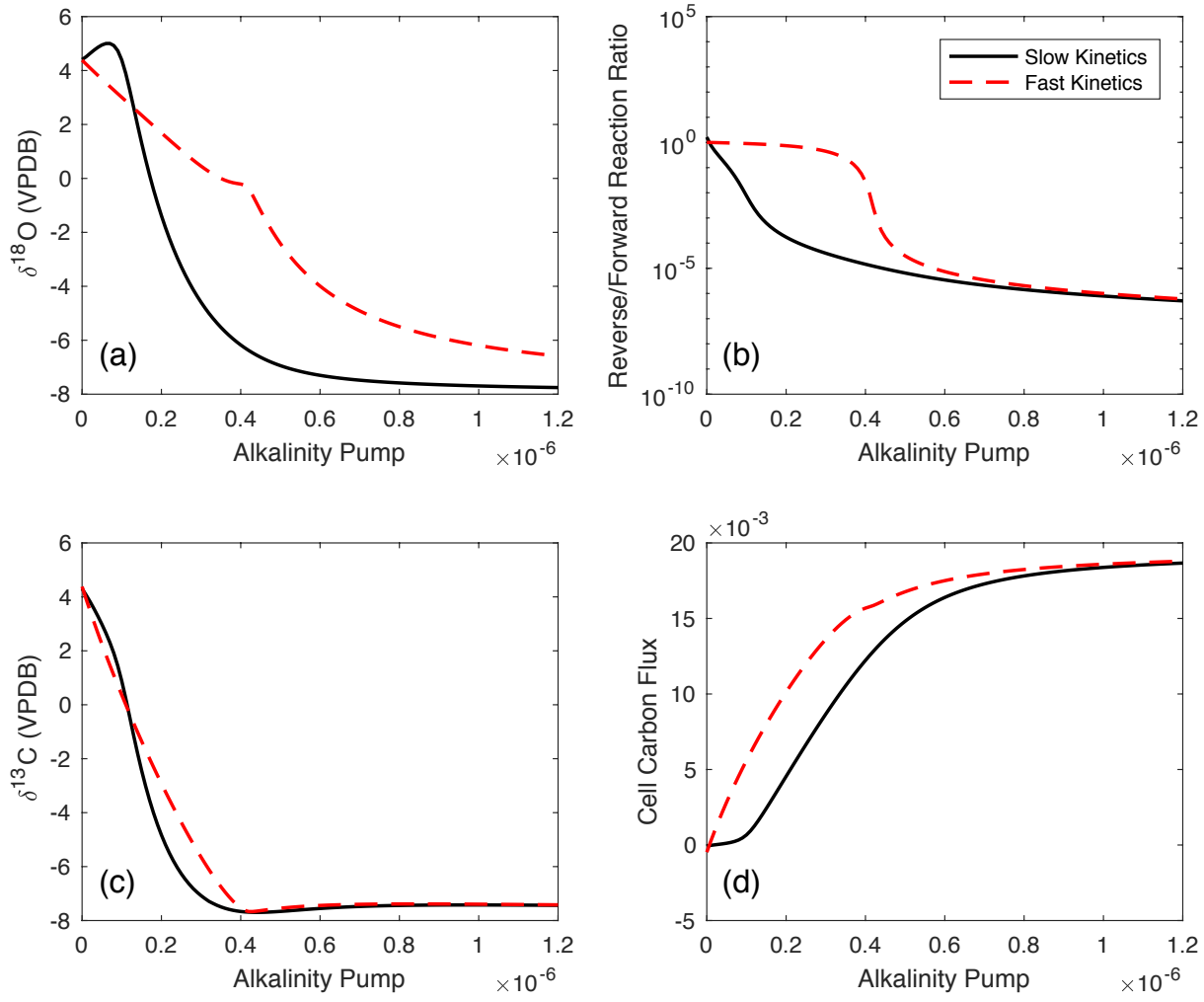

Figure 2-8 Processes that determine the isotope composition of the skeleton as a function of the alkalinity pump. The left column describes the isotope evolution of the skeleton for $\delta^{18}O$ and $\delta^{13}C$ respectively. The right column describes the main control on isotope compositions. (a-b) The range in $\delta^{18}O$ observed is mainly caused by KIEs during the CO_2(aq)-EIC inter-conversion. A measurement of the degree of oxygen isotope exchange is the ratio of reverse to forward reaction rates. A ratio of 1 represents equilibrium exchange, while smaller ratios cause stronger expression of KIEs. The presence of CA increases the exchange ratio for a given pump rate, and attenuates the $\delta^{18}O$ depletion by KIEs. (c-d) The observed $\delta^{13}C$ range is caused by the mixing of isotopically enriched seawater DIC and isotopically depleted cell CO_2(aq). As the alkalinity pump is turned up, more CO_2(aq) is converted to EIC, driving a larger cell CO_2(aq) flux. The cell CO_2(aq) is maximized beyond a threshold, causing a minimum in $\delta^{13}C$, and a kink in the $\delta^{18}O$-$\delta^{13}C$ relation.

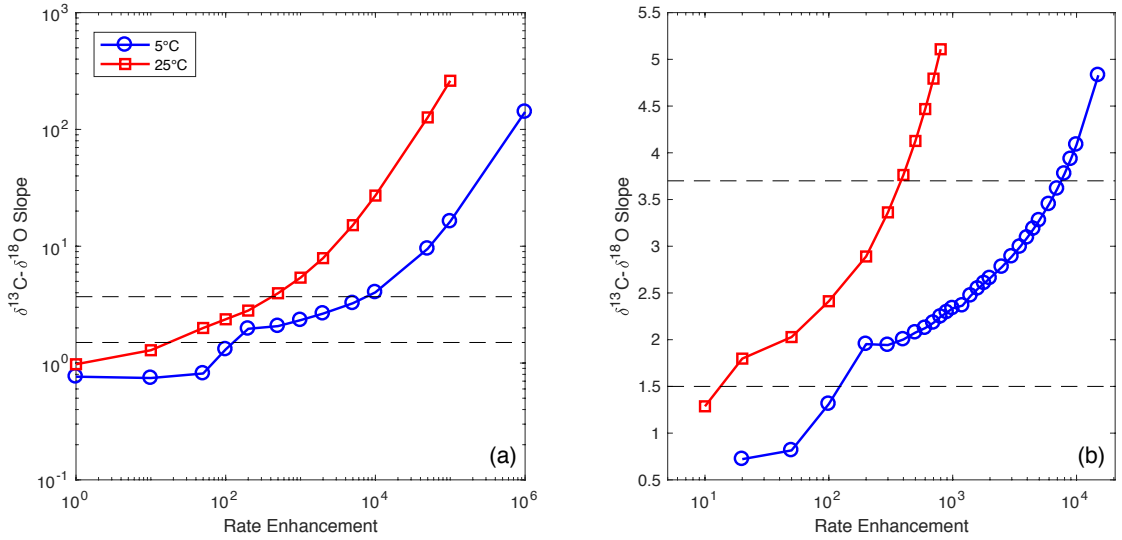

Figure 2-9 $\delta^{18}O$-$\delta^{13}C$ slope vs. CA activity. (a) The $\delta^{18}O$-$\delta^{13}C$ slope vs. CA rate enhancement factor (k_{cat}) for deep-sea coral (blue circles, 5°C) and surface ocean (red squares, 25°C) conditions. The dashed lines show the range of slopes (1.5-3.7) observed in different non-photosynthetic calcifying organisms. Panel (b) shows this range in more detail. In general, the slope increases with CA activity. The CA activity required for 25°C is lower than 5°C to have the same range of slopes. There is significant curvature in the $\delta^{18}O$-$\delta^{13}C$ plot at low CA activity that causes sharp turning points in these curves.

2.4.2.3 The $\delta^{18}O$-$\delta^{13}C$ kink

The observation that the isotope compositions of COCs in *D.dianthus* falls off the linear $\delta^{18}O$-$\delta^{13}C$ trend led Adkins et al. (2003) to propose an alternative mechanism for vital effects to McConnaughey's (1989a) KIE interpretation. The distinct isotope compositions of COCs have also been observed in other deep-sea coral species (Rollion-Bard et al., 2003; Blamart et al., 2007; Rollion-Bard et al., 2010), as well as surface corals (Juillet-Leclerc & Reynaud, 2010). Mineralogical analyses of the deep-sea coral skeletons show that both the COCs and the secondary structures are aragonite, but microscopic observations show that the COCs have more random orientation compared to c-axis aligned secondary aragonite (Gladfelter, 1984; Gagnon et al., 2007; Rollion-Bard et al., 2010; Von Euw et al., 2017). In addition to stable isotopes, the COCs also have distinct trace element concentrations compared to the secondary aragonite, including higher Mg/Ca and Li/Ca (Gagnon et al., 2007; Case et al., 2010), and lower B/Ca (Blamart et al., 2007) and U/Ca (Robinson et al., 2006). These observations have led to debate about whether the COCs formed with the same mechanism as the secondary aragonite or not.

Our stable isotope model can generate a continuous $\delta^{18}O$-$\delta^{13}C$ curve that includes both the linear relation and the kink. As proposed by Adkins et al. (2003), the mechanism of the kink is a maximum in the $\delta^{13}C$ depleted cell CO_2(aq) flux when the pH of the ECF reaches pK_{a2}. After this threshold, the $\delta^{18}O$ can keep getting more depleted due to an increasing imbalance of the forward and reverse CO_2(aq)-EIC inter-conversion reactions, but the $\delta^{13}C$ cannot get more depleted (Figure 2-8c, d). Instead, the $\delta^{13}C$ in our model gets slightly enriched after pK_{a2} due to an increasing seawater DIC influx.

Although we have a model that explains most of the features in the deep-sea coral stable isotope dataset, some caveats remain that require further investigation. A problem with our interpretation of COCs as forming from the same calcification mechanism as secondary aragonite is the corresponding pH. In our current model, the depleted $\delta^{18}O$ of the COCs correspond to a pH of 11, which is beyond the $[CO_3^{2-}]_{max}$ in Figure 2-5, and is also biologically unreasonable in a membrane supported ECF system. There are some other possibilities that could explain the composition of the COC. One is that the COCs formed from calcification rates that are distinctly higher than inorganic experiments during the early life stage of the corals. In order to initiate the calcification process, additional energy may be used by the organisms to synthesize organic templates that facilitate the skeleton growth rate (Cuif & Dauphin, 2005; De Yoreo et al., 2007). If the growth rate of the COCs were an order of magnitude higher than inorganic experiments due to organic templating, we could explain an additional 1‰ depletion in $\delta^{18}O$ in the COC at pK_{a2} (Watkins et al., 2013). An alternative explanation involves the role of amorphous calcium carbonate (ACC) in biomineralization. It has been suggested that calcifying organisms can take advantage of the disordered structure of ACC to increase growth rates at early stages of calcification (Addadi et al., 2003), and later transform ACC into more stable calcite or aragonite. ACC has been observed in a variety of calcifying organisms (Jacob et al., 2008; Gago-Duport et al., 2008; Gong et al., 2012). Although no direct evidence of ACC has been reported for deep-sea corals, the distinct microscopic structure, as well as isotopic and trace element composition of COCs have led some authors to suggest the role of ACC as the precursor phase of the skeleton (Rollion-Bard et al., 2010; Von Euw et al., 2017). The trace element compositions of the coral COCs are in many ways similar to ACC observed in other organisms (Jacob et al., 2008). In addition, a recent study of ACC in speleothems suggests that ACC is depleted in $\delta^{18}O$ relative to

companion calcite by 2.4±0.8‰ (Demeny et al., 2016). As a result, the composition of COC aragonite could also be explained as an inherited signal from its ACC precursor. More detailed studies of the coral skeleton structures and characterization of ACC in biogenic carbonates are required to resolve this problem.

2.4.3 Parameter sensitivity and other calcifying organisms

We have shown that our model can fit the stable isotope data from several different deep-sea corals with a single set of parameters (Figure 2-4), and discussed in detail the effect of CA on the $\delta^{18}O$-$\delta^{13}C$ slope. Yet, there are other tunable parameters in our model that may change the results. Two important biological parameters are the diffusivity of $CO_2(aq)$ in the calicoblastic cell membranes, and the rate of seawater DIC turnover in the ECF. These two parameters determine the relative contribution of the two carbon sources for coral calcification, and may have significant impacts on the resulting isotope composition of the skeleton. A seawater DIC turnover timescale that fits the observed range in deep-sea coral $\delta^{13}C$ is 230 seconds for the cell diffusivity we used (Sultemeyer & Rinast, 1996). Figure 2-10 shows example model outputs corresponding to different cell diffusivities and seawater turnover timescales. Increasing the cell diffusivity or decreasing the seawater turnover timescale can make the pH of the ECF more strongly buffered against the alkalinity pump. Changing the relative rate of these two fluxes also changes the range of $\delta^{13}C$ calculated by the model, due to the distinct isotope composition of the two carbon sources. However, in the parameter range we explored, the difference between the slow kinetics case and the CA-enhanced case always exists (as in Figure 2-4 and 2-5). Including CA rate enhancement in our model is necessary to generate reasonable ECF chemistry and stable isotope results that fit the data. In addition, some features in the model are robust with a range of parameter sets, including the maximum in $[CO_3^{2-}]$, the $\delta^{18}O$-$\delta^{13}C$ slope with a particular CA rate enhancement, and a $\delta^{18}O$-$\delta^{13}C$ kink. It should be noted that the kink is a persistent feature in the model as long as the pH of the ECF reaches pK_{a2} of seawater. The fact that the kink is lacking in other surface calcifying organisms may suggest that they do not raise their pH as much as the deep-sea corals.

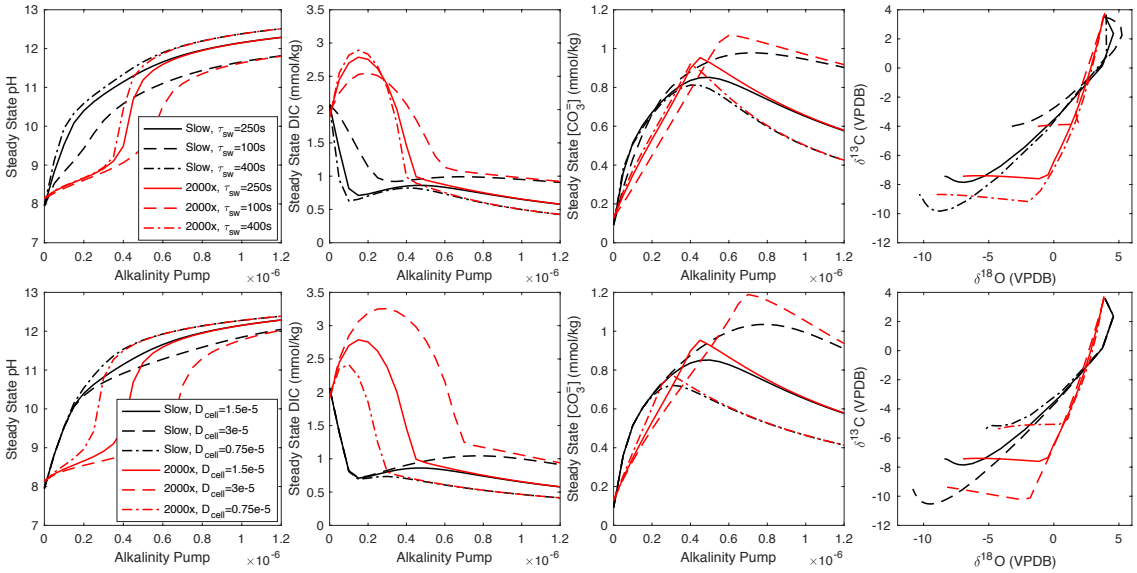

Figure 2-10 Model sensitivity to biological parameters. The top row shows the sensitivity of important variables to the seawater turnover timescale. The bottom row shows the sensitivity of the same variables to CO_2 diffusivity in cell membranes. The black curves show the slow kinetics case, while the red curves show the 2000× CA enhanced case. Faster seawater turnover or higher cell diffusivity makes the pH of the ECF more strongly buffered. In the parameter range explored, the differences in the shape of the pH, DIC and $[CO_3^{2-}]$ curves remain for the slow kinetics and CA enhanced cases, showing the robustness of the model results. Changing the two parameters causes a change in the range of $\delta^{13}C$ in the model, but does not change the $\delta^{18}O$-$\delta^{13}C$ slope significantly. The $\delta^{18}O$-$\delta^{13}C$ kink is also a robust feature in the model, though the $\delta^{13}C$ value of the kink is a strong function of the balance of the seawater and cell carbon flux.

Examining the sensitivity of our model to biological parameters may help us understand the isotope composition of other marine calcifiers. Different calcifiers may change their membrane permeability to adjust their carbon budget. The seawater turnover timescales may also be different for different organisms, due to wide variance in the geometry of the calcification space and its access to the surrounding seawater. The seawater turnover timescale has important implications for paleoclimate reconstructions as it determines how much of the ambient environmental signal can be recorded in the biogenic carbonates. For example, in a culture experiment by Spero et al. (1997), it was observed that both $\delta^{18}O$ and $\delta^{13}C$ in foraminifera shells decreased with increasing carbonate ion concentration in the ambient seawater. The slope of $\delta^{18}O$ vs. $[CO_3^{2-}]$ was explained by Zeebe (1999) as the equilibrium isotope effect of pH-driven DIC speciation, and modified by Watkins et al. (2014) as a combined effect of pH and carbonate growth rate. The slope of $\delta^{13}C$ vs. $[CO_3^{2-}]$ in the culture experiment, however, varies from -0.006‰ to -0.014‰ per μmol/kg $[CO_3^{2-}]$ between

different species, and is steeper than the $\delta^{18}O$-$[CO_3^{2-}]$ slope of -0.002‰ per μmol/kg $[CO_3^{2-}]$. In our model, the $\delta^{13}C$-$[CO_3^{2-}]$ slope can be simulated at a constant alkalinity pump rate, when the seawater turnover timescale is shortened to <100 s, the CA rate enhancement factor is <100, and with a significant amount (>50%) of $\delta^{13}C$-depleted metabolic CO_2 involved in the calcification process. In this case, the cell CO_2(aq) flux can respond readily to changes in seawater CO_2(aq) in the culture conditions. The necessity to include metabolic CO_2 to produce the $\delta^{13}C$ vs. $[CO_3^{2-}]$ slope is consistent with a diffusion-reaction model proposed by Zeebe et al. (1999), although their model requires a response of respiration to changes in ambient Alk:DIC ratio. The more rapid seawater turnover in foraminifera suggested by our model may also explain why their shells are good paleoceanographic archives. Details of a foraminifera based calcification model will be presented in a separate paper.

2.5 Conclusions

We have developed a fully kinetic model of biomineralization based on deep-sea corals that can explain the trends in skeletal $\delta^{18}O$ and $\delta^{13}C$. We found that carbonic anhydrase plays an important role in the calcification process, because it buffers the pH and concentrates carbon in the ECF. The existence of carbonic anhydrase also influences the oxygen isotope exchange kinetics, and changes the $\delta^{18}O$-$\delta^{13}C$ slope in the skeleton. A particular CO_2(aq) hydration rate enhancement by CA in the model produces a tight fit to the deep-sea coral stable isotope data, when the correct fractionation factors between the solid carbonate and DIC species are applied. This fit works across multiple different deep-sea corals with minimal changes in the model parameters. Variability in natural CA activity may explain the range of $\delta^{18}O$-$\delta^{13}C$ slopes observed in different marine calcifying organisms. In addition, the kink in $\delta^{18}O$-$\delta^{13}C$ found in COCs of deep-sea corals is a robust feature of pH up-regulation beyond pK_{a2} in our model, the mechanism of which requires further investigation. The extension of our model to organisms other than deep-sea corals shows some prospects for a ubiquitous mechanism for stable isotope vital effects. Better biomineralization models with carbonate chemistry dynamics can not only help us develop better paleoceanographic tracers, but also advance our understanding of biological calcification response to future climate change.

2.6 Appendix: Differential Equations in the Model

Our model tracks the following chemical and isotope exchange reactions:

$$CO_2 + H_2O \overset{k_{+1}/k_{-1}}{\Longleftrightarrow} H^+ + HCO_3^-$$

$$CO_2 + OH^- \overset{k_{+4}/k_{-4}}{\Longleftrightarrow} HCO_3^-$$

$${}^{13}CO_2 + H_2O \overset{k'_{+1}/k'_{-1}}{\Longleftrightarrow} H^+ + H^{13}CO_3^-$$

$${}^{13}CO_2 + OH^- \overset{k'_{+4}/k'_{-4}}{\Longleftrightarrow} H^{13}CO_3^-$$

$$CO_2 + H_2^{18}O \overset{a_{+1}/a_{-1}}{\Longleftrightarrow} H^+ + HC^{18}OO_2^-$$

$$CO_2 + {}^{18}OH^- \overset{a_{+4}/a_{-4}}{\Longleftrightarrow} HC^{18}OO_2^-$$

$$C^{18}OO + H_2O \overset{b_{+1}/b_{-1}}{\Longleftrightarrow} H^+ + HC^{18}OO_2^-$$

$$C^{18}OO + OH^- \overset{b_{+4}/b_{-4}}{\Longleftrightarrow} HC^{18}OO_2^-$$

Following Zeebe & Wolf-Gladrow (2001), rate constants with subscripts +1 and -1 correspond to hydration and dehydration reactions, while subscripts +4 and -4 correspond hydroxylation and dehydroxylation reactions. Constants for ^{13}C substituted species are denoted as k'. Constants for ^{18}O substituted species are denoted 'a' or 'b,' with 'a' representing substitution on H_2O or OH^-, and 'b' representing substitution on CO_2. The ratios for these rate constants are equal to the equilibrium constants of the reactions, and are listed in Table 2.1.

As shown in Figure 2, the model tracks the evolution of carbonate chemistry and the isotopically substituted species with time toward steady state. There are eight differential equations in the model as listed below:

$$(1)\ \frac{d[CO_2]}{dt} = -(k_{+1} + k_{+4}[OH^-])[CO_2] + (k_{-1}[H^+] + k_{-4})[EIC]\chi_1 + \frac{D_{cell}}{z}([CO_2]_{cell} - [CO_2]) + \frac{1}{\tau_{sw}}([CO_2]_{sw} - [CO_2])$$

$$(2)\ \frac{d[EIC]}{dt} = (k_{+1} + k_{+4}[OH^-])[CO_2] - (k_{-1}[H^+] + k_{-4})[EIC]\chi_1 + \frac{1}{\tau_{sw}}([EIC]_{sw} - [EIC]) - \frac{F_{CaCO_3}}{z}$$

$$(3)\ \frac{d[Alk]}{dt} = \frac{1}{\tau_{sw}}([Alk]_{sw} - [Alk]) + \frac{1}{z}(F_{Alk} - 2F_{CaCO_3})$$

$$(4)\ \frac{d[Ca^{2+}]}{dt} = \frac{1}{\tau_{sw}}([Ca^{2+}]_{sw} - [Ca^{2+}]) + \frac{1}{z}(\frac{1}{2}f_{Ca}F_{Alk} - F_{CaCO_3})$$

$$(5)\ \frac{d[^{13}CO_2]}{dt} = -(k'_{+1} + k'_{+4}[OH^-])[^{13}CO_2] + (k'_{-1}[H^+] + k'_{-4})[^{13}EIC]^{13}\chi_1 + \frac{D_{cell}}{z}\frac{1}{\alpha_{diff}}\left(^{13}R_{CO_{2(cell)}}[CO_2]_{cell} - [^{13}CO_2]\right) + \frac{1}{\tau_{sw}}(^{13}R_{CO_{2(sw)}}[CO_2]_{sw} - [^{13}CO_2])$$

$$(6)\ \frac{d[^{13}EIC]}{dt} = (k'_{+1} + k'_{+4}[OH^-])[^{13}CO_2] - (k'_{-1}[H^+] + k'_{-4})[^{13}EIC]^{13}\chi_1 + \frac{1}{\tau_{sw}}\left(^{13}R_{EIC_{(sw)}}[EIC]_{sw} - [^{13}EIC]\right) - \frac{1}{z}F_{CaCO_3}\frac{[^{13}EIC]}{[EIC]}{}^{13}\alpha_{CaCO_3-EIC}$$

$$(7)\ \frac{d[C^{18}OO]}{dt} = -(b_{+1} + b_{+4}[OH^-])[C^{18}OO] + (b_{-1}[H^+] + b_{-4})[^{18}EIC]^{18}\chi_1 + \frac{D_{cell}}{z}\frac{1}{\alpha_{diff}}\left(^{18}R_{CO_{2(cell)}}[CO_2]_{cell} - [C^{18}OO]\right) + \frac{1}{\tau_{sw}}(^{18}R_{CO_{2(sw)}}[CO_2]_{sw} - [C^{18}OO])$$

$$(8)\ \frac{d[^{18}EIC]}{dt} = \frac{2}{3}(b_{+1} + b_{+4}[OH^-])[C^{18}OO] - \frac{2}{3}(b_{-1}[H^+] + b_{-4})[^{18}EIC]^{18}\chi_1 + \frac{1}{3}(a_{+1}{}^{18}R_{H_2O} + a_{+4}{}^{18}R_{OH}[OH^-])[CO_2] - \frac{1}{3}(a_{-1}[H^+] + a_{-4})[^{18}EIC]^{18}\chi_1 + \frac{1}{\tau_{sw}}\left(^{18}R_{EIC_{(sw)}}[EIC]_{sw} - [^{18}EIC]\right) - \frac{1}{z}F_{CaCO_3}\frac{[^{18}EIC]}{[EIC]}{}^{18}\alpha_{CaCO_3-EIC}$$

As discussed in the main text, we write HCO_3^- and CO_3^{2-} together as EIC, by assuming instantaneous equilibrium between these two species. The 2/3 and 1/3 factors in Eq. (8) represent the stoichiometric contribution of oxygen atoms to EIC from CO_2 and H_2O/OH^-, and are necessary to produce reasonable isotope compositions in the calculation. A similar formulation can be found in the appendix of Uchikawa & Zeebe (2012). Activity of carbonic anhydrase is implemented by multiplying k_{+1}, k_{-1}, k'_{+1}, k'_{-1}, a_{+1} , a_{-1}, b_{+1}, b_{-1} each with the rate enhancement factor k_{cat}, assuming no additional isotope effect from CA itself. The R's in the equations represent isotope ratios of EIC and CO_2(aq) from seawater and cell fluxes, and are calculated from equilibrium fractionation factors between the DIC species (Zhang et al., 1995; Beck et al., 2005; Wang et al., 2013). Definitions and values of the parameters and constants in the equations are listed in Table 2.1.

Table 2.1: Constants and parameters in the model

Part I Model Parameters			
Symbol	**Meaning**	**Value**	**Reference/Note**
z	ECF thickness	10 μm	Adkins et al., 2003; Gagnon et al., 2012
$\boldsymbol{D_{cell}}$	Cell permeability of CO_2	0.0015 cm/s (variable)	Sultemeyer & Rinast, 1996
$\boldsymbol{\tau_{sw}}$	Seawater turnover timescale in ECF	230s (variable)	Tuned to fit data
$\boldsymbol{[CO_2]_{cell}}$	Cell CO_2 concentration	13 μmol/kg	Adkins et al., 2003
$\boldsymbol{F_{alk}}$	Alkalinity pump rate	0-1.2 μmol/m^2/s	Specified independent variable in model
$\boldsymbol{f_{Ca}}$	Ca^{2+} fraction in Alk pump	0-1	Does not change basic model result
$\boldsymbol{[Alk]_{sw}}$	Seawater alkalinity	2200 μmol/kg	Variable with corals
$\boldsymbol{[EIC]_{sw}/[CO_2]_{sw}}$	Seawater EIC/CO_2(aq)	DIC=2000 μmol/kg	Calculated from Alk and DIC with CO2SYS, variable with corals
$\boldsymbol{[Ca]_{sw}}$	Seawater Ca^{2+} concentration	10.3 mmol/kg	
Part II Physical Chemical Constants and Parameters			
Symbol	**Meaning**	**Value**	**Reference/Note**
$\boldsymbol{F_{CaCO_3}}$	Aragonite precipitation flux (mol/m^2/s)	$F_{CaCO_3} = k_{rate}(\Omega - 1)^n$ $\Omega = \frac{[Ca^{2+}][CO_3^{2-}]}{K_{sp}}$ (Calculated by CO2SYS) $n = 1.7$ $\ln k_{rate} = 11.54 - \frac{8690}{T(K)}$	Romanek et al., 2011
$\boldsymbol{k_{+1}}$	Rate constant of CO_2 hydration (s^{-1})	$\ln k_{+1} = 1246.98 - \frac{61900}{T(K)} - 183.0 \ln T(K)$	Johnson (1982)
$\boldsymbol{k_{-1}}$	Rate constant of HCO_3^- dehydration ($M^{-1}\cdot s^{-1}$)	$k_{-1} = k_{+1}/K_{a1}$	K_{a1} from CO2SYS
$\boldsymbol{k_{+4}}$	Rate constant of CO_2 hydroxylation ($M^{-1}\cdot s^{-1}$)	$\ln k_{+4} = 17.67 - \frac{2790.47}{T(K)}$	Johnson (1982); Zeebe & Wolf-Gladrow (2001)

$\boldsymbol{k_{-4}}$	Rate constant of HCO_3^- dehydroxylation (s^{-1})	$k_{-4} = k_{+4}\frac{K_w}{K_{a1}}$	K_{a1} and K_w from CO2SYS
$\boldsymbol{\chi_1}$	Fraction of HCO_3^- in EIC	$\chi_1 = \frac{1}{1+\frac{K_{a2}}{[H^+]}}$	K_{a2} from CO2SYS

Part III Isotope Related Parameters and Fractionation Factors

Symbol	Meaning	Value	Reference/Note
$\boldsymbol{\alpha_{diff}}$	Fractionation factor of CO_2 diffusion across membrane	1.0007	O'Leary, 1984 Assumed the same for ^{13}C and ^{18}O
$\boldsymbol{^{13}\chi_1}$	Fraction of $H^{13}CO_3^-$ in ^{13}EIC	$^{13}\chi_1 = \frac{1}{1+\frac{K_{a2}\cdot {}^{13}\alpha_{CO_3-HCO_3}}{[H^+]}}$	
$\boldsymbol{^{18}\chi_1}$	Fraction of $HC^{18}OO_2^-$ in ^{18}EIC	$^{18}\chi_1 = \frac{1}{1+\frac{K_{a2}\cdot {}^{18}\alpha_{CO_3-HCO_3}}{[H^+]}}$	
$\boldsymbol{k'_{+1}}$	Rate constant for $^{13}CO_2$ hydration (s^{-1})	$k_{+1}/k'_{+1} = 1.0013$	O'Leary et al, 1992
$\boldsymbol{k'_{-1}}$	Rate constant for $H^{13}CO_3^-$ dehydration ($M^{-1}\cdot s^{-1}$)	$k'_{+1}/k'_{-1} = K_{a1}\cdot {}^{13}\alpha_{HCO_3-CO_2(aq)}$	Calculated from k'_{+1} and $^{13}\alpha_{HCO_3-CO_2(aq)}$
$\boldsymbol{k'_{+4}}$	Rate constant for $^{13}CO_2$ hydroxylation (s^{-1})	$k_{+4}/k'_{+4} = 1.0011$	Zeebe et al., 1999; Zeebe & Wolf-Gladrow, 2001
$\boldsymbol{k'_{-4}}$	Rate constant for $H^{13}CO_3^-$ dehydroxylation ($M^{-1}\cdot s^{-1}$)	$k'_{+4}/k'_{-4} = \frac{K_{a1}}{K_w}\cdot {}^{13}\alpha_{HCO_3-CO_2(aq)}$	Calculated from k'_{+4} and $^{13}\alpha_{HCO_3-CO_2(aq)}$
$\boldsymbol{a_{+1}, b_{+1}}$	Rate constants for hydration with ^{18}O species (s^{-1})	$k_{+1}/a_{+1} = 1.007$ $k_{+1}/b_{+1} = 1.010$ When k_{cat}=2000	Zeebe, 2014 A range of values can fit data, and fit depends on k_{cat}
$\boldsymbol{a_{-1}, b_{-1}}$	Rate constants for dehydration with ^{18}O species ($M^{-1}\cdot s^{-1}$)	$a_{+1}/a_{-1} = K_{a1}\cdot {}^{18}\alpha_{HCO_3-H_2O}$ $b_{+1}/b_{-1} = K_{a1}\cdot {}^{18}\alpha_{HCO_3-CO_2}$	Calculated from a_{+1}, b_{+1}, $^{18}\alpha_{HCO_3-H_2O}$, $^{18}\alpha_{HCO_3-CO_2}$
$\boldsymbol{a_{+4}, b_{+4}}$	Rate constants for hydroxylation with ^{18}O species ($M^{-1}\cdot s^{-1}$)	Assumed the same as a_{+1}, b_{+1}	No constraint available, does not influence $\delta^{18}O$-$\delta^{13}C$ slope, and only changes isotope values after the kink
$\boldsymbol{a_{-4}, b_{-4}}$	Rate constants for dehydroxylation with ^{18}O species (s^{-1})	$a_{+4}/a_{-4} = \frac{K_{a1}}{K_w}\cdot\frac{{}^{18}\alpha_{HCO_3-H_2O}}{{}^{18}\alpha_{OH-H_2O}}$	Calculated from a_{+4}, b_{+4} and the corresponding

		$b_{+4}/b_{-4} = \frac{K_{a1}}{K_w} \cdot {}^{18}\alpha_{HCO_3-CO_2}$	equilibrium fractionation factors
$^{13}\alpha_{DIC-CO_2(g)}$	^{13}C fractionation between DIC species and CO_2(g)	Temperature dependent	Zhang et al., 1995
$^{18}\alpha_{DIC-H_2O(g)}$	^{18}O fractionation between DIC species and H_2O	Temperature dependent	Wang et al., 2013
$^{18}\alpha_{OH-H_2O(g)}$	^{18}O fractionation between OH^- and H_2O	Temperature dependent	Wang et al., 2013
$^{13}\alpha_{CaCO_3-EIC}$, $^{18}\alpha_{CaCO_3-EIC}$	^{13}C and ^{18}O fractionation between solid carbonate and EIC	Temperature, pH and growth rate dependent	Wang et al., 2013; Watkins et al., 2014; Watkins & Hunt, 2015

C h a p t e r 3

Variability of Minor and Trace Elements in Deep-Sea Corals from a Numerical Model and Micromilled Growth Bands

3.1 Introduction

3.1.1 The $\delta^{18}O$ Attribution Problem

In addition to complications from the vital effects in the ^{18}O thermometer discussed in Chapter 2, the foraminifera-based marine $\delta^{18}O$ record is influenced by both the temperature of the ocean and the $\delta^{18}O$ of seawater, the latter of which is mainly controlled by the growth and decay of continental ice sheets during the Pleistocene glacial cycles. While Emiliani (1955) initially attributed the full glacial-interglacial foraminifera $\delta^{18}O$ variability to temperature changes, Shackleton (1967) first pointed out that the ~1.5‰ glacial-interglacial $\delta^{18}O$ change can be largely attributed to the ice volume effect instead, by showing similar magnitude of glacial-interglacial $\delta^{18}O$ changes in planktonic and benthic foraminifera. Deconvolving the effects of temperature and ice volume on the $\delta^{18}O$ record has been a long-standing problem in paleoceanography that has triggered the development of new observation strategies and proxy tools. One of the early efforts to isolate the temperature effect was to use foraminifera faunal assemblages to develop empirical transfer functions (Imbrie et al., 1973; CLIMAP, 1976). Despite being widely used in the early days, this approach has a number of problems given its empirical basis, and has generated controversial sea surface temperature (SST) estimates (especially in the tropics) during the last glacial maximum (LGM) (Sachs et al., 1977; Rind & Peteet, 1985; Hostetler & Mix, 1999). It has since been largely replaced by more quantitative thermometers such as Me/Ca ratios in biogenic carbonates with the development of measurement techniques in the 1990s (detailed in the following section). In the past decade, the carbonate clumped isotope thermometer has been developed and provides an additional proxy that is independent of the water $\delta^{18}O$ composition (Ghosh et al., 2006; Eiler, 2011). The other approach to the $\delta^{18}O$ attribution problem is to separately estimate changes in the $\delta^{18}O$ of seawater. This can be achieved through mass balance calculations based on the sea level record (Chappell & Shackleton, 1986; Cutler et al., 2003), or

directly measuring the pore fluid in marine sediments that are remains of the glacial ocean (Schrag et al., 1996; Schrag et al., 2002; Adkins et al., 2002). These studies reveal a glacial seawater $\delta^{18}O$ change of 0.8–1‰, and deep-ocean temperature changes of 2-4°C in different ocean basins. Extending these estimates to deeper times in earth history remains an area of active research.

3.1.2 Me/Ca Thermometers in Biogenic Carbonates

Among the proxies developed to separate different aspects of the climate system over glacial cycles, Me/Ca proxies have the advantage of relatively quick and simple measurements with small sample requirements, thanks to the development of high-precision measurement techniques such as ICP-MS and ICP-OES (Rosenthal et al., 1999; Schrag et al., 1999). These methods allow multiple Me/Ca ratios to be determined in a short time, which provides the potential for high-resolution climate records. Among the element impurities in biogenic carbonates, Mg and Sr are incorporated at parts per thousand levels. They are considered "minor elements" in this context, as opposed to other less abundant "trace elements." Given their relative compatibility in different crystal structures, Mg/Ca in calcitic foraminifera shells and Sr/Ca in aragonitic coral skeletons have been developed as temperature proxies (Beck et al., 1992; Alibert & McCulloch, 1997; Rosenthal et al., 1997; Lea et al., 1999; Anand et al., 2003; Bryan & Marchitto, 2008), and used to address the glacial $\delta^{18}O$ attribution problem (Guilderson et al., 1994; Mashiota et al., 1999; Elderfield et al., 2012).

The idea behind Me/Ca thermometers is that the temperature dependence of a distribution coefficient ($D=(Me/Ca)_{carbonate}/(Me/Ca)_{fluid}$) is imprinted in the $CaCO_3$ as minor and trace elements substitute for Ca^{2+} in the lattice. The distribution coefficients can be constrained through inorganic precipitation experiments or theoretical calculations, which provide a reference frame for biogenic carbonates. However, experimental setup and conditions can vary in different precipitation experiments, giving rise to a range of estimates for the distribution coefficients (e.g. Mucci et al., 1989; Dietzel et al., 2004; Gaetani & Cohen, 2006; Gabitov et al., 2008). Application of the inorganic reference frame to biogenic carbonates is further complicated by vital effects, as reflected in the following aspects: (1) difference in the Me/Ca vs. temperature relations between inorganic and biogenic carbonates, in terms of both the absolute values and temperature sensitivities of D's (Rosenthal et al., 1997; Lea et al., 1999; Gaetani & Cohen et al., 2006); (2)

inter-species and intra-species differences in Me/Ca vs. temperature relations (Anand et al., 2003; Correge, 2006; Elderfield et al., 2006; Bryan & Marchitto, 2008); (3) dependence of Me/Ca on growth conditions other than temperature, such as salinity, pH, light and presence of photosymbionts (Lea et al., 1999; Cohen et al., 2002; Reynaud et al., 2007; Elderfield et al., 2006); and (4) large variability in Me/Ca observed within an individual organism or in individual organisms growing under the same environmental conditions (Allison & Finch, 2004; Meibom et al., 2008; Cohen et al., 2006; Gagnon et al., 2007; Case et al., 2010).

Several strategies have been applied to account for vital effects in the Me/Ca thermometers. The empirical approach uses species-specific temperature calibrations from culture experiments or plankton tow/core top data (Lea et al., 1999; Lear et al., 2002; Anand et al., 2003; Rosenthal et al., 2006; Bryan & Marchitto, 2008; Gray et al., 2018). In many such calibrations, especially for the Mg/Ca thermometer in benthic foraminifera, a correction is applied for the effect of bottom water [CO_3^{2-}], based on the observed effect of bottom water saturation state on the Mg/Ca ratios (Elderfield et al., 2006; Rosenthal et al., 2006; Bryan & Marchitto, 2008; Lear et al., 2010). It has been suggested that the observed [CO_3^{2-}] effect for the Me/Ca thermometers is a result of the biomineralization response to the bottom water saturation state instead of a postmortem partial dissolution signal (Elderfiled et al., 2006; Rosenthal et al., 2006), although the exact mechanism is not well understood.

In addition to the empirical calibrations, different approaches have been taken to parse out vital effects from temperature signals, which rely to different degrees of our understanding of the biomineralization processes. One way of removing vital effects is to find the "equilibrium endmember" in individual foraminifera or parts of the coral skeleton that take on an extreme isotopic and Me/Ca composition that reflects direct precipitation from seawater. This is aimed at bringing biogenic carbonates as close to the inorganic reference frame as possible. Interestingly, the opposite way was also proposed for the carbon and oxygen isotopes in corals by McConnaughey (1989). By sampling contemporaneous growth bands in different growth directions (thus with different extension rates), McConnaughey (1989) observed that $\delta^{18}O$ and $\delta^{13}C$ decreased at low extension rates, but stayed constant when the extension rates reached a threshold, and proposed that sampling the parts with lowest $\delta^{18}O$ and $\delta^{13}C$ (farthest from equilibrium, but with maximized and constant vital effects) would yield the most robust estimates of environmental

conditions. While both "endmember" approaches can be applied in practice, a natural bulk sample typically sits somewhere in between, and finding the endmember compositions are not always straightforward. A different approach is to use multiple tracers to normalize for the vital effects, assuming incorporation of these tracers follow similar calcification dynamics in the organisms. It was first suggested in foraminifera that cations such as Sr^{2+}, Ba^{2+} and Cd^{2+} are incorporated into the calcite in a closed pool of calcifying fluid through the Rayleigh distillation process, and a combination of these elements with different distribution coefficients can be used to constrain the utilization percentage of Ca^{2+} (1–F in the Rayleigh process) in the calcifying fluid (Elderfield et al., 1996). This approach was extended to corals to reconstruct temperature with a combination of Mg/Ca, Sr/Ca and Ba/Ca measurements and a numerical optimization algorithm (Gaetani et al., 2011). By measuring Mg/Ca, Sr/Ca and Ba/Ca at multiple spots in a single coral, the Rayleigh-based multi-element method calculates the initial composition of the calcifying fluid, temperature and the Rayleigh F in an over-constrained system (Gaetani et al., 2011). This method has not been widely used due to its complicated numerical scheme, as well as the need to find optimized parameters for each individual coral without a complete mechanistic understanding. A simpler approach to account for vital effects in a thermometer is to use Me/Me ratios instead of Me/Ca ratios, so that the effects of the calcification process on two different Me/Ca ratios cancel out, and the remaining information is related to the distribution coefficients with different temperature dependence. This approach has been successfully demonstrated for Li/Mg in corals and the aragonitic foraminifera *Hoeglundina elegans* (Bryan & Marchitto, 2008; Case et al., 2010; Montagna et al., 2014; Marchitto et al., 2018). It was observed that Li/Mg in biogenic aragonites has a much tighter relation with temperature than Li/Ca and Mg/Ca, and Li/Mg in corals and *H.elegans* have the same relation to temperature. Another example based on a similar idea is the Sr-U thermometer in corals (DeCarlo et al., 2016). One purpose of this chapter is to evaluate how well these approaches work in deep-sea corals and whether the mechanism underlying the minor/trace element vital effects can be better understood.

3.1.3 Carbonate Chemistry Proxies

In addition to temperature and ice volume changes, atmospheric CO_2 has been another key player in global climate change during the Pleistocene ice ages (Barnola et al., 1987; Petit et al., 1999). A key component that buffers atmospheric CO_2 is the marine carbonate system (Broecker &

Peng, 1987), and understanding the interaction between the two is not only important to glacial-interglacial CO_2 changes, but also crucial for future projections of marine calcification under increasing atmospheric CO_2 conditions. Over the past three decades, multiple proxies in biogenic carbonates have been developed for the carbonate chemistry of the ocean. These include Ba/Ca in foraminifera as an alkalinity proxy (Lea & Boyle, 1989; Lea, 1993), boron isotopes ($\delta^{11}B$) in foraminifera and corals as a pH proxy (Hemming & Hanson, 1992; Hönisch et al, 2004; Hönisch & Hemming, 2004; Foster et al., 2008; Rae et al., 2011; Anagnostou et al., 2011; Stewart et al., 2016), B/Ca in foraminifera and corals as a $[CO_3^{2-}]$ proxy (Yu & Elderfield, 2007; Yu et al., 2010; Allen et al., 2012; Rae et al., 2011), U/Ca in corals as a $[CO_3^{2-}]$ or pH proxy (Anagnostou et al., 2011; Inoue et al., 2011; Raddatz et al., 2014) and lithium isotopes (δ^7Li) in foraminifera as a DIC proxy (Vigier et al., 2015). Some of these proxies have been applied to reconstruct the pH and alkalinity of the LGM ocean (Lea, 1993; Sanyal et al., 1995; Hönisch & Hemming, 2005), as well as timing and location of CO_2 release during the last deglaciation (Martinez-Boti et al., 2015; Rae et al., 2018).

As the second most important element in buffering seawater acid-base chemistry, boron is perhaps the most widely studied and used among the carbonate chemistry proxies. Boron isotopes and B/Ca can provide two separate variables of the marine carbonate system, which can then be used to fully constrain the carbonate system. While $\delta^{11}B$ has a nice physicochemical basis as a pH proxy (pH-dependent speciation and thermodynamic fractionation between boric acid and borate ion, and incorporation of only borate ion in the carbonate), B/Ca as a $[CO_3^{2-}]$ proxy is largely based on empirical calibrations without a full mechanistic understanding. Both proxies are subject to a number of complications, including debates about which boron species is actually incorporated in different carbonate minerals (Rollion-Bard et al., 2011; Uchikawa et al., 2015; Branson et al., 2015; Holcomb et al., 2016; Balan et al., 2016), other influencing factors such as DIC and growth rates (Uchikawa et al., 2017; Farmer et al., 2018), and most notably, the vital effects associated with pH elevation in biogenic carbonates (as discussed in Chapter 1 and 2). As a result, applications of both $\delta^{11}B$ and B/Ca proxies again rely on species-specific calibrations. In fact, the combination of $\delta^{11}B$ and B/Ca has been used recently to constrain the composition of the calcifying fluid of corals instead of external environmental conditions (Allison et al., 2014;

D'Olivo & McCulloch, 2017; McCulloch et al., 2017). In the case of deep-sea corals, boron proxies provide a test case for the model framework set up in Chapter 2.

3.2 Numerical Model for Minor/Trace Elements Incorporation During Coral Calcification

The numerical model for the incorporation of minor/trace elements during coral calcification is developed from the stable isotope model in Chapter 2. A simpler steady state version of the model has been previously published for Mg/Ca and Sr/Ca in corals that did not account for the key kinetic processes discussed in Chapter 2 (Gagnon et al., 2012). In addition, more elements are added to the model, and a more systematic survey of model sensitivity to different parameters is performed. The system follows the same calcification dynamics as in Chapter 2, and a differential equation is written for each minor/trace element in addition to calcium. As discussed in Section 2.1, it is assumed that the minor and trace elements are brought into the ECF by direct seawater transport. They each get incorporated into the skeleton by a distribution coefficient, which is either from inorganic aragonite experiments, empirical calibrations, or assigned values to fit the observations (Table 3.1). There is no consistent way of picking the distribution coefficients due to limited and variable experimental constraints on aragonite, especially at low temperatures (Kinsman & Holland, 1969; Mucci et al., 1989; Dietzel et al., 2004; Marriott et al., 2004; Gaetani & Cohen, 2006; Holcomb et al., 2016; Marchitto et al., 2018), which are detailed in the model description. However, as in Chapter 2, the main focus of the numerical model is to provide a guideline to understanding the correlations between Me/Ca in deep-sea coral skeletons and which biomineralization processes contribute to these correlations, thus revealing the underlying mechanisms of the Me/Ca vital effects.

3.2.1 The Equations and Important Parameters

The equations for the cations in the model are listed below:

$$\frac{d[Ca^{2+}]}{dt} = \frac{1}{\tau_{sw}}([Ca^{2+}]_{sw} - [Ca^{2+}]) + \frac{1}{z}(\frac{1}{2}f_{Ca}F_{Alk} - F_{CaCO_3})$$

$$\frac{d[Sr^{2+}]}{dt} = \frac{1}{\tau_{sw}}([Sr^{2+}]_{sw} - [Sr^{2+}]) - \frac{1}{z}F_{CaCO_3}D_{Sr}\frac{[Sr^{2+}]}{[Ca^{2+}]}$$

$$\frac{d[Mg^{2+}]}{dt} = \frac{1}{\tau_{sw}}([Mg^{2+}]_{sw} - [Mg^{2+}]) - \frac{1}{z}F_{CaCO_3}D_{Mg}\frac{[Mg^{2+}]}{[Ca^{2+}]}$$
$$\frac{d[Li^{+}]}{dt} = \frac{1}{\tau_{sw}}([Li^{+}]_{sw} - [Li^{+}]) - \frac{1}{z}F_{CaCO_3}D_{Li}\frac{[Li^{+}]}{[Ca^{2+}]}$$
$$\frac{d[Ba^{2+}]}{dt} = \frac{1}{\tau_{sw}}([Ba^{2+}]_{sw} - [Ba^{2+}]) - \frac{1}{z}F_{CaCO_3}D_{Ba}\frac{[Ba^{2+}]}{[Ca^{2+}]}$$

These equations are combined with the equations in Chapter 2 to solve the full ECF system at steady state for different rates of alkalinity pumping. The left hand side of the equations is the rate of change for the concentrations of cations in the ECF. For cations other than Ca^{2+}, there are two terms on the right hand side. The first term reflects seawater flushing of the ECF, which transports the cations by the concentration gradient between seawater and the ECF at a timescale of τ_{sw}. An optimal τ_{sw} of 230s was found to fit the range of $\delta^{13}C$ in *D.dianthus* in Section 2.4.3, and here the sensitivity of Me/Ca to τ_{sw} is tested. The second term reflects incorporation into the $CaCO_3$ by precipitation with a distribution coefficient for each element. The thickness of the ECF (z) (assumed to be 10 μm as in Table 2.1) is needed to match the dimensions of the terms, because the precipitation flux F_{CaCO_3} has units of mol/m^2/s. For [Ca^{2+}], there is an additional term that reflects the pumping process by Ca-ATPase (F_{Alk}). A factor of ½ is added because F_{Alk} is in units of alkalinity, and a factor of f_{Ca} is added to account for the fact that not all ion transporters on the ECF membrane of corals are Ca^{2+} pumps (Jokiel, 2011; Barott et al., 2015; Barron et al., 2018). The value of f_{Ca} does not have a major effect on the stable isotope results in Chapter 2, because carbon is the limiting factor in calcification instead of calcium. However, f_{Ca} has a strong influence on all Me/Ca ratios given that it changes the Ca^{2+} balance and thus its steady state concentration in the ECF. Changing f_{Ca} yields very different Me/Ca correlation patterns as discussed below. It is also noted that despite having a major impact on the carbon budget, the effect of carbonic anhydrase activity on the Me/Ca results is not as significant. The same rate enhancement factor of 2000 as in Chapter 2 is used in all the Me/Ca simulations.

The equation for boron is less straightforward compared to the cations, given the ongoing debates about how boron gets incorporated into $CaCO_3$. The traditional wisdom is that only $B(OH)_4^-$ gets incorporated (Hemming & Hanson, 1992), which has been challenged by NMR characterizations of boron in carbonates (Klochko et al., 2009; Rollion-Bard et al., 2011) and the observed growth rate dependence of B/Ca (Gabitov et al., 2014; Uchikawa et al., 2017; Farmer et

al., 2018). However, most of these complications were found in calcite, and aragonite was considered a simpler system that is dominated by $B(OH)_4^-$ incorporation (Balan et al., 2018; Farmer et al., 2018). Even so, there is still the question of what is the denominator in boron partition coefficients in the aqueous phase. Early calibrations in foraminifera used HCO_3^-, which is the dominant species in the seawater DIC pool (Yu et al., 2007). In contrast, recent inorganic experiments in calcite and aragonite have found a stronger dependence of B/Ca on total DIC (Holcomb et al., 2016; Uchikawa et al., 2017). In the aragonite experiments, an even stronger correlation was found between B/Ca in the aragonite and $[B(OH)_4^-]/[CO_3^{2-}]^{0.5}$ in the solution (Holcomb et al., 2016). The authors suggested that this could be explained by a charge balanced exchange reaction (it takes two borate ions to balance the charge of one carbonate ion), although it is unclear how a carbonate site could incorporate two borate ions physically. These different rules can be tested in the model to see which one best explains the observed tracer correlations. Here is an example of the differential equation with the $B(OH)_4^-$/DIC partition rule:

$$\frac{d[B]}{dt} = \frac{1}{\tau_{sw}}([B]_{sw} - [B]) - \frac{1}{z} F_{CaCO_3} D_B \frac{[B]\chi_4}{[EIC] + [CO_2(aq)]}$$

In the equation, χ_4 is the fraction of borate ions in total boron, which can be calculated with the pH of the ECF. Given the low $[CO_2(aq)]$ concentrations in the pH range of the model, there is no essential difference in the model results by replacing the denominator of total DIC with EIC, and the model results with this partition rule has used this simplification. A list of boron partition rules and distribution coefficients is given in Table 3-1.

Table 3-1 A Summary of Aragonite Distribution Coefficients in the Literature

Element	Equation	Typical Value (5°C)	Method	Reference
Mg	$\ln D_{Mg} = \frac{1930}{T(K)} - 13.1$	2.11×10^{-3}	Precipitation in seawater	Gaetani & Cohen (2006)
	$D_{Mg} = 1.71\times10^{-4} + 2.62\times10^{-5}T(℃)$	2.48×10^{-4}	Coral culture	Raynaud et al. (2007)
	$D_{Mg} = 0.00053\exp[-0.0205T(℃)]$	4.78×10^{-4}	Coral calibration combinted with Gaetani & Cohen (2006)	Montagna et al. (2014)

Sr	$\ln D_{Sr} = \frac{605}{T(K)} - 1.89$	1.33	Precipitation in seawater	Gaetani & Cohen (2006)
	$D_{Sr} = 1.32 - 0.005091T(℃)$	1.29	Precipitation in Ca-Mg-Cl solution	Dietzel et al. (2004)
	$D_{Sr} = 1.24 - 004375T(℃)$	1.22	Precipitation in seawater	Kinsman & Holland (1969)
Ba	$\ln D_{Ba} = \frac{2913}{T(K)} - 9.0$	4.36	Precipitation in seawater	Gaetani & Cohen (2006)
	$D_{Ba} = 2.42 - 0.03595T(℃)$	2.24	Precipitation in Ca-Mg-Cl solution	Dietzel et al. (2004)
Li	$D_{Li} = 0.01 \exp[-0.049T(℃)]$	7.83×10^{-3}	Coral calibration	Marriott et al. (2004)
	$D_{Li} = 0.0056 \exp[-0.0675T(℃)]$	4.00×10^{-3}	Coral Li/Mg calibration combined with Gaetani & Cohen (2006)	Montagna et al. (2014)
	$D_{Li} = 0.0252 \exp[-0.0707T(℃)]$	1.77×10^{-2}	Coral/*H.elegans* Li/Mg calibration combined with Gaetani & Cohen (2006)	Marchitto et al. (2018)
B	$D_B = \frac{[HBO_3^{2-}/CO_3^{2-}]_{arag}}{[B(OH)_4^-]/[HCO_3^-]}$	0.004–0.01	Precipitation in $CaCl_2$-NH_4Cl solution	Hemming et al. (1995)
	$D_B = \frac{[B/Ca]_{arag}}{[B(OH)_4^-]/[HCO_3^-]}$	0.001–0.002	*H.elegans* calibration	Yu & Elderfield (2007)
	$D_B = \frac{[B/Ca]_{arag}}{[B(OH)_4^-]/[CO_3^{2-}]}$	$10^{-6.7}$–$10^{-3.6}$	Precipitation in 0.1–0.2M NaCl solution	Mavromatis et al. (2015)
	$D_B = \frac{[B/Ca]_{arag}}{[B(OH)_4^-]/[HCO_3^-]}$	0.0014-0.052	Precipitation in seawater	Holcomb et al. (2016)
	$D_B = \frac{[B/Ca]_{arag}}{[B(OH)_4^-]/[CO_3^-]^{0.5}}$	0.0013-0.0041	Precipitation in seawater	Holcomb et al. (2016)

3.2.2 Basic Model Behavior

As in Chapter 2, the initial composition of the ECF is set at seawater values. An alkalinity pump rate is assigned as the primary perturbation to the system. The model is run toward steady state at each alkalinity pump rate to solve for the carbonate chemistry of the ECF and the isotope and Me/Ca composition of the skeleton. Figure 3-1 shows the steady state solutions to different Me/Ca ratios at a range of alkalinity pump rates with different combinations of τ_{sw} and f_{Ca} values, at a temperature of 5°C and a depth of 500 m.

From Figure 3-1, we see three types of behavior for the Me/Ca ratios with pump rates, which depend on their distribution coefficients. Mg and Li both have D's that are much smaller than 1, and share similar behavior at different τ_{sw} and f_{Ca}. With D<<1, precipitation does not remove Mg^{2+} or Li^{+} to any significant extent from the ECF as compared to Ca^{2+}. So the Mg/Ca and Li/Ca of the skeleton are completely dependent on the Ca^{2+} dynamics. When f_{Ca}=0, both Mg/Ca and Li/Ca increase with pump rate, as Ca^{2+} in removed by precipitation. When f_{Ca}=1, the Ca^{2+} supply from the pump almost balances the loss by precipitation over the range of pump rates, so Mg/Ca and Li/Ca stay almost constant. When f_{Ca}=0.5, the ranges in Mg/Ca and Li/Ca are between the two extremes. A kink in Mg/Ca and Li/Ca vs. pump rate is observed at ~4×10^{-7} mol/m^2/s, which corresponds to the [CO_3^{2-}] maximum in the ECF as discussed in Chapter 2 (Figure 2-5c). After the [CO_3^{2-}] maximum, the Ca^{2+} removal by precipitation is much less sensitive to increases in the alkalinity pump rate (Figure 2-5f), and is balanced by the supply from seawater as well as the alkalinity pump if f_{Ca}>0. Therefore [Ca^{2+}] in the ECF has much less change after the threshold, causing the kinks in Mg/Ca and Li/Ca. As shown later, the kink does not influence the correlation between Mg/Ca and Li/Ca (Figure 3-2), since both ratios are dominantly controlled by ECF [Ca^{2+}] in the model. In contrast, Sr and Ba both have D's that are larger than 1, so they always are preferentially removed relative to Ca. As a result, both Sr/Ca and Ba/Ca always decrease with pump rates, and decrease more rapidly when f_{Ca} increases. Ba/Ca has a larger distribution coefficient than Sr/Ca, so the relative changes in Ba/Ca are greater than Sr/Ca over the same range of pump rates. Both Sr/Ca and Ba/Ca change more gradually at higher pump rates, for the same reason of [Ca^{2+}] budget changes that caused the kinks in Mg/Ca and Li/Ca. The B/Ca results shown in Figure 3-1 are based on the [$B(OH)_4^-$]/[HCO_3^-] partition rule. B/Ca does not change significantly with f_{Ca}, given that its incorporation is controlled by the DIC system. The increase in B/Ca with pump rates reflects both an increase in [$B(OH)_4^-$] and a decrease in [HCO_3^-] as pH is increased. Finally, changes in all Me/Ca ratios are reduced over the same range of pump rates with shorter seawater turnover timescales, since a faster seawater turnover rate more strongly buffers the effect of alkalinity pumping in the ECF.

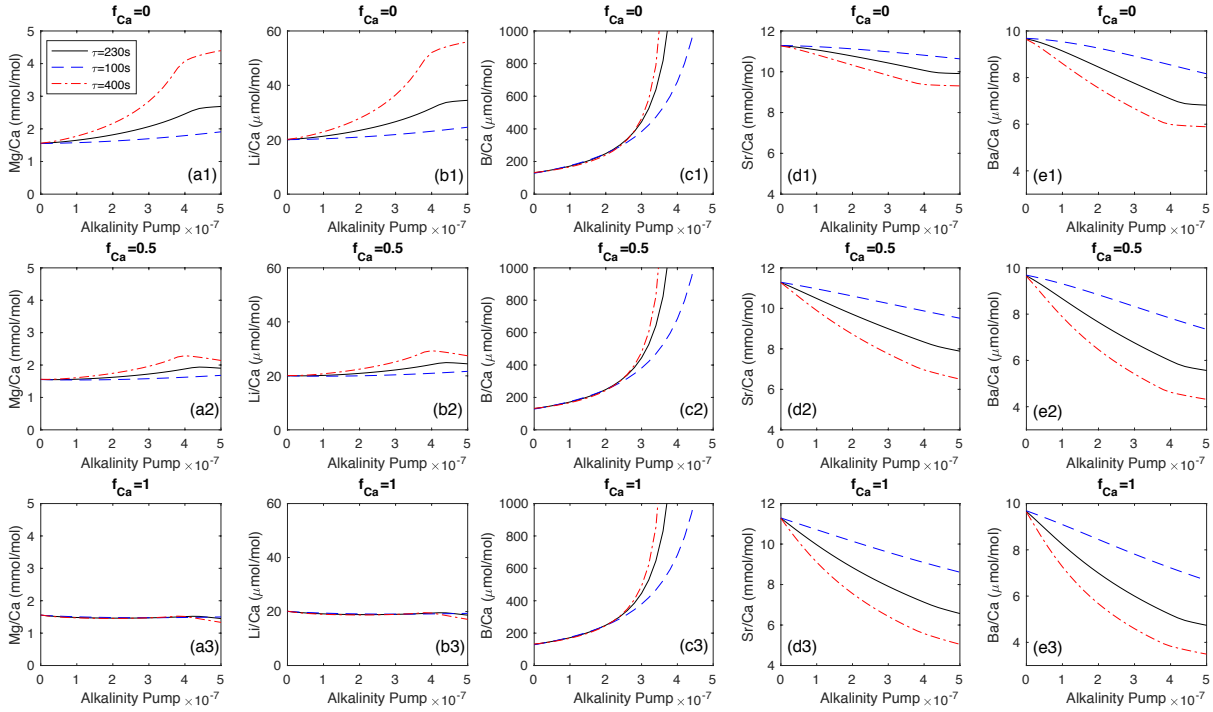

Figure 3-1 Steady state Me/Ca ratios in the coral skeleton vs. alkalinity pump rate (mol/m^2/s). The five columns are (a) Mg/Ca, (b) Li/Ca, (c) B/Ca, (d) Sr/Ca and (e) Ba/Ca respectively. Each row represents a different f_{Ca} value between 0 and 1 (from no Ca^{2+} pump in Row 1 to half Ca^{2+} pump in Row 2 to full Ca^{2+} pump in Row 3). In each panel, there are three model simulations corresponding to different seawater turnover timescales. The black solid lines represent the optimal timescale of 230s found in Chapter 2, while the blue dashed lines and red dash-dot lines represent a faster (100s) and slower (400s) turnover respectively. Distribution coefficient for Mg/Ca is from Raynaud et al. (2007), for Li/Ca from Marriott et al. (2004), for Sr/Ca from Gaetani & Cohen (2006), and for Ba/Ca from Dietzel et al. (2004). The B/Ca ratios are calculated based on the $[B(OH)_4^-]/[HCO_3^-]$ partition rule, with a D_B value of 0.003. These values are picked to match the measured compositions in deep-sea corals. B/Ca is cut off at 1000 μmol/mol due to unreasonably high values at higher pump rates.

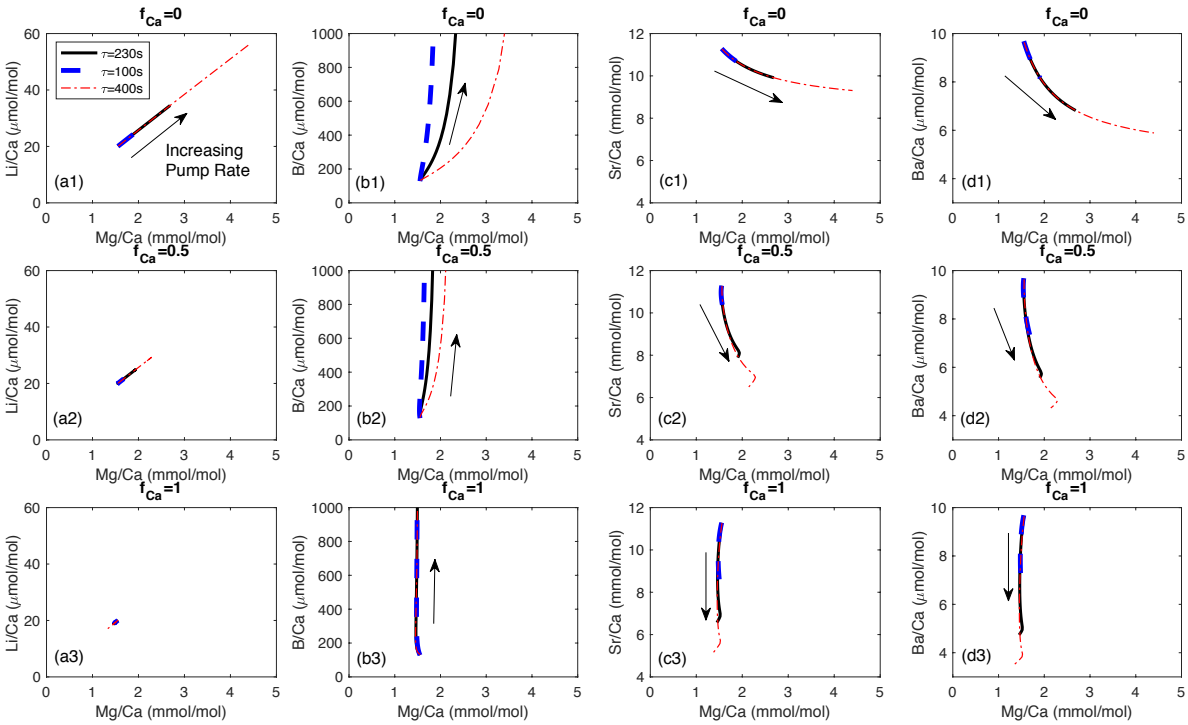

Figure 3-2 Me/Ca correlations predicted by the model. Mg/Ca is plotted on the x-axis for all panels, and different columns are (a) Li/Ca, (b) B/Ca, (c) Sr/Ca and (d) Ba/Ca respectively. The three rows represent f_{Ca} values of 0, 0.5 and 1 as in Figure 3-1. In each panel there are three different curves corresponding to different τ_{sw}. The arrows in the panels point in the direction of increasing alkalinity pump rate. For Mg/Ca vs. Li/Ca at f_{Ca} of 0.5 and 1, there is a change in direction for Mg/Ca and Li/Ca with pump rate, and the range of values in Mg/Ca and Li/Ca has largely shrunk, so no arrows are drawn. Note that the model curves correspond to the same range of pump rates as in Figure 3-1.

3.2.3 Tracer Correlations in the Model

Figure 3-2 shows the correlation trends between different Me/Ca ratios and Mg/Ca predicted by the model. We see that Mg/Ca and Li/Ca are always linearly correlated, with the range of variability determined by f_{Ca} and τ_{sw} over a given range of pump rates. When f_{Ca}=1, the delicate Ca^{2+} balance between pump and precipitation keeps Mg/Ca and Li/Ca at almost constant values, as seen in other Me/Ca correlations with Mg/Ca. When f_{Ca}<1, Mg/Ca is positively correlated with B/Ca, but with different slopes and degrees of curvature in the correlation at different τ_{sw}. In contrast, Mg/Ca is negatively correlated with Sr/Ca and Ba/Ca when f_{Ca}<1, and

the correlation trend is independent of τ_{sw}. The seawater turnover timescale only influences how far Mg/Ca, Sr/Ca and Ba/Ca go down the correlation trend.

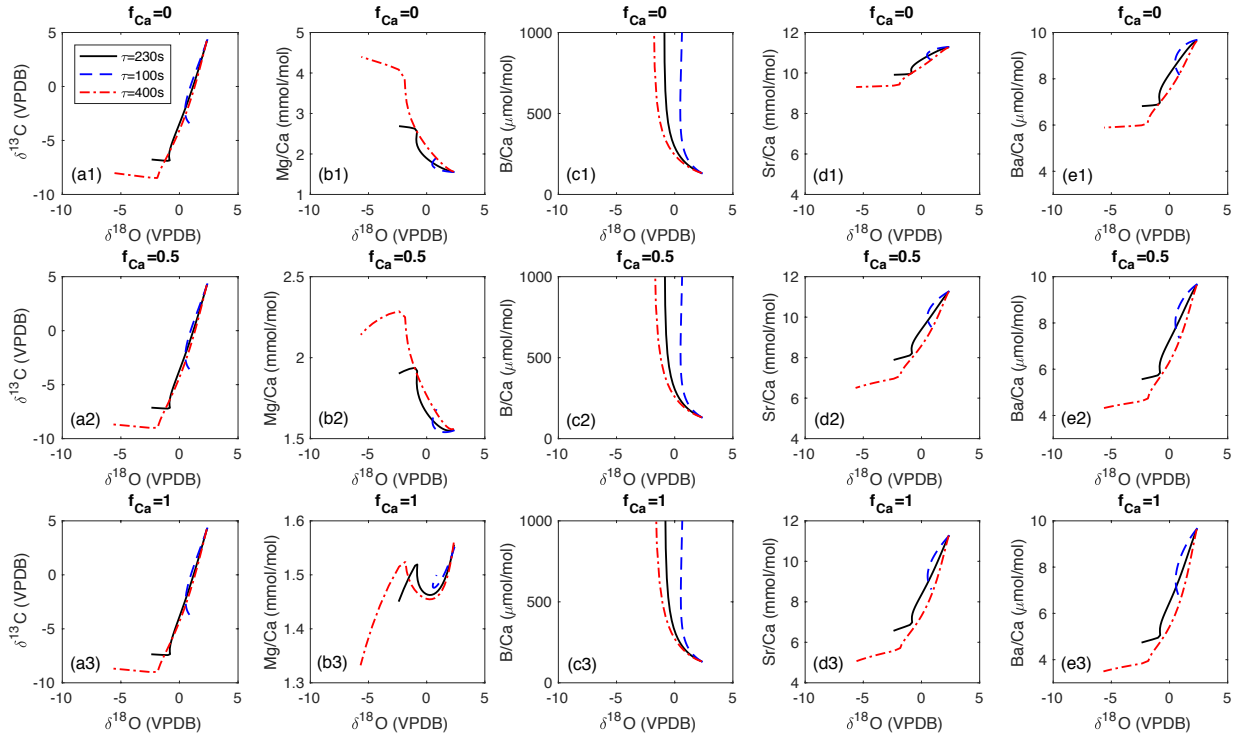

Figure 3-3 Correlations between Me/Ca and $\delta^{18}O$ predicted by the model. As in Figure 3-1 and 3-2, the three rows represent different f_{Ca} values, while the columns represent (a) $\delta^{13}C$, (b) Mg/Ca, (c) B/Ca, (d) Sr/Ca and (e) Ba/Ca respectively. Each panel has three different curves that correspond to different τ_{sw}. In each panel, $\delta^{18}O$ always decreases with increasing pump rate. Note that the scale of Mg/Ca is changed between rows to visualize the small changes within the narrow ranges shown in Figure 3-1 and 3-2.

As demonstrated in Chapter 2, $\delta^{18}O$ of the *D.dianthus* skeletons can be used as an indicator of the degree of pH elevation in the ECF. Figure 3-3 shows different Me/Ca ratios with $\delta^{18}O$ values predicted by the model. We see that Mg/Ca increases with more depleted $\delta^{18}O$ (stronger pump) at f_{Ca}=0, while the relations are more complicated at f_{Ca}=0.5 and 1 despite narrow ranges in Mg/Ca. B/Ca always increases with $\delta^{18}O$ depletions, while Sr/Ca and Ba/Ca always decreases with $\delta^{18}O$ depletions. All these correlations in the model have significant curvatures that can be used as diagnostic features in a model-data comparison. It is also noted that the Me/Ca vs. $\delta^{18}O$ trends all have a kink at the same $\delta^{18}O$ value as the $\delta^{18}O$-$\delta^{13}C$ kink. In the stable isotope model, the kink

represents the COCs in the coral skeleton. The Me/Ca composition of the COCs can be used to test whether or not COCs can be explained with this simple biomineralization mechanism.

3.2.4 Temperature Information in Tracer Correlations

One goal of looking at tracer correlations in deep-sea corals is to see if environmental conditions can be extracted by correcting for the vital effects with one of the tracers. The mathematic basis for this idea from the numerical model was previously presented by Gagnon et al. (2012). Assuming steady state to the differential equations listed in Section 3.2.1, analytical solutions can be obtained for Me/Ca ratios (where Me is a cation) and their relations. Here are two examples for Li/Ca, Mg/Ca and Sr/Ca:

$$\left(\frac{Sr}{Ca}\right)^{-1} = \left[\frac{D_{Sr} - 1 + \gamma}{D_{Mg} - 1 + \gamma}\right]\left[\frac{(Mg/Ca)_0}{(Sr/Ca)_0}\right]\left(\frac{Mg}{Ca}\right)^{-1} + \left(\frac{Sr}{Ca}\right)_0^{-1}\left[1 - \frac{D_{Sr} - 1 + \gamma}{D_{Mg} - 1 + \gamma}\right] \quad (a)$$

$$\left(\frac{Li}{Ca}\right)^{-1} = \left[\frac{D_{Li} - 1 + \gamma}{D_{Mg} - 1 + \gamma}\right]\left[\frac{(Li/Ca)_0}{(Mg/Ca)_0}\right]\left(\frac{Mg}{Ca}\right)^{-1} + \left(\frac{Li}{Ca}\right)_0^{-1}\left[1 - \frac{D_{Li} - 1 + \gamma}{D_{Mg} - 1 + \gamma}\right] \quad (b)$$

In these equations, the term γ is the ratio of the Ca^{2+} supply by the alkalinity pump and removal by precipitation:

$$\gamma = \frac{Pump}{Precip} = \frac{f_{Ca}F_{Alk}}{2F_{CaCO_3}}$$

The Me/Ca ratios without subscripts are those in the coral skeleton, while those with subscripts of "0" represent Me/Ca of precipitation from an unmodified initial calcifying fluid (in our case seawater):

$$(Mg/Ca)_0 = D_{Mg}(Mg/Ca)_{sw}$$
$$(Sr/Ca)_0 = D_{Sr}(Sr/Ca)_{sw}$$
$$(Li/Ca)_0 = D_{Li}(Li/Ca)_{sw}$$

Equations (a) and (b) are written in terms of $(Me/Ca)^{-1}$ to obtain the form of a linear relation with a slope and intercept that are independent of skeletal Me/Ca variabilities. It should be noted that γ is not always a constant as the alkalinity pump is increased, so some curvature is expected for the Me/Ca correlations, as seen in Figure 3-2. However, simplifications can be made in certain cases. For the case of no Ca^{2+} pumping (f_{Ca}=0), γ is always 0, so $(Me/Ca)^{-1}$ values have a linear relation,

and a monotonous correlation trend for Me/Ca ratios are expected (Figure 3-2 Row 1). For the case of Mg/Ca and Li/Ca, further simplifications can be made because both D_{Mg} and D_{Li} are much smaller than 1. In this case, unless γ is very close to 1, the slope and intercept in Equation (b) can be largely simplified regardless of γ values by neglecting the D_{Mg} and D_{Li} terms:

$$\left(\frac{Li}{Ca}\right)^{-1} = \left[\frac{(Li/Ca)_0}{(Mg/Ca)_0}\right]\left(\frac{Mg}{Ca}\right)^{-1} = \left[\frac{D_{Li}(Li/Ca)_{sw}}{D_{Mg}(Mg/Ca)_{sw}}\right]\left(\frac{Mg}{Ca}\right)^{-1}$$

This simplification predicts a linear relation between $(Li/Ca)^{-1}$ and $(Mg/Ca)^{-1}$ with a negligible intercept, and therefore a linear relation between Li/Ca and Mg/Ca, as seen in Figure 3.2. The actual model results for Li/Ca vs. Mg/Ca have a small intercept (excess Li) that reflect differences in the values for D_{Mg} and D_{Li}. The relation for Mg/Ca and Sr/Ca is more complicated due to very different distribution coefficients. Since $D_{Sr}>1$, the term $D_{Sr} - 1 + \gamma$ in Equation (a) is always positive, but the denominator $D_{Mg} - 1 + \gamma$ can switch signs depending on γ. This is demonstrated in Figure 3-2 (c2) and (c3), where a kink is observed in the Mg/Ca-Sr/Ca correlation.

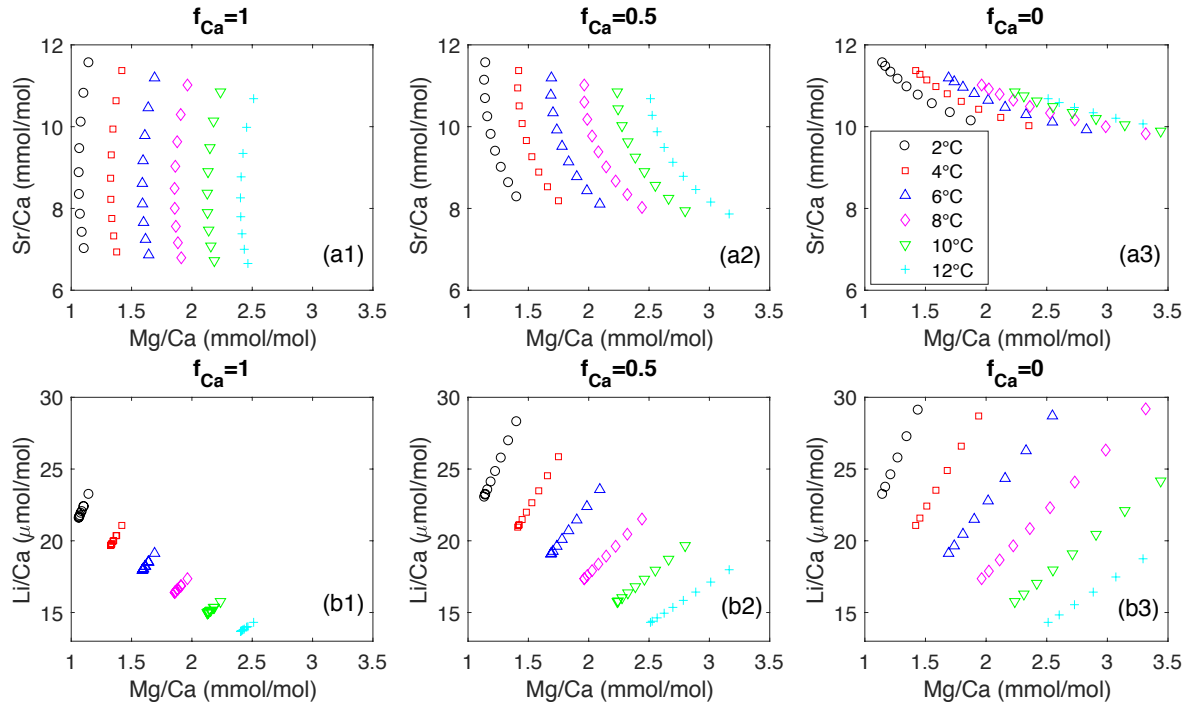

Figure 3-4 Model simulations of Me/Ca correlations at different temperatures. The top row (a1–a3) shows Mg/Ca and Sr/Ca correlations, while the bottom row (b1–b3) shows Mg/Ca and Li/Ca correlations. At each temperature, the change in Me/Ca is caused by different alkalinity pump rates as shown in Figure 3-1. This figure shows a narrower range of pump rates than Figures 3-2 and 3-3.

The analytical solutions are not only helpful in explaining the numerical results of Me/Ca correlations, but they provide a way to extract environmental information such as temperature from the Me/Ca correlations. The slopes of the Me/Ca correlations contain the distribution coefficients that are temperature dependent, so a change in temperature would be reflected in the slope based on different temperature sensitivities of the distribution coefficients for different elements. This is especially obvious for the simple pair of Li/Ca and Mg/Ca, when the vital effects from γ largely cancel out for both elements. Figure 3-4 shows simulations of Li/Ca, Mg/Ca and Sr/Ca at different temperatures to illustrate this approach. It is another target to test with observations.

3.3 Characterizing Me/Ca Variability in Deep-sea Corals with Micromilled Growth Bands

As outlined in Section 1.3, minor and trace element variability in individual deep-sea corals were measured on three different scales in this study. From coarse to fine scales, they are micromilling plus ICP-MS, SIMS and nanoSIMS measurements. The *D.dianthus* specimens selected for these measurements are listed in Table 1-1. Estimates of the environmental conditions of their growth are listed in Table 5-1 in Chapter 5 on bulk sample tracer calibrations. This chapter will focus on stable isotope and Me/Ca variabilities from micromilled samples, and their comparisons to the numerical model. SIMS and nanoSIMS measurements will be reported and discussed in Chapter 4.

3.3.1 Sampling and Measurements

Micromilling is a sampling tool initially developed to characterize isotope and minor element variability in geological materials (especially carbonates) at scales as fine as 20 μm. The Merchantek micromill model used in this study was originally developed at University of Michigan by K.C. Lohmann. The micromill uses a computer-controlled stepper-motor driven x-y-z micro-positioning stage to control movement of the sample under a stationary rotating drill bit, with a spatial accuracy of 1 μm (Dettman & Lohmann, 1995). The sample stage is placed under a Leica GZ6 microscope with a digital camera that transmits the sample image to the monitor, so that spatial patterns and structures can be defined on the sample surface and drilled. The sampling strategy for deep-sea corals is similar to that of Adkins et al. (2003). A “pie slice” was cut from a

coral calice and mounted on a glass slide by epoxy. A flat surface was cut on the mount with a Buehler diamond wafer blade to generate a "top view" section of the coral (Adkins, 1998). After cutting, the sample surface was hand polished on sequentially finer polishing papers until 4000 grit (3 μm). To sample the growth bands of the corals, a trench (~500 μm wide) is first milled next to the area of interest. Materials from the trench are collected if it is within the coral skeleton. The growth bands are then sequentially milled off the wall of the trench. The initial target of this project was to generate enough material for $\delta^{18}O$, $\delta^{13}C$, Me/Ca and $\delta^{11}B$ measurements on the same band. The powder was collected with a pointed scalpel blade, weighed on a micro-balance and transferred for storage. Compressed air was used to remove residual powder between samples. During the process, 30-100 μg of powder was collected for $\delta^{18}O$ and $\delta^{13}C$ measurements, and 100-500 μg (mostly 100-200 μg) of powder was collected for Me/Ca and $\delta^{11}B$ measurements. Collecting this amount of powder required milling 100 μm wide bands to a depth of at least 150 μm (and as much as 500 μm), which could introduce significant averaging in the z-direction of the section. As a result, a COC band identified on the surface of the sample may be mixed with secondary aragonite material due to its complex geometry in the 3D structure of the coral skeleton.

Samples for $\delta^{18}O$ and $\delta^{13}C$ analyses were weighed and stored in 3.5×9 mm silver capsules made by Costech Analytical Technologies Inc. with polished inner surfaces, and later transferred to Kiel device vials. The samples were run by Chris Charles on a Finnigan MAT 252 mass spectrometer coupled to a Kiel device at Scripps Institution of Oceanography. The CO_2 gas evolved from the samples by phosphoric acid digestion was cryogenically purified and measured against a reference gas that was calibrated against the NBS 19 standard. Three NBS 19 standards were run for every 20 samples to check the consistency of the instrument. During the sample transfer, some samples lost significant amount of powder due to improper storage. To measure these small samples (<30 μg), NBS 19 standards of similar sizes were measured to build a calibration based on the pressure of the CO_2 generated. The calibration was strongly non-linear with large uncertainties on the low-pressure end. As a result, the following discussion of data will focus on the large samples with good data quality.

Samples for Me/Ca and $\delta^{11}B$ were weighed in Costech silver capsules, transferred to HCl leached centrifuge tubes and transported to University of St Andrews for the measurements. In the St. Andrews Isotope Geochemistry (STAiG) lab, the sample powder in the centrifuge tubes was

first gathered at the bottom by adding 1 ml MilliQ water and centrifuging at 13,000 rpm for 3 minutes. After removing the MilliQ, a typical next step was oxidative cleaning with 0.1M NH_4OH+1% H_2O_2 to remove organic materials and with 0.0005M HNO_3 to remove the surface layers of the carbonates that are most likely contaminated by handling. A cleaning test was performed on splits of large samples and it was found that the cleaning process could cause ~1/3 sample loss while removing the cleaning solutions with pipettes, and no systematic offset was observed for most Me/Ca ratios (except for Li/Ca and B/Ca, which have lower values and are less variable in a single coral after cleaning). Given the limited amount of materials collected, no cleaning was applied to the majority of the samples. The next step is to dissolve samples with 200 μL MilliQ+75 μL 0.5M HNO_3. The high-purity HNO_3 was distilled from reagent grade acid and diluted to different concentrations for different purposes. The centrifuge tubes were ultrasonicated for 5 minutes after acid addition. For samples that did not dissolve completely, an additional 25 μL 0.5M HNO_3 was added followed by 5 minutes of ultrasonication. The process was repeated until no powder was visible. Controlling the amount of acid is important in this step, because it determines how much buffer solution to add for column separation of boron for boron isotope measurements. After dissolution, the sample solutions were transferred to new clean centrifuge tubes for storage. An aliquot of 2 μL of each sample solution was taken and diluted with 198 μL 0.5M HNO_3, to check the [Ca^{2+}] in each sample. The [Ca^{2+}] of the sample solutions were estimated by comparing their ^{43}Ca and ^{48}Ca intensities on an Agilent 7500a ICP-MS to a 1 mM [Ca^{2+}] standard solution. Depending on sample size and possible loss through all previous steps, [Ca^{2+}] of the primary solutions vary from 0.25 mM to 23 mM. Most samples (86%) have [Ca^{2+}] greater than 1 mM, and were diluted to a 300 μL 1 mM [Ca^{2+}] for multi-element Me/Ca measurements. To save solutions for boron isotope measurements, some of the samples were diluted to 0.5 mM [Ca^{2+}] instead, and measured against the standard solution of the same [Ca^{2+}]. 40% of the samples had more than 2 ng of boron after the Me/Ca analyses, which is approximately the lower limit for good boron isotope measurements in the STAiG lab. Boron isotope measurements were also attempted on a few samples with 1-2 ng boron remaining. The method for boron isotope measurements have been described elsewhere (Rae et al., 2018), and is not detailed here. Relatively little progress has been made in understanding and interpreting this boron isotope dataset, so it will see limited discussion below.

Me/Ca measurements of the samples were performed on an Agilent 7500a quadruple ICP-MS. A Teflon spray chamber with a sapphire injector was used to minimize boron blanks. The multi-element method collects ^{7}Li, ^{11}B, ^{23}Na, ^{24}Mg, ^{25}Mg, ^{27}Al, ^{43}Ca, ^{48}Ca, ^{55}Mn, ^{88}Sr, ^{111}Cd, ^{138}Ba, ^{146}Nd and ^{238}U in the standard and sample solutions, as well as blank 0.5M HNO_3 solutions. The isotopes are all detected in pulse counting mode for the blanks. For standards and samples, ^{23}Na, ^{24}Mg, ^{25}Mg, ^{43}Ca, ^{48}Ca and ^{88}Sr are detected in analog mode, while other elements are detected in pulse mode. A pulse-analog conversion factor is calibrated with a 1 mM [Ca^{2+}] standard solution during each analytical session. The calibration standard (named STGTE or BSGS) is a gravimetric mixture of single element solutions with Me/Ca ratios in the range of foraminifera shells. Five samples are bracketed by two standards and two blanks in a sequence for Me/Ca calibrations, and 3 internal cycles (a cycle is a complete scan of the isotope list) are run for each blank, standard and sample. Between two measurements, the nebulizer probe is rinsed with a 0.5M HNO_3+0.3M HF solution for 1 minute to avoid cross-contamination. HF was added to the rinse solution to lower the boron blanks. Three consistency standards (STGCS1, STGCS2, STGCS3) were run daily against BSGS, and regularly inserted as samples during a sequence to check the long-term reproducibility of the measurements. These consistency standards are also single element mixtures with Me/Ca compositions similar to benthic foraminifera (STGCS1), corals (STGCS2) and planktonic foraminifera (STGCS3), respectively. A number of analytical issues were found during the 4-week run at St. Andrews that have not been completely resolved. Some of the issues are discussed in detail in Chapter 5 when comparing Me/Ca measurements at St. Andrews and Caltech. This chapter is mainly focused on the observed Me/Ca variances in the corals.

3.3.2 Stable Isotope Variability

Figure 3-5 shows the $\delta^{18}O$ and $\delta^{13}C$ data measured in five *D.dianthus* individuals. As in Adkins et al. (2003), strong linear correlation is found between $\delta^{18}O$ and $\delta^{13}C$ in each individual with a slope between 1.8 and 2.6. No points clearly deviate from the linear trend that is indicative of COCs, although COC bands were identified and sampled from the sample surface during micromilling (Figure 3-6, 3-7). In fact, the group of data points with low $\delta^{18}O$ and $\delta^{13}C$ values for coral 47413 are all influenced by COC bands (Figure 3-6). They do not stand out as deviations from the linear trend partially due to the limited number of data points as compared to Adkins et al. (2003), and partially due to significant averaging during the micromilling process as the bands

were milled to depths of hundreds of microns. The thick central COC band in 47413 may have been mixed with the most amount of secondary aragonite so that it has a slightly more enriched $\delta^{18}O$ value compared to the thinner COC bands on either side. Similarly, data for coral Titan-top may also be subjected to some averaging effects, which caused the apparent COC bands to fall on the linear trend despite having depleted $\delta^{18}O$ and $\delta^{13}C$ values (Figure 3-7).

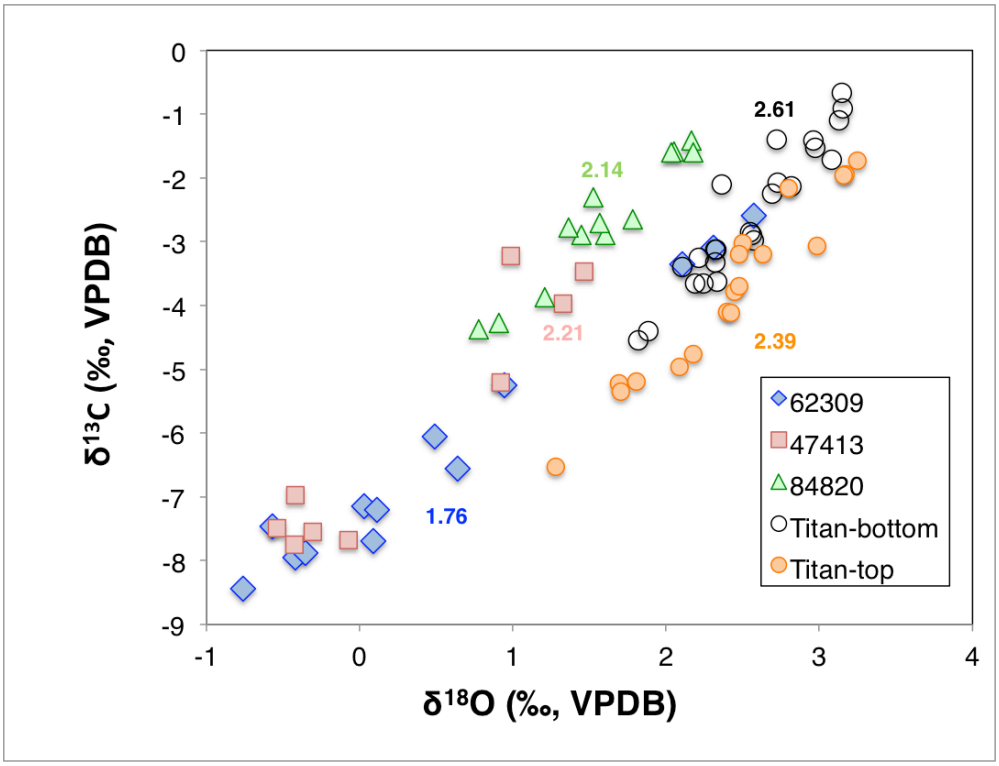

Figure 3-5 $\delta^{18}O$ and $\delta^{13}C$ in micromilled coral samples. Data are shown for 5 individual corals: 62309 (North Atlantic), 47413 (South Pacific), 84820 (Eastern Equatorial Pacific), Titan-top and Titan-bottom (South Pacific). Titan-top and Titan-bottom are two individual polyps whose skeletons are cemented together in the vertical direction with the calice of another polyp (Titan-middle) in between. There could be a time offset of at least a few decades for these two individuals. The numbers mark the slopes of the $\delta^{18}O$-$\delta^{13}C$ correlation for datasets of the same color.

There is a distinction among different corals in the range of $\delta^{18}O$ and $\delta^{13}C$ they span. Two corals (62309 and 47413) have data points with very low $\delta^{18}O$ and $\delta^{13}C$ values ($\delta^{18}O$ lower than 1‰ and $\delta^{13}C$ lower than -5‰), while these low $\delta^{18}O$ and $\delta^{13}C$ values are almost absent in the other three corals (84820, Titan-bottom and Titan-top). This is unlikely a sampling bias given that both COCs and secondary aragonite were sampled for different corals. Interestingly, both 62309 and 47413 grew in seawater that is oversaturated with respect to aragonite (Ω_A=1.4 for 62309, 1.6 for

47413), while 84820 and Titan grew in undersaturated seawater (Ω_A=0.78 for 84820, 0.80 for Titan). Given the interpretation of $\delta^{18}O$ and $\delta^{13}C$ as indicators of the strength of the alkalinity pump in Chapter 2, this difference would imply that corals growing in undersaturated seawater do not have as strong an alkalinity pump as those growing in supersaturated seawater. This may also reflect a change in the biomineralization scheme by the corals living under stress of undersaturated conditions, as was previously proposed in ocean acidification studies (Cohen et al., 2009; Gagnon et al., 2013; Mollica et al., 2018).

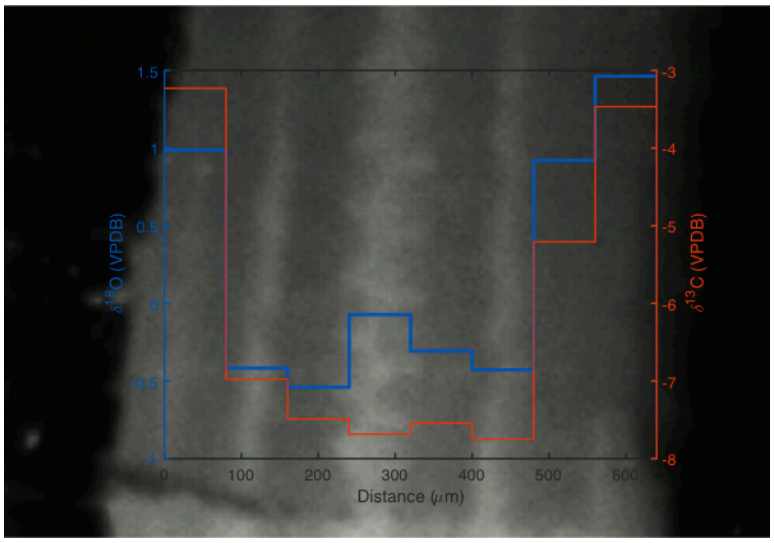

Figure 3-6 Micromilled $\delta^{18}O$ (blue) and $\delta^{13}C$ (red) profiles on a main septum (reflected light image) of 47413. The bands were milled at a resolution of 80 μm. There are 3 COC (white) bands on this septum, a thick one in the center and a thin one on each side.

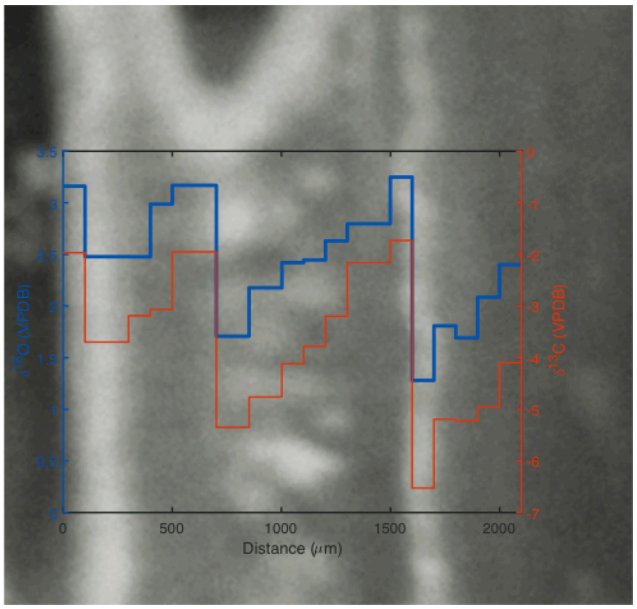

Figure 3-7 Micromilled $\delta^{18}O$ (blue) and $\delta^{13}C$ (red) profiles on the theca between two septa (reflected light image) of Titan-top. The bands were milled at a resolution of 100 μm. There is one COC band on each septum, and a COC-like white region in the middle between the two septa.

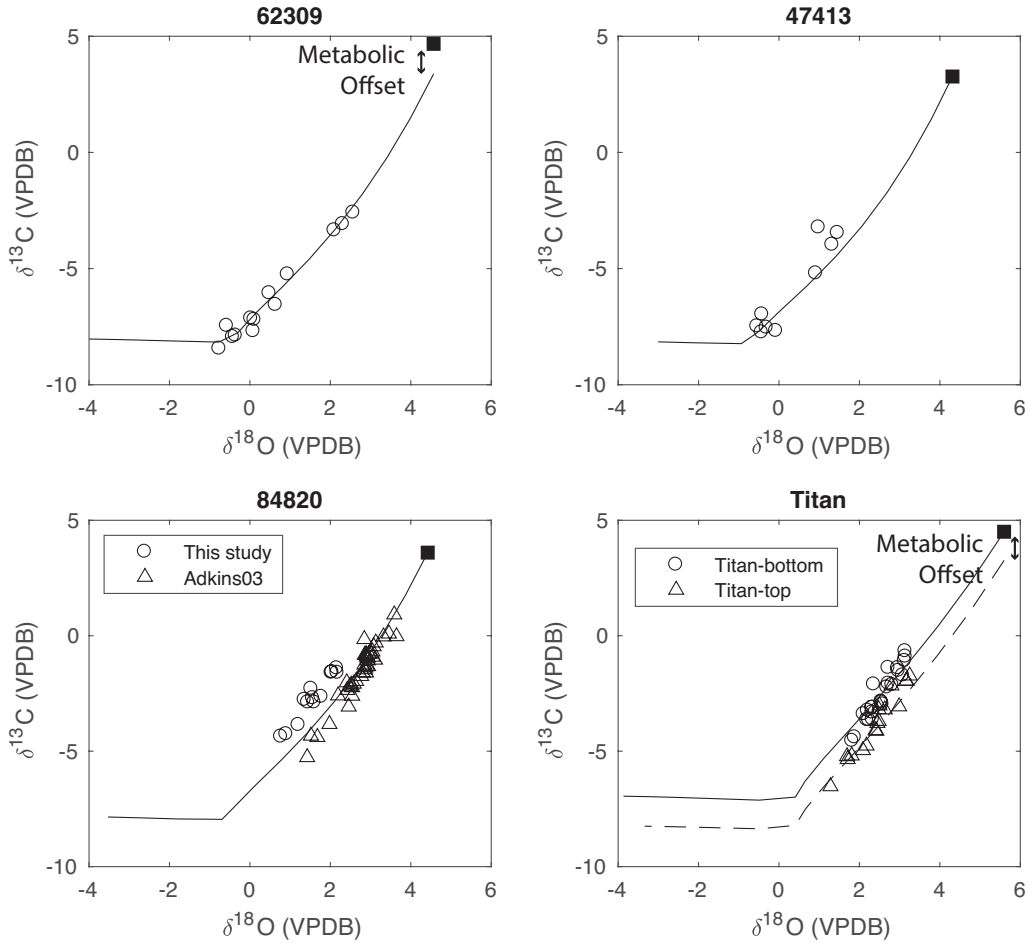

Figure 3-8 Model fits to the stable isotope data in Figure 3-5. The same set of model parameters are used to generate the model lines except for changing the environmental conditions of each coral, and an adjustment of the $\delta^{13}C$ of the cross-membrane CO_2(aq) in some cases. The solid squares mark the equilibrium composition of the skeletons with no metabolic CO_2 contribution. For 62309 and Titan-top, a 2‰ offset is applied to the $\delta^{13}C$ of the CO_2(aq) (~15% metabolic CO_2) to make the model lines go through the data. For 84820, data from this study is plotted with those of Adkins et al. (2003). The $\delta^{18}O$ values for 84820 from this study are lower than the Adkins et al. (2003) data, which may be related to variability within the individual or a calibration offset during the measurements. The model line goes through most of the Adkins et al. (2003) data, but is not too far from data in this study.

To quantify the degree of pH up-regulation in these corals, the stable isotope numerical model in Chapter 2 was run at the growth condition of each coral to generate fit to the data (Figure 3-8). As shown in Chapter 2 (Figure 2-4), minimum tuning was required to fit the general trend in the data in different corals in Figure 3-5, and the only parameter that needs to be adjusted is the $\delta^{13}C$ of the cross-membrane CO_2(aq), which reflects a contribution from metabolic carbon to DIC in the ECF. A 2‰ adjustment to the CO_2(aq) was required for 62309 and Titan-top to make the

model go through the data. From the model fit, we see that 62309 and 47413 have data points that reach the expected $\delta^{18}O$-$\delta^{13}C$ kink, while 84820 and Titan do not. Based on the observed range in $\delta^{18}O$-$\delta^{13}C$ and the model fits, we calculate the maximum ECF pH that was obtained by the corals (neglecting COCs), and plot them with the ambient pH (Figure 3-9a). According to the model framework, we see that corals living in supersaturated seawater (and high ambient pH) can reach an ECF pH slightly above pK_{a2}, while those living in undersaturated waters cannot. However, the corals living in undersaturated seawater can still reach an ECF pH that is more than 1 pH unit higher than seawater, with an aragonite saturation index in the range of 9–11 (Figure 3-9b). Although the differences in Ω_A may not seem large between corals living in undersaturated and supersaturated seawater, the difference could result in a 30-60% decrease in maximum growth rate for the corals living in undersaturated conditions according to the model. It should be cautioned that these interpretations are all based on the model fits to the stable isotope data, and requires validation by independent observations (such as culture experiments and direct ECF chemistry measurements). Given the difficulties in culturing deep-sea corals, there are no direct observations of the actual pH in their ECF, so the high pH values predicted by the model await to be tested. A higher ECF pH in *D.dianthus* than in surface corals is supported by boron isotope evidence (Anagnostou et al., 2012; Stewart et al., 2016), although the absolute ECF pH values calculated from boron isotope data (8.5–8.9) are lower than the model predictions. Nevertheless, given that the model can fit the $\delta^{18}O$-$\delta^{13}C$ pattern across multiple corals with minimum adjustment to the parameters, we continue to use it as a guideline to investigate the Me/Ca patterns and their relations to the stable isotopes.

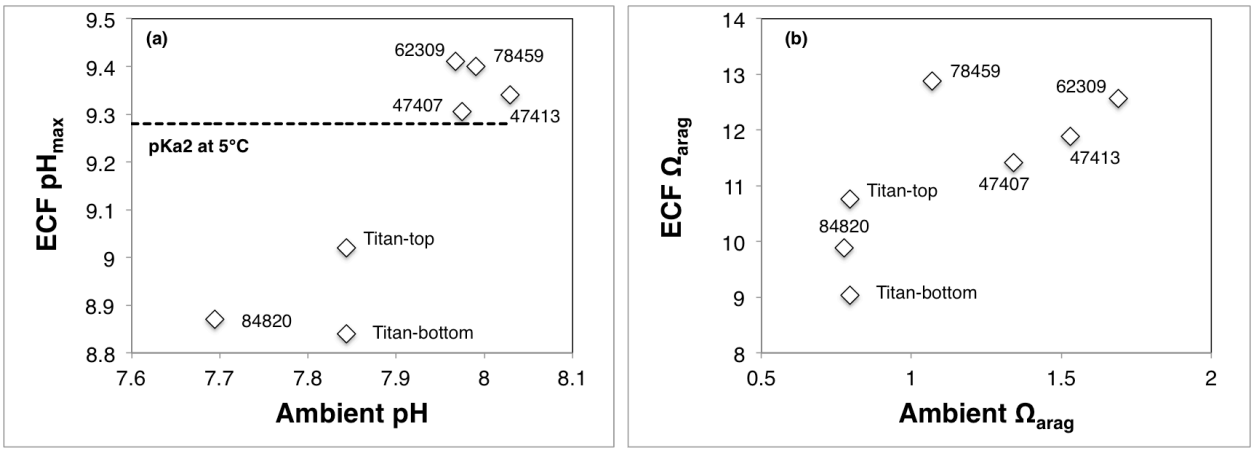

Figure 3-9 Maximum ECF pH and aragonite saturation state predicted by the model as compared to the ambient seawater conditions for different corals.

3.3.3 Me/Ca Variability

During the sample preparation and analysis, a number of problems arose due to both instrument issues (random computer shutdown for the Agilent, plasma gas ran out, etc.) and some bad decisions I made in the lab. For example, samples for coral 47407 were contaminated by epoxy during micromilling, with anomalously high Mg/Ca, Al/Ca and Mn/Ca that are strongly correlated. After identifying the problem, an effort was made to separate the epoxy in other samples by centrifuging (to make epoxy float on MilliQ) and overflowing multiple times until no epoxy was visible on top of the MilliQ. During this process, some samples were left in MilliQ overnight, and got partially dissolved by this undersaturated water (measurable [Ca^{2+}] in the MilliQ compared to blanks). It was found that the Me/Ca in the MilliQ for these samples are almost always higher than the remaining aragonite powder, suggesting a component in the coral skeleton with higher trace element impurities that is preferentially dissolved. These problems have compromised the quality and size of this dataset, and limited robust characterization of Me/Ca patterns in different *D.dianthus* individuals from this dataset alone.

Figure 3-10 shows some Me/Ca profiles in coral Big Beauty, which did not suffer from the problems listed above. There is a single COC on this main septum of Big Beauty. As observed in previous studies, the COC is elevated in Mg/Ca and Li/Ca, while depleted in B/Ca, $\delta^{11}B$ and U/Ca compared to the secondary aragonite (Robinson et al., 2006; Gagnon et al., 2007; Blamart et al., 2007; Case et al., 2010). Sr/Ca of the COC does not have an extreme value, also consistent with previous studies for *D.dianthus* (Gagnon et al., 2007). In this profile, the COC is also elevated in Ba/Ca, which was not observed previously by laser ablation ICP-MS (Anagnostou et al., 2011). Outside the COC, Mg/Ca shares similar trends with Li/Ca and opposite trends with Sr/Ca. The 30% depletion in U/Ca seems to extend beyond the COC by 100–200 μm, which has been previously observed by Robinson et al. (2006). The low B/Ca in the COC is not unique in the skeleton, as similarly low B/Ca values are also observed away from the COC. The $\delta^{11}B$ in the COC is depleted by ~1.3‰ compared to the mean value in the secondary aragonite in the profile. B/Ca and $\delta^{11}B$ have similar patterns across the growth bands (including the COC), consistent with previous studies in deep-sea corals (Blamart et al., 2007; Stewart et al., 2016). The correlation between B/Ca and $\delta^{11}B$ suggests that they are coupled through the pH up-regulation in the biomineralization process. Ba/Ca is almost constant in the secondary aragonite, which is consistent

with laser ablation ICP-MS measurements (Anagnostou et al., 2011). These distribution patterns can be further explored with Me/Ca cross plots, and by comparison with model simulations.

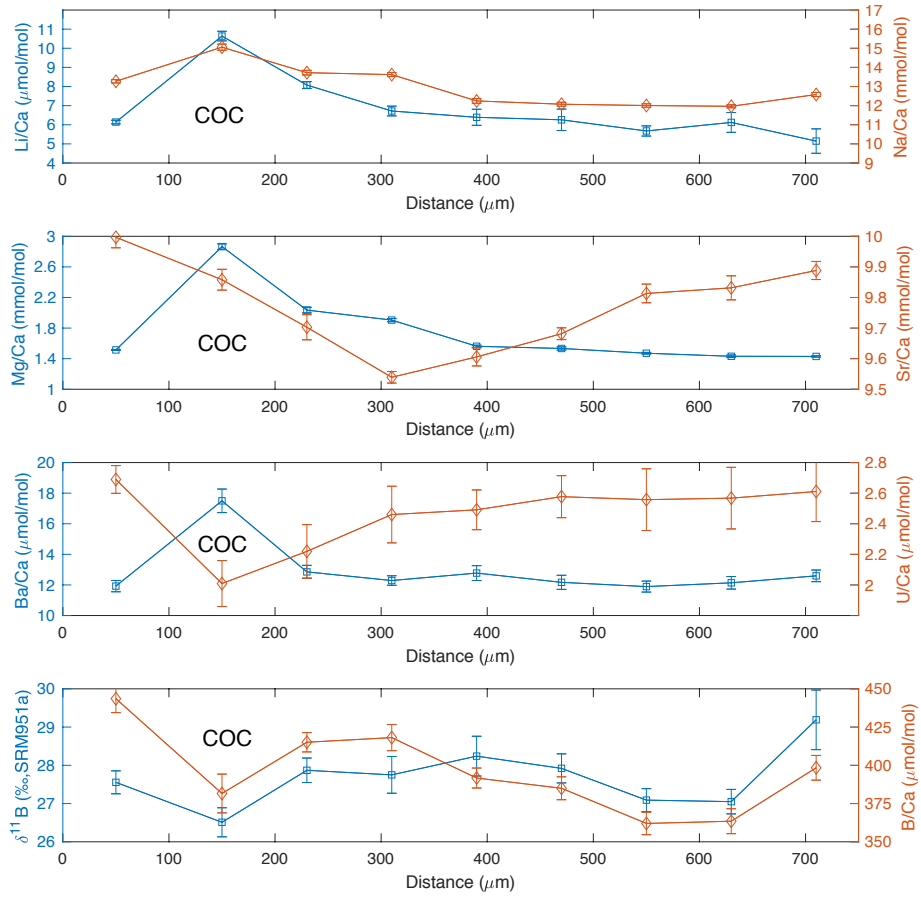

Figure 3-10 Me/Ca and $\delta^{11}B$ profiles across a septum in Big Beauty. Error bars for Me/Ca ratios (2 SE, standard error) are from 3 internal cycles of each sample. Error bars for $\delta^{11}B$ (2SE) are from 3 replicate measurements of the same sample solution and have been corrected for procedural blanks. The blue squares correspond to the left axes while the red diamonds correspond to the right axes.

Figure 3-11 shows cross plots of Li/Ca, B/Ca, Sr/Ca and U/Ca vs. Mg/Ca in different *D.dianthus* individuals that did not have processing/analytical problems. We see that Mg/Ca and Li/Ca are linearly correlated in most samples in individual corals, consistent with previous observations (Case et al., 2010; Marchitto et al., 2018) and the numerical model. This correlation is broken with samples that went through oxidative cleaning. In coral 84820, the cleaned samples are significantly lower in Li/Ca and B/Ca and have less variability. It is likely that the cleaning procedure removes a more soluble component that has higher Li and B content. In coral Titan, there are a group of points that have very low Li/Ca and B/Ca that fall off the trend defined by

other points. These Li/Ca and B/Ca values are anomalously low and have not been reported for *D.dianthus* before. Given that chemical cleaning can cause lower Li/Ca and B/Ca values by partial dissolution, and that Titan has a brown crust on the surface (suggesting it may not be a modern coral), it is possible that these samples have been subjected to some diagenetic alteration that removed the more soluble phase with higher Li and B. It is also possible that this reflects some unidentified biomineralization mechanism for this particular coral living in undersaturated seawater that is both deep (2066 m) and cold (2°C).

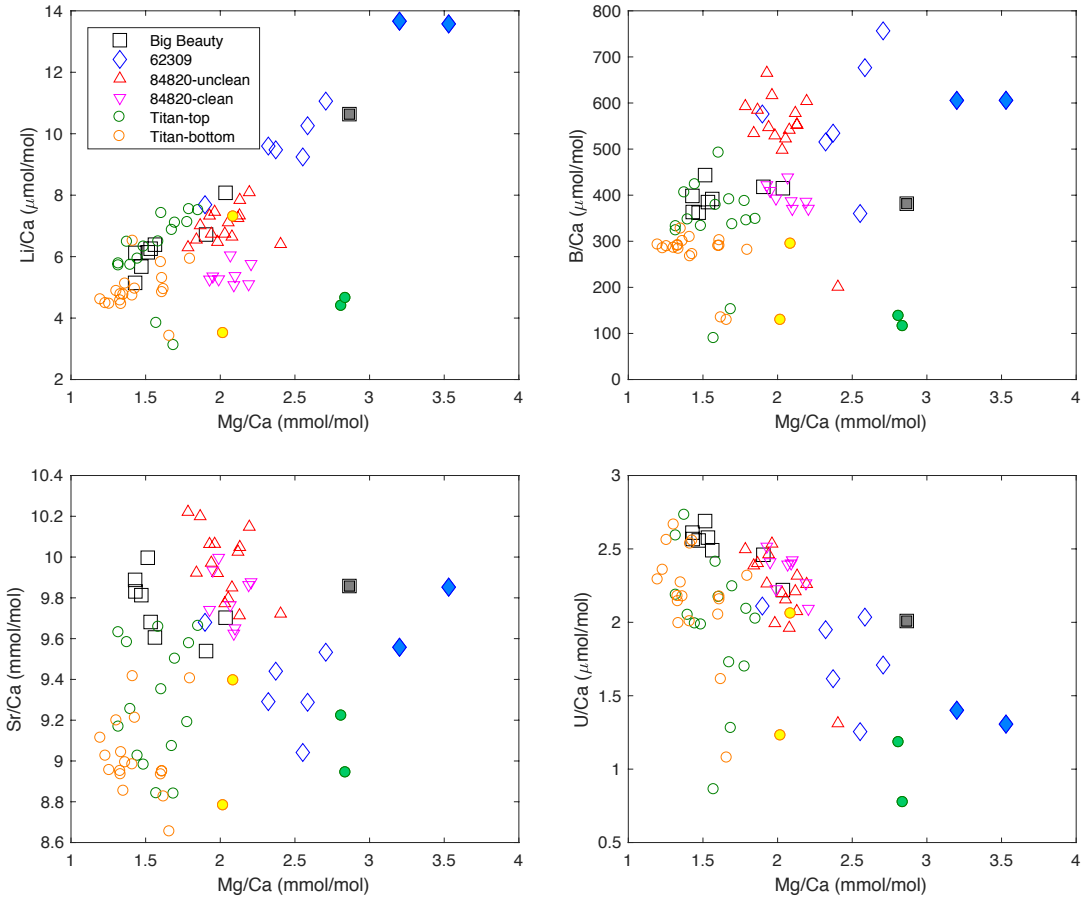

Figure 3-11 Me/Ca correlations in individual *D.dianthus* specimens. Each individual coral is plotted with a different symbol. Open symbols represent secondary aragonite, while filled symbols represent COCs or COC-like bands. Two datasets are shown for 84820, one of them with oxidative cleaning (down triangle) and one without oxidative cleaning (up triangle). Cleaning gives rise to lower Li/Ca and B/Ca (potentially by removing a more soluble phase with significantly higher Li and B) and removes most of the variability in these ratios. All other data points are from uncleaned samples.

In addition to Li/Ca, Mg/Ca is weakly positively correlated with B/Ca in the secondary aragonite. B/Ca in the COCs are low in general, but similar to the low B/Ca values in the secondary aragonite. There is a negative correlation trend between Mg/Ca and Sr/Ca in the secondary aragonite, with COCs having intermediate Sr/Ca values, although there is significant scatter in the data. The Mg/Ca-Sr/Ca trend is consistent with previous observations by Gagnon et al. (2007), as well as the model predictions for low f_{Ca} values. Mg/Ca and U/Ca are also negatively correlated in the secondary aragonite, with lower U/Ca in COCs.

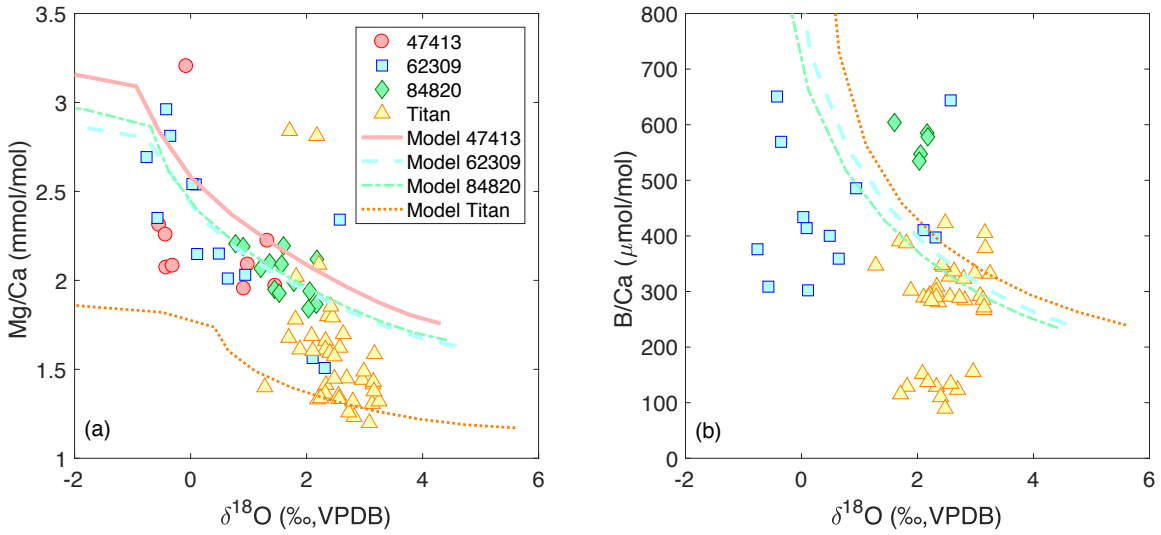

Figure 3-12 Mg/Ca and B/Ca vs. $\delta^{18}O$ data-model comparison. (a) Mg/Ca vs. $\delta^{18}O$ in different *D.dianthus* individuals compared to the numerical model with f_{Ca}=0 and τ_{sw}=230s. The model was run at the growth conditions of each coral and plotted with the same color as the corresponding data. The kink on the upper left of the model curve represents transition toward COC composition. (b) B/Ca vs. $\delta^{18}O$ in different *D.dianthus* individuals compared to the numerical model prediction with the $[B(OH)_4^-]/[HCO_3^-]$ partition rule.

3.3.4 Relations between Me/Ca and Stable Isotopes

Since sample loss happened to both the stable isotope and Me/Ca dataset for separate reasons, the points available to relate these two datasets are even more limited in number, making it difficult to identify robust relations. Figure 3-12 shows the available data for Mg/Ca and B/Ca vs. $\delta^{18}O$ in different corals compared to model outputs at the growth conditions of each coral. Although there is significant scatter in the data, a general trend of increasing Mg/Ca with decreasing $\delta^{18}O$ is observed, with a steepening slope at lower $\delta^{18}O$ values, which is also produced

by the model. Given the interpretation of $\delta^{18}O$ as the strength of the alkalinity pump, this trend suggests that Mg^{2+} is raised relative to Ca^{2+} in the ECF at higher pump rates, which requires a relatively low Ca^{2+} supply by the pump. The model curve presented in Figure 3-12a already has f_{Ca} set at zero, and cannot get to the high Mg/Ca values in the data before taking a kink toward COC composition. Most notably, the model poorly simulates the range of Mg/Ca in Titan in the range of measured $\delta^{18}O$ values.

One way in the model to get to higher Mg/Ca values is to reduce the seawater turnover rate (increase τ_{sw}, as in Figure 3-3). Although the same τ_{sw} of 230s was used to fit the stable isotope data in different corals, many of them do not have a clean COC data point to constrain the spot of the kink, so it is likely that τ_{sw} is slightly different between different individuals. Another possibility is that the measured Mg has contributions from both the aragonite and organic phases in the skeleton, and the Mg contribution from organics is not captured by the model. The other complication is uncertainties in D_{Mg} for aragonite. The D_{Mg} used in the current model is from coral culture experiments by Reynaud et al. (2007), which were performed between 20–30°C. Although using their empirical D_{Mg} calibration gives model Mg/Ca ratios that are close to the observed range in deep-sea corals, the calibration itself may have convolved vital effects by the corals.

To my knowledge, the only calibration for the temperature dependence of D_{Mg} available from inorganic aragonite precipitation is from Gaetani & Cohen (2006). Their experiments span a temperature range of 5°C–75°C, but it is suspected that their experiments were not run at equilibrium precipitation conditions and involved strong kinetic effects. Their measured distribution coefficients for Mg, Sr and Ba at 5°C also deviate from the trend defined by their data at higher temperatures, further complicating the calibration. In addition, the current model has not accounted for the growth rate dependence of the minor and trace elements. D_{Mg} was found to increase with precipitation rate in aragonite by Gabitov et al. (2008), although it is hard to quantitatively incorporate their results into the model due to very different experimental conditions and estimates of growth rates. More systematic precipitation experiments, especially aragonite experiments at low temperatures, are needed to improve our understanding of the inorganic reference frame of Me/Ca ratios for biogenic carbonates.

Apart from Mg/Ca, the relations between $\delta^{18}O$ and other Me/Ca ratios are generally more scattered and lack a clear pattern. It is partly because Mg/Ca is less susceptible to the preparation/analytical problems mentioned above, and also likely related to more complicated biomineralization mechanisms for the other elements that have not been accounted for in the current model framework. For example, with the commonly used $[B(OH)_4^-]/[HCO_3^-]$ partition rule, the model predicts an increase in B/Ca with more depleted $\delta^{18}O$ values, with a steepening slope along the trend. Part of the data from 62309 and Titan suggests a similar pattern might exist in the corals, but overall the data are much more scattered to be explained by this simple model (Figure 3-12b). A better understanding of the physicochemical principles of boron incorporation in aragonite is key to unraveling the mechanisms of B/Ca variability in coral skeletons.

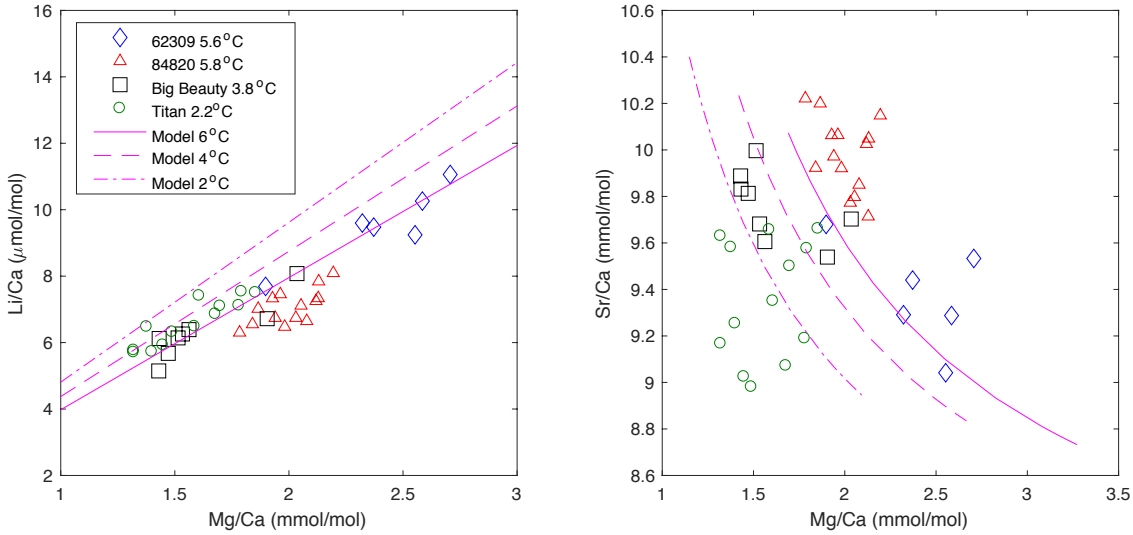

Figure 3-13 Model-data comparison of temperature information in Me/Ca correlations. Only data for secondary aragonite without preparation/measurement artifacts are shown for four different corals. Model curves are generated for 3 different temperatures at f_{Ca}=0 and τ_{sw}=230s. The temperature sensitivities of D_{Mg} is taken from Reynaud et al. (2007), D_{Li} from the Li/Mg thermometer calibration by Marchitto et al. (2018), and D_{Sr} from Gaetani & Cohen (2006). Some adjustments were made to the absolute values of the distribution coefficients to match the observed range in the data (a factor of 4 for Li, 10% for Sr). These adjustments could reflect distribution coefficients that are not well constrained for aragonite, or could be equivalently caused by biological manipulation of the Me/Ca ratios of the initial ECF relative to seawater, which is not considered so far in the model.

3.3.5 Possible Environmental Information in the Me/Ca Data

The ultimate goal of the study is not only to understand the biomineralization process behind the observed tracer correlations, but also to deconvolve the environmental information from the vital effects. As discussed in Section 3.2.4, the slopes of Me/Ca correlations could contain temperature information, if the biomineralization process can be reasonably simplified.

Figure 3-13 shows two examples of model-data comparison for Li/Ca vs. Mg/Ca and Sr/Ca vs. Mg/Ca. As expected from the model and observed in different coral species and the foraminifera *H.elegans*, the slope of Li/Ca vs. Mg/Ca should be a function of temperature with minimal impact from vital effects. Using the empirical distribution coefficients determined from a compilation of coral data (Marchitto et al., 2018), the model can predict linear relations in Li/Ca vs. Mg/Ca with slopes similar to the *D.dianthus* data, although there is some offset in absolute Me/Ca values that cannot be accounted for by the simple model. For Mg/Ca and Sr/Ca, the model with f_{Ca}=0 predicts shallower slopes at higher temperatures. The Mg/Ca and Sr/Ca data are too scattered to show the expected patterns from the model. The Mg/Ca and Sr/Ca data for the low temperature corals (Big Beauty and Titan) seem to have a steeper slope than the model predictions, which could suggest a change in f_{Ca} in the alkalinity pump (Figure 3-2c), and needs to be tested with more data. Despite these complications, model-data comparisons for different tracers throughout this chapter suggest a relatively low fraction (possibly zero) of Ca^{2+} in the alkalinity pump. This may seem odd intuitively, but may not be too surprising given that Ca^{2+} is five times more concentrated in seawater than DIC, and the corals are not limited by Ca^{2+} as long as they maintain a seawater flux into the ECF. The next chapter presents more Me/Ca data on finer scales to address these questions.

3.4 Conclusions

In this chapter, the numerical model for stable isotopes is extended to the incorporation of minor and trace elements during coral calcification. A series of model predictions were generated for Me/Ca and stable isotope correlations over a range of parameter space, and in particular, at different seawater turnover timescales and fraction of Ca^{2+} in the alkalinity pump. These model

predictions are compared to stable isotope and Me/Ca data from micromilled bands of *D.dianthus* individuals. As in previous studies, strong positive correlations were found for $\delta^{18}O$ and $\delta^{13}C$, but the range of isotope variability in individual corals may depend on the saturation state of the ambient seawater. A few Me/Ca correlations were found for these corals that are generally consistent with previous studies, including positive Mg/Ca-Li/Ca and Mg/Ca-B/Ca correlations and negative Mg/Ca-Sr/Ca and Mg/Ca-U/Ca correlations. A negative correlation was also found between Mg/Ca and $\delta^{18}O$ of the growth bands. A model-data comparison suggests that the fraction of Ca^{2+} in the alkalinity pump is likely very low (close to zero) in these corals. Extraction of environmental information such as temperature from the observed Me/Ca correlations is limited by the size and quality of the dataset, although some patterns (Li/Ca vs. Mg/Ca and Sr/Ca vs. Mg/Ca) in the data show agreement with the model predictions. The next chapter tries to further address these issues with SIMS and nanoSIMS measurements.

Chapter 4

Variability of Minor and Trace Elements in Deep-Sea Corals from SIMS and nanoSIMS measurements and Implications for the Biomineralization Mechanisms

4.1 Introduction

Secondary ion mass spectrometry (SIMS) has emerged as a useful tool to characterize the chemical composition and fine scale heterogeneities in geological materials (Shimizu & Hart, 1982; Reed, 1984; MacRae, 1995). It has been used to study the minor and trace element and isotopic compositions of a variety of carbonates over the past decades (e.g. Allison, 1996; Rollion-Bard et al., 2003; Meibom et al., 2004; Weber et al., 2005; Gaetani & Cohen, 2006; Blamart et al., 2007; Holcomb et al., 2009; Kita et al., 2009; Gagnon et al., 2012; Gabitov et al., 2013; Paris et al., 2014; Gothman et al., 2015). In particular, its applications to biogenic carbonates can help reveal the isotopic, minor and trace element variability associated with different biomineralization features and provides clues to the underlying mechanisms of vital effects (Kunioka et al., 2006; Blamart et al., 2007; Meibom et al., 2008; Rollion-Bard et al., 2010; Rollion-Bard & Blamart, 2015). While traditional SIMS measurements have a similar spatial resolution to laser-ablation ICP-MS, applications of nanoSIMS techniques to biogenic carbonates have allowed measurements of minor and trace elements at spatial resolutions (1 μm or less) comparable to electron probes and secondary electron microscopes (Kunioka et al., 2006; Meibom et al., 2004; Meibom et al., 2007; Paris et al., 2014; Fehrenbacher et al. 2017). The consistent finding in these nanoSIMS studies is the quasi-rhythmic compositional banding in a number of minor and trace elements in both foraminefera (Kunioka et al., 2006; Paris et al., 2014; Fehrenbacher et al., 2017) and corals (Meibom et al., 2004; Meibom et al., 2007; Frankowiak et al., 2016).

Following chapter 3, this chapter continues to explore the variance of minor and trace elements at finer spatial scales in deep-sea corals with SIMS and nanoSIMS techniques, with the same goal of understanding the biomineralization mechanisms driving Me/Ca variability and disentangling the vital effects from environmental information in Me/Ca ratios. It is expected that these measurements can better characterize the full range of variability in Me/Ca ratios and their

association with the growth bands in the skeletons by minimizing the averaging effect of micromilling. Despite higher spatial resolution and less aliasing, the disadvantage of SIMS and nanoSIMS as compared to solution based ICP-MS is the challenge in getting accurate and precise measurements from solid samples. The precision is influenced by the stability of the ionization process through the interaction of the primary ion beam with the sample surface.

By replicate measurements of single spots on carbonate standards, Gabitov et al. (2013) found systematic trends in Me/Ca ratios in the first tens of cycles that approach a quasi-steady state as the cycle numbers are increased. Within the quasi-steady state, the uncertainty in mean Me/Ca ratios follows counting statistics (Gabitov et al., 2013). As a result, a good SIMS measurement would require this quasi-steady state in ionization to be reached, after which the precision is limited by the number of total ion counts collected. Accuracy calibration with SIMS measurements is more challenging due to a number of issues. First, the ionization process is influenced by the physical and chemical properties of the solid samples, usually referred to as a "matrix effect" (Slodzian et al., 1980). The same element in different solid matrices can have different ionization efficiencies, and an accurate concentration measurement can require the sample and standard to be closely matched in chemical composition as well as physical properties and preparation. Second, there is usually significant compositional heterogeneity in solid samples compared to solutions, which is also the case for carbonate standards. By comparing SIMS measurements of a number of carbonate standards, Gabitov et al. (2013) found that most of the commonly used solid carbonate standards have higher variability in Mg, Sr and Ba content than previously thought. To minimize the uncertainties caused by heterogeneities in the standards, some small regions in certain standards were identified by Gabitov et al. (2013) as relatively homogeneous and ideally suited for accuracy calibrations. Third, and specific for the purpose of this study, few or no appropriate standards are currently available at Caltech for calibration of some key trace elements of interest (e.g. Li and B), and there is limited knowledge about the homogeneities of these trace elements as well as the matrix effects in different standards. As a result, accuracy calibration for Me/Ca in deep-sea corals for this study takes a mixture of approaches. We compare samples to both solid carbonate standards and bulk ICP-MS measurements, and the differences between these approaches are discussed. This is not ideal for comparing the deep-sea coral Me/Ca data directly to the inorganic reference frame and the numerical model. However, as long as the same method is

applied and the samples are similarly prepared, the relative changes in Me/Ca ratios should be robust and can be used to address the effects of biomineralization on the range of Me/Ca values in deep-sea corals.

4.2 Methods

4.2.1 SIMS measurements

The SIMS measurements were performed on a Cameca ims 7f-Geo instrument at the Caltech Microanalysis Center. A "top view" section of each *D.dianthus* specimen (see Section 3.3.1) was mounted on a 1'' round glass slide and hand polished on polishing papers down to ~200 μm thickness and 1 μm grain size, followed by vibrational polishing on a polishing cloth with 30 nm colloidal silica. This polishing procedure was found to best remove cracks and small height changes on the sample surfaces and made it easier to identify the growth bands under the video camera of the instrument. After polishing, the samples were rinsed with DI water and isopropanol and dried, and coated with 20 nm gold before SIMS analysis. Transmitted and reflected light images were taken on the samples before and after SIMS analysis.

During the one-week analytical session in March of 2019, ^{7}Li, ^{11}B, ^{26}Mg, ^{42}Ca and ^{88}Sr were measured on a suite of *D.dianthus* specimens that span a relatively wide range of environmental conditions (mainly temperature and $[CO_3^{2-}]$), together with different calibration standards. An 8000 eV primary O^- beam was focused on ~30 μm spots on the coral to generate the secondary ions. The primary beam current varied between 5–6.5 nA during this session. Due to the aging of the O^- source, the primary beam current would slowly drop as the analytical session went on, and ion lenses in the source were constantly adjusted to increase the primary beam current at the start of a profile of multiple spots. Despite these adjustments, the change in the primary current for a single spot (20–25 minutes) before and after analysis is less than 0.05 nA. The secondary ions were selected with a field aperture of 300 μm, a contrast aperture of 250 μm, an entrance slit at 109 μm and an energy slit of 47 μm, with a mass resolving power (MRP) of 3002. This MRP is sufficient to distinguish most molecular interferences (mostly hydrides) for the elements of interest, except for $^{87}SrH^+$ and $^{44}Ca_2^+$ on $^{88}Sr^+$ which require MRP to be over 8000. Each spot was pre-sputtered for 1 minute before analysis started with the same beam current as the analysis. During

analysis, 30–40 cycles were run on each spot, and each cycle consisted of 3 seconds of counting for ^{7}Li, 5s for ^{11}B, and 1s each for ^{26}Mg, ^{42}Ca and ^{88}Sr, with detection by an ETP electron multiplier. A waiting time of 2–7s was applied between isotopes for the adjustment of the magnet. The typical counting rate was 100–200 cps for ^{7}Li and ^{11}B, 6,000–7,000 cps for ^{26}Mg, 80,000–100,000 cps for ^{42}Ca and 100,000–120,000 cps for ^{88}Sr.

The carbonatite standard OKA was used to calibrate Mg/Ca and Sr/Ca ratios in the samples. It was measured between samples on three different days during the one-week session, with multiple spots on each day. This standard was chosen because Gabitov et al. (2013) previously found a relatively homogeneous matrix region that was ideal for accuracy calibrations. No carbonate standards are currently available at Caltech for Li/Ca and B/Ca calibrations. A group of glass standards developed by USGS that span a range in Li and B concentrations was used for this purpose, which is clearly subjected to the matrix effect as previously mentioned. As a result, we also compare the calibrated numbers with ICP-MS measurements of bulk coral powder as an additional constraint on the absolute Me/Ca ratios.

It should be noted that this was not the only session where we made SIMS measurements on deep-sea corals. Three other SIMS sessions were run between 2016 and 2017, with some of them focusing on the development of the method. During a session in January of 2017, a method was used to measure more elements than listed in the method above (including ^{23}Na, ^{32}S, ^{55}Mn, ^{138}Ba). Adjustments to the instrument conditions were made to accommodate these trace elements, and the most notable change was an MRP of 1799 and a raster size of 50 μm. While increasing the raster size reduced the number of cycles it took to reach the quasi-steady state for most elements, measuring a longer list of elements (with more magnet peak hopping) at lower MRP potentially caused this dataset to be noisier than the one collected in 2019. The sample preparation (sample thickness and polishing) was also not ideal for this session in 2017, further compromising the quality of this dataset. The discussion of the results will focus on the relatively clean dataset collected in 2019.

4.2.2 nanoSIMS imaging

The nanoSIMS measurements were performed with the imaging mode of a Cameca nanoSIMS 50-L instrument at the Caltech Microanalysis Center over three different analytical sessions for both minor and trace elements with an 8000 eV O^- source. The primary beam current from the source varied between 15–300 nA over each analytical session. Ion images were generated for the samples at raster sizes of 20-40 μm with 256×256 or 512×512 pixels per image. Through a series of focusing lenses, the primary ions that reached the sample surface had a current intensity between 20–100 pA at each pixel. It should be noted that the physical size of the primary ion beam (~200 nm, depending on current intensity) was sometimes larger than the size of a pixel, so some aliasing is incorporated into the images. This is of lesser importance to our target of characterizing Me/Ca variability over length scales of a few microns. There are seven detector channels for different isotopes on the instrument. A different element list was used for each session, but ^{7}Li, ^{11}B, ^{24}Mg, ^{42}Ca and ^{88}Sr were measured in all three sessions. The other isotopes that were mapped include ^{23}Na, ^{32}S, ^{35}Cl and ^{138}Ba. During the measurements, each pixel was collected for 5–15 ms, and a full image usually takes 30–60 minutes to collect. Multiple images (3–30, more for overnight measurements) were collected for each spot to accumulate as many counts as possible for the trace elements and reduce the noise in the images. Since nanoSIMS imaging is very sensitive to surface contamination, 30-60 minutes of pre-sputtering with a larger primary beam (a few nA) was applied before data collection. The raw data were loaded into Matlab with the package Look@NanoSIMS (Polerecky et al., 2012) for further image processing, such as averaging, smoothing and ratio calculations. The interactive processing software L'image (developed by Larry Nittler) was used to help generate Me/Ca profiles following the growth bands of the coral skeletons with uncertainty estimates. The carbonatite standard OKA was also imaged with the same method to provide accuracy calibration for some Me/Ca ratios.

4.2.3 Measurement Precision and Accuracy

When the primary ion beam interacts with the sample surface, it takes time for the ionization process to reach a steady state, after which the Me/Ca ratios vary within a relatively narrow range with uncertainties in the mean values described by counting statistics (Gabitov et al., 2013). Figure 4-1 shows the typical evolution of Me/Ca ratios with cycle number for single spots

in the SIMS measurements. We see that for the spot on secondary aragonite, Li/Ca, B/Ca and Mg/Ca ratios seem to already reach a steady state after pre-sputtering, but it takes Sr/Ca about 10 cycles to get to a steady state. For the spot on COC, Sr/Ca shows the same behavior of increasing toward steady state over ~10 cycles, while it takes Li/Ca, B/Ca and Mg/Ca about 6-7 cycles to reach steady state. I suspect that Sr/Ca ratios drift for more cycles because ^{88}Sr is of highest abundance among the measured isotopes, and it takes longer for the ionization to reach a steady state with all the Sr ions in and around the SIMS spot. It is generally true that other Me/Ca ratios drift for more cycles before reaching steady state on the COCs than the secondary aragonite, suggesting slightly different interactions with the primary ion beam for these two structures. To account for the drift, each spot is individually examined and the first few cycles that have not reached steady state are removed.

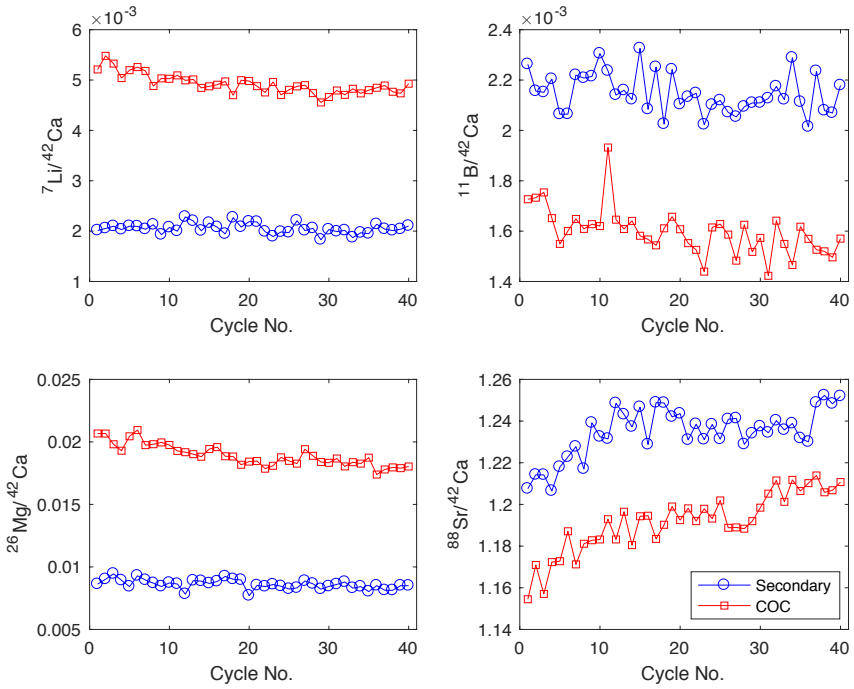

Figure 4-1 Changes in Me/Ca ratios over 40 analytical cycles for a spot on secondary aragonite (blue circles) and one on COC (red squares) of coral 80358.

After removing the first few cycles before a steady state is reached for each spot, an outlier test is run for the remaining cycles and points outside the 3σ range are further removed. The relative standard errors for Me/Ca ratios of the remaining cycles are compared against counting

statistics in Figure 4-2. We see that most data points scatter around the expected counting statistics line for Li/Ca, B/Ca and Mg/Ca, while the points scatter above the counting statistics line (by a factor of 2–3) for Sr/Ca. It is likely that the additional variability in Sr/Ca is caused by interference from $^{87}SrH^+$ and $^{44}Ca_2^+$ on $^{88}Sr^+$ that cannot be resolved by the current method. However, the internal precision on Sr/Ca measurements is 2–3‰ and much smaller than the expected variability in the coral skeletons (percent level), so the precision should be sufficient to characterize real Sr/Ca variability even though it is not ideal compared to counting statistics. The precision for Li/Ca, B/Ca and Mg/Ca ranges from a percent to sub-percent levels, also much lower than the expected variability in the corals.

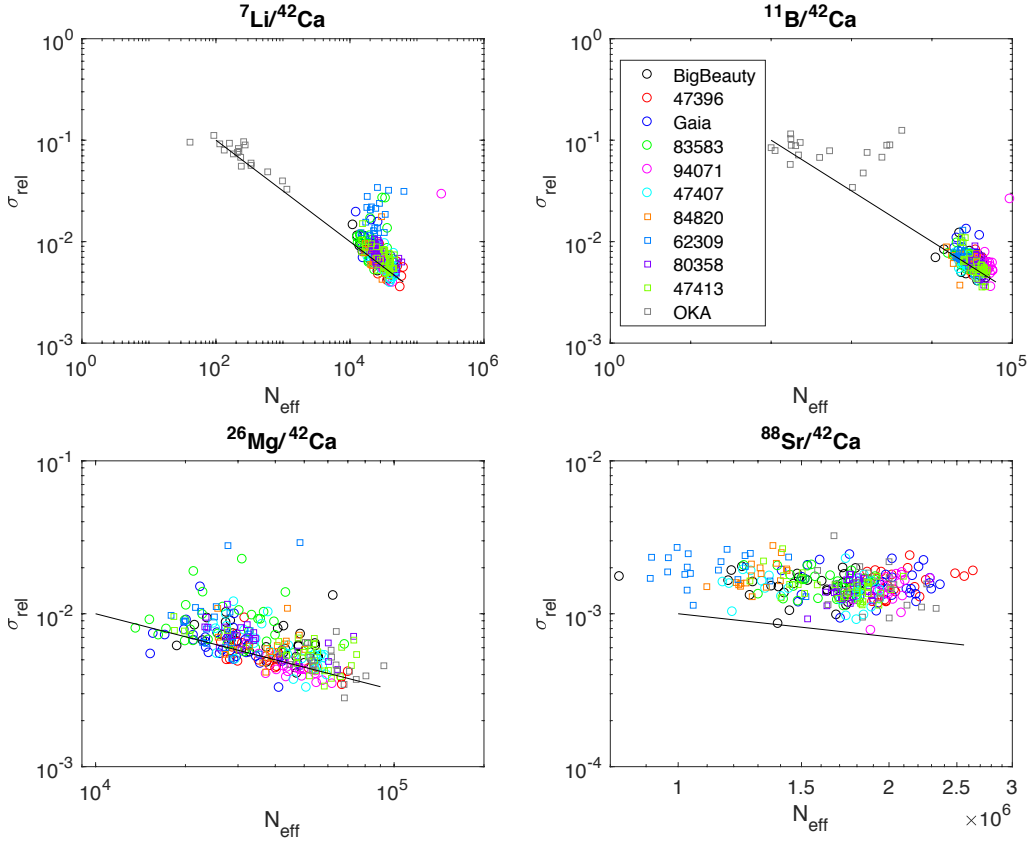

Figure 4-2 Relative standard error of SIMS Me/Ca measurements vs. effective counts in samples compared against counting statistics. Each symbol represents a different coral, the black squares represent the carbonatite standard OKA (with low, but measurable Li and B), and the lines represent counting statistics expectations. According to John & Adkins (2010), the relative standard errors of Me/Ca ratios expected from counting statistics should be the square root of $1/N_{eff}$, where $N_{eff}=N_{Me}N_{Ca}/(N_{Me}+N_{Ca})$ and N represents total ion counts collected. So the lines are expected to have a –1/2 slope on a log-log scale.

While the measurement precision may not be a limiting factor for the purpose of the study, accuracy calibration presents another challenge to get Me/Ca ratios that are comparable to the inorganic reference frame and the numerical model. During this analytical session, the carbonatite standard OKA was used to calibrate Mg/Ca and Sr/Ca ratios. Figure 4-3 shows the Mg/Ca vs. Sr/Ca cross plot on multiple spots of OKA measured over three different days during the SIMS session in 2019. Although I chose spots in the relatively homogeneous region previously identified by Gabitov et al. (2013), significant heterogeneity remains that cannot be accounted for by measurement precisions. However, the trends in Mg/Ca-Sr/Ca correlation observed are very similar to Gabitov et al. (2013), with a group of points clustered in the upper left corner. For accuracy calibration, I only use this cluster of points that show minimum heterogeneity, and standard ratios of 4.67 mmol/mol and 19.43 mmol/mol are used for Mg/Ca and Sr/Ca respectively based on solution ICP-MS measurements of the OKA standard (Gabitov et al., 2013).

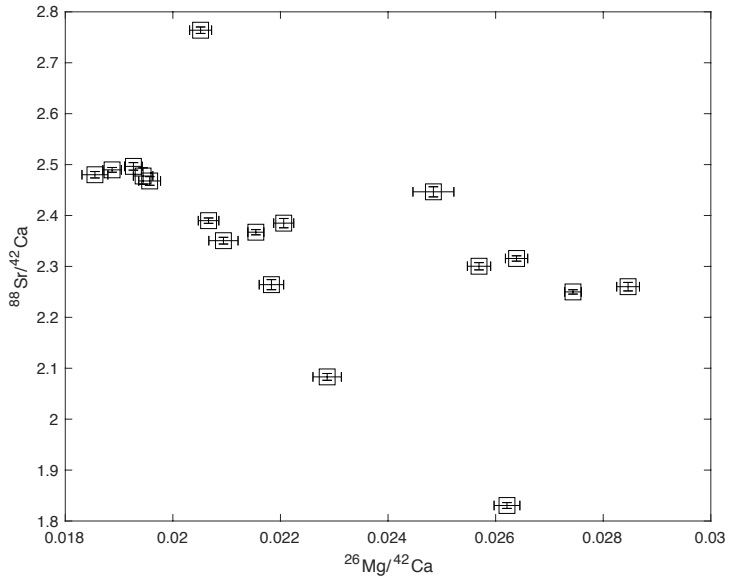

Figure 4-3 $^{26}Mg/^{42}Ca$ and $^{88}Sr/^{42}Ca$ on multiple spots measured on OKA over 3 days (with 2σ error bars). There is significant heterogeneity across the spots, and two separate linear trends are observed, with a group of points clustered on the upper left corner. The trends and range of heterogeneity is very similar to what Gabitov et al. (2013) observed.

Since no carbonate standard is currently available for Li/Ca and B/Ca measurements at Caltech, a series of USGS glass standards were used for this purpose. The minor and trace element content of these standards have been previously reported in the literature as measured by multiple micro-analytical techniques (Jochum et al., 2006). The Li and B content of these standards span a

several-fold range and can be used to construct calibration lines. The calibration lines can be constructed in two ways: with Li/Ca and B/Ca ratios, or with mass fractions of Li and B and their respective intensities. Both ways are influenced by the matrix effects when compared to the carbonates, so the calibrated Li/Ca and B/Ca (as well as Sr/Ca and Mg/Ca above) are further compared to ICP-MS measurements of bulk coral powder to assess these effects. Figure 4-4 presents the calibration lines for Li and B for both methods. We see that other than Li intensity vs. [Li], all other calibration lines have R^2>0.99 and can be used for calibration purposes with relatively low uncertainties. Since the ratio-based calibration method has higher R^2 and lower residuals, it is the preferred method when comparing to ICP-MS data.

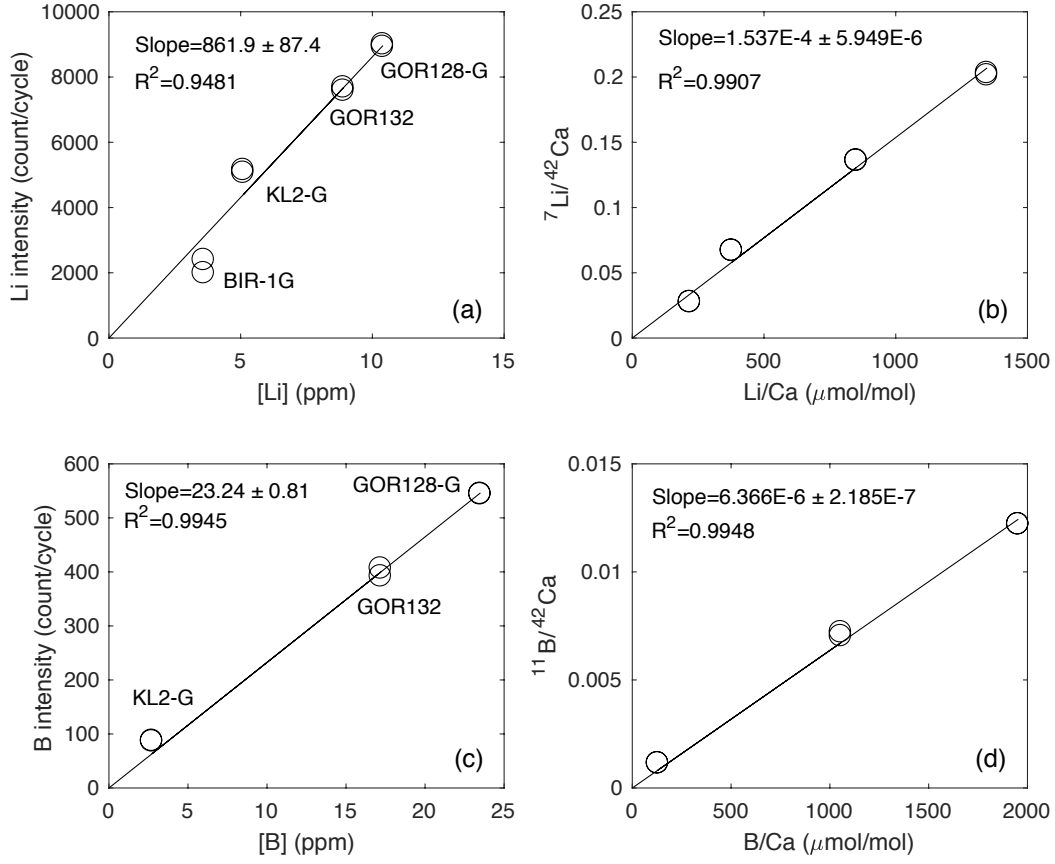

Figure 4-4 Calibration for (a, b) Li and (c, d) B contents from USGS glass standards. Two spots were measured on each standard with the same method as the samples (two spots have overlapping values if only one spot is visible). The names of the standards are shown beside the data points. The slopes are calculated by the least squares method and forcing the lines through the origins. Panels (a) and (c) show calibration based on intensity and mass fractions of [Li] and [B]. Panels (b) and (d) show calibration based on Li/Ca and B/Ca ratios. Using Li/Ca and B/Ca ratios generates more robust calibration lines with higher R^2 values, especially for Li.

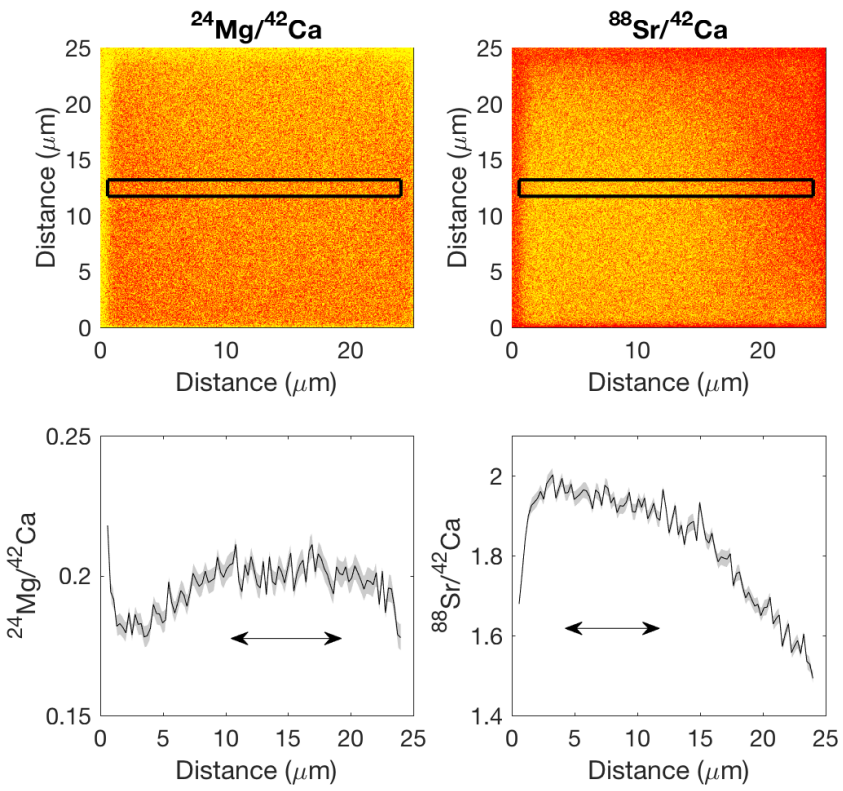

Figure 4-5 NanoSIMS images of Mg/Ca and Sr/Ca on a 25 μm spot on OKA (512×512 pixels, average of 4 images) with profiles extracted from a 30-pixel (1.5 μm) wide horizontal transect along the center of the image (black rectangle). The gray shading on the Mg/Ca and Sr/Ca profiles represent 2σ standard deviations across pixels in the y-direction. Both Mg/Ca and Sr/Ca suffer from an edge effect, and only points in the middle of the profile that are relatively constant (double-head arrows) are used for calibrations.

Calibrating Me/Ca ratios for nanoSIMS data presents further challenges. As shown in Figure 4-5, both Mg/Ca and Sr/Ca across a 25 μm spot show substantial variability, and are mainly influenced by the edges which have different surface charging conditions. As a result, only a relatively homogeneous part in the middle of the profile is used for Mg/Ca and Sr/Ca calibrations. This yields a Mg/Ca uncertainty of 2.5% and Sr/Ca uncertainty of 2.8% in the relatively homogeneous part of OKA that did not suffer from analytical artifacts. Variations in the samples are considered significant only when they exceed these uncertainties in the standard.

4.3 SIMS Results

4.3.1 Me/Ca Transect Profiles across Septa

Figure 4-6 shows Me/Ca measurements across four parallel transects on a single septum of coral 80358 (Northeast Atlantic). Each transect has a COC spot in the middle that aligns them in the direction across growth bands (defined as the x-direction here and below). On either side of the COC, aligned spots fall approximately on the same growth band. We see that the COCs have the highest Li/Ca and Mg/Ca, and the Li/Ca and Mg/Ca profiles are very reproducible at different positions along growth bands (defined as the y-direction). Sr/Ca in the COCs are low for these profiles, but are not the lowest across the bands. The pattern of lower Sr/Ca in and around the COC and higher Sr/Ca toward the edges is similar for the four transects, although the absolute Sr/Ca values are different. B/Ca is depleted in the COC for 3 of the transects, and the two spots next to the COCs generally have the highest B/Ca in the profiles. Although COCs have low B/Ca, similarly low B/Ca is also observed in the secondary growth bands on the edges. Figure 4-7 shows another example of parallel Me/Ca transects in coral 83583 (Northeast Pacific).

Similar patterns are observed for different Me/Ca ratios, and the notable difference is that the COCs for this specimen have much higher Sr/Ca than the adjacent bands, although they are still lower than other secondary aragonite bands. Figure 4-8 shows one more example of parallel Me/Ca transects in coral Big Beauty (Drake Passage). The two transects also share the same pattern, although there is significant difference for the two Sr/Ca profiles. On this septum, the COC band is highest in Mg/Ca, but not in Li/Ca, although Li/Ca in the COCs are still on the high end among the bands. The COCs on this septum also have the lowest B/Ca and highest Sr/Ca among the spots measured. To summarize, these transects show that the COCs are almost always higher in Mg/Ca and Li/Ca (by up to a factor of 2) than the secondary aragonite, and are usually among the lowest in B/Ca. The Sr/Ca of the COCs are more complicated, and can be either higher or lower than the surrounding bands. While Li/Ca, Mg/Ca and B/Ca vary by approximately a factor of 2, Sr/Ca varies by less than 10% across bands. In addition, there is usually a sharp contrast in Li/Ca, Mg/Ca and B/Ca between the COCs and their adjacent bands, but the contrast is less pronounced for Sr/Ca. These observations are generally consistent with previous work in *D.dianthus* (Gagnon

et al., 2007; Case et al., 2010) as well as the micromill data presented in Chapter 3. The next section looks at cross-correlations between the Me/Ca ratios.

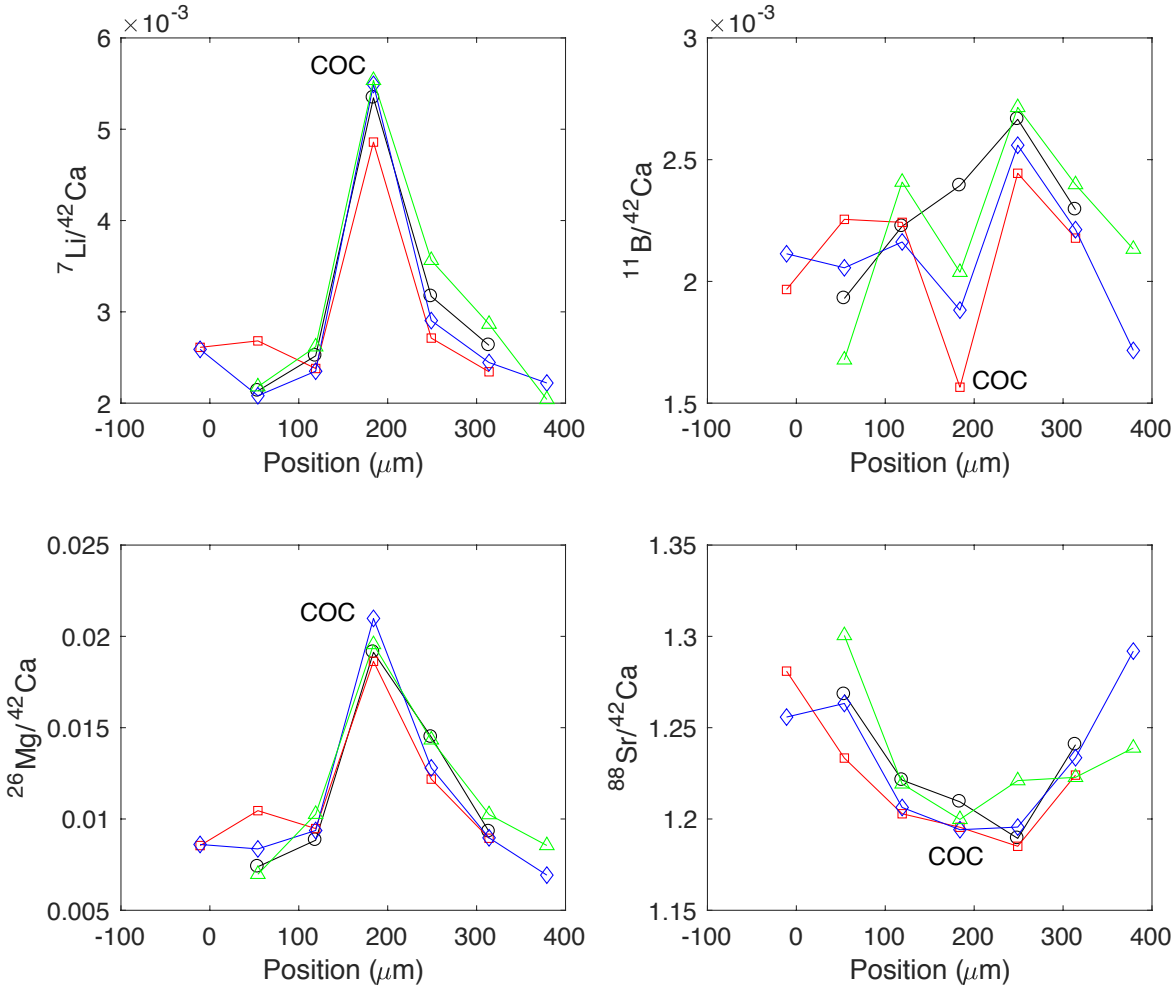

Figure 4-6 Me/Ca profiles across a septum on coral 80358. These four profiles are parallel to each other and are aligned with a COC band in the middle. The spots are ~30 µm in size and separated by 65 µm in the direction across growth bands (x-direction) of the septum. The profiles are separated in the direction along growth bands (y-direction) of the septum by 70-140 µm, and span a total range of 350 µm. A corresponding transmitted light image is shown in Figure 4-9 with the Me/Ca cross plots. Error bars are generally the size of the symbols or smaller and are not shown.

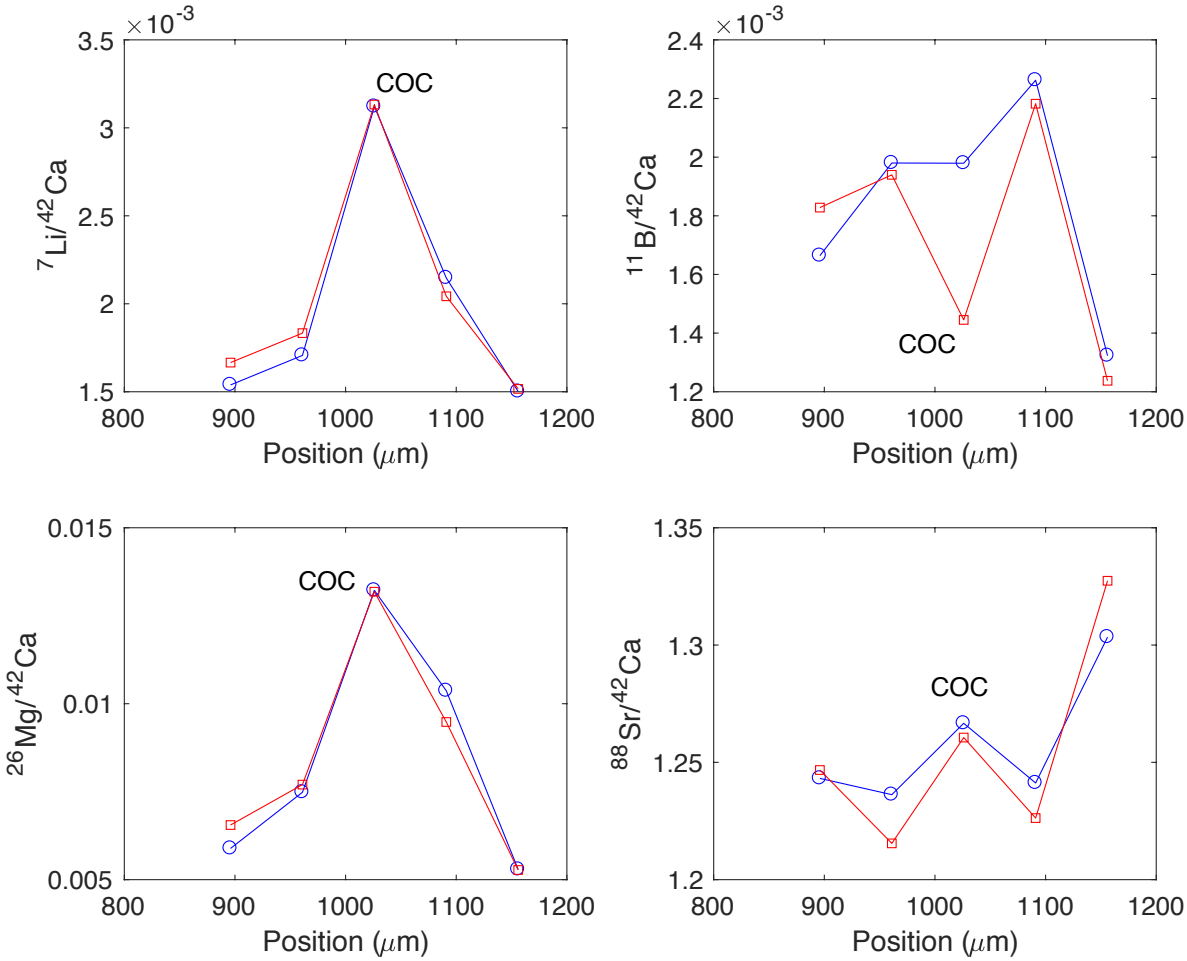

Figure 4-7 Me/Ca profiles across a septum on coral 83583. The two profiles are parallel to each other in the x-direction and separated by 109 μm in the y-direction.

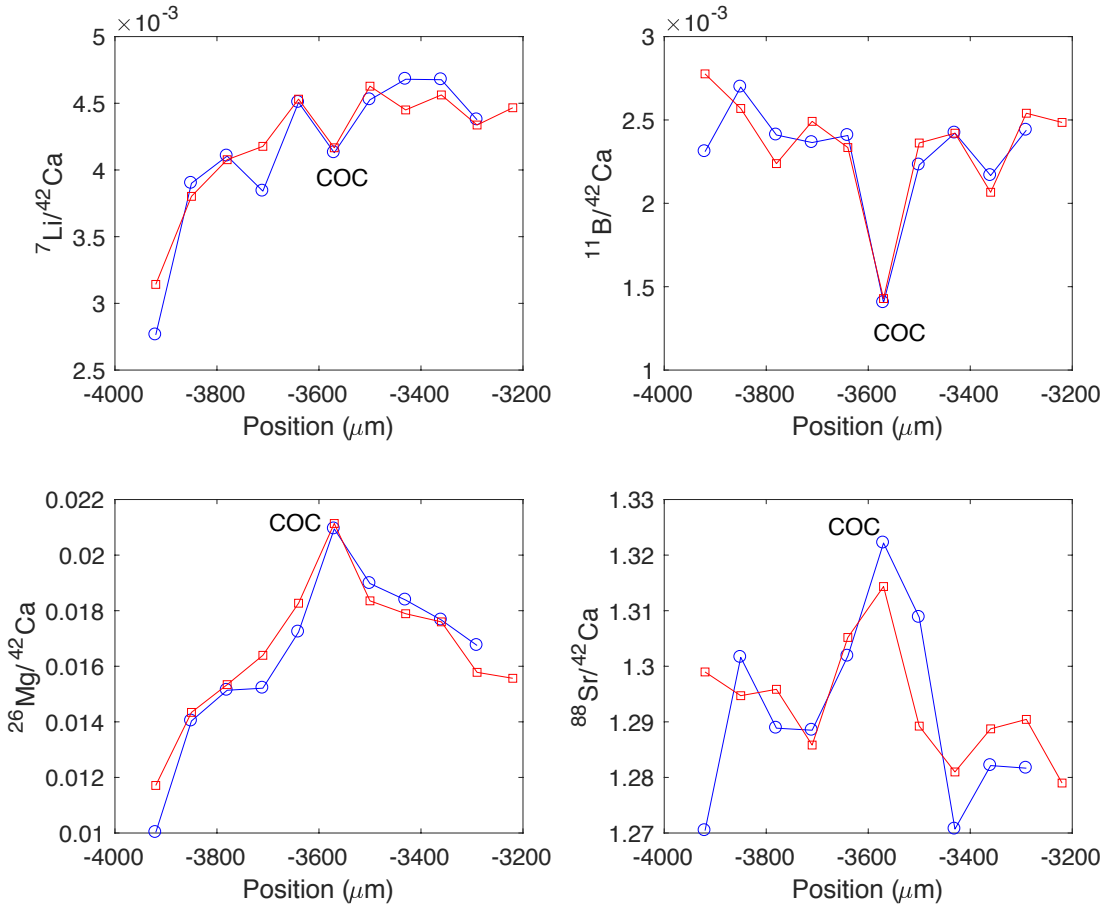

Figure 4-8 Me/Ca profiles across a septum on coral Big Beauty. The two profiles are parallel to each other in the x-direction and separated by 98 μm in the y-direction.

4.3.2 Me/Ca Cross Correlations

Figure 4-9 shows correlations between Mg/Ca and other Me/Ca ratios in coral 80358 (the same data as in Figure 4-6). As expected from the profile plots (Figure 4-6), we see that Mg/Ca and Li/Ca are positively and linearly correlated in the secondary aragonite, with COCs having very distinct values but seemingly falling on the same trend as the secondary aragonite. Mg/Ca and B/Ca are also positively correlated in the secondary aragonite with some curvature, and the COCs fall on a different trend with higher Mg/Ca but lower B/Ca. Although the B/Ca of the COCs have a relatively large range, it may reflect a mixture of pure COC material with the adjacent bands that have high B/Ca ratios. The positive Mg/Ca-B/Ca correlation in the secondary aragonite is much cleaner in the SIMS data than the micromilled data in Chapter 3. Mg/Ca and Sr/Ca are negatively

correlated with some curvature in the secondary aragonite, as previously reported for *D.dianthus* (Gagnon et al., 2007), and the COCs again fall off the trend defined by the secondary aragonite with high Mg/Ca and low Sr/Ca.

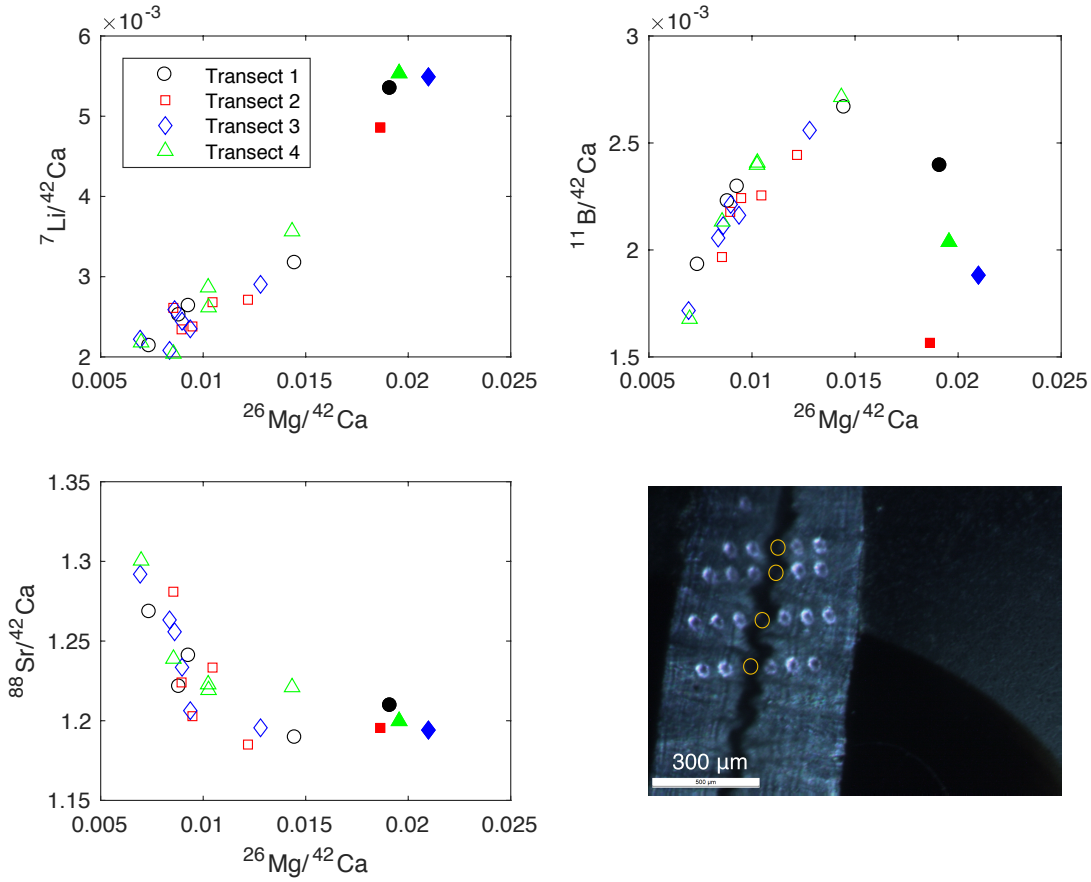

Figure 4-9 Me/Ca correlations in coral 80358 with a transmitted light image showing the SIMS spots. Each transect is plotted with a different symbol, with COCs in filled symbols. Horizontal transects in the image are labeled 1–4 from top to bottom in the cross plots. The dark band in the center is the COC, and the spots on the COC band are labeled with yellow circles to increase their visibility.

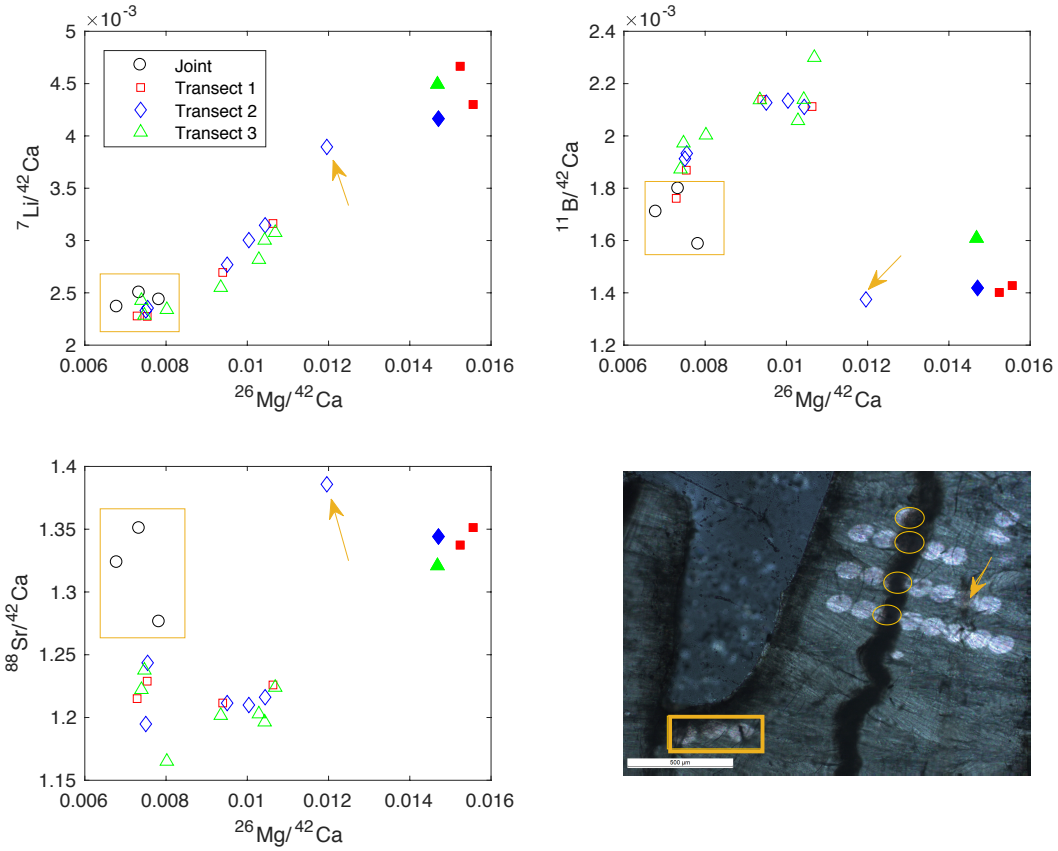

Figure 4-10 Me/Ca correlations in coral 47396 with a transmitted light image showing the SIMS spots (bottom left scale bar 300 µm). Each transect is plotted with a different symbol, with COCs in filled symbols. Horizontal transects on the septum in the image are labeled 1–3 from top to bottom in the cross plots. Transect 1 on the top includes a COC spot above it. Three spots were measured in the joint region between two septa, and are marked with a rectangle in the image as well as the cross plots (black circles). The arrow points to a spot in the secondary aragonite with abnormal compositions. In the image, some dark material runs through this spot.

Figure 4-10 shows another example of Me/Ca cross correlation in coral 47396 (Drake Passage). We see similar correlation patterns to those of 80358, including positive correlation between Mg/Ca and Li/Ca as well as Mg/Ca and B/Ca in the secondary aragonite, and negative correlation between Mg/Ca and Sr/Ca in the secondary aragonite. The COCs in 47396 have higher Mg/Ca, Li/Ca and lower B/Ca like 80358, but have higher Sr/Ca instead. The COCs seem to be on the Li/Ca-Mg/Ca correlation trend defined by the secondary aragonite, but fall off the trend in Mg/Ca-B/Ca and Mg/Ca-Sr/Ca plots. In this coral, there is a group of points in the secondary aragonite that have intermediate Mg/Ca between the low Mg/Ca points and the COCs. These

points have a relatively constant and low Sr/Ca and high B/Ca. They seem to be on a mixing trend between the low Mg/Ca points and COCs in Mg/Ca-Li/Ca and Mg/Ca-Sr/Ca space, but not in Mg/Ca and B/Ca space. These points are from certain bands on the septum on both sides of the COC band, but there is nothing obviously different about them in the transmitted light image compared to other low Mg/Ca bands. In addition, three points were measured in the joint area between two septa on this coral. These points tend to have the lowest Mg/Ca, B/Ca and Li/Ca and highest Sr/Ca among all points, possibly due to least influence from COCs. The same phenomenon is also observed in other corals.

To summarize, some relatively robust Me/Ca correlations are observed in the secondary aragonite in different *D.dianthus* individuals, including a linear positive Mg/Ca-Li/Ca correlation, a positive Mg/Ca-B/Ca correlation that concaves down at high Mg/Ca ratios, and a negative Mg/Ca-Sr/Ca correlation that concaves up at high Mg/Ca ratios. The COCs have high Li/Ca, Mg/Ca and low B/Ca compared to the secondary aragonite, but the Sr/Ca of COCs are less well-defined. The variable Sr/Ca in the COCs could cause complicated Mg/Ca-Sr/Ca correlation in some corals, if there is very fine COC-like structure within the secondary aragonite bands that cannot be identified with light microscopy. However, we see that the Me/Ca correlations observed in the micromill data in Chapter 3 are much better defined with the SIMS measurements, and these correlations can be used to inform which biomineralization processes drive these patterns.

4.4 NanoSIMS Results

Given the resolution of the nanoSIMS images (100 nm–1 μm, which is about 150–1500 aragonite unit cells), we expect the measurements to characterize the calcification process and the incorporation of minor and trace elements at much finer spatial and temporal scales. However, it is also expected that the Me/Ca correlations will be more noisy, assuming that the measurement uncertainties are governed by counting statistics. For trace elements such as Li and B, the signal intensity is very low (a few total counts per pixel over several hours) and revealing clear patterns would require a long time of collection. This section shows nanoSIMS images of the best quality (with stable primary beam and long collection time) to discuss the Me/Ca patterns.

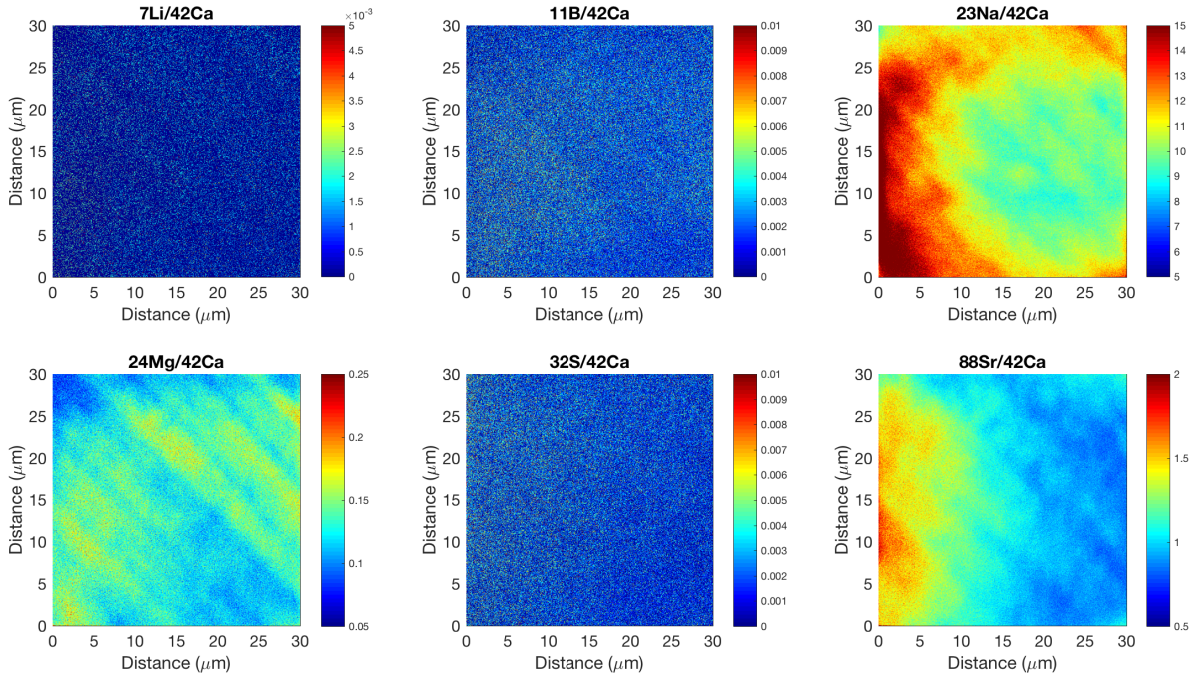

Figure 4-11 Me/Ca images of a 30 μm spot on the secondary aragonite of 47407 (512×512 pixels, average of 5 images collected over 3 hours). The growth bands run in the diagonal direction due to an angled placement of this septum in the holder of the instrument.

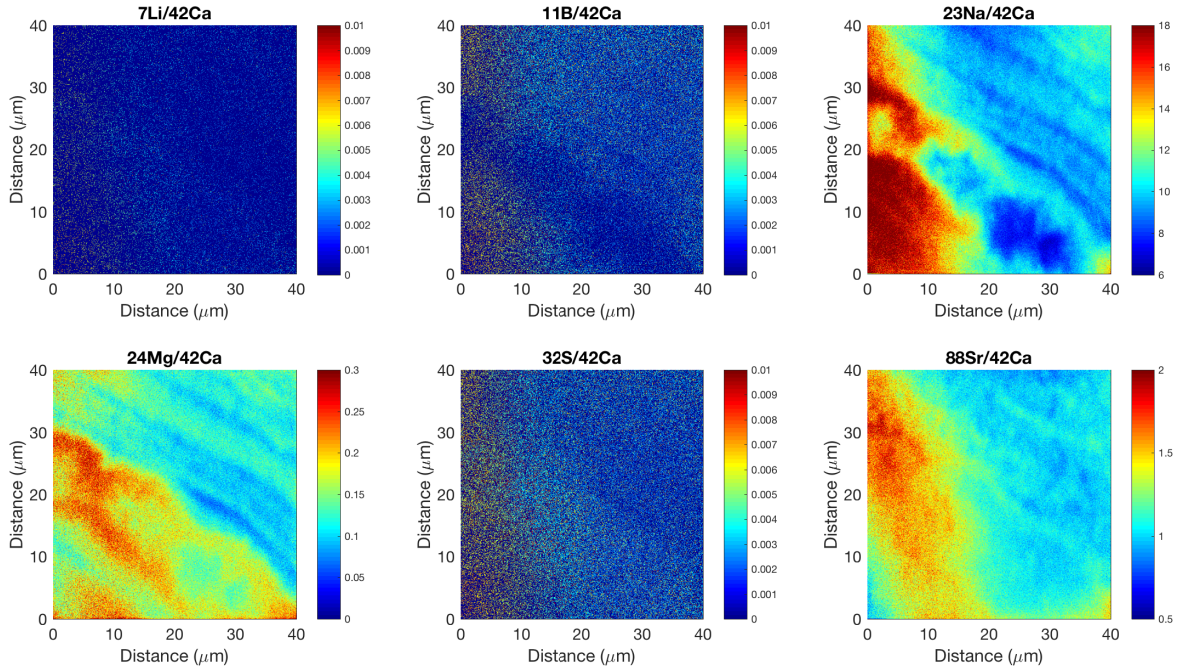

Figure 4-12 Me/Ca images of a 40 μm spot across a COC (lower left) in 47407 (512×512 pixels, average of 5 images collected over 3 hours). The COC band shows higher Mg/Ca and lower B/Ca, and less clearly, higher Li/Ca and S/Ca.

Figure 4-11 shows Me/Ca images of a 30 μm spot in the secondary aragonite of coral 47407 (Southern Ocean). The most striking pattern is the rhythmic Mg/Ca bands that are 2-3 microns thick. Similar banding patterns also seem to exist for other Me/Ca ratios, but they are compromised by low signal intensity (for Li/Ca, B/Ca and S/Ca) or edge contamination (Na/Ca and Sr/Ca). Figure 4-12 shows Me/Ca images of another 40 μm spot on 47407 that goes across a COC. The COC band stands out with high Mg/Ca and low B/Ca compared to the secondary aragonite, as well as higher Li/Ca and S/Ca. The Na/Ca and Sr/Ca of the COC band is influenced by the edge effect, but the unaffected part suggests that it has similarly low Na/Ca and Sr/Ca compared to the secondary aragonite. It is also noted that the quasi-rhythmic Mg/Ca bands in the secondary aragonite do not continue through the COC. The COC seems to be composed of stacked nodules with high Mg/Ca on the edge and low Mg/Ca in the interior. This difference in texture between COCs and the secondary aragonite is consistent with light microscopy and SEM observations of *D.dianthus* skeletons (Robinson et al., 2006; Gagnon et al., 2007).

Given the analytical noise in the images, some smoothing and averaging is needed to better characterize the Me/Ca correlation patterns. For example, Figure 4-13 shows Me/Ca profiles from a diagonal transect across images in 4-12 together with the cross plots. We see that Mg/Ca and B/Ca are positively correlated in the secondary aragonite, although with more scatter compared to the SIMS data. The COC is characterized by high Mg/Ca and low B/Ca that falls on a different trend from the secondary aragonite, which has been observed in different corals in the SIMS data. Both Mg/Ca and B/Ca vary by 50% in the secondary aragonite bands, with Mg/Ca elevated by a factor of 2 in the COC, also consistent with the SIMS observations. We also see that Mg/Ca and Li/Ca are positively correlated across the bands (including COCs), although the correlation is more scattered due to significant noise in the Li/Ca data. Sr/Ca is strongly influenced by the edge effect on the left side in the image in Figure 4-12, so the COC appears to be elevated in Sr/Ca by an anomalously high 40% compared to the secondary bands. However, when we only look at the right half of the profile which is not influenced by the edge effect, the Mg/Ca and Sr/Ca bands in Figure 4-13e in the secondary aragonite are anti-correlated, which also shows up in cross plot in Figure 4-13f as the group of points in the lower left corner.

To summarize, we have so far observed positive Mg/Ca-Li/Ca and Mg/Ca-B/Ca correlation as well as negative Mg/Ca-Sr/Ca correlations in the secondary aragonite of *D.dianthus* that are

coherent across scales of nanoSIMS, SIMS and micromilled bands. The extreme compositions of the COCs have also been reproducibly observed across these scales. These observations together suggest that the incorporation of these elements is strongly coupled in the biomineralization process. The correlation patterns as well as the range of variability in Me/Ca ratios in individual corals can help us diagnose the relevant processes for the observed vital effects.

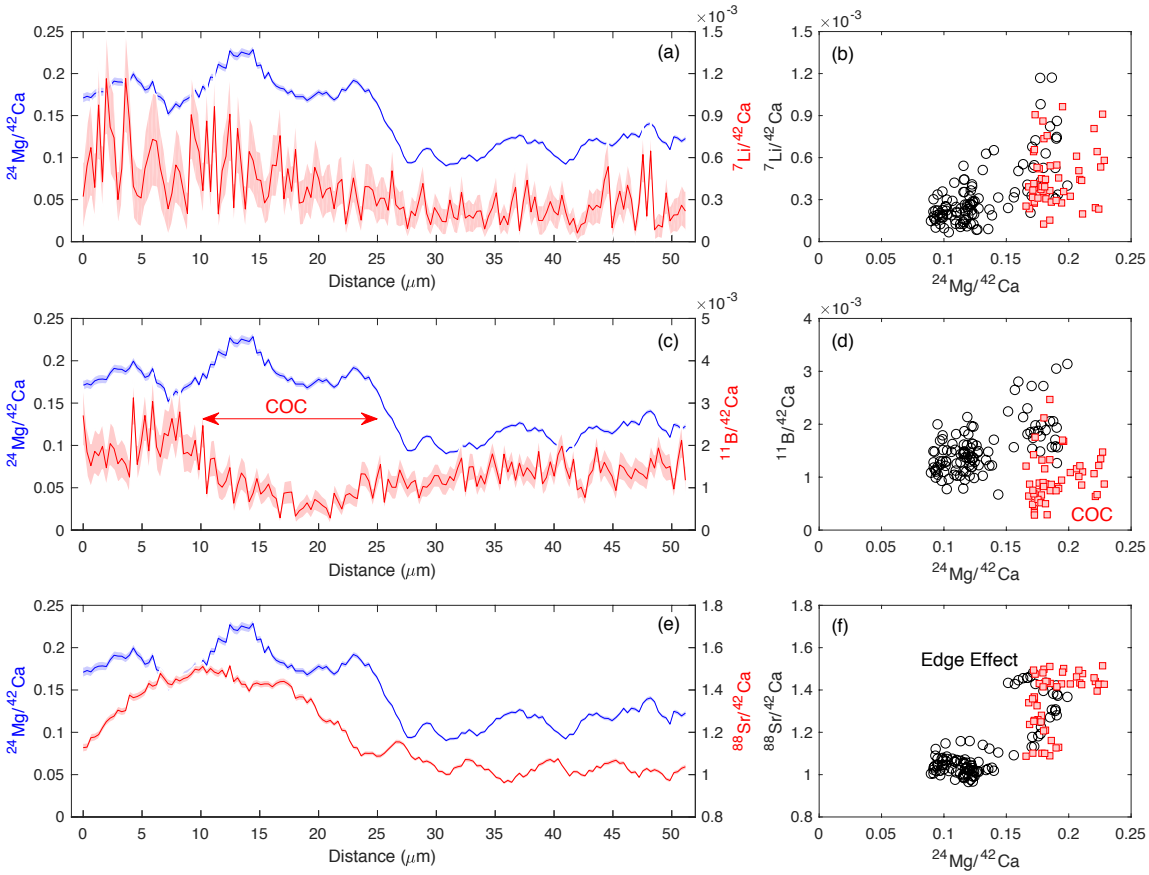

Figure 4-13 Me/Ca profiles extracted from the spot across COC in Figure 4-12 with Me/Ca cross plots. The COC in Figure 4-12 is marked in panel (c) and plotted with a different symbol in the cross plots. The profiles come from a 20-pixel wide diagonal transect and the shading in (a, c, e) show 2σ standard deviations of pixels across the widths of the bands. The left half points of the Sr/Ca profile is influenced by edge contamination and have anomalously high Sr/Ca. The right half of the Sr/Ca profile is not affected by the edge and corresponds to the group of points that are negatively correlated on the lower left corner of panel (f).

4.5 Discussion

4.5.1 Accuracy calibration across measurement scales

Given that the measurements on different spatial scales (bulk, micromill, SIMS, nanoSIMS) are independently calibrated for accuracy, it is possible to compare the calibrated Me/Ca values to assess the consistency between methods. While SIMS and nanoSIMS measurements were calibrated against solid standards, micromilled and bulk samples were measured with solution-based ICP-MS and these two were each calibrated against a different accuracy standard solution. The method for the bulk sample measurements at Caltech will be detailed in Chapter 5. Calibration with solid standards is influenced by heterogeneity within the standard and the matrix effect. The bulk samples, on the other hand, may be subjected to sampling bias in the selected region that is not representative of the whole skeleton.

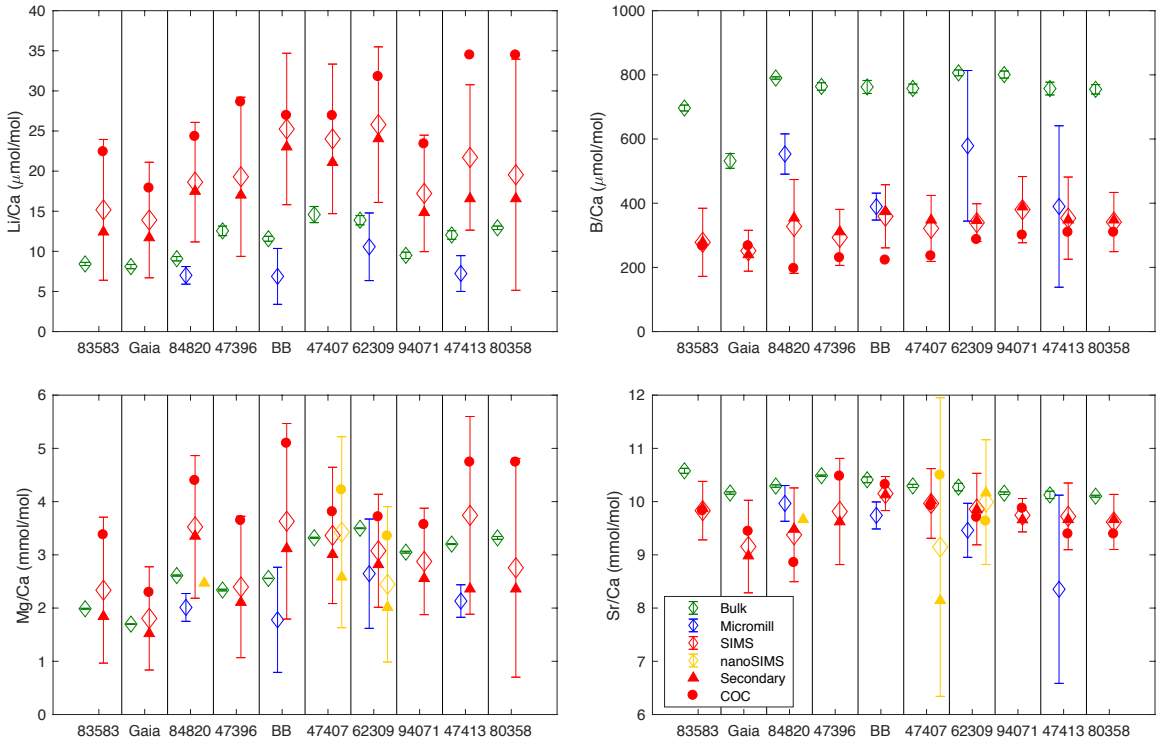

Figure 4-14 Comparison of Me/Ca measurements across scales. The x-axis is coral names, and they are listed in the order of increasing aragonite saturation state in the ambient seawater. The corals are separated by vertical lines. For each coral, the diamonds represent the mean value for a measurement scale, ordered from left to right as bulk (green), micromill (blue), SIMS (red) and nanoSIMS (gold). The error bars for the bulk samples (2 SE) are from 3 replicate measurements of the same solution, and for the other scales are 2σ standard deviations of all sample points. For SIMS and nanoSIMS samples, the filled circles represent average COC compositions, while the filled triangles represent the average secondary aragonite compositions. Calibration for nanoSIMS was done by comparing representative coral Me/Ca profiles to profiles on OKA of the same width.

Figure 4-14 shows a comparison of calibrated Me/Ca values on different measurement scales. We see that for Li/Ca and B/Ca, there is a systematic offset between the SIMS measurements and the solution based ICP-MS measurements. Li/Ca from the SIMS calibration are 50–100% higher than the bulk samples, while B/Ca from SIMS calibration are 50–60% lower than the bulk samples. These offsets are likely caused by the matrix effect when using glass standards for Li/Ca and B/Ca calibrations on carbonates. An intriguing observation is that the micromill data are closer to the bulk data for Li/Ca (although micromill data have lower average Li/Ca), but closer to the SIMS data for B/Ca. The offset between the micromill and bulk data is a combined result of sample size, blank contamination, instrument sensitivity between different labs and the different calibration standards used, and will be detailed in Chapter 5. The range of Mg/Ca measurements generally overlap with each other across different measurement scales, and the differences in mean Mg/Ca between different scales may mainly reflect sampling region bias, although matrix effect and calibration offset may still be present for SIMS and nanoSIMS data. The mean Sr/Ca in the bulk samples are higher than the mean values found at other scales by up to 10%, although they are generally within the range in Sr/Ca observed at finer scales, also suggesting a sampling bias. However, the Sr/Ca offset between the bulk samples and other scales is more systematic than Mg/Ca, so there may still be a calibration offset for Sr/Ca (e.g. the actual Sr/Ca ratio for OKA in the particular region used for this study may be different from the ratio measured by ICP-MS used for calibration in Gabitov et al., 2013 that came from a larger piece). These calibration offsets will have a large impact in comparing the deep-sea coral data to the inorganic reference frame and the numerical model. However, for relative changes in a single coral, the observed range in Me/Ca can still be used to explore the relevant biomineralization processes for these tracers.

4.5.2 Mg/Ca-B/Ca correlation and B partition rules

Across different measurement scales, Mg/Ca and B/Ca have been found to be positively correlated in the secondary aragonite of the *D.dianthus* skeleton. While Mg partitions into the skeleton with Ca in the calcification process, B partitions with the DIC pool or a subset of the DIC species. As a result, their correlation suggests a strong coupling between Ca and DIC in the biomineralization process that influences both elements. In addition, both Mg/Ca and B/Ca vary by approximately a factor of 2 in the secondary aragonite, and the positive correlation seems to

concave down at higher Mg/Ca values. All these structures in the data can be used as diagnostic features when compared to model outputs.

While Mg^{2+} simply substitutes for Ca^{2+} in the model presented in Chapter 3, B incorporation can follow a number of different rules as detailed in Section 3.2.1. The Mg/Ca-B/Ca correlation, as well as the range of their variability, can be used to distinguish between these rules. Figure 4-15 shows a data-model comparison in Mg/Ca-B/Ca space with different boron partition rules. Very different behavior is observed for these rules. Since these models all used f_{Ca}=0, Mg/Ca always increases with an increasing alkalinity pump rate. There are three rules that makes B/Ca always increase with Mg/Ca: borate ion partitioning with bicarbonate ion (Figure 4-15a), with DIC (Figure 4-15b) or following the square root of $[CO_3^{2-}]$ (Figure 4-15d). Among these cases, the $[B(OH)_4^-]/[HCO_3^-]$ rule predicts a steep increase in B/Ca as the alkalinity pump is turned up. This is because the fraction of $B(OH)_4^-$ in total boron (B_T) increases, while HCO_3^- fraction in DIC decreases rapidly as the pH of the ECF is raised. The increase in B/Ca with pump rate is more buffered with the $[B(OH)_4^-]$/DIC rule because DIC in the ECF is elevated over a range of pump rates with the help of carbonic anhydrase (Section 2.4.1). Although the prediction from this rule partly matches the data at τ_{sw}=400s, the increase in B/Ca with Mg/Ca is still too steep compared to the data. The $[B(OH)_4^-]/[CO_3^{2-}]^{0.5}$ rule, on the other hand, changes more gradually with pump rate because the increase in $[CO_3^{2-}]$ (Section 2.3.1, Figure 2-5c) partly cancels out the $[B(OH)_4^-]$ increase. When the seawater turnover timescale is 230s (optimal for the stable isotope fits in Chapter 2), the predicted Mg/Ca-B/Ca slope matches that of the data when D_B is set at 0.0013. This rule also seems to predict the concave-down curvature in the Mg/Ca-B/Ca data, although inflection points in the model and data do not match exactly. Although the physical basis for this partition rule is questionable, Holcomb et al. (2016) found that this rule could explain most of the variance in their inorganic aragonite precipitation experiments over a wide range of conditions, and they estimated D_B to have a range of 0.0013–0.0033 based on this rule. It should be noted that the D_B value in the model fit is dependent on the B/Ca calibration used for the SIMS data. As discussed in the previous section, there is discrepancy between calibrated SIMS B/Ca values from the glass standards and from bulk sample measurements, which could result in a different D_B. However, the D_B value that fits the Mg/Ca-B/Ca slope in the data (0.0031) would still fall in the range of values estimated by Holcomb et al. (2016) if the accuracy calibration is based on the bulk

measurements (assuming it represents the average of the SIMS spots). Finally, the $[B(OH)_4^-]/[CO_3^{2-}]$ rule predicts a decrease in B/Ca with increasing pump rate (because $[CO_3^{2-}]$ increases more rapidly than $[B(OH)_4^-]$ with pH), which is contrary to the trend in the data. I have also run model simulations with total boron (B_T) instead of borate as the numerator in the partition rule. Since D_B is much less than 1, B_T in the ECF does not change much from seawater value, and the predicted B/Ca changes are just opposite to the variable in the denominator (Figure 2-5). As a result, all the rules with B_T in the numerator predict an initial decrease in B/Ca with increasing Mg/Ca at low pump rates, followed by a turnaround with B/Ca increasing at high pump rates, which is not observed in the data.

Given the comparisons above, the three rules that predict a positive Mg/Ca-B/Ca correlation are likely to be related to the mechanism of boron incorporation, although none of them perfectly matches all the features in the data. The $[B(OH)_4^-]/[CO_3^{2-}]^{0.5}$ rule seems to best explain the observed range in B/Ca and even fits the Mg/Ca-B/Ca slope, but it is based on a charge-balanced exchange reaction without validation by any observations. Both the $[B(OH)_4^-]/[HCO_3^-]$ and the $[B(OH)_4^-]$/DIC rule have a stronger physical basis, but they predict a larger range in B/Ca and a steeper Mg/Ca-B/Ca slope than the data at a variety of seawater turnover timescales. However, it should be pointed out that some of the misfit in the model to the data is from Mg/Ca instead of B/Ca. With the current setup, most of the model scenarios cannot predict the full Mg/Ca range observed in the data. A similar observation was made for the Mg/Ca-$\delta^{18}O$ correlation in Chapter 3 (Section 3.3.4, Figure 3-12). Explanation of the full Mg/Ca range would require either a more closed ECF to seawater (higher τ_{sw}), or factors that have not been accounted for in Mg partitioning such as a growth rate dependence of D_{Mg}. Experimental constraints on the growth rate dependence of D_{Mg} in aragonite show that it increases with growth rate (Gabitov et al., 2008), and the growth rates of deep-sea corals fall in a range that is sensitive to the growth rates according to these experiments. However, the D_{Mg} values determined by Gabitov et al. (2008) are extremely low (10^{-5}) compared to other experiments as well as empirical values from corals, preventing a direct comparison to the deep-sea coral data in this study. A better inorganic reference frame in aragonite is needed for both B and Mg to improve the model. In addition, Mg has been suggested to be associated with the organic phase in biogenic carbonates (Bentov & Erez, 2006; Finch & Allison, 2008), which is not currently quantified in the model. However, if the organic phase is

important for the observed Mg variability, the observed correlations between Mg/Ca and other Me/Ca would suggest all other elements have different affinities to the organic phase relative to aragonite. In this case, the COCs which are rich in organic matter are expected to have extreme contents of Li, B and Sr that fall at one end of the trend in the secondary aragonite. This is in contrast to the observed Mg/Ca-B/Ca and Mg/Ca-Sr/Ca patterns, suggesting a more complicated influence of organic matter or a different calcification mechanism for the COCs.

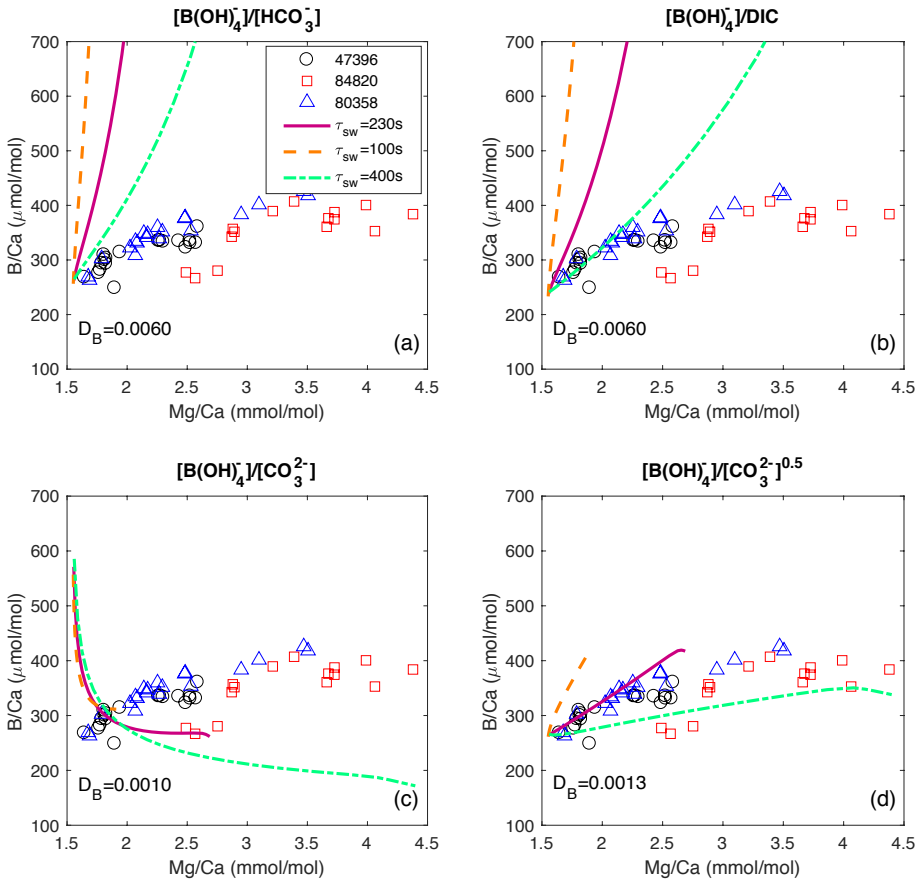

Figure 4-15 Mg/Ca-B/Ca data-model comparison with a different boron partition rule in each panel: (a) borate partition with bicarbonate ion; (b) borate partition with DIC; (c) borate partition with carbonate ion; (d) borate partition with square root of $[CO_3^{2-}]$. Mg/Ca-B/Ca SIMS data are presented for secondary aragonite points in coral 47396 (circles), 84820 (squares) and 80358 (triangles). Mg/Ca in the corals are calibrated against OKA while B/Ca are calibrated against the glass standards as in Figure 4-4d. In each panel, 3 model curves are presented with different seawater turnover rates (solid-230s, dashed-100s, dash-dot 400s). All models used a f_{Ca} of zero to generate the maximum range in Mg/Ca, and an increase in alkalinity pump rate always corresponds to an increase in Mg/Ca. D_{Mg} is calculated from Reynaud et al. (2007), while D_B's are arbitrarily picked to match the range of measured values in the data and listed in the bottom left corner.

4.5.3 Mg/Ca-Sr/Ca correlation and biomineralization response to environment

The negative correlation between Mg/Ca and Sr/Ca has been reproducibly observed in individual deep-sea corals (Cohen et al., 2006; Gagnon et al., 2007) as well as surface corals (Fallon et al., 1999; Sinclair, 2005), and different calcification models have been developed to describe the incorporation of Mg and Sr as a Rayleigh distillation process (Gagnon et al., 2007; Gaetani et al., 2011; Gagnon et al., 2012). As proposed by these models and discussed in Chapter 3, the correlation between Mg/Ca and Sr/Ca may be used to deconvolve the vital effects and extract temperature information.

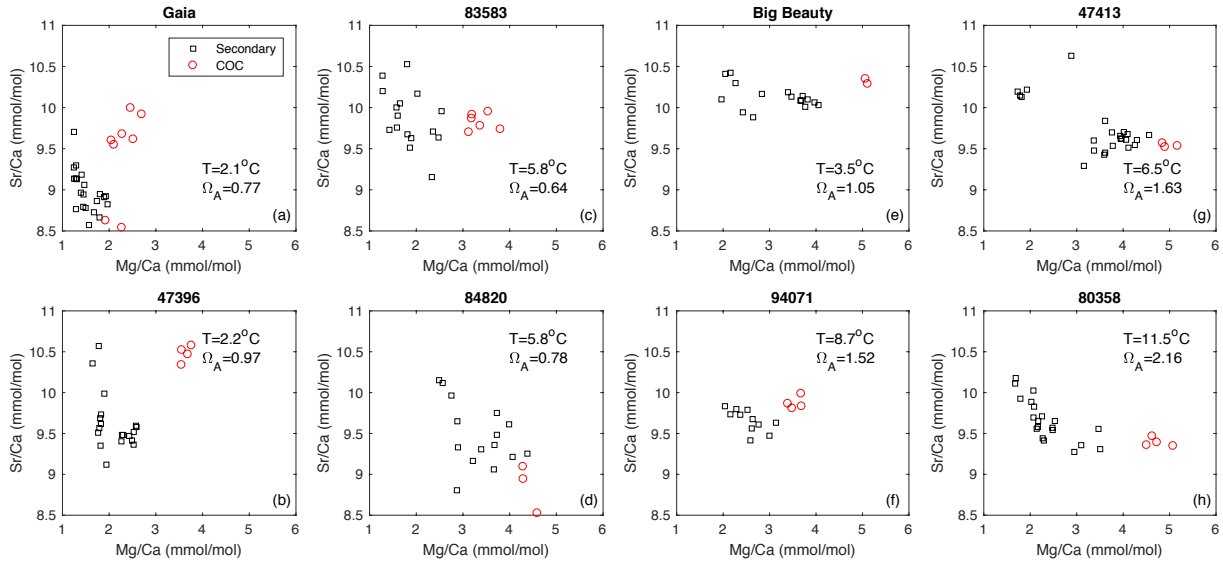

Figure 4-16 Mg/Ca-Sr/Ca cross plots (SIMS data) in individual *D.dianthus*. The Mg/Ca and Sr/Ca ratios are calibrated with OKA. The black squares are secondary aragonite and the red circles are COCs. The corals are classified by temperature and aragonite saturation state (labeled in each panel) in columns: (a, b) cold and undersaturated; (c, d) warm and undersaturated; (e, f, g, h) supersaturated. Although each individual coral shows negative correlation between Mg/Ca and Sr/Ca in the secondary aragonite, the range in Mg/Ca and Sr/Ca and the slope of the correlations are different. Corals living in undersaturated water tend to have a larger range in Sr/Ca and a narrower range in Mg/Ca, thus a steeper Mg/Ca-Sr/Ca slope.

Figure 4-16 shows the Mg/Ca-Sr/Ca cross plots from SIMS measurements on individual *D.dianthus*. Although a negative correlation between Mg/Ca and Sr/Ca is observed in each individual coral, we see that Mg/Ca and Sr/Ca span different ranges in different corals, and thus the Mg/Ca-Sr/Ca slopes are different. The corals living in undersaturated water tend to have a larger

range in Sr/Ca and smaller range in Mg/Ca, thus a steeper slope in the Mg/Ca-Sr/Ca correlation. The two corals living in ~2°C undersaturated water have a group of points that are on an almost vertical trend, and another group of points that point toward the high Sr/Ca COCs. The two corals living in ~6°C undersaturated water have a similar range in Sr/Ca, but a larger range in Mg/Ca, and shallower Mg/Ca-Sr/Ca slopes, compared to their cold counterparts. The corals living in supersaturated waters have similar or shallower slopes compared to the ones living in warm undersaturated waters.

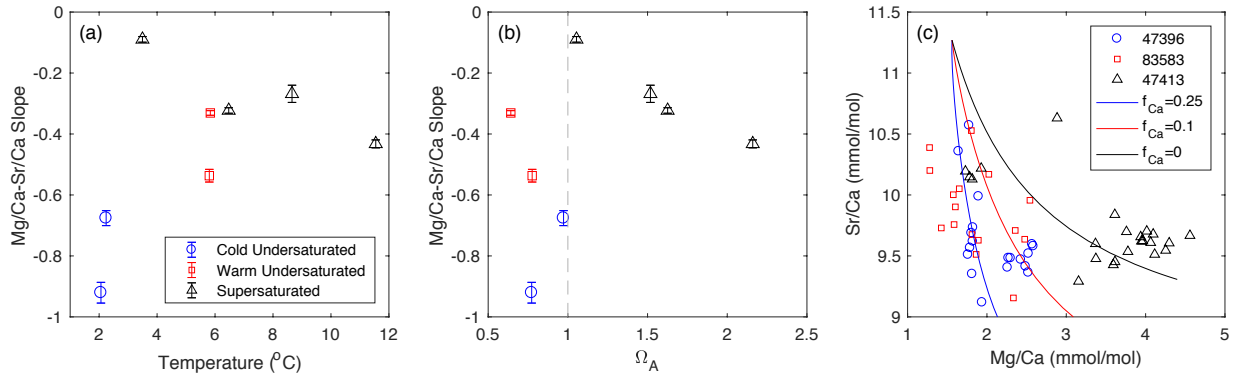

Figure 4-17 Environmental and biomineralization impacts on Mg/Ca-Sr/Ca slopes in *D.dianthus*. (a) Estimated Mg/Ca-Sr/Ca slopes vs. temperature. Slopes and associated uncertainties (2σ) are calculated following York et al. (2004) that has accounted for data errors. (b) Estimated Mg/Ca-Sr/Ca slopes vs. aragonite saturation state. (c) Example Mg/Ca-Sr/Ca data from the three groups of corals (only secondary aragonite) compared to model simulations of different f_{Ca} values at τ_{sw}=400s (to maximize the range in Mg/Ca). Steeper slopes in Mg/Ca-Sr/Ca space correspond to higher f_{Ca} values.

Figure 4-17 shows the relation between temperature, aragonite saturation state (Ω_A) and estimated Mg/Ca-Sr/Ca slopes. We see that the Mg/Ca-Sr/Ca slopes of corals from supersaturated seawater have a different trend with temperature and Ω_A than those from undersaturated seawater. When the seawater is undersaturated, temperature seems to have a stronger influence on the slope than Ω_A. When the seawater is oversaturated, the slope decreases with both temperature and Ω_A, although the relation with Ω_A is closer to a straight line. In the biomineralization model presented in Chapter 3, the key factor controlling the range in Mg/Ca and Sr/Ca (and thus the slope of their correlation) is the fraction of Ca^{2+} in the alkalinity pump (f_{Ca}), due to very different distribution coefficients for Mg and Sr in aragonite. Figure 4-17c shows some model outputs of different f_{Ca} as compared to the data in three corals from different environmental categories. According to the model, the steep Mg/Ca-Sr/Ca slopes in corals from cold undersaturated seawater can be explained

with an increase in f_{Ca}. Increasing the fraction of Ca^{2+} in the alkalinity pump could potentially compensate for the low saturation state in the ambient seawater. It is also possible that the corals living in undersaturated conditions may "intelligently" reduce the turnover rate of this undersaturated water to help with the pH up-regulation, which also cuts off the Ca^{2+} supply and requires more Ca^{2+} to be actively pumped into the ECF. This idea from the model can be further tested with culture experiments in the future.

Based on the analysis above, it is possible to extract information about temperature and/or saturation state from Mg/Ca-Sr/Ca slopes in supersaturated conditions, but undersaturation could complicate this relation. It is cautioned that the Mg/Ca-Sr/Ca data in Figure 4-16 still has significant scatter (sometimes with two different trends), and the model has not accounted for all the variability in the data, especially in Mg/Ca. It is likely that the secondary aragonite contains small fractions of COC-like materials that cannot be visually identified that complicate the correlations. It is also possible that a coral may change its biomineralization scheme for different parts of its skeleton, which gives rise to additional Me/Ca variability that can be accounted for by a simple model.

4.5.4 Mg/Ca-Li/Ca correlation and temperature

Given the low distribution coefficients for Mg and Li in aragonite, it is expected that these elements are incorporated into the coral skeleton in a very similar way, and a positive linear correlation is expected for Mg/Ca and Li/Ca. As discussed in Section 3.2.4, the slope of the Mg/Ca-Li/Ca correlation should contain temperature information given the difference in the temperature dependence of D_{Mg} and D_{Li}. In bulk measurements, the equivalence of the slope is the Li/Mg ratio in the aragonite (assuming zero intercept in the Mg/Ca-Li/Ca correlation). This idea has been successfully applied in different coral species as well as the aragonitic foraminifera *H.elegans* to generate empirical calibrations of Li/Mg vs. temperature (Bryan & Marchitto, 2008; Case et al., 2010; Montagna et al., 2014; Marchitto et al., 2018). It was found that the Li/Mg-temperature relation is more tightly constrained than Mg/Ca or Li/Ca, and that corals and *H.elegans* follow the same Li/Mg-temperature relation (Marchitto et al., 2018). This observation

suggests a universal rule in controlling Li and Mg incorporation in biogenic aragonite that is independent of the vital effects, or that the vital effects for these two elements nearly perfectly cancel out. What has not been satisfactorily explained is the absolute values of Mg/Ca and Li/Ca ratios observed in corals and *H.elegans*. The available D_{Mg} and D_{Li} for inorganic aragonite (Marriott et al., 2004; Gaetani & Cohen, 2006) predicts Mg/Ca and Li/Ca values that are several-fold higher than the observed range in corals, and an order of magnitude higher for *H.elegans*. Given that D_{Mg} and D_{Li} are much smaller than 1, concentrations of Li and Mg in the ECF do not change significantly from seawater in the calcification process, so the measured Mg/Ca and Li/Ca ratios would suggest a dilution of Mg and Li by $[Ca^{2+}]$ that is a few to more than ten times higher than seawater in a simple scenario, which is physically impossible for the organisms. So there has to be a way that the organisms modulate the concentration of Mg and Li in the ECF, or the inorganic D_{Mg} and D_{Li} for aragonite are severely overestimated. Nevertheless, the Li/Mg-temperature relation is empirically robust and theoretically supported by the biomineralization model, and is worth testing with the *D.dianthus* dataset.

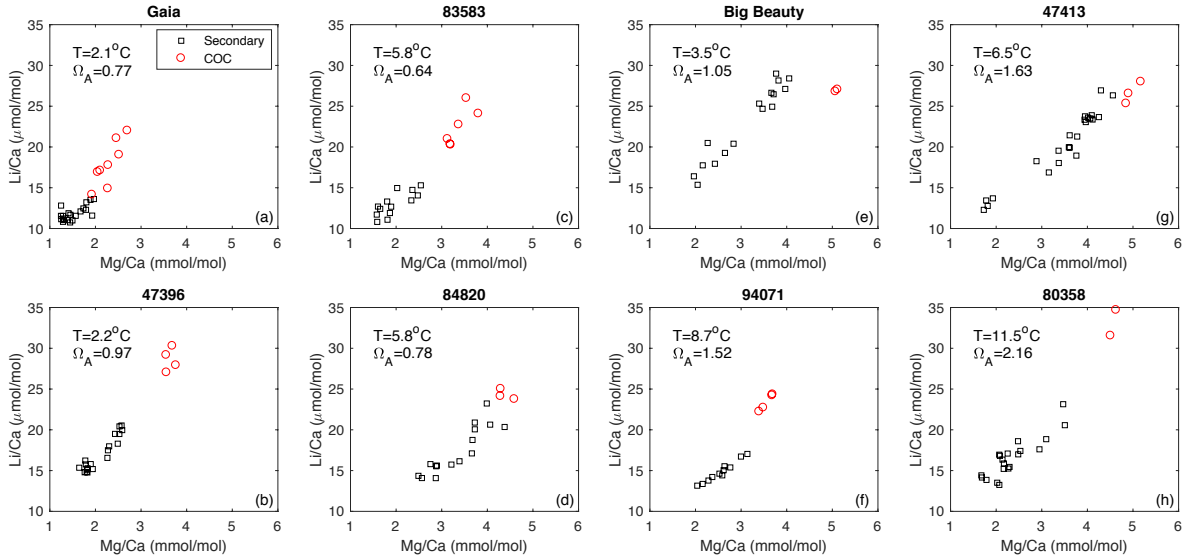

Figure 4-18 Mg/Ca-Li/Ca cross plots (SIMS data) in individual *D.dianthus*. The Mg/Ca ratios are calibrated with OKA, while the Li/Ca ratios are calibrated against the USGS glass standards as in Figure 4-4b. The black squares are secondary aragonite and the red circles are COCs. The corals are arranged in the same order as in Figure 4-16. All corals show a linear Mg/Ca-Li/Ca correlation in the secondary aragonite. The linear correlation seems to extend to COCs in the corals from undersaturated seawater (a–d), while the COCs are not on the same Li/Ca-Mg/Ca trend as the secondary aragonite in corals from supersaturated seawater.

Figure 4-18 shows the Mg/Ca-Li/Ca cross plots from SIMS measurements on individual *D.dianthus*. We see that a linear Mg/Ca-Li/Ca correlation trend is observed in the secondary aragonite of each coral, and the COCs have distinctly high Li/Ca and Mg/Ca. In general, the ranges in Li/Ca and Mg/Ca in the secondary aragonite are smaller in the corals from undersaturated seawater compared to those from supersaturated seawater. The COCs of corals from undersaturated seawater seem to fall on the same Mg/Ca-Li/Ca trend as the secondary aragonite, while the COCs of corals from supersaturated seawater fall off the linear trend in the secondary aragonite, sometimes with a Mg-excess (Big Beauty and 47413), and sometimes with a Li-excess (94071 and 80358). Comparing the Mg/Ca-Li/Ca slopes across corals, the cold-water corals generally have steeper slopes than the warm-water corals.

Figure 4-19 shows the estimated Mg/Ca-Li/Ca slopes with temperature and aragonite saturation state. When only points from secondary aragonite are used to estimate the slopes, there is no clear relation between the slopes and temperature or Ω_A. However, when all data points are used to extend the data range and estimate the slopes for the corals from undersaturated seawater (as suggested by the cross plots in Figure 4-18), we get steeper slopes that are better defined (smaller uncertainties) for these corals, and the new slopes fall on the trend defined by the secondary aragonite of corals from supersaturated seawater. We have previously discussed the calibration offset for Li/Ca in the SIMS data compared to ICP-MS measurements (Section 4.5.1, Figure 4-14), which is attributed to the matrix effect associated with the SIMS calibration with glass standards. As a result, the glass-calibrated Li/Ca ratios are 50–100% higher than the ICP-MS measurements, and the estimated Mg/Ca-Li/Ca slopes are higher than the calibration by Marchitto et al. (2018) from compiled coral data. When we instead use bulk Li/Ca and Mg/Ca measurements to calibrate the SIMS measurements (assuming the bulk values equal the average of all points), and recalculate the slopes, we get a slope-temperature relation that is similar to Marchitto et al. (2018) in terms of temperature sensitivity, but lower in absolute values. The offset in absolute values could be caused by a number of reasons. First, the bulk samples may have a different COC-secondary aragonite mixture compared to the SIMS spots, which could significantly influence the absolute Mg/Ca and Li/Ca ratios. The potential sampling bias in the bulk samples is detailed in Chapter 5. Second, the slope of Mg/Ca-Li/Ca correlation is not equivalent to a bulk Li/Mg ratio as compiled by Marchitto et al. (2018), unless the Mg/Ca-Li/Ca correlation has an intercept of zero.

In the numerical model, a small positive intercept (0.2–0.6 μmol/mol in Li/Ca) is predicted for the correlation due to differences in the values of D_{Mg} and D_{Li}. In the SIMS data, a positive intercept in Li/Ca of 1–3 μmol/mol is observed for different corals. A positive intercept in Li/Ca (1.2 μmol/mol) has also been observed in *D.dianthus* in laser ablation data by Case et al. (2010). The reason for this excess Li is unclear from the current biomineralization model. It has been suggested that Li could leak into the calcifying fluid through the Na^+-H^+ exchangers on the membranes in foraminifera to cause a Li isotope effect (Vigier et al., 2015), but it has not been observed in corals, though this process could be tested with culture experiments. The existence of the Li/Ca excess may contribute to the bulk Li/Mg measurements and give rise to higher Li/Mg ratios.

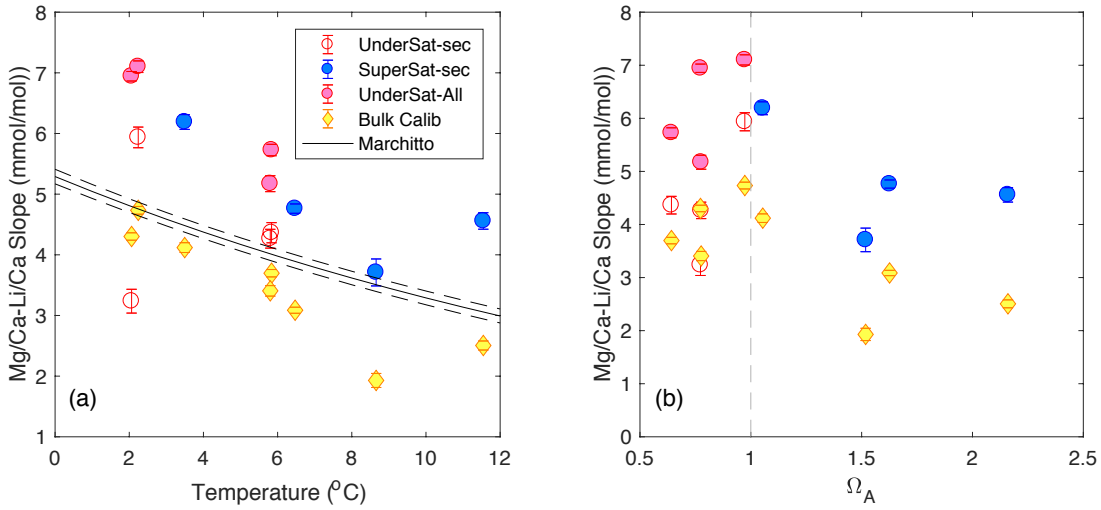

Figure 4-19 Estimated Mg/Ca-Li/Ca slopes vs. (a) temperature and (b) aragonite saturation state. Slopes and associated uncertainties (2σ) are calculated following York et al. (2004) that has accounted for data errors. In each panel, the red circles represent corals from undersaturated seawater, and blue circles represent corals from supersaturated seawater. For corals from undersaturated seawater, the open red circles represent slopes calculated from only the secondary aragonite, while the filled red circles represent slopes calculated from all data points including COCs. For supersaturated seawater, the filled blue circles are calculated from the secondary aragonite only. All the filled symbols define a relatively good relation with temperature, while the open symbols for corals from undersaturated seawater have shallower slopes. The black line represents the Li/Mg-temperature calibration equation for corals by Marchitto et al. (2018) (dashed lines are 2σ ranges). Li/Ca ratios calibrated by the glass standards in the SIMS data are systematically higher than ICP-MS measurements of corals, reflecting the matrix effect. Therefore the estimated slopes from the SIMS data are higher than the Marchitto (2018) calibration. When we use bulk Li/Ca and Mg/Ca measurements for each coral to calibrate the SIMS data (assuming bulk value equals average of all spots), the slopes (only secondary aragonite for supersaturated corals and all points for undersaturated corals) are shown in yellow diamonds, which are lower than the Marchitto calibration but with a similar temperature dependence. Panel (b) shows that there is not a clear dependence of Mg/Ca-Li/Ca slopes on aragonite saturation state.

Finally, it is unclear why the COCs of corals from undersaturated seawater seem to fall on the Mg/Ca-Li/Ca calibration trend defined by the secondary aragonite, while the COCs of corals from supersaturated seawater do not. Given that the corals from undersaturated water generally have a smaller range in Li/Ca and Mg/Ca, this may reflect an overall lower alkalinity pump rate, which causes a pH that is lower than pK_{a2} when the COCs are made. This is consistent with the stable isotope results presented in Chapter 3 (Section 3.3.2). It is likely that the formation of COCs in corals is also influenced by environmental conditions such as temperature and aragonite saturation state, which requires further investigation by other techniques (e.g. X-ray spectroscopy, other high-resolution microscopy, NMR). However, the SIMS data provide evidence that the Li/Ca-Mg/Ca correlation in deep-sea corals contains temperature information, and is less influenced by the aragonite saturation state (Figure 4-19). The Li/Mg thermometer will be further tested in Chapter 5 with bulk *D.dianthus* samples from a wide range of oceanic settings.

4.6 Conclusions

This chapter has presented SIMS and nanoSIMS data of Me/Ca variability in a suite of *D.dianthus* specimens from a wide range of temperatures and aragonite saturation states. Robust Me/Ca correlation patterns have been observed in different corals over a range of measurement scales, suggesting close coupling of the incorporation of these elements through a common biomineralization process. The patterns include positive and linear Mg/Ca-Li/Ca correlation, positive and concave-down Mg/Ca-B/Ca correlation, and negative and concave-up Mg/Ca-Sr/Ca correlation in the secondary aragonite of the corals. The COCs are enriched in Li and Mg, depleted in B, and have variable Sr contents, and do not share the Me/Ca correlation trends in the secondary aragonite. These correlation patterns have been used to address questions such as rules for boron partitioning into biogenic aragonite, response of coral biomineralization strategy to the environment, as well as potentially extracting environmental information from the slopes of the Me/Ca correlations. While Mg/Ca-Sr/Ca slopes may contain information about temperature or aragonite saturation state, Mg/Ca-Li/Ca slopes seems to be dominated by the temperature effect. Developing these relations into better tracer calibrations remains a challenge due to inconsistencies in accuracy calibration across different measurement scales as well as some observations that

cannot be fully explained by the current biomineralization model. However, the important biomineralization processes and parameters identified in the fine scale Me/Ca correlations may provide clues to the observed scatter in empirical calibration data as well as ways to normalize for the vital effects. In the next Chapter, I will present empirical tracer calibrations with the modern *D.dianthus* collection at Caltech, and discuss possible vital effects on different tracers learned from the biomineralization model and fine scale observations.

4.7 Appendix A: nanoSIMS Imaging of Organic Bands in *D.dianthus*

In addition to using the O^- source to probe elements that form cations, the Cs^+ source of nanoSIMS has also been used to map elements that prefer to form anions in biogenic carbonates and other geological materials, which are typically elements associated with organic matter (Meibom et al., 2007; Oehler et al., 2010; Wacey et al., 2010; Bontognali et al., 2012; Paris et al., 2014). These elements include carbon, nitrogen (measured as CN^- due to higher ion yield), sulfur, silicon and phosphorous. Mapping the distribution of organic matter in coral skeletons may provide useful information about how the living polyp organisms interacted with the skeletons during the biomineralization process. Comparison between the distribution of organic matter and minor and trace metals may also shed light on the mechanism of tracer incorporation into the coral skeletons, thus "visualizing" the vital effects. Deep-sea coral skeletons contain up to a few percent organic matter that consists of a variety of compounds including amino acids, sulfated polysaccharides and phospholipids (Cuif & Dauphin, 2005; Farre et al., 2010). The organic matter in coral skeletons have been suggested to act as templates to facilitate calcification (Cuif & Dauphin, 2005; De Yoreo et al., 2007; Cusack & Freer, 2008). A few proxies have been developed on the organic associated elements in deep-sea corals, including P/Ca, carbon isotopes and nitrogen isotopes (of organic matter) to trace the nutrient dynamics in the ocean (Anagnostou et al., 2011; Guilderson et al., 2013; Sherwood et al., 2014; Wang et al., 2014).

Here I present nanoSIMS images of the organic-associated elements in *D.dianthus* skeletons collected with the Cs^+ source on the nanoSIMS 50-L instrument at Caltech. A primary Cs^+ beam of 20–30 nA at 8000 eV was used for the image collections, and the beam intensity was tuned to 2–10 pA at pixel level when images (15–40 μm in size, 256×256 or 512×512 pixels) were collected. The Cs^+ source on the instrument is more stable than the O^- source and can be tuned to finer scales (~100 nm) to yield images of higher resolution, due to differences in the physical design and thus ion densities of the sources. The Cs^+ beam was used to map ^{12}C, $^{12}C^{14}N$, ^{31}P, ^{32}S and ^{35}Cl in the coral skeletons. Mg and Ca were also mapped as oxide anions ($^{24}Mg^{16}O^-$ and $^{40}Ca^{16}O^-$) to compare the organic bands to Mg/Ca bands. The low ion yield for MgO^- and CaO^- resulted in noisy images and caused difficulties in direct comparison to the organic-associated elements. In some cases, we measured the same spot with both the Cs^+ beam for the anions and O^-

beam for the cations for better comparison. The organic associated elements are highly susceptible to contamination on the sample surface. As a result, a large beam current (hundreds of pA to a few nA) was used to pre-sputter each spot for 30–60 minutes. During the pre-sputtering, the ion counts for ^{12}C and $^{12}C^{14}N$ were monitored, and the surface contamination (very high ^{12}C and $^{12}C^{14}N$ that is over the detection limit) was removed until a relatively uniform image with low ^{12}C and $^{12}C^{14}N$ intensity was exposed (~10,000 cps ^{12}C and ~500 cps $^{12}C^{14}N$ per pixel). Given this intense pre-sputtering and the observed patterns in the elements that follow the directions of skeletal extension in the corals, we are convinced that our images represent the actual distribution of these elements in the coral skeletons. The image collection used a counting time of 12–28 ms on each pixel, 1–15 images were collected on each spot.

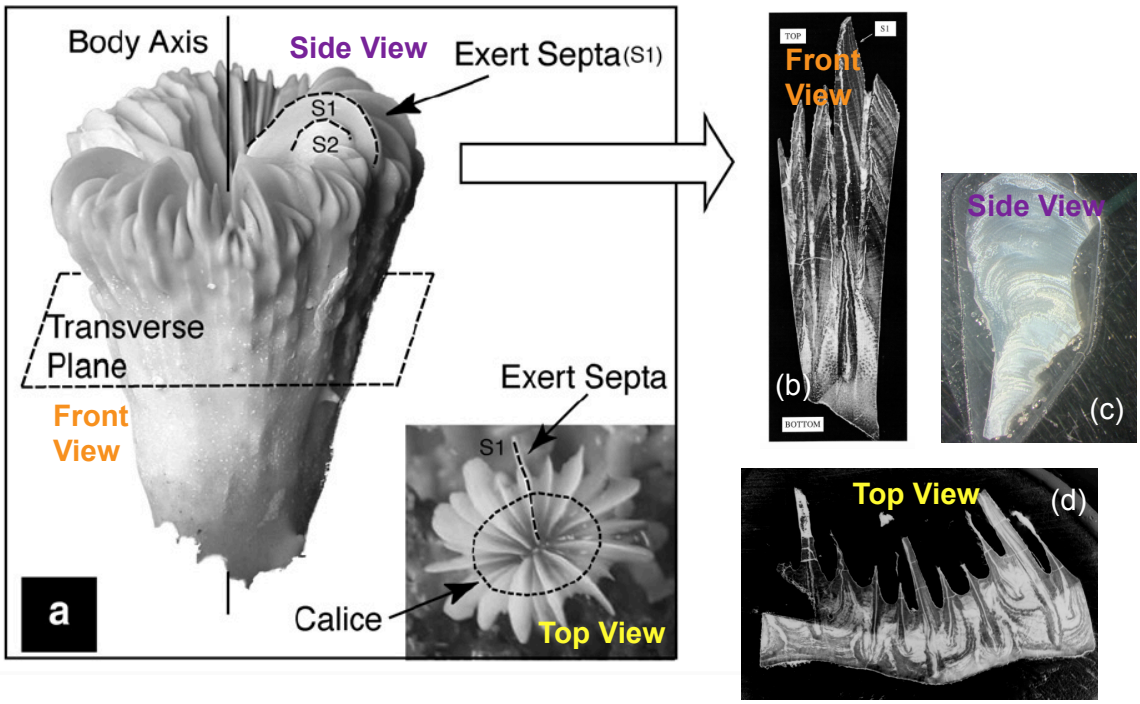

Figure 4-20 Geometry and cross sections of *D.dianthus* skeletons. Panel (a) shows the front view (main) and top view (bottom right inset) of a *D.dianthus* calice. From a top view, the exert septa are radially distributed with the polyp living in the center. Panels (b), (c) and (d) show cross section images of the front view, side view and top view respectively. The front view mainly shows the vertical extension of the skeleton with "Λ" shaped bands stacked around vertical COC bands. The side view shows the side surface of a single septum with bands extending upward and to the exterior. The top view shows the radially distributed septa pointing toward the center of the calice, with COCs running through the middle of each septum. The septa are connected by the thick theca of the skeleton.

The 3D geometry of the coral skeleton is important to the understanding of measured elemental distributions. Figure 4-20 shows a *D.dianthus* calice with cross section views from three different directions. The micromill, SIMS and nanoSIMS measurements for minor and trace elements were mostly performed in the top view, when quasi-parallel bands can be sampled in the direction of septa thickening to cover a wide range of Me/Ca variabilities. The nanoSIMS measurements of organic-associated elements were performed in different views to examine their distribution with respect to the growth directions of the coral skeletons.

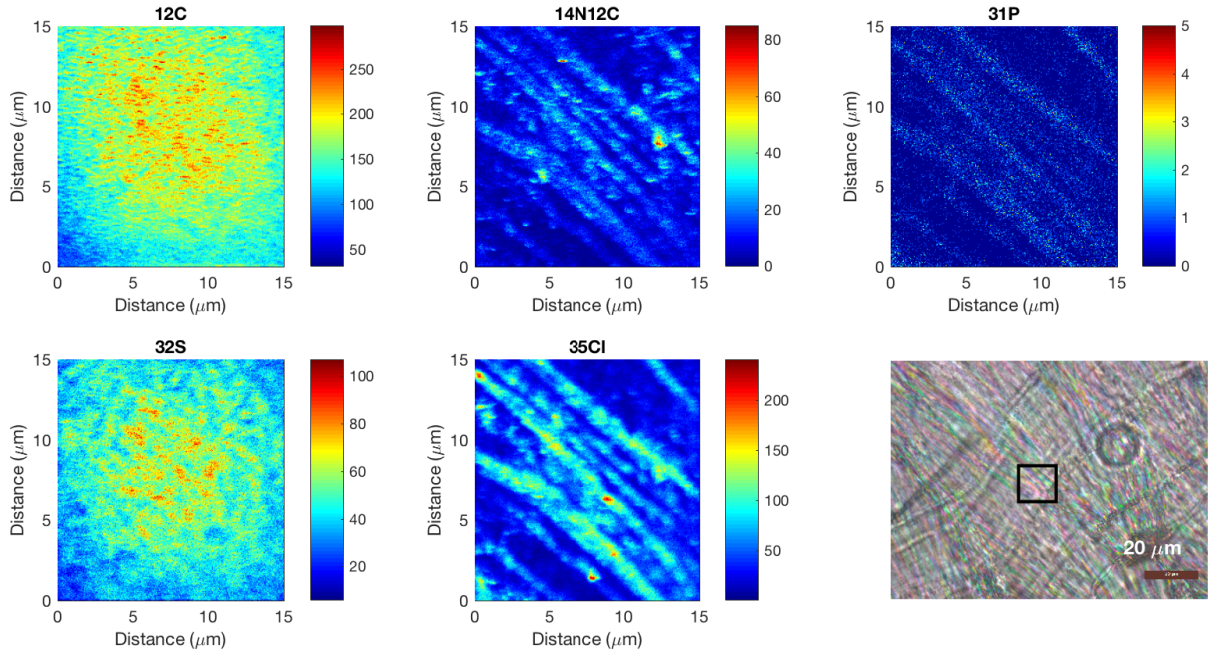

Figure 4-21 NanoSIMS map of organic associated elements from side view of a septum of coral TW1 (Tasmania). Images are from a 15 μm spot (256×256 pixels) and colors represent total ion counts. A whole image was collected over 45 minutes. The lower right panel shows a transmitted light image of the aragonite needles in the area, with the square marking the nanoSIMS spot.

4.7.1 Organic Bands in D.dianthus Skeletons

Figure 4-21 shows maps of C, N, P, S and Cl on the side of a septum from coral TW1. The most striking feature is the micron-scale quasi-rhythmic bands that are collocated in CN, P and Cl. A similar banding pattern is also observed in C and S, although C and S both have high background counts in the images compared to CN, P and Cl. We infer that the background in C represents the aragonite skeleton, while the high carbon region represents organic carbon that has high ionization efficiency under the Cs^+ beam. The background in sulfur is most likely carbonate-

associated sulfate (CAS) in the coral skeleton, and the high sulfur region corresponds to the organic sulfur phase. This is consistent with previous studies that have identified both sulfate and organic sulfur phases in coral skeletons, with the former as the dominant sulfur component (Cuif & Dauphin, 2005; Farfan et al., 2018). The phosphorous bands are also collocated with the organic layers as suggested by CN (nitrogen is primarily in organic form in coral skeletons), suggesting organic phosphorous as the major form of phosphorous in the coral skeleton, also consistent with previous studies that tried to develop P/Ca in corals as a [PO_4^{3-}] proxy (LaVigne et al., 2008; Anagnostou et al., 2011). It is unclear why Cl is collocated with the organic bands. A first guess may be interaction between seawater and the organic templates, but other ideas (e.g. chloroperoxidase enzyme) have been suggested among the group working on the project that requires further investigation. The orientation of the organic bands follows the growth direction of aragonite needles in the transmitted light image, suggesting the organics were incorporated between formation of aragonite layers in the skeleton.

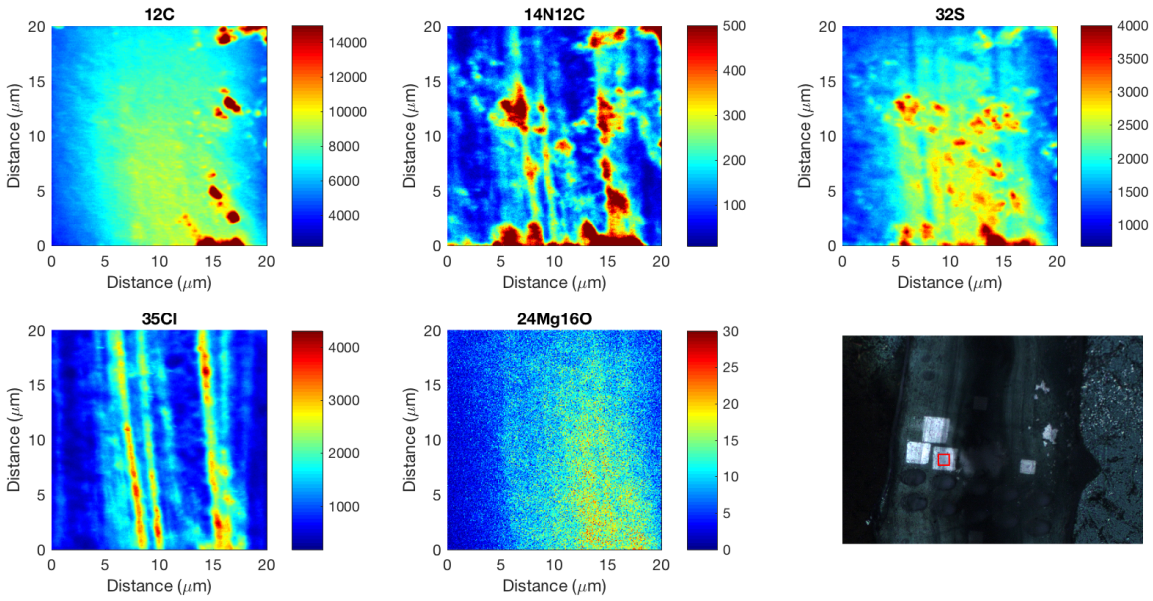

Figure 4-22 NanoSIMS map of organic associated elements and Mg (measured as MgO^-) in the secondary aragonite of a top view section of coral 62309 (North Atlantic). Images are from a 20 μm spot (256×256 pixels) and colors represent total ion counts accumulated over 15 image frames with 30 minutes of collection on each frame. The lower right panel is a transmitted light image of the septum, with the red square marking the position of the spot. The illuminated squares in the image are different nanoSIMS spots, while the oval pits are from SIMS measurements.

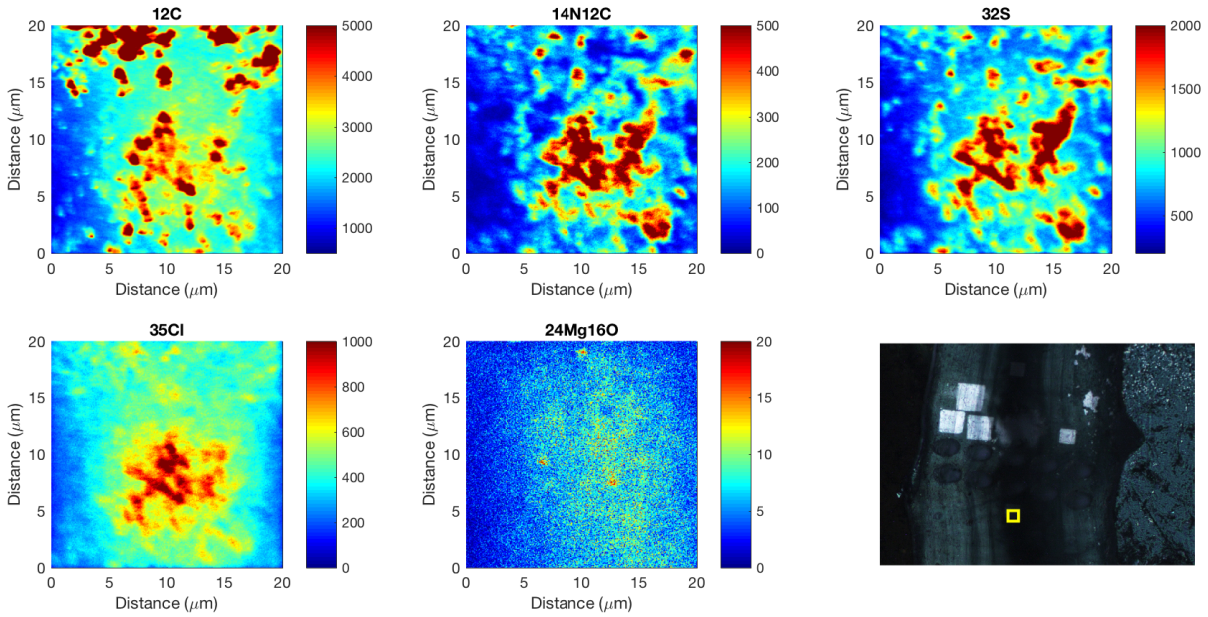

Figure 4-23 NanoSIMS map of organic associated elements and Mg (measured as MgO^-) in the COC of a top view section of coral 62309. Images are from a 20 μm spot (256×256 pixels) and colors represent total ion counts accumulated over 8 image frames with 30 minutes of collection on each frame. The lower right panel is a transmitted light image of the septum, with the yellow square marking the position of the spot.

Figure 4-22 and 4-23 show the distribution of C, N, S, Cl and Mg (measured as MgO^-) in the secondary aragonite and COC in a top view section of coral 62309, respectively. In the secondary aragonite, we again see the organic bands running parallel to the optical bands in the septum of the coral, and the bands alternate in the direction of septum thickening. Quasi-rhythmic bands are seen in CN and Cl, as well as S with a high background inferred as CAS in the crystal lattice. The MgO image also seems to have vertical bands, but the signal is too low to tell clearly. The textures of these elements are completely different in the COC, with hotspots in C, N, S and Cl and less clearly, in Mg, but the quasi-rhythmic bands are not observed. The hotspots in C, N, S and Cl are generally collocated, but not everywhere, suggesting that the organic molecules may take a variety of forms. The high Mg area in the center of the image is also collocated with high organic contents, but it is challenging to examine their exact relation with the low Mg counts collected. It is estimated that the C/Ca ratio in the COC is at least 50% higher than the secondary aragonite, suggesting higher contribution to the carbon ions from the organic phase.

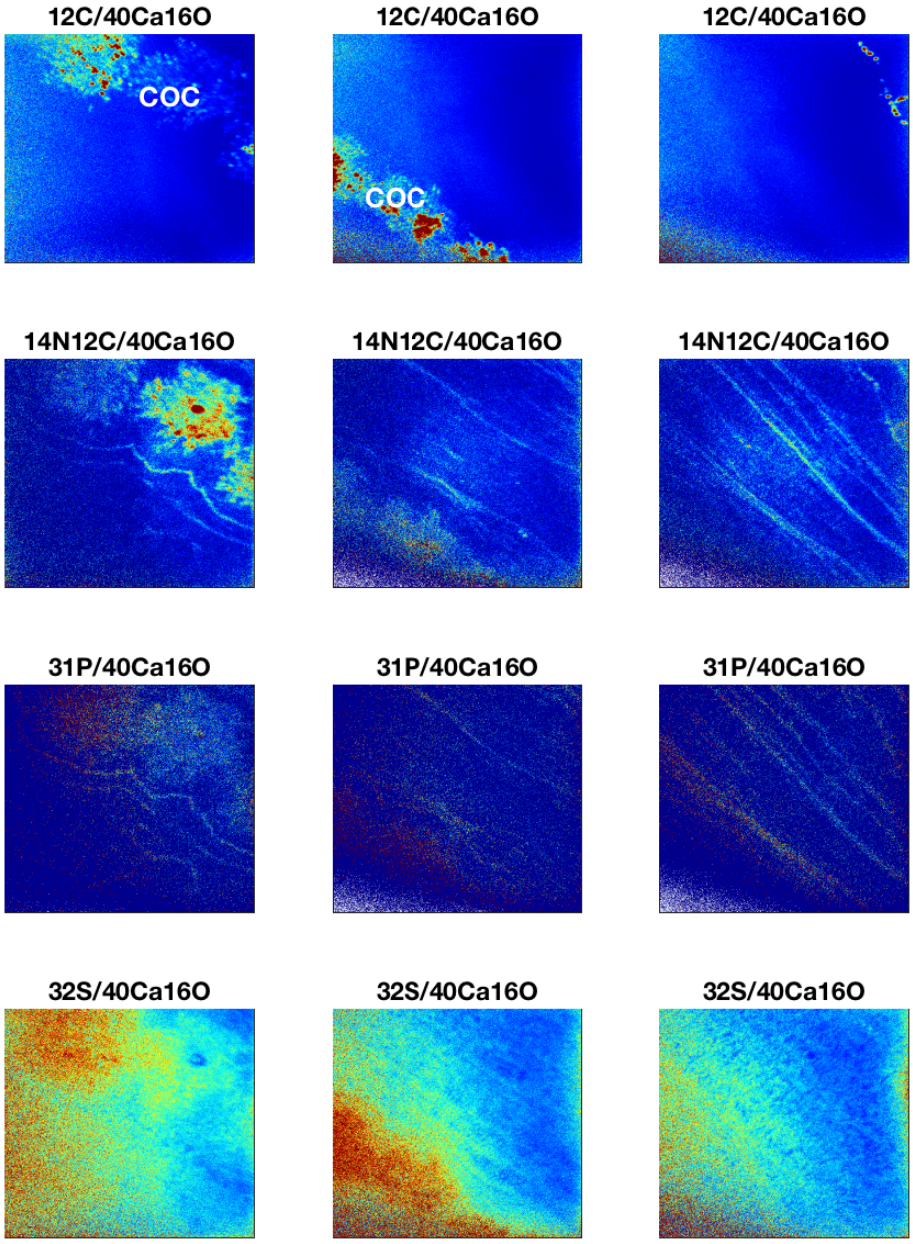

Figure 4-24 NanoSIMS map of organic associated elements on three adjacent spots across a septum on a top view section of coral 47407. Each spot is 40 μm in size (512×512 pixels) and are spaced by 10 μm in between. Each image was collected over 2 hours. The C, CN, P and S images are normalized by $^{40}Ca^{16}O$. There is a COC band running through the two spots on the left, with elevated C/CaO, CN/CaO, P/CaO and S/CaO ratios. To the upper right of the COC band, quasi-rhythmic banding is seen in CN/CaO, P/CaO ans S/CaO. The lower left part of each image is affected by the edge effect and the pattern is less clear.

To better compare the COC and secondary aragonite, Figure 4-24 shows nanoSIMS images of 3 adjacent spots across a COC band on a septum of coral 47407, in terms of element to calcium ratios. We see that the COC band is enriched in organic content with higher C, N, P and S intensity, while the secondary aragonite has quasi-rhythmic bands in N, P and S that alternate in the direction of septum thickening. Two questions arise from the observed organic bands in *D.dianthus* skeletons: (1) What is the spatial and temporal frequency of the bands? (2) How do these organic bands compare to the minor and trace elements?

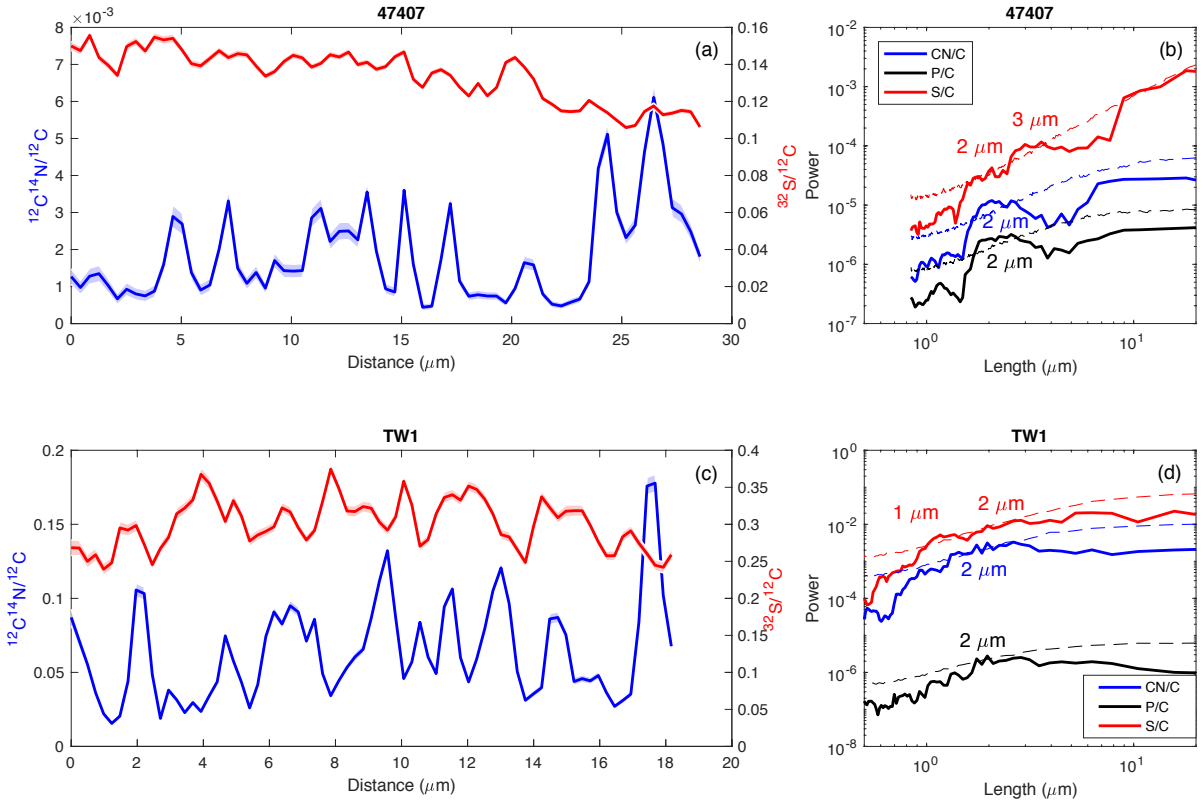

Figure 4-25 Profiles and spectra of organic associated elements in *D.dianthus* skeletons. Panels (a) and (c) show profiles (20 pixels in width) extracted across nanoSIMS images of 47407 (top view) and TW1 (side view) in terms of CN/C and S/C ratios. The shadings represent 2σ standard deviations across the 20-pixel width. We see the quasi-rhythmic bands in both CN/C and S/C, although there is phase offset between CN/C and S/C in certain parts of the profiles. Panels (b) and (d) show multi-taper spectra of the profiles (solid lines) compared to 95% red noise (dashed lines). A first-order autocorrelation (AR(1)) model was generated for each profile with uncertainties of the autocorrelation coefficients, and a Monte-Carlo simulation (N=500) was run to estimate the 95% quantiles of the AR(1) models. CN/C and P/C have very similar spectra in both corals, with a statistically significant peak around 2 μm. The S/C spectra have different structure with weaker (but still significant) peaks at 2 μm and other peaks both above and below 2 μm.

4.7.2 Frequency of organic bands

Figure 4-25 shows profiles and multi-taper spectra of element to carbon ratio profiles extracted from the nanoSIMS images of 47407 and TW1. We see that the quasi-rhythmic banding in organic layers (CN) occur at approximately 2 μm frequencies in both corals (from different views), which show up as statistically significant peaks in the spectra (Figure 4-25 b,d). Phosphorous is strongly collocated with CN, and the spectral structures of CN/C and P/C are very similar. In comparison, S/C is not always in phase with CN/C, and their spectral structures are different, with S/C having significant spectral peaks at length scales other than 2 μm. It should also be noted that the CN/C and S/C ratios are very different between the two corals. This may be related to different instrument conditions for the two analytical sessions, different cross-section views from which the images were generated, as well as real difference in organic content in these two corals. However, the organic bands at a frequency of a few microns seem to be a robust feature between different corals in different directions of skeletal extension.

Converting the spatial frequency to time intervals is challenging due to uncertainties in the growth rate estimates of deep-sea corals. Averaged over a century, the vertical extension rates of *D.dianthus* skeletons was estimated at 0.5–2 mm/yr (Adkins et al., 2004). Given these estimates, a banding frequency of 2 μm would correspond to daily timescales. Given the growth environment of the corals, it is hard to imagine why they would sense the diurnal cycles in the environment. It is also hard to directly compare the vertical extension rates to the spatial scales of the side view (radial extension of septa) and the top view (septa thickening). Therefore, an ideal specimen to further test the temporal frequency of the bands is one with known growth rates and cut in the front view. We obtained such a specimen from Rob Sherrell at Rutgers University. This *D.dianthus* specimen (N5) was collected alive in the Chilean Fjord and transported to an aquarium in Barcelona for culture and tracer calibration experiments. The coral was cultured in complete darkness and fed daily (except weekends), and the chemical and isotopic composition of certain elements ($[PO_4^{3-}]$, $[Ba^{2+}]$, Ba and Pb isotopes, etc.) in the seawater it grew in was modified for empirical tracer calibration purposes. The fluorescent dye calcein was put into the seawater to mark the start and end of the culture experiments.

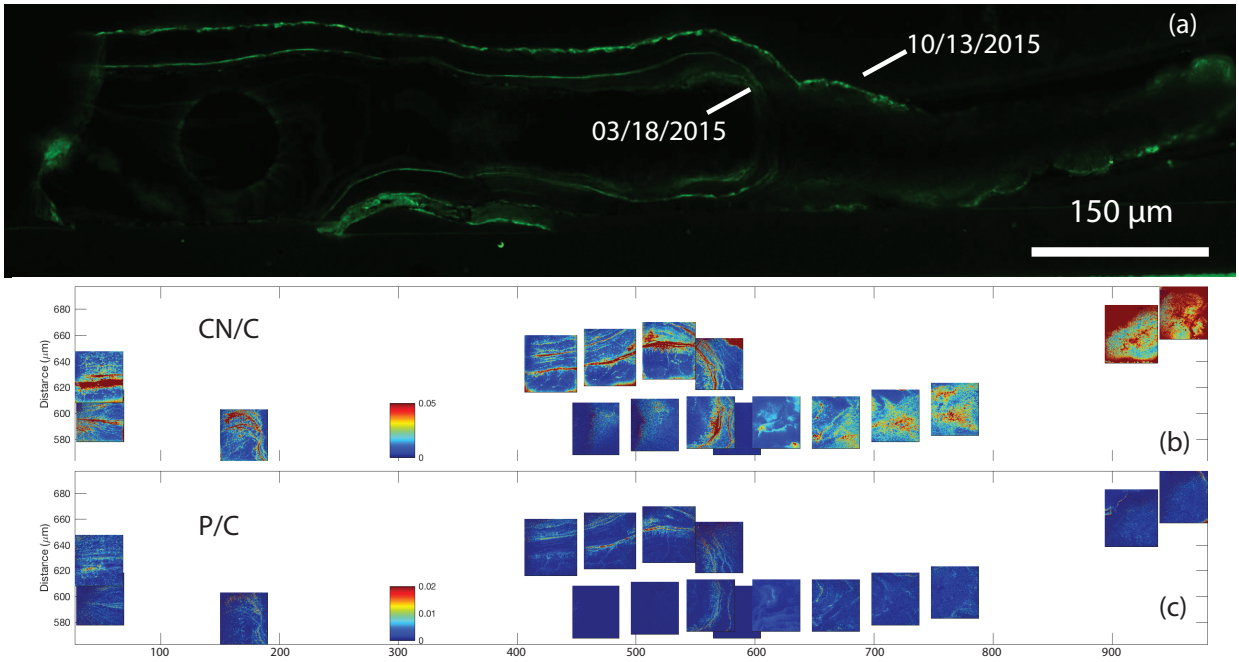

Figure 4-26 Fluorescence image of N5 septum from front view with tiled CN/C and P/C nanoSIMS images. (a) Fluorescence image of a septum of N5. The septum was cut in the front view section. The direction of vertical extension is from left to right in the image. Two calcein labels were put into the seawater and incorporated into the coral skeleton as time markers, with the dates labeled on the image. (b) nanoSIMS maps of CN/C ratio at different spots measured on N5 that are tiled together. Each tile is 40 µm in size (512×512 pixels). The interior calcein band can be seen with high CN/C ratio. (c) Stack of P/C map tiles of N5.

Figure 4-26 shows the fluorescence image of the N5 septum with two labeled calcein bands. During the 209 days of the experiment, this septum extended vertically by 420 µm, with an average growth rate of 2 µm/day. The organic associated elements were mapped in different parts of the septum and tiled together as element to carbon ratios (Figure 4-26b, c). We see the interior calcein band show up as high CN/C that has the same shape as the fluorescence image, and the new growth bands that developed from the calcein band follow the expected orientations. When we focus on the new growth in the vertical direction (to the right of the vertical part of the calcein band in the image) and extract profiles for spectral analysis, we see that the characteristic frequencies in CN/C and P/C are 1, 2 and 4 µm (Figure 4-27), corresponding to daily timescales. The observation that both cultured and natural *D.dianthus* have micron-scale organic bands suggests that there is a daily rhythm in the coral calcification process, potentially driven by the circadian clock in the organism. If that is the case, deep-sea corals may have inherited the circadian clock from surface

corals during the evolution process. The other possibility of daily rhythm in deep-sea corals is related to food supply, which could be influenced by tidal forced suspension of sediment particles. This could be tested with a different feeding frequency in the culture experiments, which is currently work under progress.

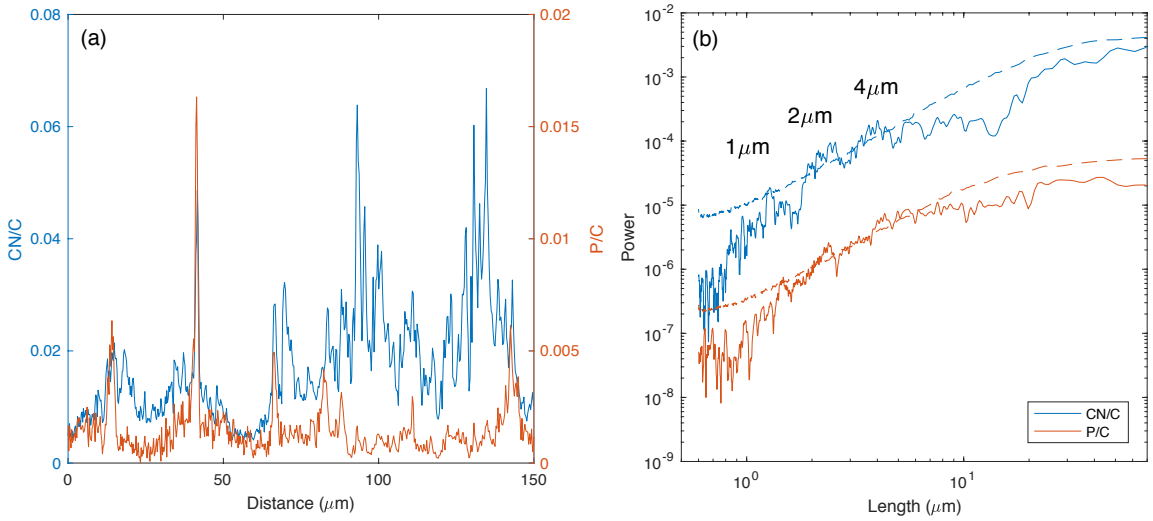

Figure 4-27 Profiles and spectra of CN/C and P/C from cultured growth of specimen N5. (a) CN/C and P/C profiles extracted from four nanoSIMS maps in the cultured growth part of N5. The 40 μm images are separated by 10 μm. A horizontal profile was extracted from each image and simply connected together assuming the same rhythm occurs through the septum. (b) Multi-taper spectra of CN/C and P/C from the profiles in panel (a) (solid lines) compared to 95% red noise (dashed lines). The statistically significant peaks occur at 1, 2 and 4 μm for both CN/C and P/C.

4.7.3 Spatial relations between organic and Me/Ca bands

It has been suggested that Mg in biogenic carbonates is associated with the organic component, and the variability in Mg/Ca could be explained by a mixture of an organic rich high Mg phase and an inorganic $CaCO_3$ like low Mg phase (Meibom et al., 2004; Bentov & Erez, 2006; Finch & Allison, 2008). The proportions of these two phases that are made during the biomineralization process may respond to environmental conditions, thus giving rise to the Mg/Ca thermometer in biogenic carbonates with a higher temperature sensitivity than inorganic precipitation experiments (Bentov & Erez, 2006). The analogy in deep-sea corals may be the proportion of COCs (or COC-like structures) relative to secondary aragonite, although it has been

observed that the COCs and secondary aragonite do not fall on a single mixing trend in Me/Ca correlations. The high Mg/Ca ratios found in COCs, however, may be associated with the organic phase. Figure 4-28 provides evidence of it, in which the hotspots in the organic associated elements in the COC band of 47407 are also hotspots in Mg/Ca ratios. Unfortunately, we do not have another good example due to the generally very low MgO intensities in the analytical session.

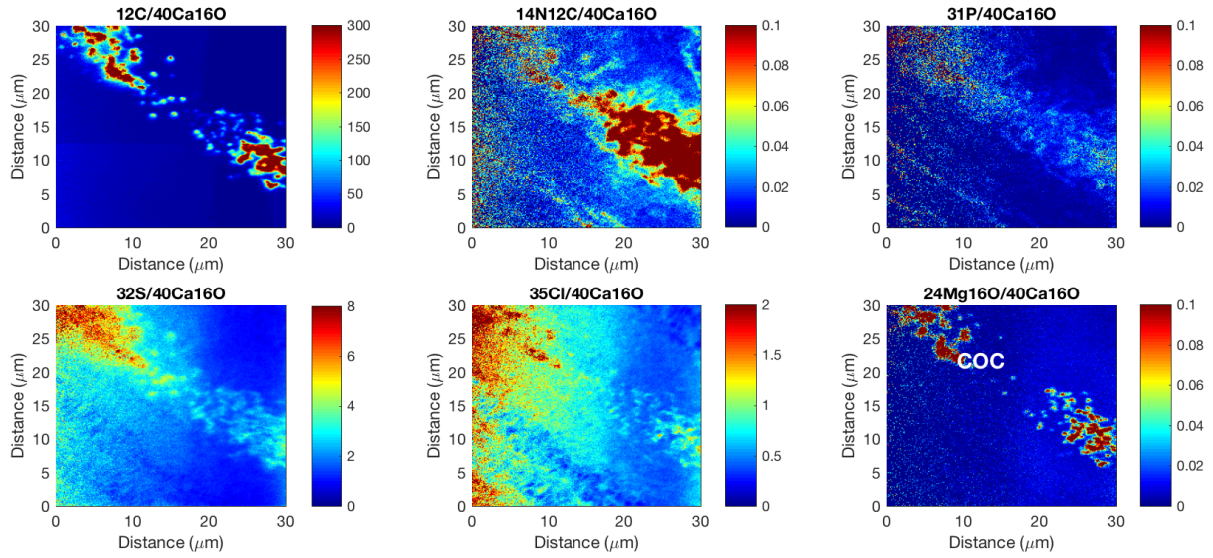

Figure 4-28 NanoSIMS maps of organic associated elements and Mg/Ca on a 30 μm spot (256× 256 pixels) across a COC on a top view section of coral 47407. Images are presented as element to calcium (measured as CaO) ratios. The COC band running across the image is elevated in C, N, P, S and Mg relative to the secondary aragonite on both sides. The collocation of the hotspots in different elements suggests that the high Mg in the COC is associated with organic matter.

While the high Mg in the COCs may be attributed to the organic phase, it is unclear whether the Mg bands in the secondary aragonite can be attributed to the same mechanism. The robust correlation between Mg/Ca and Li/Ca, B/Ca and Sr/Ca in the secondary aragonite would suggest a Rayleigh-like inorganic precipitation mechanism as discussed earlier in this chapter. Although the high Mg/Ca bands and organic bands share the same orientations and are sometimes collocated, they do not look exactly alike in that the Mg/Ca bands measured with the O^- beam are typically thicker than the organic bands measured with the Cs^+ beam (Figure 4-29). This is partly influenced by the physical size of the primary beams, in that the Cs^+ beam can be tuned to finer spatial scales than the O^- beam (by a factor of 2–3). The characteristic frequency in the Mg/Ca bands is also about 2–3 times lower than the CN bands (Figure 4-30). Therefore it is difficult to

distinguish the difference in band thickness and frequencies from analytical artifacts of the instrument at this stage, but it is a question worth further investigation in the future with images of higher resolution.

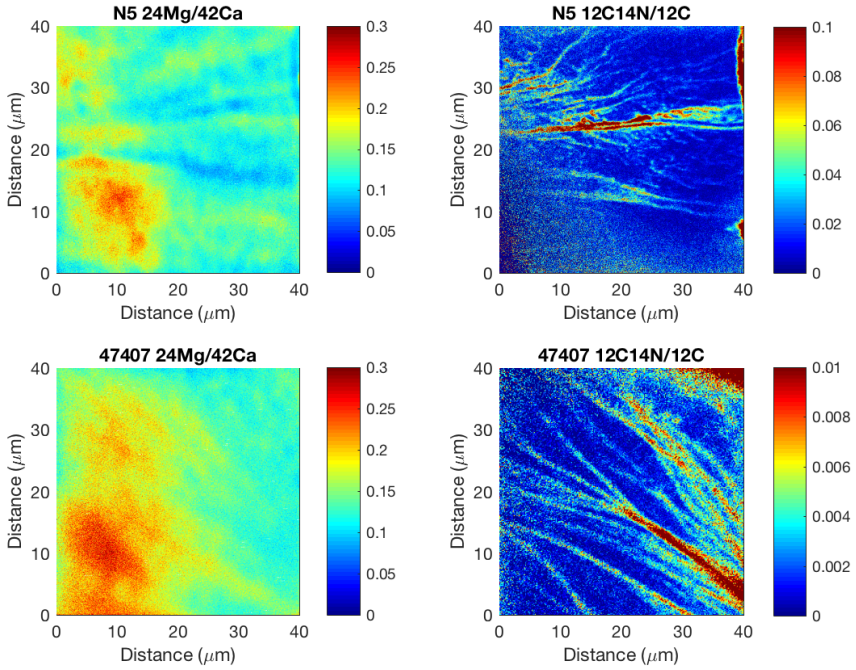

Figure 4-29 Comparison of O^- measurements of Mg/Ca and Cs^+ beam measurements of CN/C at the same spot in coral N5 (top panels) and 47407 (bottom panels).

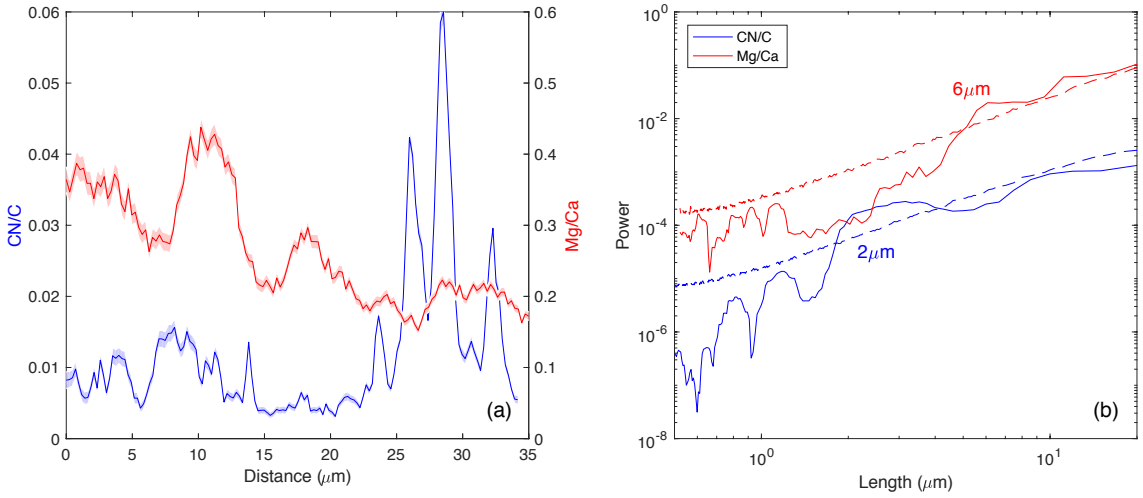

Figure 4-30 Comparison of CN/C and Mg/Ca profiles and spectra from N5 images in Figure 4-29. (a) CN/C (blue) and Mg/Ca (red) profiles extracted from images of the same spot on N5 in Figure 4-29. (b) Multi-taper spectra of CN/C and Mg/Ca (solid lines) compared to 95% red noise (dashed lines). Mg/Ca has a significant peak at ~6 μm, while CN/C has a peak at 2–3 μm.

4.8 Appendix B: X-ray absorption spectra of Ca and Sr in *D.dianthus* skeletons

Complementary to chemical composition analysis, X-ray absorption spectroscopy (XAS) is a technique that can be used to probe the bonding environment of atoms in crystal lattices. Understanding the bonding environment of different elements can shed light on their incorporation mechanisms into the crystals and help explain the variabilities in their concentrations in different mineral phases. This technique has been applied to the two minor elements Mg and Sr to understand the vital effects associated with the Mg/Ca and Sr/Ca thermometers in biogenic carbonates (Greegor et al., 1997; Finch et al., 2003; Allison et al., 2005; Finch & Allison, 2008; Foster et al., 2009; Branson et al., 2013). The X-ray absorption spectra of Ca, on the other hand, have been applied to study the involvement of amorphous calcium carbonate (ACC) in the biomineralization process (Politi et al., 2008; Gong et al., 2012; Mass et al., 2017). XAS has also been used to identify organic and inorganic sulfur species in biogenic carbonates such as coral skeletons (Tamenori et al., 2014; Farfan et al., 2018).

The Sr/Ca thermometer in corals is based on the substitution of Sr for Ca in the aragonite lattice. An early XAS study by Greegor et al. (1997) found that at least 40% of Sr in coral skeletons is in the form of strontianite ($SrCO_3$), challenging this assumption. In contrast, a later more refined XAS study on a larger number of coral species found that Sr in corals is indistinguishable from Sr substituted into aragonite lattice, and that the Sr bonding environment is indistinguishable between COCs and secondary aragonite fibers (Finch et al., 2003; Allison et al., 2005). Deep-sea corals have not been widely studied with XAS techniques. Given their clear banding patterns and variability in Me/Ca ratios, it is helpful to understand if changes in Sr/Ca are related to changes in the bonding environment of Sr and Ca, and if the COCs have a different bonding environment than the secondary aragonite. Therefore, we conducted XAS measurements of Sr and Ca on a few *D.dianthus* specimens at the Stanford Synchrotron Radiation Lightsource (SSRL). The Sr XAS were measured on beamline 2-3 and Ca XAS were measured on beamline 14-3 of SSRL. The methods will not be detailed in here. In brief, an incident X-ray beam was focused on a spot of the sample surface. The energy of the incident beam is continuously increased until the K-shell electrons of Ca or Sr in the coral skeleton are excited, at which point an absorption edge is observed. The features near the absorption edge (XANES) can provide information such as the oxidation state and coordination number/geometry of the absorbing atoms. The excited

electrons that are ejected may be scattered by the neighboring atoms and create self-interfering electromagnetic waves that interact with the initial X-ray absorbing atom to produce post-edge absorption features. These features are called extended X-ray absorption fine structure (EXAFS) and can provide information about the bonding environment of the absorbing atoms. In this study, we measured EXAFS spectra of Ca and Sr in both COCs and secondary aragonite in different *D.dianthus* specimens, which also include the XANES energy range. We replicated the spectra 5–14 times on each spot to reduce noise and generate high-quality spectra.

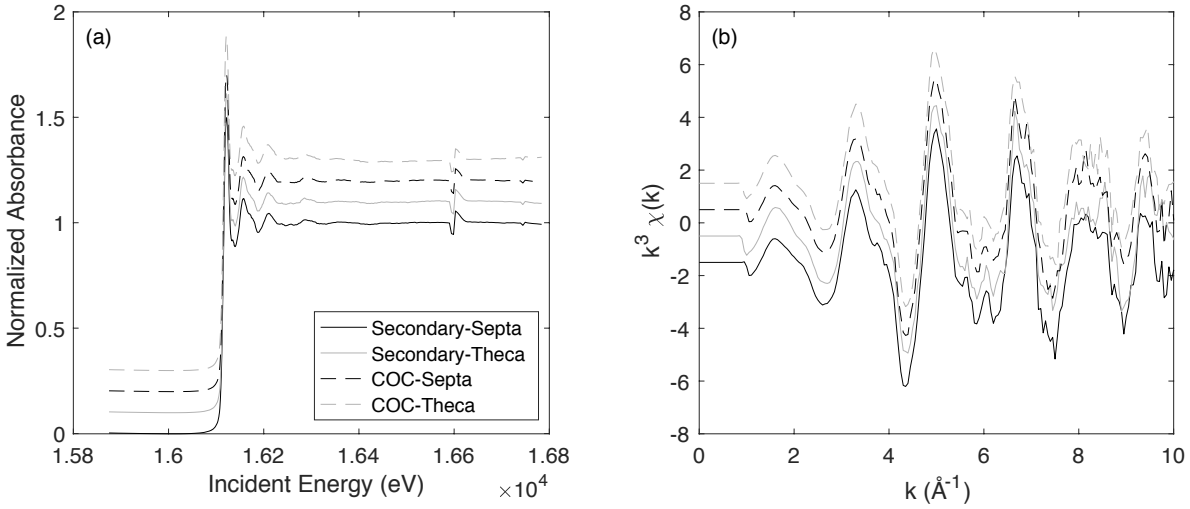

Figure 4-31 Sr X-ray absorption spectra in *D.dianthus* specimen 62309. Panel (a) shows the spectra over the full incident beam energy range, while panel (b) shows the Fourier transformed post-edge features (EXAFS) weighted by the cube of the wavenumber (k^3). The solid lines represent secondary aragonite while the dashed lines represent COCs. The blank lines are from the septa and the gray lines are from the theca. The spectra are offset on the y-axis by 0.1 unit in (a) and 0.5 unit in (b) to increase visibility. The bonding environments of Sr in different parts of the skeleton are very similar and indistinguishable from each other.

Figure 4-31 shows the XAS spectra of Sr in coral 62309 as well as the post-edge fine features (EXAFS). At different spots measured in the specimen, including both COC and secondary aragonite on the septa and theca, the Sr spectra are indistinguishable from each other, suggesting very similar bonding environment of Sr in different parts of the coral. Our EXAFS data are very similar to those of Finch et al. (2003), suggesting that Sr substitutes for Ca in *D.dianthus* skeletons instead of forming strontianite. The Sr variability observed in an individual *D.dianthus* is generally 10–15%, much smaller than other elements, which may be related to the constancy of the

bonding environment. In contrast, we observe a clear difference in the XANES features between COCs and secondary aragonite in two different *D.dianthus* individuals (Figure 4-32). Like inorganic aragonite, the secondary aragonite has two absorption features before and after the main absorption peak, which are missing in the COCs. Lack of these features suggests that the COCs are aragonites with less crystalline structures or more random orientations. It should be noted that while ACC also lacks these fine features on the main absorption peak (Figure 4-32c, Brinza et al., 2013), there is marked difference between the COC and ACC, in that COCs still have weak features on and after the edge that are totally muted in ACC. As a result, this dataset may provide another clue to why the minor and trace element compositions of COCs are distinct from the secondary aragonite in terms of the bonding environment of Ca, but cannot be used to definitely tell if COCs formed from ACC precursors.

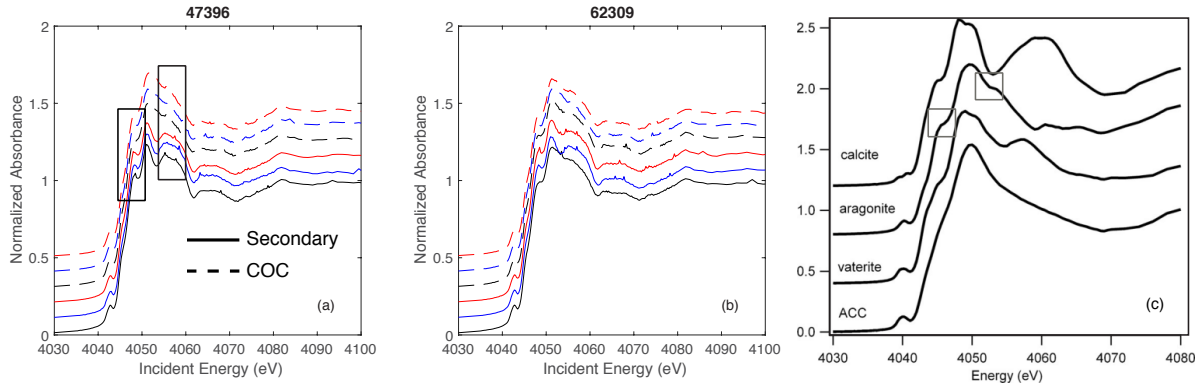

Figure 4-32 Ca XANES spectra of coral 47396 (a) and 62309 (b) compared to different forms of $CaCO_3$ (c) according to Brinza et al. (2013). The solid lines in (a) and (b) represent different spots on the secondary aragonite, while the dashed lines represent different spots on COCs. The lines are offset by 0.1 unit on the y-axis for better visibility. While both secondary aragonite and COCs generally have similar absorption structure to a speleothem aragonite in (c), two features are missing in the COCs compared to the secondary aragonite, one before the highest absorption peak and one after the peak, as marked by the black boxes. This suggests that COCs are composed of aragonite with less crystalline structure or more random orientations.

Chapter 5

EMPIRICAL MULTI-ELEMENT TRACER CALIBRATION IN *DESMOPHYLLUM DIANTHUS*

5.1 Introduction

Despite all the complications in understanding the mechanisms underlying paleoceanographic tracers that have been discussed in previous chapters, most of the tracers have been successfully applied to the reconstruction of the climate history during the Pleistocene ice ages and deeper times based on empirical calibrations (Beck et al., 1992; Lea, 1993; Lea et al., 2000; Zachos et al., 2001; Hönisch & Hemming, 2005; Elderfield et al., 2012; Penman et al., 2014; Rae et al., 2018; Farmer et al., 2019; Hasenfratz et al., 2019). Robust empirical calibrations in biogenic carbonates not only form the basis for the applications of tracers, but also provide clues to the potential mechanisms of vital effects by comparison to theoretical expectations and the inorganic precipitation reference frame. Some tracers have been found in deep-sea corals that follow simple theoretical expectations, including radiocarbon (Adkins et al., 2002), Nd isotopes (van de Flierdt et al., 2010), clumped isotopes (Thiagarajan et al., 2011), and nitrogen isotopes of organic matter in the coral skeletons (Wang et al., 2014). These tracers have been applied in fossil corals to reveal the close coupling between climate, the carbon cycle and deep ocean changes over the last glacial period (Robinson et al., 2005; Eltgroth et al., 2006; Thiagarajan et al., 2014; Hines et al., 2015; Wang et al., 2017). Some tracers in deep-sea corals have been empirically calibrated for paleoceanographic applications, despite an incomplete understanding of the potential vital effects. These include the Li/Mg thermometer (Case et al., 2010; Raddatz et al., 2013; Montagna et al., 2014), boron isotopes as a pH proxy (Anagnostou et al., 2012; Wall et al., 2015; Martin et al., 2016; Stewart et al., 2016; Rae et al., 2018), P/Ca as a [PO_4^{3-}] proxy (Anagnostou et al., 2011), Cd/Ca as a water mass tracer (Adkins et al., 1998), Ba/Ca and Ba isotopes as [Ba] proxies (Anagnostou et al., 2011; Hemsing et al., 2018; Spooner et al., 2018), and U/Ca as a pH or [CO_3^{2-}] proxy (Anagnostou et al., 2011; Raddatz et al., 2014). Other tracers in deep-sea corals have been found to be dominated by vital effects and mostly used to study the mechanisms of the

biomineralization process, including carbon and oxygen isotopes (Adkins et al., 2003; Rollion-Bard et al., 2010; Martin et al., 2016), Mg/Ca and Sr/Ca (Gagnon et al., 2007).

In the previous chapters, I have used the numerical biomineralization model and fine-scale observations in individual *D.dianthus* corals to understand the vital effects in stable isotope and Me/Ca ratios, and proposed some possible ways the vital effects may be sensitive to environmental conditions such as the saturation state of the ambient seawater. I have also discussed possible ways to deconvolve environmental information from the vital effects with cross-correlations between different tracers. In this chapter, I report empirical tracer calibrations of bulk aragonite powder from a suite of *D.dianthus* individuals collected from a wide range of oceanic settings. Both carbon and oxygen isotopes and Me/Ca ratios were measured for the bulk samples to test if the biomineralization model can be used to correct for the vital effects in the tracers.

5.2 Method

5.2.1 Coral Selection

A total of 22 *D.dianthus* specimens were selected for this tracer calibration study from the Caltech deep-sea coral collection. These corals were either provided by the Smithsonian Museum of Natural History or collected from seamounts south of Tasmania during cruise TN-228 in 2008–2009 on the R/V Thompson with the deep submergence vehicle JASON. Most of these corals were collected with tissue remains attached to the skeletons and considered modern, although a few of them are suspected to be fossil corals given a significant amount of black/brown coatings on the aragonite skeleton (which needs to be further tested with radiocarbon or U-Th dating). These corals were selected to represent a relatively wide range in depth (2185 m), temperature (12°C), [CO_3^{2-}] (158 μmol/kg) and [PO_4^{3-}] (2.6 μmol/kg) for this species. The locations of these corals have been listed and mapped in Chapter 1 (Table 1-1, Figure 1-2).

The ambient seawater conditions of these corals are estimated with the GLODAP version 2 dataset (Key et al., 2015; Olsen et al., 2016) and the Ocean Data View (ODV) software (Schlitzer, 2018). Some corals have stations close by and representative stations are used to estimate the

environmental conditions. Other corals do not have stations nearby with seawater property measurements, and the 3D estimation tool in ODV was used to estimate the environmental conditions in a ~2°×2° domain around the location of the corals. This tool uses all data points within the defined domain to calculate an average value for the target location that is weighted by distance and data quality. The two methods give similar estimates for most of the corals, although significant differences can occur for certain variables when the available data are sparse. This could influence some of the tracer calibration results as discussed below. For carbonate chemistry parameters, alkalinity and DIC were measured for most of the stations in GLODAP v2. I estimated alkalinity and DIC in ODV and used them to calculate other parameters such as [CO_3^{2-}], pH and aragonite saturation state (Ω_A) with CO2SYS. For non-conservative trace elements such as Ba and Cd, estimates of their concentrations in the seawater are important for understanding the measured Ba/Ca and Cd/Ca in the coral skeletons. The ODV version of the GEOTRACES data product (Schlitzer et al., 2018) was used to estimate [Ba] and [Cd] in the seawater for these corals. Due to differences in the spatial coverage of the GEOTRACES stations and the deep-sea coral locations, not all corals can be reliably estimated for their ambient [Ba] and [Cd]. As a result, [Ba] and [Cd] in the seawater were calculated from their empirical relations with silicate and phosphate respectively for these sites. The estimated ambient seawater conditions are listed in Table 5-1.

5.2.2 Stable Isotope and Me/Ca Analyses

Aragonite powders were sampled from the selected *D.dianthus* specimens with an agate mortar/pestle or micromill. The specimens were rinsed with ethanol and distilled water before sampling. For relatively large specimens, a thick section was made in the top view or front view, and a Merchantek Micromill was used to generate powder across growth bands that cover both the septa and theca. For smaller specimens, a relatively clean piece (without significant amount of visible surface coating) that includes both septa and theca was picked and crushed with the mortar and pestle. The micromill method usually generates a few milligrams of powder, while the crushing method generates tens of milligrams of powder. Three aliquots of the powder (~100 μg each) were collected for each coral for stable isotope measurements, and 1–2 mg of the powder was used for one batch of Me/Ca measurements. The remaining powder was stored for future replicate measurements.

Table 5-1 Estimates of Environmental Conditions of Selected *D.dianthus*

Coral	Lon	Lat	Average Depth (m)	Estimation Method	Temperature (°C)	Salinity (psu)
19249	240.5	34.0	274	Station	8.2	34.25
Big Beauty	297.8	-54.7	816	3Dest	3.5	34.28
47409	320.6	-54.5	672.5	3Dest	1.9	34.65
Leda-b[a]	147.3	-44.3	1460	Station	2.7	34.57
Leda-t[a]	147.3	-44.3	1460	Station	2.7	34.57
47396	291.2	-59.7	1124.5	Station	2.2	34.65
Gaia	150.3	-44.8	2395	3Dest	2.1	34.72
83583	232.2	32.9	464	Station	5.8	34.10
82065	230.2	-54.8	585.5	3Dest	5.6	34.30
94071	173.3	-30.7	615	Station	8.7	34.60
47407	230.2	-54.8	549	3Dest	5.7	34.30
84820	268.4	0.2	806	Station	5.8	34.58
62309	292.3	40.4	521.5	Station	5.6	34.99
47394	162.0	-51.0	352	3Dest	7.0	34.41
53377	167.8	-51.1	210	3Dest	7.0	34.36
48744	9.8	43.3	627.5	Station	13.9	38.70
80404	355.8	35.4	395	Station	13.3	38.50
80358	352.2	48.0	358	Station	11.5	35.60
47413	167.6	-50.6	421	3Dest	6.5	34.36
Titan-b[a]	147.3	-44.4	2066	Station	2.2	34.71
Titan-t[a]	147.3	-44.4	2066	Station	2.2	34.71
97275	117.6	21.7	421	3Dest	9.6	34.41

Table 5-1 Estimates of Environmental Conditions of Selected *D.dianthus* (continued)

Coral	Alk (µeq/kg)	DIC (µmol/kg)	$[CO_3^{2-}]$ (µmol/kg)	$\Delta[CO_3^{2-}]$ (µmol/kg)	Ω_A	$pH_{in\ situ}$
19249	2289	2252	55.5	-13.7	0.80	7.65
Big Beauty	2299	2201	81.5	4.2	1.05	7.89
47409	2347	2258	76.9	0.9	1.01	7.88
Leda-b	2335	2250	74.0	-13.8	0.84	7.83
Leda-t	2335	2250	74.0	-13.8	0.84	7.83
47396	2349	2254	80.2	-2.2	0.97	7.88
Gaia	2361	2259	81.1	-23.8	0.77	7.85
83583	2291	2275	46.2	-25.7	0.64	7.60
82065	2285	2154	100.2	26.4	1.36	7.97
94071	2290	2140	111.6	38.1	1.52	7.96
47407	2284	2150	102.1	28.8	1.39	7.98
84820	2345	2297	59.5	-17.2	0.78	7.69
62309	2311	2177	102.3	29.3	1.40	7.97
47394	2285	2130	115.0	44.6	1.63	8.02
53377	2285	2114	124.7	56.2	1.82	8.06
48744	2608	2323	204.4	130.5	2.77	8.08
80404	2585	2336	181.1	109.9	2.54	8.04
80358	2347	2137	151.2	81.2	2.16	8.05
47413	2286	2128	116.1	44.7	1.63	8.03
Titan-b	2351	2255	78.6	-20.2	0.80	7.84
Titan-t	2351	2255	78.6	-20.2	0.80	7.84
97275	2280	2113	122.0	51.2	1.72	8.00

Table 5-1 Estimates of Environmental Conditions of Selected *D.dianthus* (continued)

Coral	$[PO_4^{3-}]$ (µmol/kg)	$[O_2]$ (µmol/kg)	$[SiO_4]$ (µmol/kg)	$[Ba]_{sw}$ (nmol/kg)	$[Cd]_{sw}$ (nmol/kg)	Sampling Method[d]
19249	2.52	52	46.1	42.6[b]	0.35[b]	MP
Big Beauty	2.09	225	28.4	76.9	0.69	MM
47409	2.28	178	87.0	75.6	0.77	MP
Leda-b	2.27	171	71.3	72.5[b]	0.73	MP
Leda-t	2.27	171	71.3	72.5[b]	0.73	MP
47396	2.27	178	79.6	83.9	0.79[b]	MM
Gaia	2.25	184	93.8	91.8[c]	0.67	MP
83583	2.93	47	67.3	44.5[b]	0.68[b]	MM
82065	1.70	256	14.6	53.2[b]	0.39[b]	MM
94071	1.43	209	7.7	45.6[c]	0.29	MM
47407	1.65	260	13.3	51.1[b]	0.37[b]	MM
84820	2.48	50	67.6	66.7	0.89[b]	MM
62309	1.28	225	12.0	46.9	0.29	MM
47394	1.52	258	10.2	46.8[c]	0.28	MM
53377	1.32	283	6.1	44.9[c]	0.21	MP
48744	0.33	176	7.8	49.5[b]	0.07	MM
80404	0.46	163	9.3	45.8	0.09	MP
80358	0.63	223	4.2	44.3	0.11	MP
47413	1.44	270	9.3	46.3[c]	0.29	MM
Titan-b	2.15	180	86.2	71.3[b]	0.69	MM
Titan-t	2.15	180	87.2	71.3[b]	0.69	MM
97275	1.41	131	37.4	44.4[b]	0.74[b]	MM

a. Leda-b and Leda-t are two individuals whose skeletons are cemented together, so are Titan-b and Titan-t. The labels "b" and "t" stand for bottom and top respectively.
b. The red numbers are "poor estimates" according to the 3D estimation of ODV due to limited number of data points in stations nearby.
c. The blue numbers are calculated from a global $[Ba]$-$[SiO_4]$ relation because ODV 3D estimation was not available for these locations.
d. MP stands for "mortar & pestle" while "MM" stands for micromill.

The stable isotope measurements were performed by Chris Charles on a Finnigan MAT 252 mass spectrometer coupled to a Kiel device at Scripps Institution of Oceanography, with the same method as the micromilled samples in Chapter 3. The plan was to measure three aliquots for each coral to characterize the heterogeneity within the powder samples. Some of the aliquots were not recovered during the storage and transfer process, but at least one stable isotope measurement was available for each coral to estimate where on average the sample powder sits on the $\delta^{18}O$-$\delta^{13}C$ trend, i.e. how much vital effect from alkalinity pumping is incorporated in the bulk sample according to the biomineralization model.

For Me/Ca measurements, 1–2 mg of the bulk sample was dissolved with 2 mL of a 5% v/v HNO_3 solution in 5 mL Teflon beakers. Because the external surfaces of the skeletons were

intentionally avoided during the sampling process, no chemical cleaning was applied to the sample powder. This was also intended to evaluate how much certain contamination-sensitive elements (e.g. B, Na, Al, Mn, Fe, Cd) may be affected and if such simple treatment would produce good tracer calibrations. After dissolution, 10 μL of each primary solution was drawn and diluted with 250 μL of 5% v/v HNO_3. This solution was used to check the [Ca^{2+}] using the ^{48}Ca intensity relative to a 1 mM [Ca^{2+}] standard on the Agilent 7500cx ICP-MS at Caltech. The [Ca^{2+}] of the primary solutions ranged from 5.9–9.5 mM, and these values were used to make 500 μL of a 1 mM [Ca^{2+}] secondary solution for each sample to be run for matrix matched Me/Ca measurements on the ICP-MS. Each primary solution has been measured in 3 different analytical sessions between March and April of 2019. To better characterize the Me/Ca variability in the solid powder, it would be ideal to dissolve 1–2 more batches of powder samples and run replicate measurements on each batch. This has not been completed due to the time constraints when this thesis is written, This work is expected to be done in the near future.

The 1 mM [Ca^{2+}] secondary dilutions were measured on an Agilent 7500cx quadruple ICP-MS at Caltech. The isotopes collected for the samples were: ^{7}Li, ^{11}B, ^{23}Na, ^{24}Mg, ^{25}Mg, ^{27}Al, ^{43}Ca, ^{44}Ca, ^{48}Ca, ^{55}Mn, ^{57}Fe, ^{86}Sr, ^{87}Sr, ^{88}Sr, ^{111}Cd, ^{138}Ba, ^{146}Nd, ^{238}U. Multiple Mg, Ca and Sr isotopes were collected to check for isobaric interferences from doubly charged ions. Five samples were bracketed by two calibration standards and two blank 5% v/v HNO_3 solutions for accuracy calibrations. All isotopes were detected in pulse counting mode for the blank solution. For samples and standards, the Na, Mg, Ca and Sr isotopes were detected in analog mode. A NIST 8301c solution (currently under development and not yet certified) was provided by Joe Stewart and Russell Day for accuracy calibrations. It is a gravimetric standard developed for boron isotopes in biogenic carbonates, with multiple minor and trace elements added to mimic the composition of coral skeletons. The Me/Ca ratios have been measured across 7 different labs with their own calibration standards. It is most suitable for calibrating our samples due to their similarities in Me/Ca ratios. During each analytical session, two other standard solutions were inserted in the sample sequence as consistency standards: a surface coral standard (Jcp-1) and a deep-sea coral standard (SCCS). In each analytical session, four internal cycles were run on every blank, standard, and sample solution, where one cycle is a scan of the full list of isotopes. A 90 s rinse was applied between samples with a 5% v/v HNO_3 + 0.5% v/v HF solution. The sample solutions were

introduced into the instrument through a Teflon spray chamber with a sapphire injector to reduce boron blanks (as recommended by the STAiG lab at University of St. Andrews). This setup reduced the boron blank in freshly prepared HNO_3 solutions by almost an order of magnitude, but the boron blank still builds up during an analytical session most likely due to the volatile component of boron contamination in the lab, which I have not been able to solve yet. This blank component adds additional variability to the B/Ca measurements as detailed below.

5.3 Analytical Issues with ICP-MS Me/Ca Measurements

In the past two decades, multi-element ICP-MS methods have been developed in many different labs for Me/Ca ratio measurements in natural carbonates (Lea & Martin, 1996; Sinclair et al., 1998; Rosenthal et al., 1999; Inoue et al., 2004; Foster, 2008; Case et al., 2010; Anagnostou et al., 2011; Rae et al., 2011; Raddatz et al., 2013; Stewart et al., 2016). These methods have the advantage of quickly scanning through a large number of elements with a wide range of masses and concentrations. The precision of the measurements is generally limited by counting statistics, and can be easily improved by larger sample sizes or longer collection times. Accuracy calibration is a bigger problem due to the difficulty in making ideal standards that can be shared across labs, as well as different method setups in different labs. Systematic inter-laboratory studies have only been performed on a limited number of carbonate standards for minor elements such as Mg and Sr (Rosenthal et al., 2004; Hathorne et al., 2013), and large inconsistencies remain for the trace elements (e.g. Li, B, Ba, U) between different labs. During my thesis study, I have used a number of different trace element standards for calibration purposes in two different labs at Caltech and St. Andrews. Most notably, the STAiG lab at St. Andrews uses a foraminifera-like standard (BSGS) for routine calibrations, while I have used a coral-like solution (NIST 8301c) for calibrations at Caltech. There are systematic offsets in many Me/Ca ratios when calibrating samples with these two different standards. In this section, I try to break down how these differences may have occurred and discuss how we may improve inter-laboratory agreement for Me/Ca measurements in biogenic carbonates in the future.

5.3.1 Internal precision of ICP-MS Me/Ca measurements

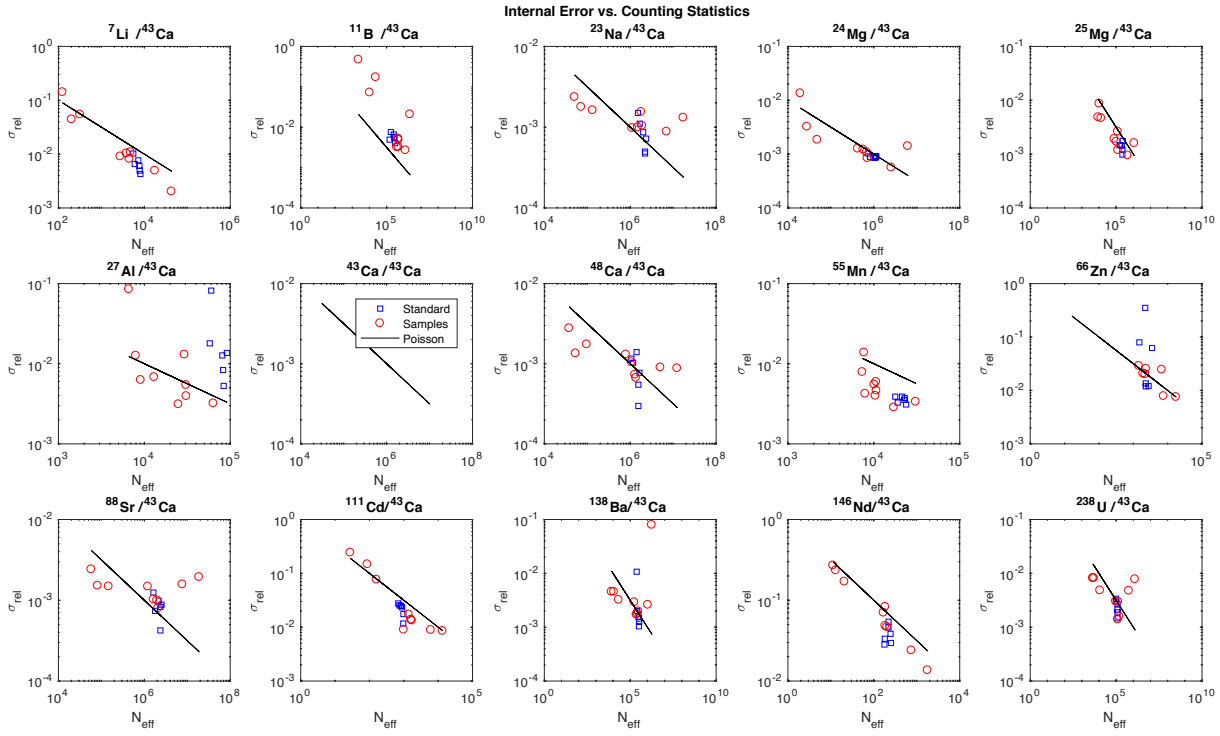

Figure 5-1 Internal errors of ICP-MS Me/Ca measurements compared with counting statistics in a serial dilution experiment. Each panel shows the internal relative standard errors of a ratio of an isotope to ^{43}Ca measured over 10 cycles, with a series of coral solutions at 0.06, 0.18, 0.55, 1, 1.66, 5 and 9 mM [Ca^{2+}] (red circles). A standard solution at 1 mM [Ca^{2+}] was also run during this experiment (blue squares). Counting statistics (or Poisson statistics) predicts a line of slope –1/2 on a log-log plot of relative standard error vs. effective counts (N_{eff}=$N_{Me}N_{Ca}$/(N_{Me}+N_{Ca})) (black lines).

In a study of iron isotope measurements in seawater, John & Adkins (2010) proposed three different schemes to account for internal errors in plasma mass spectrometry measurements: Johnson noise at low ion counts (errors scale with 1/N), counting statistics at intermediate ion counts (errors scale with $1/N^{0.5}$), and plasma flicker at high ion counts (errors constant and independent of counts). The multi-element method used for the corals here includes elements that span a concentration range of five orders of magnitude (10^{-2} for Sr, 10^{-7} for Cd and Nd), and all three schemes may occur for these elements. The best way to characterize this is a serial dilution experiment, in which the same solution was diluted to different concentrations for measurements under the same conditions. Figure 5-1 shows the relative internal errors of different Me/Ca ratios compared to the total effective counts collected for these serial dilutions. We see that most Me/Ca ratios follow the counting statistics trend over a 150× concentration range. A few ratios deviate

from the counting statistics predictions at high concentrations, including $^{23}Na/^{43}Ca$, $^{24}Mg/^{43}Ca$, $^{48}Ca/^{43}Ca$, $^{88}Sr/^{43}Ca$ and $^{238}U/^{43}Ca$. Other than ^{238}U, all other isotopes have signal intensities at 10^7–10^8 cps at high concentrations, which probably fall in the plasma flicker regime in terms of errors. In the low concentration range, a few elements are influenced by blank contaminations and deviate from the counting statistics prediction, including B, Al and Zn. B/Ca and Al/Ca ratios are most significantly influenced by blank contamination during an analytical session, with B/Ca errors always above counting statistics, while Al/Ca errors are above counting statistics in many cases. Overall, this method can generate data of permil precision for the minor elements and percent to sub-percent precision for different trace elements.

5.3.2 External reproducibility of ICP-MS Me/Ca measurements

Due to daily changes in blank contamination, sample processing and instrument conditions, external errors for Me/Ca ratios are expected to be equal to or larger than internal errors. A way to characterize this is to calculate the error-normalized deviates statistic (END), defined as the ratio of the external standard errors to the root mean square of the individual internal standard errors:

$$END = \frac{\sigma_{external}}{\sqrt{\frac{1}{n}\sum_{i=1}^{n}\sigma_i^2}}$$

Note that this definition is for any population of repeat measurements, and is different from the definition in John & Adkins (2010) that was only concerned with two replicates. An END value of 1 indicates that the external variability is well predicted by the internal errors of that sample population, indicating good reproducibility within multiple replicates of the same session or across different analytical sessions. Figure 5-2 shows the calibrated Me/Ca ratios during the 3 analytical sessions for the bulk *D.dianthus* samples, and Figure 5-3 shows histograms of END values for different Me/Ca ratios. We see that most Me/Ca ratios have an END mode around 1, suggesting good reproducibility across sessions that is mainly limited by counting statistics. The consistency standard SCCS has END values around 1 for most Me/Ca ratios, with similar intra-session and inter-session reproducibility. Some samples have END values higher than 1 probably due to chemical processing. A new 1 mM [Ca^{2+}] dilution was made from the primary solutions for each sample during each session. In comparison, a large batch of 1 mM [Ca^{2+}] solution was already

made for the consistency standard and can be poured directly into the autosampler vials for the measurements. The Me/Ca ratios that frequently have high END values are B/Ca, Mn/Ca, Fe/Ca and Al/Ca. All of these elements are very sensitive to blank contamination. B/Ca, Mn/Ca and Fe/Ca have END values that mostly range between 2–4. The END distributions for Mn/Ca and Fe/Ca are very similar, suggesting a common source of contamination. B/Ca has a couple of END values above 4, and the consistency standard has END values between 4 and 5. As mentioned earlier, the boron blank would build up from ~2000 cps to ~9000 cps during a 4-hour analytical session, which adds substantial variability to the measurements (changes in the boron blank are 20–30% of the count rate in samples). The ratio with the worst reproducibility is Al/Ca, which has high END values that are not seen in other ratios (Figure 5-3). It is suspected that the high variability in Al/Ca may come from the polypropylene autosampler vials used for the measurements, which likely contain Al blanks. Despite these external sources of variability, it seems that the other Me/Ca ratios are not significantly affected by the B, Al, Mn and Fe contaminants and can be interpreted as the real compositions of the coral skeletons.

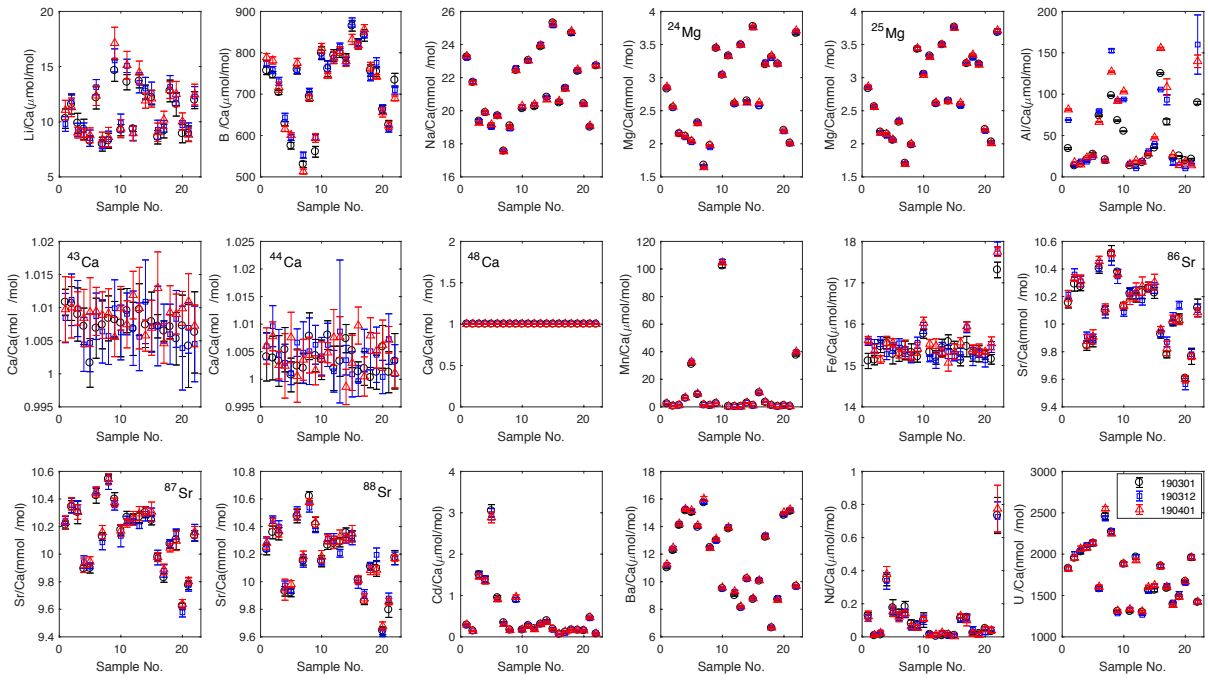

Figure 5-2 Reproducibility of Me/Ca ratios of 22 bulk *D.dianthus* samples across 3 sessions on 03/01/19 (black circles), 03/12/19 (blue squares) and 04/01/19 (red triangles). Each symbol is plotted with 2SE (internal) errors. The samples are numbered in the order listed in Table 5-1. All Me/Ca ratios are calculated with ^{48}Ca due to minimum interference from doubly charged Sr. The ratios are calibrated against the NIST 8301c standard.

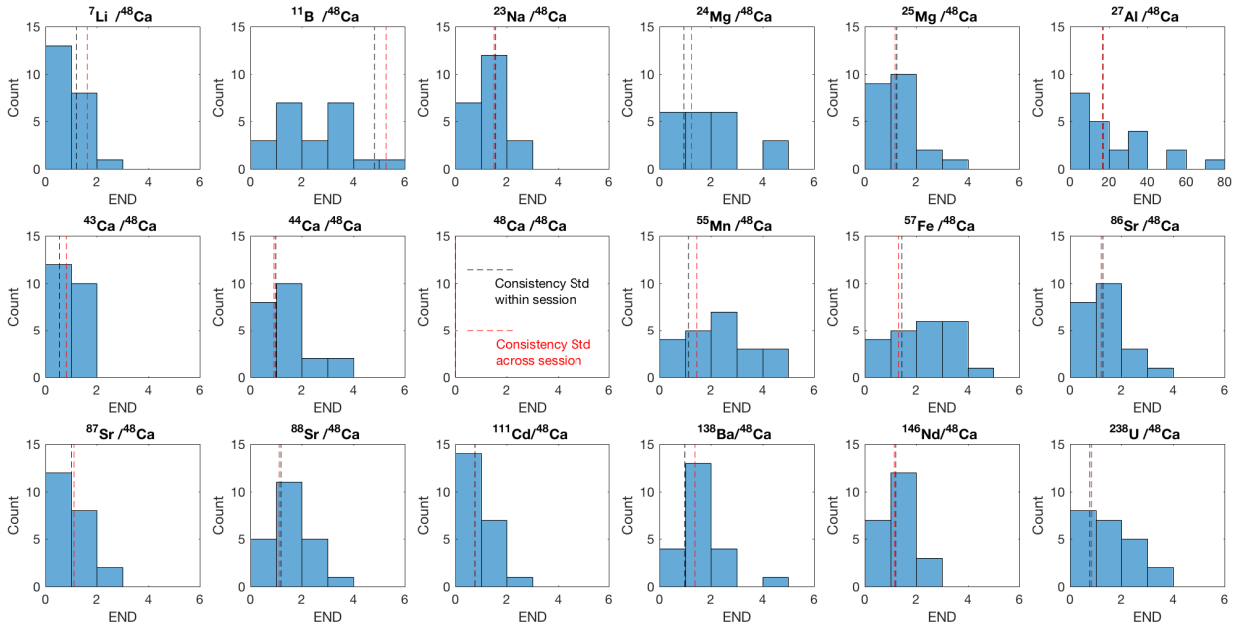

Figure 5-3 END histograms of Me/Ca ratios for the *D.dianthus* samples and consistency standard SCCS. The black dashed lines mark the average END for SCCS within 3 sessions (4 measurements of the same solution in a session, 4 cycles each), while the red dashed lines mark the END for SCCS across 3 sessions (12 measurements altogether). For most Me/Ca ratios the mode END is around 1. B/Ca, Al/Ca, Mn/Ca and Fe/Ca are the exceptions. B/Ca, Mn/Ca and Fe/Ca have END values that mainly spread between 2–4. Al/Ca has END values that are much higher than all other ratios and the x-axis is on a different scale.

5.3.3 Accuracy calibration between standards and laboratories

As mentioned earlier, systematic inter-laboratory calibrations of Me/Ca ratios has only been performed for a limited number of elements, and large inter-laboratory differences remain for a number of trace elements (Rosenthal et al., 2004; Hathorne et al., 2013). It is not always clear what caused these inconsistencies, given that the raw data of the Me/Ca measurements are rarely published. Since I have measured Me/Ca ratios with two different calibration standards on similar instruments in two different labs, it is possible to examine some details of the differences between the two labs.

One way to check the accuracy of Me/Ca calibrations with different standards is to measure two standards with known Me/Ca ratios against each other. Figure 5-4 shows the Me/Ca ratios measured in the NIST 8301c standard with BSGS as the bracketing calibration standard at St. Andrews and at Caltech. We see that most of the Me/Ca ratios agree within 2 standard errors for the two different labs, and are within the ranges of reported interlab values. The major exception is

B/Ca, in that the B/Ca ratios measured at Caltech deviate from the St. Andrews and interlab values, mainly due to the build-up of boron blanks during analysis. It should be noted that while most Me/Ca ratios scatter around the average interlab values, some are systematically biased toward one end of the interlab ranges, such as B/Ca and Sr/Ca (biased toward the low end). It is also noted that the $^{43}Ca/^{48}Ca$ ratio in NIST 8301c is higher than BSGS by ~2%. This is unlikely a Ca isotopic composition difference due to the magnitude of natural Ca isotope fractionations (up to a few ‰). It is most likely a signature of $^{86}Sr^{2+}$ interference on $^{43}Ca^{+}$. A measurement of a high-purity Sr solution from Inorganic Ventures (diluted to the same $[Sr^{2+}]$ as the coral standard, with $[Ca^{2+}]$ on the level of blanks) at Caltech shows a mass 43 peak that is 2.4% the intensity of the mass 86 peak, consistent with the magnitude of the relative changes in $^{43}Ca/^{48}Ca$ between the coral and foraminifera-like standards. Since the coral-like NIST standard has higher Sr/Ca ratios (8.1 mmol/mol) than the foraminifera-like BSGS standard (1.5 mmol/mol), it is more likely to be influenced by this doubly charged ion interference. As a result, I used ^{48}Ca as the isotope to normalize for the Me/Ca ratios instead of ^{43}Ca or ^{44}Ca in the measurements.

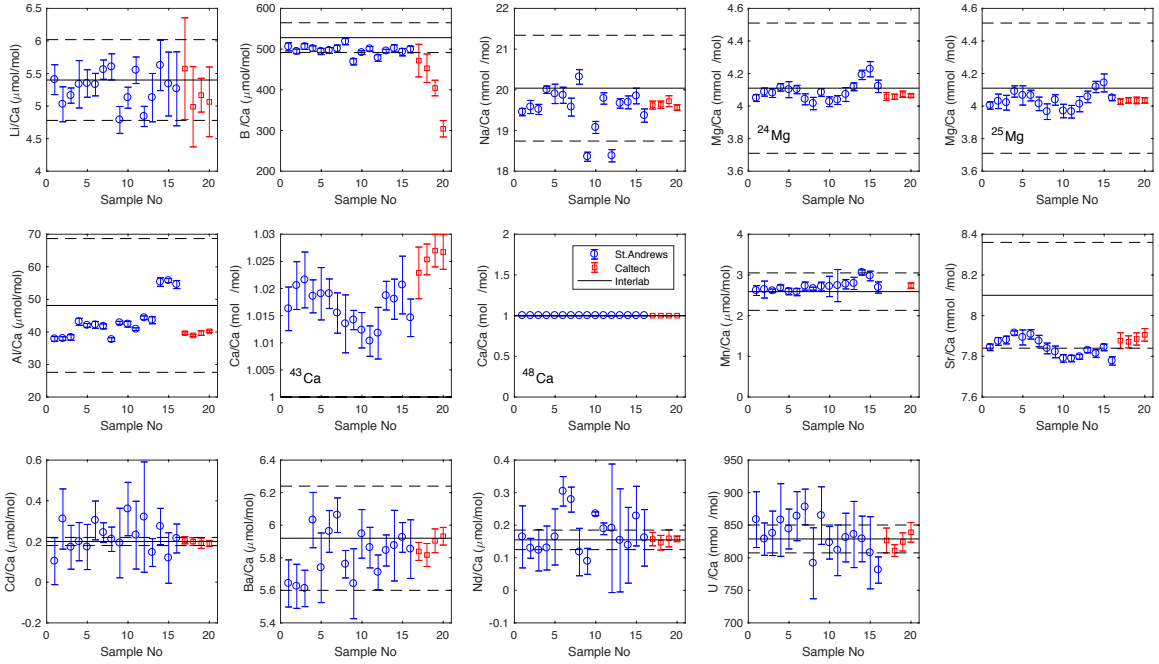

Figure 5-4 Me/Ca ratios of NIST 8301c standard calibrated by BSGS standard at St. Andrews (blue circles) and Caltech (red squares), compared to the interlab average values (black lines). The data points are plotted with 2SE internal error bars, and the dashed lines mark the 2σ ranges of interlab standard deviations (provided by Joe Stewart and James Rae). All Me/Ca ratios are normalized to ^{48}Ca during the calibration calculations. The ^{43}Ca panel shows the $^{43}Ca/^{48}Ca$ (actually mass 43/mass 48) measured in NIST 8301c relative to the BSGS standard.

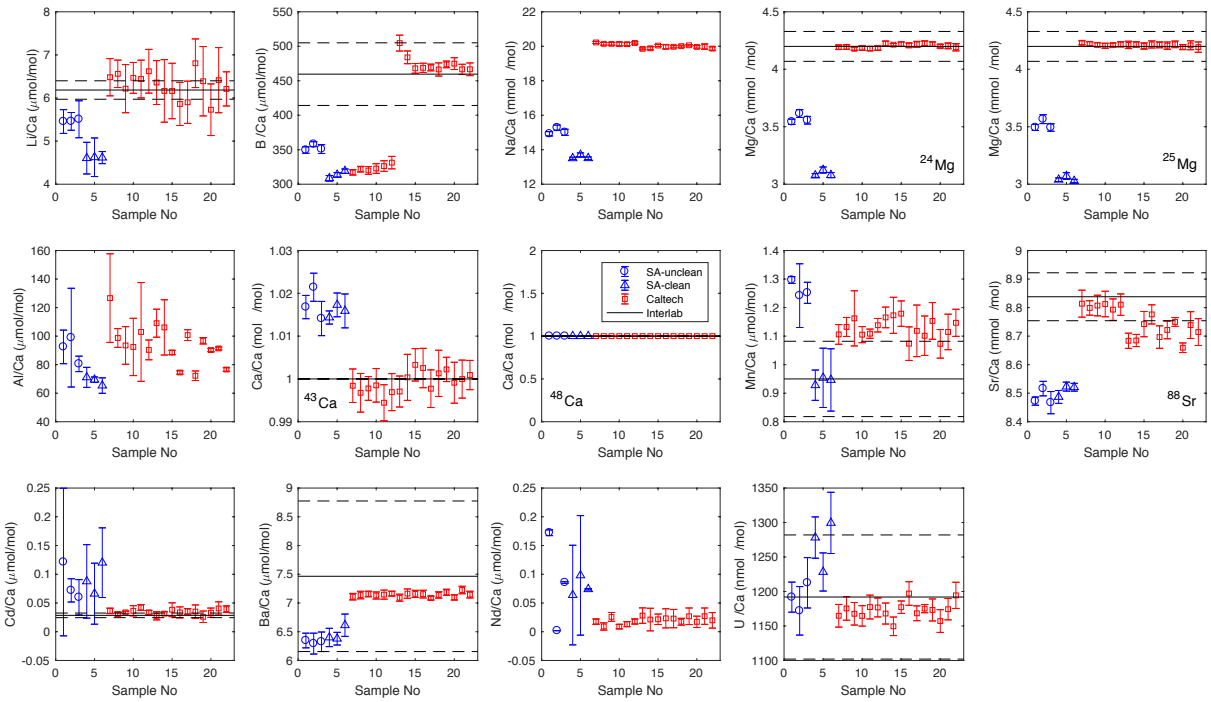

Figure 5-5 Me/Ca ratios of Jcp-1 standard (coral powder) calibrated by BSGS standard at St. Andrews (blue) and by NIST 8301c standard at Caltech (red squares), compared to values from the literature (black lines, Inoue et al., 2004; Hathorne et al., 2013). At St. Andrews, a cleaning test was done on Jcp-1 to evaluate how oxidative cleaning changes Me/Ca ratios. The blue circles represent the uncleaned samples while the blue triangles represent the cleaned samples. No cleaning was performed on the Caltech samples.

Figure 5-5 shows another example of possible calibration offset between St. Andrews and Caltech. The Jcp-1 coral powder standard was dissolved and measured in both labs, with BSGS as the calibration standard at St. Andrews, and NIST 8301c as the calibration standard at Caltech. We see that the Me/Ca ratios measured at Caltech are almost always closer to the average literature values, while the ratios measured at St. Andrews are biased toward low values for most elements, and are sensitive to the oxidative cleaning procedure. When we look at the relative change in $^{43}Ca/^{48}Ca$ ratios, we see that they scatter around 1 in the Caltech data when comparing NIST 8301c and Jcp-1, but is elevated to ~1.02 in the St. Andrews data when comparing Jcp-1 to BSGS. Since both NIST 8301c and Jcp-1 are coral standards, they have similar Sr/Ca ratios and thus similar doubly charged Sr interferences that cancel out when calibrated against each other. When using a foraminifera-like standard to calibrate a coral solution, there is a systematic offset introduced by

the doubly charged Sr interferences due to very different Sr/Ca ratios in the solutions. As a result, it would be ideal to use standard solutions that are as close in composition to the samples as possible to get accurate Me/Ca measurements in biogenic carbonates. In our case, we chose to use NIST 8301c as the accuracy standard to calibrate all the bulk deep-sea coral samples.

Table 5-2 Interlab Comparison of Trace Element Blanks and Sensitivity

Isotope	BSGS				NIST 8301C			
	St. Andrews		Caltech		St. Andrews		Caltech	
	Sensitivity[a]	S/N[b]	Sensitivity	S/N	Sensitivity	S/N	Sensitivity	S/N
^{7}Li	6.2E+03	43.7	4.3E+03	128	1.5E+03	10.6	8.8E+02	26.4
^{11}B[c]	8.9E+03	30.4	8.5E+03	15.0	5.0E+04	171	3.4E+04	60.4
^{23}Na[c]	5.2E+06	496	5.8E+06	360	1.2E+07	1119	1.1E+07	701
^{24}Mg	2.3E+06	4981	2.7E+06	41738	1.6E+06	3523	1.7E+06	25202
^{25}Mg	3.1E+05	2402	3.7E+05	26157	2.2E+05	1680	2.2E+05	15668
^{27}Al	2.8E+04	46.4	4.9E+04	1299	2.8E+04	46.8	3.6E+04	971
^{43}Ca	1.5E+06	3865	2.2E+06	32008	1.5E+06	3628	1.8E+06	26256
^{48}Ca	2.4E+06	3547	3.7E+06	38879	2.2E+06	3302	2.9E+06	31113
^{55}Mn	7.0E+04	201	1.4E+05	1167	3.1E+03	8.9	1.4E+04	117
^{88}Sr[c]	2.5E+06	25399	5.1E+06	10671	1.2E+07	122918	2.2E+07	45212
^{111}Cd	3.2E+01	0.5	9.6E+01	47.8	4.3E+01	0.7	1.1E+02	54.3
^{138}Ba	2.4E+03	42.9	8.7E+03	2615	1.1E+04	193	3.2E+04	9661
^{146}Nd	3.0E+03	62.0	1.1E+04	1823	8.6E+01	1.8	2.3E+02	39.1
^{238}U	5.4E+02	12.0	1.8E+03	650	2.8E+03	62.6	7.6E+03	2710

a. Sensitivity here is the counting rate (CPS) for a 1 mM [Ca^{2+}] solution.
b. S/N stands for signal-to-noise ratio. The signal is the counting rate of the 1 mM [Ca^{2+}] solution, while the noise is the typical variability in counting rates of blanks in a session.
c. For the shaded rows, the signal-to-noise ratio is better at St. Andrews than at Caltech. For all other rows, the signal-to-noise ratio is better at Caltech than at St. Andrews.

In addition to the calibration standard used, two other possible causes for a calibration offset between different labs are blank contamination and instrument sensitivity. Table 5-2 lists the typical counting rate of 1 mM [Ca^{2+}] standard solutions at St. Andrews and at Caltech. We see that with a few exceptions (^{11}B, ^{23}Na, ^{24}Mg, ^{25}Mg), the isotopes measured have very different sensitivities for the same 1 mM [Ca^{2+}] solution on the two different instruments at Caltech and at St. Andrews. The Agilent 7500cx at Caltech has higher sensitivities than the Agilent 7500a at St. Andrews for most isotopes, by ~20% and up to a factor of 4 in some cases. Only the ^{7}Li sensitivity is higher at St. Andrews by ~50%. It was also found that the sensitivities for different elements generally change by a few percent for concentration changes that are over an order of magnitude, causing small non-linearities in the calibrations in both labs. In addition to sensitivity, the

calibrated Me/Ca ratios are also influenced by the contribution from blank contamination. A high and variable blank will significantly impact the accuracy and precision of Me/Ca measurements. When we compare the variability in blank intensities relative to the signal intensities from the 1 mM [Ca^{2+}] solutions, we see that the signal to noise ratios at Caltech are higher for most isotopes, especially the high mass elements ^{111}Cd, ^{138}Ba, ^{146}Nd and ^{238}U. This is due to the ~10 times lower blanks for these elements at Caltech than at St. Andrews. We see in Figure 5-4 and 5-5 that the error bars for Cd/Ca, Ba/Ca, Nd/Ca and U/Ca are much smaller at Caltech. The St. Andrews lab, which specializes in boron isotope measurements, has lower and less variable boron blanks, and thus higher signal-to-noise ratios for this element. These differences in sensitivities and signal-to-noise ratios, plus very different Me/Ca ratios in the two calibration standards, are important contributors to the offsets observed for the Jcp-1 measurements at Caltech and at St. Andrews. The bulk deep-sea coral data presented in this chapter were all measured at Caltech with the coral-like calibration standard NIST 8301c, which should have minimized the impact of the analytical issues listed above. It is suggested that standard solutions with similar Me/Ca ratios (ideally within an order of magnitude) to the samples is best for accurate Me/Ca measurements in biogenic carbonates. It is also important to understand the effects of blanks and instrument sensitivities when comparing Me/Ca data collected in different labs.

5.4 Empirical Tracer Calibrations in *D.dianthus*

The measured Me/Ca and stable isotope data in the bulk *D.dianthus* samples are listed in Table 5-3. This section presents observed empirical correlations between the Me/Ca ratios and environmental conditions (mainly temperature and carbonate chemistry of the ambient seawater) in the context of previous tracer calibration work in deep-sea corals. Despite significant scatter, some Me/Ca ratios do have strong correlations with the environmental conditions. The next section discusses potential imprints of vital effects that could give rise to the scatter in the tracer calibrations.

Table 5-3 Me/Ca Ratios of Bulk *D.dianthus* Powder

Coral	Li/Ca (µmol/mol)	Err Li/Ca (µmol/mol)	B/Ca (µmol/mol)	Err B/Ca (µmol/mol)	Na/Ca (mmol/mol)	Err Na/Ca (mmol/mol)
19249	10.38	0.37	773.2	9.3	23.24	0.03
Big Beauty	11.57	0.15	762.3	10.2	21.72	0.02
47409	9.38	0.25	717.4	7.8	19.34	0.04
Leda-b	9.13	0.15	629.4	8.0	19.89	0.01
Leda-t	8.50	0.16	590.6	7.9	19.07	0.05
47396	12.55	0.30	763.9	5.9	19.70	0.01
Gaia	8.10	0.13	531.8	11.5	17.55	0.01
83583	8.43	0.10	696.7	4.5	19.01	0.05
82065	15.78	0.73	583.3	11.3	22.49	0.05
94071	9.50	0.20	800.9	5.5	20.21	0.05
47407	14.59	0.50	757.7	6.8	23.03	0.00
84820	9.08	0.13	790.1	1.8	20.33	0.05
62309	13.88	0.29	806.3	4.5	23.94	0.04
47394	12.54	0.33	782.5	3.2	20.76	0.05
53377	12.29	0.16	856.9	12.4	25.23	0.05
48744	8.97	0.20	821.0	1.6	20.53	0.03
80404	9.64	0.30	847.7	4.6	21.36	0.03
80358	12.93	0.11	755.0	7.3	24.74	0.03
47413	12.04	0.27	757.3	9.9	22.43	0.03
Titan-b	9.54	0.33	661.2	2.8	20.41	0.01
Titan-t	9.02	0.15	621.6	3.0	19.05	0.03
97275	12.24	0.15	711.2	12.8	22.73	0.01

Table 5-3 Me/Ca Ratios of Bulk *D.dianthus* Powder (continued)

Coral	Mg/Ca (mmol/mol)	Err Mg/Ca (mmol/mol)	Al/Ca (µmol/mol)	Err Al/Ca (µmol/mol)	Mn/Ca (µmol/mol)	Err Mn/Ca (µmol/mol)
19249	2.850	0.009	61.4	14.1	2.35	0.10
Big Beauty	2.557	0.001	15.0	1.3	0.55	0.03
47409	2.169	0.004	16.4	1.2	1.12	0.01
Leda-b	2.137	0.009	20.7	1.4	6.45	0.13
Leda-t	2.056	0.003	25.7	0.9	32.11	0.67
47396	2.339	0.008	73.3	3.8	9.26	0.19
Gaia	1.698	0.003	19.8	0.5	1.41	0.03
83583	1.987	0.004	125.9	15.7	0.95	0.03
82065	3.437	0.005	83.9	8.0	2.51	0.06
94071	3.050	0.009	83.9	14.7	104.13	1.03
47407	3.320	0.005	15.0	0.8	0.29	0.01
84820	2.611	0.005	15.1	2.7	0.20	0.03
62309	3.499	0.003	18.2	0.6	0.18	0.00
47394	2.649	0.007	28.4	1.5	2.84	0.05
53377	3.759	0.004	40.7	3.6	0.97	0.01
48744	2.589	0.015	128.7	14.6	10.32	0.12
80404	3.216	0.003	89.4	12.3	3.36	0.06
80358	3.319	0.013	22.3	2.7	1.04	0.01
47413	3.202	0.004	17.8	3.7	0.23	0.01
Titan-b	2.206	0.007	16.0	2.9	0.91	0.01
Titan-t	2.014	0.006	17.0	2.2	0.36	0.04
97275	3.697	0.009	129.7	20.9	39.06	0.80

Table 5-3 Me/Ca Ratios of Bulk *D.dianthus* Powder (continued)

Coral	Sr/Ca (mmol/mol)	Err Sr/Ca (mmol/mol)	Cd/Ca (µmol/mol)	Err Cd/Ca (µmol/mol)	Ba/Ca (µmol/mol)	Err Ba/Ca (µmol/mol)
19249	10.262	0.014	0.285	0.005	11.15	0.08
Big Beauty	10.410	0.027	0.141	0.002	12.38	0.06
47409	10.371	0.016	1.483	0.014	14.17	0.05
Leda-b	9.948	0.013	1.376	0.014	15.23	0.05
Leda-t	9.947	0.019	2.966	0.046	15.11	0.05
47396	10.486	0.006	0.919	0.013	14.02	0.04
Gaia	10.161	0.011	0.320	0.010	15.84	0.08
83583	10.579	0.023	0.161	0.004	12.45	0.01
82065	10.407	0.018	0.921	0.020	13.01	0.05
94071	10.158	0.012	0.171	0.003	9.52	0.03
47407	10.295	0.015	0.272	0.006	13.91	0.04
84820	10.292	0.011	0.192	0.006	9.19	0.10
62309	10.273	0.035	0.304	0.001	8.15	0.03
47394	10.329	0.013	0.367	0.011	10.21	0.02
53377	10.333	0.009	0.180	0.005	8.76	0.02
48744	10.007	0.006	0.066	0.003	10.09	0.03
80404	9.882	0.016	0.110	0.008	13.29	0.04
80358	10.102	0.009	0.166	0.002	6.66	0.01
47413	10.126	0.035	0.159	0.000	8.73	0.05
Titan-b	9.650	0.007	0.154	0.003	14.91	0.06
Titan-t	9.843	0.006	0.460	0.006	15.18	0.04
97275	10.172	0.009	0.078	0.004	9.66	0.02

Table 5-3 Me/Ca Ratios of Bulk *D.dianthus* Powder (continued)

Coral	Nd/Ca (µmol/mol)	Err Nd/Ca (µmol/mol)	U/Ca (µmol/mol)	Err U/Ca (µmol/mol)	$\delta^{18}O$ (‰, VPDB)	$\delta^{13}C$ (‰, VPDB)
19249	0.122	0.004	1.825	0.001	1.08±0.15	–4.82±0.20
Big Beauty	0.010	0.002	1.969	0.017	2.41±0.36	–2.97±0.23
47409	0.020	0.005	2.047	0.011	2.59±0.20	–2.72±0.24
Leda-b	0.354	0.013	2.089	0.010	2.83±0.07	–3.27±0.10
Leda-t	0.162	0.006	2.134	0.003	2.98±0.01	–2.77±0.11
47396	0.129	0.007	1.589	0.008	2.80±0.06	–7.00±0.10
Gaia	0.155	0.013	2.480	0.036	3.50±0.20	–1.35±0.25
83583	0.066	0.007	2.263	0.008	2.06±0.14	–3.40±0.29
82065	0.065	0.006	1.302	0.010	–0.11	–7.15
94071	0.104	0.002	1.880	0.002	1.85±0.18	–1.25±0.00
47407	0.013	0.003	1.324	0.009	0.24	–7.69
84820	0.008	0.003	1.951	0.014	1.30±0.05	–3.75±0.02
62309	0.019	0.006	1.290	0.012	–0.35±0.09	–8.03±0.25
47394	0.010	0.003	1.573	0.014	1.69±0.34	–3.77±0.74
53377	0.006	0.002	1.601	0.019	1.10±0.36	–3.81±0.84
48744	0.113	0.007	1.853	0.002	2.48±0.29	–0.06±0.41
80404	0.110	0.006	1.602	0.009	1.08±0.04	–4.06±0.12
80358	0.029	0.007	1.397	0.010	–0.30±0.01	–6.29±0.34
47413	0.014	0.003	1.495	0.012	0.56±0.45	–6.53±0.84
Titan-b	0.042	0.007	1.662	0.006	1.04±0.26	–6.27±0.76
Titan-t	0.038	0.004	1.961	0.004	2.33±0.35	–4.40±0.70
97275	0.744	0.015	1.421	0.002	0.70±0.11	–5.96±0.41

Note: The Me/Ca errors are 1SE of 3 replicate measurements in 3 different sessions. The stable isotope uncertainties are 1σ standard deviations of 3 aliquots of the bulk powder.

5.4.1 Thermometers

For the last several decades, the chemical and isotopic compositions of coral skeletons have been found to record the temperature of seawater at high temporal resolution. The thermometers that have been developed in coral skeletons include oxygen isotopes (Weber & Woodhead, 1972; Fairbanks & Dodge, 1979; McConnaughey, 1989; Cobb et al., 2003), clumped isotopes (Thiagarajan et al., 2011; Saenger et al., 2012; Spooner et al., 2016), Sr/Ca (Beck et al., 1992; Alibert & McCulloch, 1997; Correge, 2006) and Mg/Ca (Sinclair et al., 1998; Fallon et al., 1999; Reynaud et al., 2007). All these thermometers are to certain degrees subjected to vital effects (McConnaughey et al., 1989; Cohen et al., 2002; Correge et al., 2006; Reynaud et al., 2007; Gagnon et al., 2007; Saenger et al., 2012; Spooner et al., 2016). More recently different approaches have been proposed to account for the vital effects in Me/Ca thermometers based on their correlations. These include the Li/Mg thermometer (Bryan & Marchitto, 2008; Case et al., 2010; Raddatz et al., 2013; Montagna et al., 2014; Marchitto et al., 2018), the Sr-U thermometer (DeCarlo et al., 2016) and a Rayleigh based multi-element (Mg, Sr, Ba) thermometer (Gaetani et al., 2011). Of these, the Li/Mg thermometer has been calibrated over a relatively wide temperature range in deep-sea corals and is emerging as a promising paleo-temperature proxy that has minimum impact from vital effects (Case et al., 2010; Raddatz et al., 2013; Montagna et al., 2014; Rollion-Bard & Blamart, 2015).

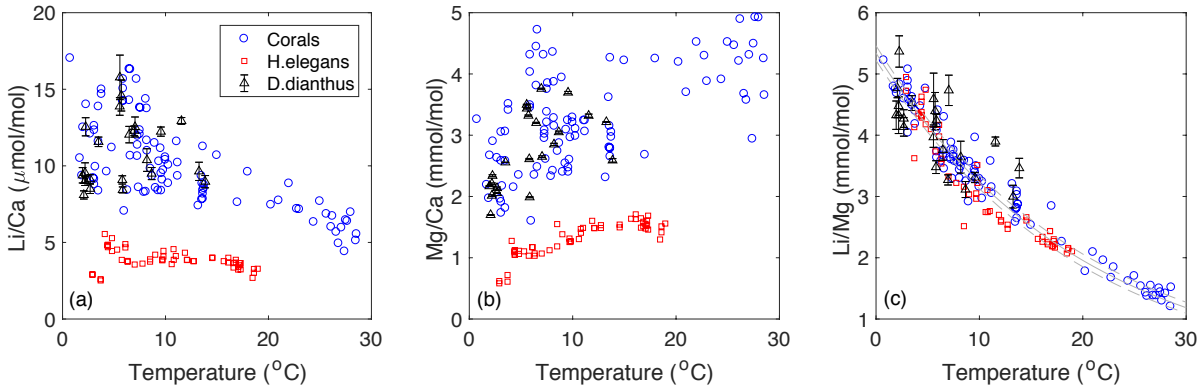

Figure 5-6 Relations between temperature and (a) Li/Ca, (b) Mg/Ca, (c) Li/Mg of bulk *D.dianthus* samples in this study (black triangles) compared to data compiled by Marchitto et al. (2018) for different coral species (blue circles) and the aragonitic foraminifera *H.elegans* (red squares). The solid gray line in panel (c) shows the calibration equation proposed by Marchitto et al. (2018) with the dashed lines showing 2σ uncertainties. Error bars on the *D.dianthus* data are 2SE of 3 replicate measurements.

Figure 5-6 shows the relationship between Li/Ca, Mg/Ca and Li/Mg of the *D.dianthus* bulk samples in this study compared to the dataset compiled by Marchitto et al. (2018). We see that both Li/Ca and Mg/Ca in *D.dianthus* show highly scattered correlations with temperature, with ranges of scatter very similar to other coral species. For Li/Mg ratios, however, most *D.dianthus* data points fall within the range of the Li/Mg-temperature relation defined by the Marchitto et al. (2018) dataset. It is noted that four *D.dianthus* data points in this study, plus a few coral data points from the Marchitto et al. (2018) compilation, sit above the 2σ range of the proposed Li/Mg-temperature relation, which is more common than points that fall below the 2σ range. There is no diagnostic feature (e.g. sampling method, location, other Me/Ca ratios) that is shared by all four *D.dianthus* individuals with higher than expected Li/Mg in this study, suggesting that these high Li/Mg ratios reflect influence from individual biomineralization processes. Other than these anomalously high Li/Mg points, the Li/Mg-temperature relation in *D.dianthus* is consistent with the one defined by *H.elegans* and other corals, strongly suggesting a universal rule for the coupled incorporation of Li and Mg in biogenic aragonite.

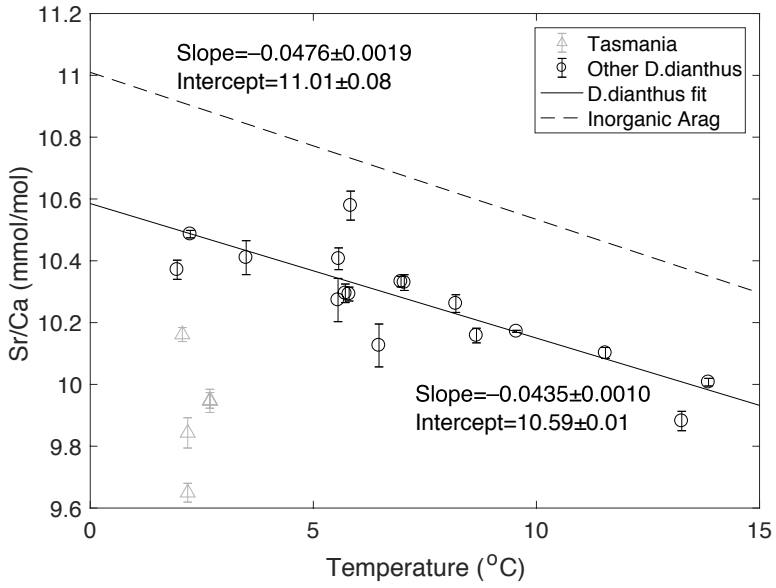

Figure 5-7 Sr/Ca of bulk *D.dianthus* samples vs. temperature compared to inorganic aragonite. The triangles represent 5 corals collected on cruise TN228 from south of Tasmania, which do not share the same trend as the other corals. The other corals define a Sr/Ca-temperature calibration that is very similar in temperature sensitivity to the expected Sr/Ca of inorganic aragonite precipitation from seawater assuming seawater Sr/Ca of 8.6 mmol/mol. The inorganic D_{Sr} are compiled from Kinsman & Holland (1969), Dietzel et al. (2004) and Gaetani & Cohen (2006).

In addition to Li/Mg, Sr/Ca is the most widely studied and used thermometer in corals. Sr/Ca-temperature calibrations have been developed in many surface coral species. Although Sr/Ca in different surface coral species all decrease with temperature, the slope and intercept of the calibrations can vary between species, or even vary in the same species at different locations (Correge, 2006). Cohen et al. (2002) found that the temperature sensitivity of Sr/Ca can increase by more than a factor of 2 with photosymbiotic activity in the coral *Astrangia poculata*, compared to the same species without photosymbiotic activity. The non-symbiotic specimens had Sr/Ca variability with the same temperature sensitivity as inorganic aragonite. From a biomineralization perspective, this suggests that photosymbionts can cause drastic changes in the calcification dynamics of the corals and thus the utilization efficiency of Ca^{2+} (and other co-precipitating cations such as Sr^{2+}) in the ECF. The temperature sensitivity of Sr/Ca in inorganic aragonite (–0.0476 mmol/mol per °C, Figure 5-7) is at the lower end of temperature sensitivities observed in surface corals (Correge, 2006). Sr/Ca-temperature calibrations in deep-sea corals are much more limited compared to surface corals, with a few studies showing a scattered relation with temperature for *Lophelia pertusa* and a few other species (Raddatz et al., 2013; Martin et al., 2016). It is expected that the Sr/Ca in deep-sea corals should have a temperature sensitivity close to that of inorganic aragonite given a lack of photosymbionts, if it works as a thermometer like surface corals. The Sr/Ca-temperature calibration for *D.dianthus* is shown in Figure 5-7. We see that most corals fall on a relatively tight Sr/Ca-temperature correlation with a temperature sensitivity that is indistinguishable from inorganic aragonite, although the intercept of the *D.dianthus* calibration is lower than inorganic aragonite by 0.4 mmol/mol.

As discussed in Chapter 3 and 4, Sr/Ca ratios always decreases with an increasing alkalinity pump rate because D_{Sr} in aragonite is larger than 1. The offset in Sr/Ca intercept may thus reflect the average pump rate of the bulk samples. It is noted that a group of points deviate from the Sr/Ca-temperature calibration defined by other corals at the low temperature end. These five corals (Leda-top and bottom, Gaia, Titan-top and bottom) were collected between 1460–2395 m depth south of Tasmania, and were bathed in deep, cold and undersaturated seawater. There are two possibilities for their low Sr/Ca values. The first one is preservation, since the skeletons of these corals likely dissolved in the undersaturated seawater and the high-Sr phase of the skeleton may dissolve preferentially. Of the five individuals, Titan-top and Titan-bottom have the lowest

Sr/Ca, and also have significant brown and black coating on the surface, suggesting that they may actually be fossil corals that have gone through post-mortem dissolution. Leda and Gaia, however, were collected with tissues remaining on the skeletons, and have relatively fresh surfaces. Although partial dissolution while the corals were alive cannot be ruled out, there is a second possibility that this is a result of a change in the biomineralization strategy by these corals living under significant environmental stress. It was observed in Chapter 3 and 4 that the Mg/Ca-Sr/Ca slopes tend to be steeper in corals from undersaturated environment, which can be explained by an increase in the fraction of Ca^{2+} in the alkalinity pump. The Sr/Ca of the five Tasmania corals at the same temperature are positively correlated with their $\delta^{18}O$ values (see Figure 5-19d), also suggesting the range in Sr/Ca in these corals is modulated by the strength of the alkalinity pump, as previously suggested in culture studies of surface corals (Cohen et al., 2009; Gagnon et al., 2013).

5.4.2 Carbonate ion proxies

In the past two decades, a few Me/Ca ratios have been developed as proxies for $[CO_3^{2-}]$ in biogenic carbonates to reconstruct the carbonate chemistry of the ocean in the past. The most widely studied and used $[CO_3^{2-}]$ proxy is B/Ca, which has been empirically calibrated in different foraminifera species (Yu & Elderfield, 2007; Yu et al., 2010; Rae et al., 2011; Allen et al., 2012). This proxy is based on the pH dependent speciation of both the DIC and boron pools, and the preferential incorporation of borate ions into the mineral lattice for carbonate ions. This idea predicts that the B/Ca of the biogenic carbonates should scale with $[B(OH)_4^-]/DIC_X$ in the ambient seawater, where DIC_X could be total DIC, $[HCO_3^-]$ or $[CO_3^{2-}]$ depending on the partition rule assumed. Yu & Elderfield (2007) chose the $[B(OH)_4^-]/[HCO_3^-]$ rule because HCO_3^- is the dominant DIC species. With this rule, they determined distribution coefficients for boron (D_B) that range between 0.001 and 0.01 for different benthic foraminifera species. The mechanism for D_B variations among different species is still poorly understood, but Yu & Elderfield (2007) found that D_B values (and thus also B/Ca ratios due to small variations in $[B(OH)_4^-]/[HCO_3^-]$) have a linear correlation with $\Delta[CO_3^{2-}]$ ($\Delta[CO_3^{2-}]=[CO_3^{2-}]_{in\text{-}situ} - [CO_3^{2-}]_{saturation}$) for different species. The calibration has since been expanded to other benthic as well as planktonic foraminifera species (Rae et al., 2011; Allen et al., 2012). B/Ca in corals is less well understood and calibrated than in foraminifera, although it has been used to infer $[CO_3^{2-}]$ in the ECF of surface corals based on assumed D_B values from inorganic aragonite experiments (Allison et al., 2014; McCulloch et al.,

2017; Ross et al., 2017). It is important to test if B/Ca in corals is indeed sensitive to $[CO_3^{2-}]$ in the ambient seawater, and the deep-sea corals that span a wide range of $[CO_3^{2-}]$ from undersaturation to supersaturation provide a good test to this hypothesis. Figure 5-8 shows the bulk *D.dianthus* B/Ca calibration against $[CO_3^{2-}]$ and $\Delta[CO_3^{2-}]$. We see that the relations are scattered, but statistically significant. The correlation between B/Ca and $\Delta[CO_3^{2-}]$ is stronger than $[CO_3^{2-}]$. A significant source of the scatter is the corals from undersaturated conditions ($\Delta[CO_3^{2-}]<0$). In general, these corals in general have lower B/Ca ratios than those from supersaturated seawater, but their B/Ca ratios can range from 500–750 μmol/mol without much change in $\Delta[CO_3^{2-}]$. This behavior is similar to the range in Sr/Ca without a significant change in temperature seen in the Tasmania corals (Figure 5-7). It is suspected that this reflects a change in the biomineralization scheme for these corals living under stress of corrosive seawater, which is also implied by the B/Ca-$\delta^{18}O$ correlation (Figure 5-19b). Finally, it is noted that the slope of the B/Ca-$\Delta[CO_3^{2-}]$ regression (1.22) in *D.dianthus* is larger than the aragonitic foraminifera *H.elegans* (0.51, Yu & Elderfield, 2007), but on the same order of magnitude as different benthic foraminifera species (0.27–1.14, Yu & Elderfield, 2007).

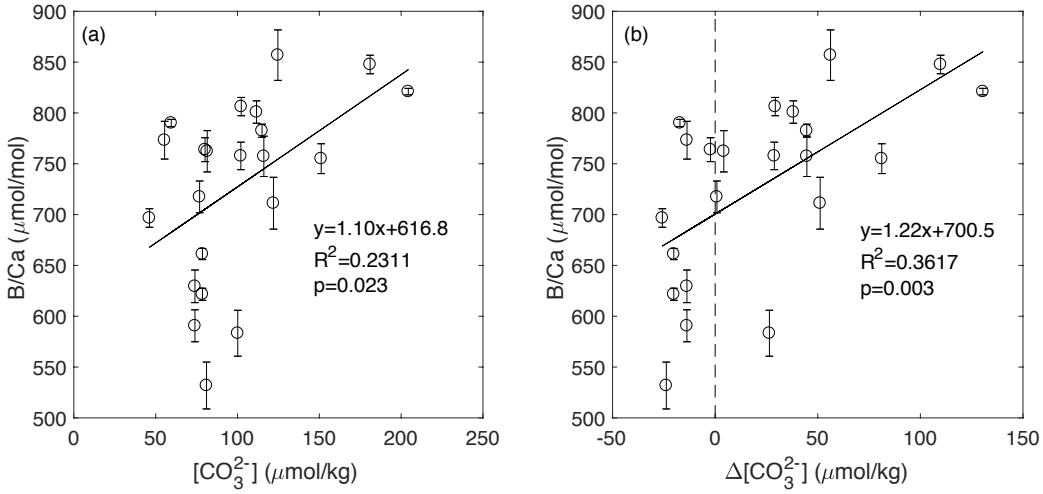

Figure 5-8 B/Ca of bulk *D.dianthus* samples (2σ external standard errors) vs. (a) $[CO_3^{2-}]$ and (b) $\Delta[CO_3^{2-}]$ of ambient seawater, with least squares linear fits to the data. The correlations are scattered, but statistically significant. The correlation is stronger for $\Delta[CO_3^{2-}]$ than $[CO_3^{2-}]$. Data points at negative $\Delta[CO_3^{2-}]$ are major contributors to the scatter.

In addition to B/Ca, U/Ca in deep-sea corals has also been proposed as a proxy for $[CO_3^{2-}]$ or pH of the ambient seawater (Anagnostou et al., 2011; Raddatz et al., 2014). U/Ca was observed to have a strong negative correlation with $[CO_3^{2-}]$ in foraminifera (Russell et al., 2004; Raitzsch et

al., 2011; Allen et al., 2016) and corals (Anagnostou et al., 2011; Raddatz et al., 2014). U exists mainly as UO_2^{2+} in seawater, which binds with different numbers of CO_3^{2-} to form a series of $UO_2(CO_3)_n$ complexes that can be incorporated into $CaCO_3$ lattices. The speciation of $UO_2(CO_3)_n$ is pH dependent, with the number of CO_3^{2-} (n) increasing at higher pH (Djogić et al., 1986; Djogić & Branica, 1991). X-ray absorption spectroscopic data show that the dominant form of U in aragonite is $UO_2(CO_3)_3^{4-}$ (which is also the dominant aqueous species at typical seawater pH of 8), while multiple species were found in calcite leading to a more disordered bonding environment (Reeder et al., 2000; Reeder et al., 2001). The U/Ca depletion with ambient $[CO_3^{2-}]$ in corals may reflect a competition for sites on the mineral surface between CO_3^{2-} and $UO_2(CO_3)_3^{4-}$ (Langmuir, 1978; Anagnostou et al., 2011). It is unlikely a growth rate effect because the U distribution coefficient was found to increase with growth rate in inorganic aragonite experiments (Gabitov et al., 2006). Figure 5-9 shows the *D.dianthus* U/Ca-$[CO_3^{2-}]$ calibration. With a few exceptions at high $[CO_3^{2-}]$ (corals from Mediterranean Sea), my bulk data are consistent with previous studies. There is no significant change (slightly worse) in the fit when using $\Delta[CO_3^{2-}]$ instead of $[CO_3^{2-}]$. The data points that deviate from the trend at high $[CO_3^{2-}]$ may reflect a saturation of the U/Ca sensitivity to $[CO_3^{2-}]$, or a different amount of vital effects for these corals with the least environmental stress.

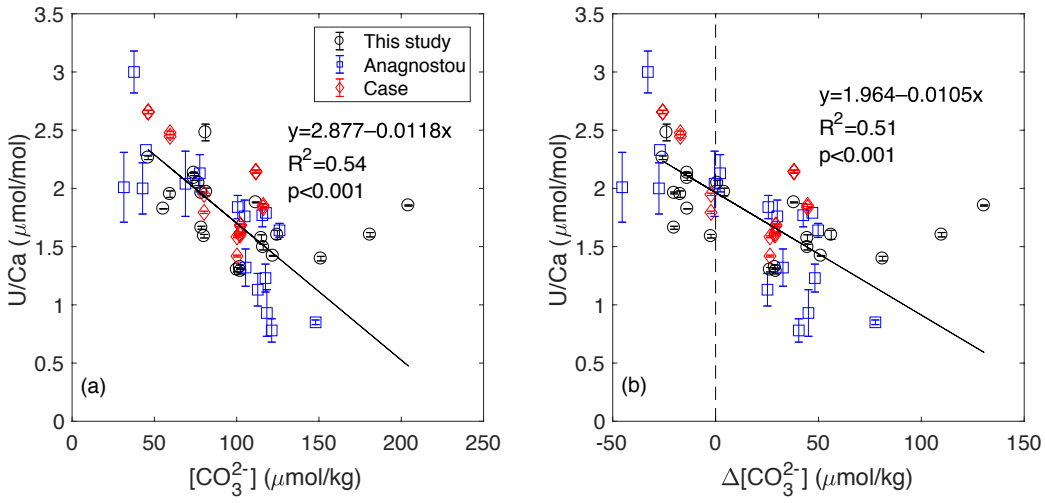

Figure 5-9 U/Ca of bulk *D.dianthus* samples (2SE external errors bars) vs. (a) $[CO_3^{2-}]$ and (b) $\Delta[CO_3^{2-}]$ of ambient seawater, with least squares linear fits to the data. The black circles are bulk *D.dianthus* data from this study. The blue squares are laser ablation ICP-MS data from Anagnostou et al. (2011). The red diamonds are unpublished data from David Case with isotope dilution ICP-MS measurements. The two data points at highest $[CO_3^{2-}]$ deviate from the trend defined by other points, and are not included in the regression. These two corals are from the Mediterranean Sea.

Besides B/Ca and U/Ca, many other Me/Ca ratios in biogenic carbonates have been found to be sensitive to the saturation state ($\Delta[CO_3^{2-}]$) of ambient seawater, especially in the range around the saturation threshold ($\Delta[CO_3^{2-}]=0$). The most well known example is probably Mg/Ca in benthic foraminifera (Elderfield et al., 2006; Bryan & Marchitto, 2008; Lear et al., 2010), which is an important bottom water thermometer in paleoceanography. The other $\Delta[CO_3^{2-}]$ sensitive Me/Ca ratios include Cd/Ca (McCorkle et al., 1995), Zn/Ca (Marchitto et al., 2000), Sr/Ca (Rosenthal et al., 2006; Cohen et al., 2009; Gagnon et al., 2013) and Li/Ca (Lear & Rosenthal, 2006; Lear et al., 2010). Two mechanisms may be responsible for the $\Delta[CO_3^{2-}]$ sensitivity of these Me/Ca ratios: a partial dissolution effect (high Me/Ca phase dissolves preferentially in undersaturated water) and a biomineralization effect. In addition, bottom water temperature and $\Delta[CO_3^{2-}]$ are almost always strongly correlated and hard to be deconvolved from each other, so the $\Delta[CO_3^{2-}]$ sensitivity of Me/Ca may actually be related to the temperature effect. The evidence for the biomineralization effect on the Me/Ca sensitivity to $\Delta[CO_3^{2-}]$ is supported by the observation that live and dead benthic foraminifera from the same core have identical Li/Ca and Mg/Ca ratios (Rosenthal et al., 2006; Lear & Rosenthal, 2006). The exact biomineralization mechanism, however, is still poorly understood.

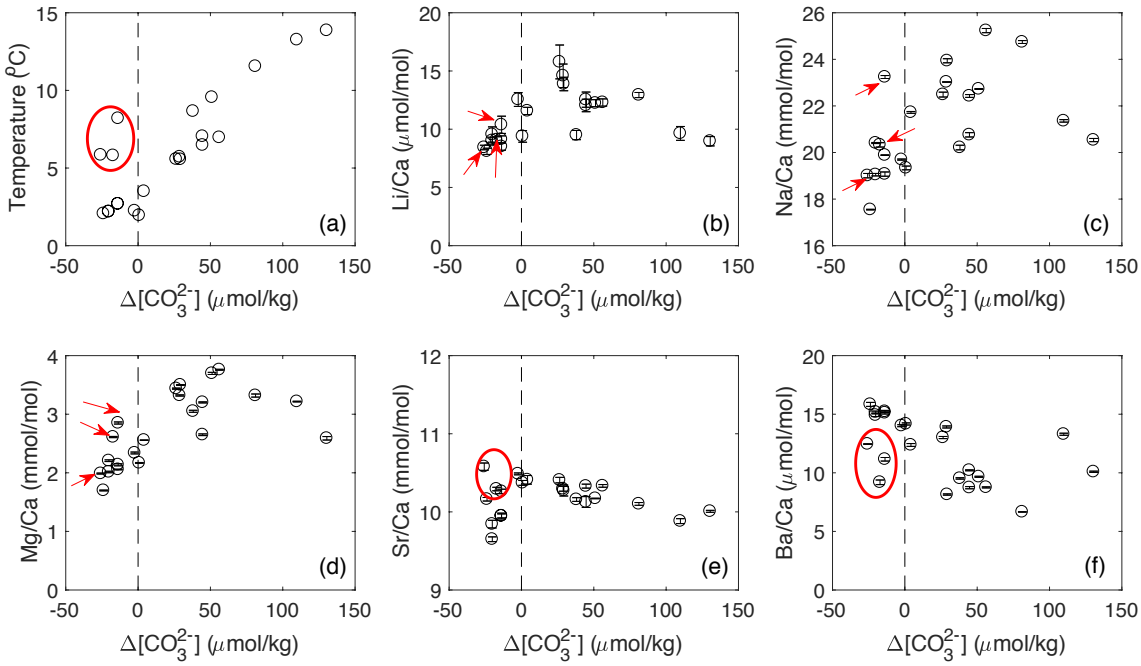

Figure 5-10 Cross plot of $\Delta[CO_3^{2-}]$ vs. (a) temperature and (b-f) different Me/Ca ratios in bulk *D.dianthus* samples. The red circle in (a) marks 3 corals from undersaturated seawater above 5°C. The corresponding points are marked in (b–f) with red circles or red arrows.

Figure 5-10 shows some examples of Me/Ca correlations with $\Delta[CO_3^{2-}]$ in the bulk *D.dianthus* dataset. As with benthic foraminifera, the temperature and $\Delta[CO_3^{2-}]$ of the deep-sea coral growing sites are strongly correlated (Figure 5-10a). Fortunately, three *D.dianthus* specimens in the collection are from low-latitude upwelling regions with undersaturated seawater that is relatively warm, which may be used to disentangle the temperature and carbonate ion effects. We see positive correlations between Li/Ca, Na/Ca, Mg/Ca vs. $\Delta[CO_3^{2-}]$ at low $\Delta[CO_3^{2-}]$ and negative correlations between Sr/Ca, Ba/Ca vs. $\Delta[CO_3^{2-}]$ under supersaturated conditions in Figure 5-10. The three corals from warm undersaturated seawater seem to deviate from the Sr/Ca-$\Delta[CO_3^{2-}]$ and Ba/Ca-$\Delta[CO_3^{2-}]$ relations defined by other points with lower Sr/Ca and Ba/Ca. This would suggest that both Sr/Ca and Ba/Ca are mainly influenced by the temperature effect, and the correlation with $\Delta[CO_3^{2-}]$ is simply due to the temperature-$\Delta[CO_3^{2-}]$ correlation in the seawater. For Sr/Ca, it is intriguing that another group of low Sr/Ca points (from Tasmania as in Figure 5-7) deviate from the Sr/Ca-$\Delta[CO_3^{2-}]$ trend defined by other points, and different individual corals from undersaturated environments fall on an almost vertical trend in Sr/Ca with relatively small changes in $\Delta[CO_3^{2-}]$. This may suggest a change in the biomineralization scheme for these corals (e.g. increase f_{Ca} in the alkalinity pump) as discussed earlier. The correlations of Li/Ca, Na/Ca, Mg/Ca vs. $\Delta[CO_3^{2-}]$ are more scattered than Sr/Ca and Ba/Ca.

However, from the fine scale Me/Ca analyses in Chapter 3 and 4, we know that Li/Ca and Mg/Ca are highly susceptible to bias in the sampling regions. Assuming the sampling regions are randomly selected for the bulk powder in different corals, positive correlations of Li/Ca and Mg/Ca vs. $\Delta[CO_3^{2-}]$ would suggest that corals living in supersaturated environment tend to produce more COC-like materials during calcification compared to those from undersaturated environment. The sampling bias is then reflected in the scatter of the correlations. For example, the two corals from the Mediterranean Sea with the highest $\Delta[CO_3^{2-}]$ have relatively low Li/Ca and Mg/Ca (Figure 5-10b, d), suggesting that the bulk powder sampled parts of the corals with higher fractions of the secondary aragonite compared to COCs. If that is the case, it could also explain their higher U/Ca values compared to the expected U/Ca-$[CO_3^{2-}]$ relations (since U/Ca is depleted in COCs compared to secondary aragonite). In general, different Me/Ca ratios in deep-sea corals show influences from both temperature and the saturation state of the ambient seawater. A multi-proxy

approach may help us better understand the underlying biomineralization mechanisms and disentangle the complicated environmental impacts.

5.4.3 Nutrient-type Tracers

5.4.3.1 Ba/Ca, Seawater [Ba] and Alkalinity

Dissolved Ba has a deeply regenerated vertical profile in the water column and is strongly correlated with silicate and alkalinity in the global ocean (Lea & Boyle, 1989; Lea, 1993). Assuming simple partitioning behavior, the Ba/Ca ratios of biogenic carbonates can record [Ba] of seawater, which can be used to reconstruct the alkalinity or nutrient status of past oceans. Lea (1993) used Ba/Ca ratios of benthic foraminifera to reconstruct the alkalinity of the LGM deep ocean, and found an increase in glacial ocean alkalinity that could account for one third of the atmospheric CO_2 drawdown. The Ba/Ca record was extended further back in time to show a general alkalinity increase in the deep ocean for the last few glacial periods (Lea, 1995). Despite the success of the proxy in paleo-applications, the mechanism of the coupling between [Ba] and alkalinity in the water column is still not fully understood, nor are the potential vital effects associated with Ba incorporation during calcification. More recently, Ba/Ca has been studied in deep-sea corals with the intention to develop tracer for deeply regenerated nutrients, given that dissolved Ba in seawater is also deeply regenerated (Anagnostou et al., 2011; Spooner et al., 2018; Hemsing et al., 2018). While the calibration by Anagnostou et al. (2011) in *D.dianthus* show a linear correlation between Ba/Ca of the coral skeletons and $[Ba]_{sw}$ with zero intercept, calibrations in other deep-sea coral species have different slopes and positive intercepts in the Ba/Ca-$[Ba]_{sw}$ correlation, suggesting the existence of vital effects (Spooner et al., 2018).

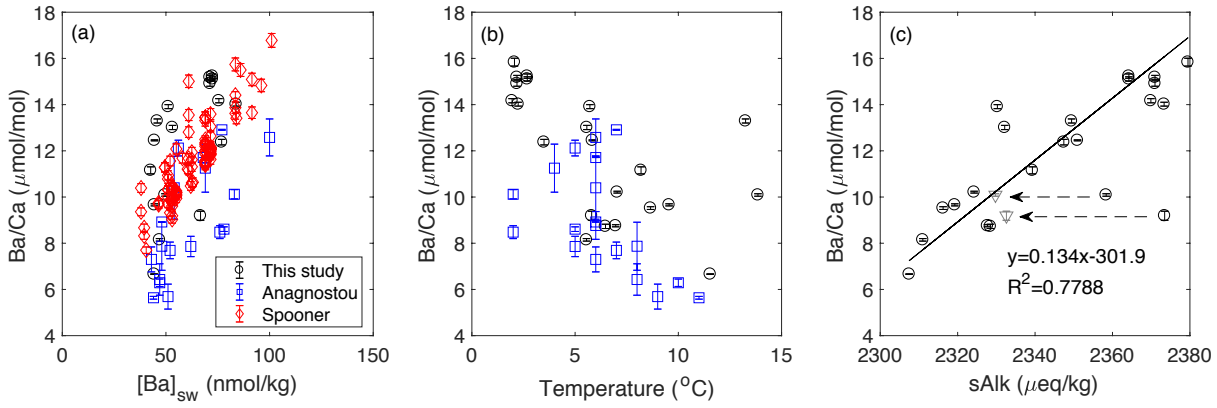

Figure 5-11 Ba/Ca in deep-sea corals vs. $[Ba]_{sw}$, temperature and sAlk. (a) Ba/Ca in deep-sea corals vs. $[Ba]_{sw}$. Black circles and blue squares are *D.dianthus* from this study and Anagnostou et al. (2011) respectively. Red diamonds are mixed species from Spooner et al. (2018). (b) Ba/Ca in *D.dianthus* vs. temperature in this study (black circles) and Anagnostou et al. (2011) (blue squares). (c) Ba/Ca in *D.dianthus* from this study vs. salinity normalized alkalinity (sAlk). Alkalinities are normalized to a salinity of 35 psu (sAlk=Alk/S×35). Two data points (84820 and 48744) fall off the linear trend defined by other points, which may be a result of uncertainties in the alkalinity estimate from the chosen stations (that are not close enough to the coral site) in ODV. If ODV 3D estimation is used for these points, sAlk of these points would shift to the positions of the triangles as indicated by the arrows. The linear fit has neglected these two points (before or after the shift).

Figure 5-11 shows the Ba/Ca calibration in *D.dianthus* bulk samples compared to previous studies. We see that the Ba/Ca-$[Ba]_{sw}$ correlation in this study falls within the scatter of previous data, but the linear relation is less obvious. This is likely a result of poor $[Ba]_{sw}$ estimates from ODV due to the limited spatial coverage of $[Ba]_{sw}$ data compared to the distribution of the corals. In fact, only 7 out of 22 $[Ba]_{sw}$ estimates are considered good estimates by ODV in this dataset (Table 5-1). In contrast to $[Ba]_{sw}$, Ba/Ca in *D.dianthus* is more strongly correlated with temperature and salinity normalized alkalinity in this study (Figure 5-11b, c). Ba/Ca in *D.dianthus* decreases by approximately a factor of 3 over a temperature range of 10°C (Figure 5-11b). Spooner et al. (2018) found that $[Ba]_{sw}$ decreased by a factor of 2–2.5 over this temperature range at their sites, which is also the case with Anagnostou et al. (2011) and this study. When I calculate D_{Ba} from Ba/Ca and estimated $[Ba]_{sw}$, I get D_{Ba} values that scatter around 2.2±0.5 (1σ) without clear temperature dependence. Spooner et al. (2018) also obtained empirical D_{Ba} values around 2 in different deep-sea coral species. Different estimates of D_{Ba} and its temperature dependence have been proposed for inorganic aragonite (Table 3-1, Dietzel et al., 2004; Gaetani & Cohen, 2006). The empirical D_{Ba} in *D.dianthus* is close to that of Dietzel et al. (2004), which estimates a D_{Ba} value of 2.24 at

5°C with a relatively weak temperature dependence (–1.4% per °C), and lower in both absolute value and temperature sensitivity compared to Gaetani & Cohen (2006) (D_{Ba}=4.32 at 5°C, sensitivity –3% per °C) (Figure 5-12a). Most notably, Ba/Ca in *D.dianthus* is strongly correlated with alkalinity in this study. With a few exceptions that may have biased alkalinity estimates, Ba/Ca in *D.dianthus* have a linear relation with alkalinity after salinity normalization (Figure 5-11c). The explanation for the Ba/Ca-alkalinity correlation in foraminifera is based on the correlation between $[Ba]_{sw}$ and alkalinity in the water column with a relatively constant D_{Ba}. The same idea seems to work for *D.dianthus*, although the positive correlation between estimated $[Ba]_{sw}$ and alkalinity in this study is more scattered than that in Lea & Boyle (1989) and Lea (1993), due to uncertainties in the $[Ba]_{sw}$ and alkalinity estimates, as well as a wider spatial distribution of the coral sites with potentially more complicated relations between alkalinity and $[Ba]_{sw}$ (Figure 5-12b).

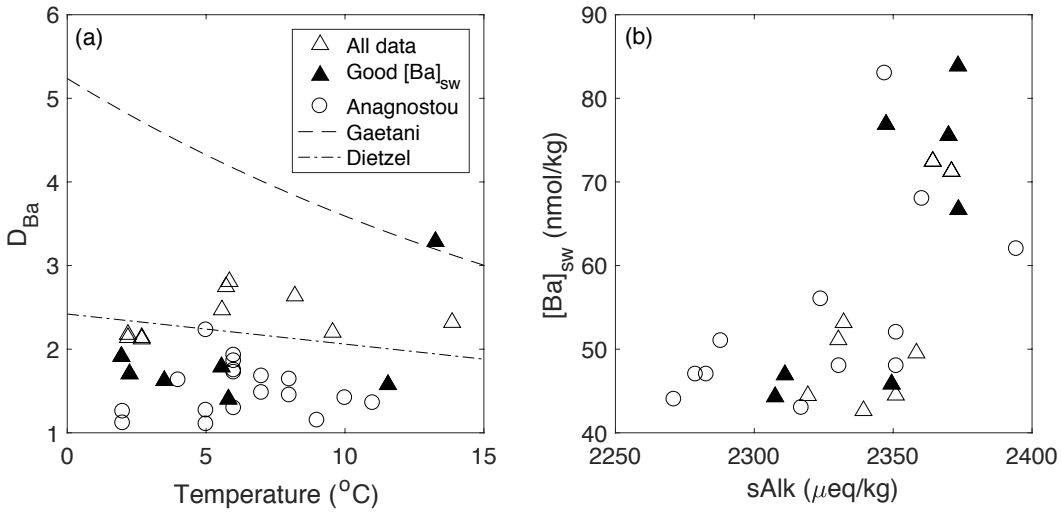

Figure 5-12 Relations between D_{Ba} and temperature in *D.dianthus* and between $[Ba]_{sw}$ and sAlk in seawater. (a) Empirical distribution coefficients for Ba from the *D.dianthus* bulk data (all triangles). Points with good $[Ba]_{sw}$ estimates from ODV are shown in filled triangles. The circles are data from Anagnostou et al. (2011). The dashed and dash-dot lines show D_{Ba} calibrations from inorganic aragonite precipitation experiments by Gaetani & Cohen (2006) and Dietzel et al. (2004) respectively. (b) $[Ba]_{sw}$ estimates from the bulk *D.dianthus* dataset vs. salinity normalized alkalinity. Points with good $[Ba]_{sw}$ estimates from ODV in this study are shown in filled symbols.

While Ba/Ca in *D.dianthus* shows promise as an alkalinity tracer from an empirical basis, there is still significant scatter in the correlation, and we also need to further understand why Ba/Ca seems to record $[Ba]_{sw}$ and alkalinity without much impact from vital effects. The distribution coefficient for Ba in aragonite is larger than that of Sr, and it is expected from the biomineralization model that Ba/Ca should show stronger vital effects (depletion from expected equilibrium) than Sr/Ca. It is interesting to note that most of the data points (with one exception) with good $[Ba]_{sw}$ estimates (with one exception) in this study fall below the D_{Ba} calibration by Dietzel et al. (2004) (Figure 5-12a). The *D.dianthus* data in Anagnostou et al. (2011) also have empirical D_{Ba} values below the Dietzel et al. (2004) calibration for *D.dianthus*, which may reflect the vital effects in Ba/Ca. The other possibility is that the Gaetani & Cohen (2006) calibration is the correct inorganic aragonite Ba/Ca reference frame. Despite suspected influence from kinetic effects, the aragonite precipitation experiments by Gaetani & Cohen (2006) were carried out in actual seawater, which has very different ionic strengths and ion complexes than low ionic strength solutions that are more commonly used. In that case, Ba/Ca ratios in *D.dianthus* contain significant vital effects compared to the inorganic reference frame.

5.4.3.2 Cd/Ca and $[PO_4^{3-}]$

Cd is another element that has a nutrient-like profile in the ocean, and is observed to be strongly correlated with phosphate concentrations in the water column (Boyle et al., 1976; Boyle, 1988). This correlation may be a result of coupled biological uptake at the surface and remineralization in the deep ocean for Cd and phosphate. Although not generally considered an essential nutrient, Cd was found as a cofactor for a specific carbonic anhydrase in phytoplankton such as diatoms and coccolithophores (Lane & Morel, 2000; Xu et al., 2007). It has been suggested that biological Cd uptake might be non-specific in that the phytoplankton could not distinguish Cd^{2+} from other divalent cations with biological functions (Horner et al., 2013). In the water column, dissolved cadmium and phosphate have a positive correlation with a kink at a $[PO_4^{3-}]$ value of ~1.3 μmol/kg, the reason for which is still debated (de Baar et al., 1994; Cullen, 2006; Middag et al., 2018). Despite incomplete understanding of the mechanisms of the Cd-$[PO_4^{3-}]$ correlation, it was found that Cd/Ca in the shells of different benthic foraminifera species could

record [Cd] of the ambient seawater with a D_{Cd} of ~2.9 (that is depth dependent), and can serve as a proxy for [PO_4^{3-}] and the nutrient status of the ocean (Boyle & Keigwin, 1982; Boyle, 1988; Boyle, 1992). The Cd/Ca proxy was extended to deep-sea corals to reveal deep-ocean nutrient changes during rapid climate change events in the last deglaciation (Adkins et al., 1998). Although early work showed limited spatial variability in Cd/Ca in individual *D.dianthus* skeletons, data points with high Cd/Ca were occasionally observed that deviated from a simple $Cd/Ca_{mineral}$-Cd/Ca_{water} calibration with a D_{Cd} of 1.6 (Adkins, 1998; Eltgroth, 2006). An expansion of the modern deep-sea coral Cd/Ca calibration showed that the high Cd/Ca ratios were more common than previously found (Eltgroth, 2006). Inorganic calcite precipitation experiments in artificial seawater constrained D_{Cd} in the range of 500–2500 (Horner et al., 2011). These D_{Cd} numbers have taken into account that only 3% of total Cd exists as free Cd^{2+} in seawater (Horner et al., 2011). When considering total Cd, these measurements yield an effective D_{Cd} of 15–75. Although no experimental data are available for aragonite, it is expected that D_{Cd} in aragonite is also much greater than 1. A strong distillation effect was suggested for Cd during calcification in benthic foraminifera (Elderfield et al., 1996), which may also occur in deep-sea corals and give rise to a wide range in Cd/Ca ratios.

Figure 5-13 shows the Cd/Ca calibration vs. [PO_4^{3-}] and Cd/Ca of the ambient seawater in the bulk *D.dianthus* samples. We see that all data points scatter above a D_{Cd}=1 line, with apparent D_{Cd} values up to 40. Cd/Ca ratios above 1 μmol/mol are uncommon in deep-sea corals (Adkins, 1998; Eltgroth, 2006), and the few data points with very high Cd/Ca may have been contaminated during the sampling process. Most of the data points fall within the 0–0.5 μmol/mol range, with the apparent D_{Cd} ranging between 1 and 10 (Figure 5-13b). The Cd/Ca-[PO_4^{3-}] plot shows similar scatter due to the correlation between [PO_4^{3-}] and [Cd] in the water column. Assuming D_{Cd} in aragonite is similar to that of calcite, the scatter in skeletal Cd/Ca reflects strong vital effects for Cd incorporation, casting uncertainty on its application as a nutrient proxy in deep-sea corals.

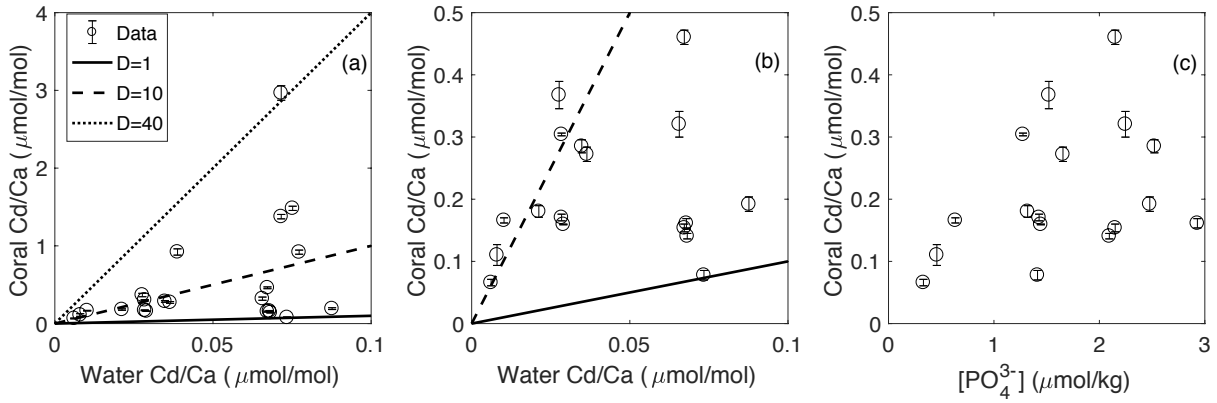

Figure 5-13 Cd/Ca in bulk *D.dianthus* samples against Cd/Ca and $[PO_4^{3-}]$ in seawater. (a) Cd/Ca in bulk *D.dianthus* samples (with 2σ external standard errors) calibrated against Cd/Ca in seawater. Different lines correspond to different distribution coefficients. The data points scatter above the D_{Cd}=1 line. (b) A zoom-in of panel (a) to the 0–0.5 μmol/mol Cd/Ca range, due to suspected contamination of high Cd/Ca samples in (a). (c) Cd/Ca in *D.dianthus* against $[PO_4^{3-}]$ in the seawater in the 0–0.5 μmol/mol Cd/Ca range. Similar scatter to panel (b) is seen due to the correlation between $[PO_4^{3-}]$ and [Cd] in the seawater.

5.5 Biomineralization Imprints on Tracer Calibrations

In the last section, some Me/Ca ratios in *D.dianthus* were found to be strongly correlated with environmental factors such as temperature, carbonate ion and alkalinity. However, none of the observed correlations are without significant scatter or notable outliers. Meanwhile, some Me/Ca ratios show strong vital effects that obscure any significant correlation with the environmental conditions. This section discusses some potential mechanisms of the imprints of vital effects in the Me/Ca-environment calibrations in deep-sea corals.

5.5.1 Tracers and Skeleton Textures

Given the range of Me/Ca variability observed in individual deep-sea corals and the extreme compositions of the COCs, it is expected that the compositions of bulk coral samples are very sensitive to bias in the sampling region. Different bulk samples may come from different fractional mixtures of COCs and secondary aragonite, as well as different end members in the secondary aragonite. Sampling bias has been a major suspect as the reason for scattered correlations between tracers and environmental conditions in deep-sea corals in previous work

(Anagnostou et al., 2011; Stewart et al., 2016). For example, by careful sampling of the low-Mg bands in *D.dianthus*, Stewart et al. (2016) constructed an improved calibration between $\delta^{11}B$ of the coral skeletons and $\delta^{11}B$ of borate in seawater compared to earlier work by Anagnostou et al. (2011), suggesting COCs as a major contributor to the scatter in previous calibrations. While it is possible to carefully sample the corals and avoid apparent COCs to build better calibrations for other tracers, this approach still relies on finding the low-Mg end member in the secondary aragonite.

It is an open question whether the relative fractions of COCs and secondary aragonite in deep-sea corals are completely random among individuals, or their proportions are influenced by the environmental conditions. In foraminifera, it has been suggested that the higher temperature sensitivity in Mg/Ca compared to inorganic calcite can be explained by a fractional change in the high Mg phase relative to the low Mg phase in their shells (Bentov & Erez, 2006). It is possible to quantify this effect in deep-sea corals with cross section images of their skeletons. Figure 5-14 shows reflected light images of a selection of the *D.dianthus* individuals with large enough skeletons to make sections for micromilling and SIMS/nanoSIMS analyses. The corals are arranged in the order of increasing temperature from bottom to top and increasing saturation state (Ω_A) from left to right. A general observation is that corals from supersaturated seawater have more diverse spatial structures and more COC-like white materials in these cross sections. Figure 5-15 shows the histograms of pixel gray scales from the images in Figure 5-14. Although the images may also be subjected to bias in sampling regions, we see similar gray scale distributions for corals from similar environments. Corals from undersaturated environments tend to have a negative skewness (except for Gaia) and less pronounced tails on the high gray scale (white) end. The two corals from warm undersaturated seawater have higher fractions of white materials than their cold counterparts. Corals from supersaturated seawater tend to have a positive skewness or a uniform distribution, with a larger fraction of COCs and COC-like structures (gray scale>0.8).

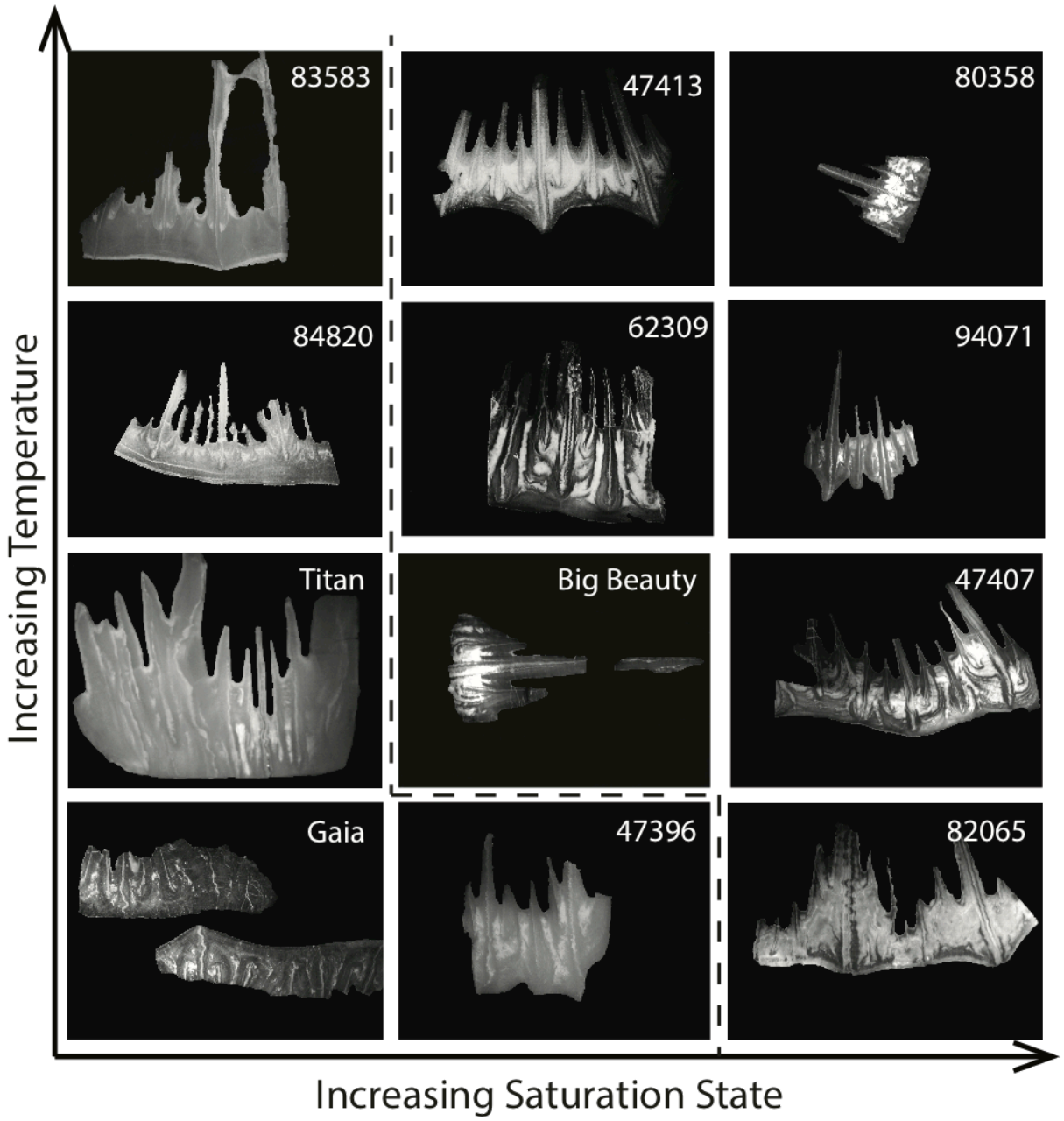

Figure 5-14 Reflected light images of thick cross sections (top view) of selected *D.dianthus* individuals arranged in the order of increasing saturation state (Ω_A) on the x-axis and increasing temperature on the y-axis. The dashed line separates corals from undersaturated seawater to the lower left and corals from supersaturated seawater to the upper right. The images were taken with a Q-imaging micropublisher 5.0 RTV camera mounted on an Olympus SZ-CTV microscope at 18× magnification under similar lighting conditions. The horizontal dimension of each image is 1.3 cm.

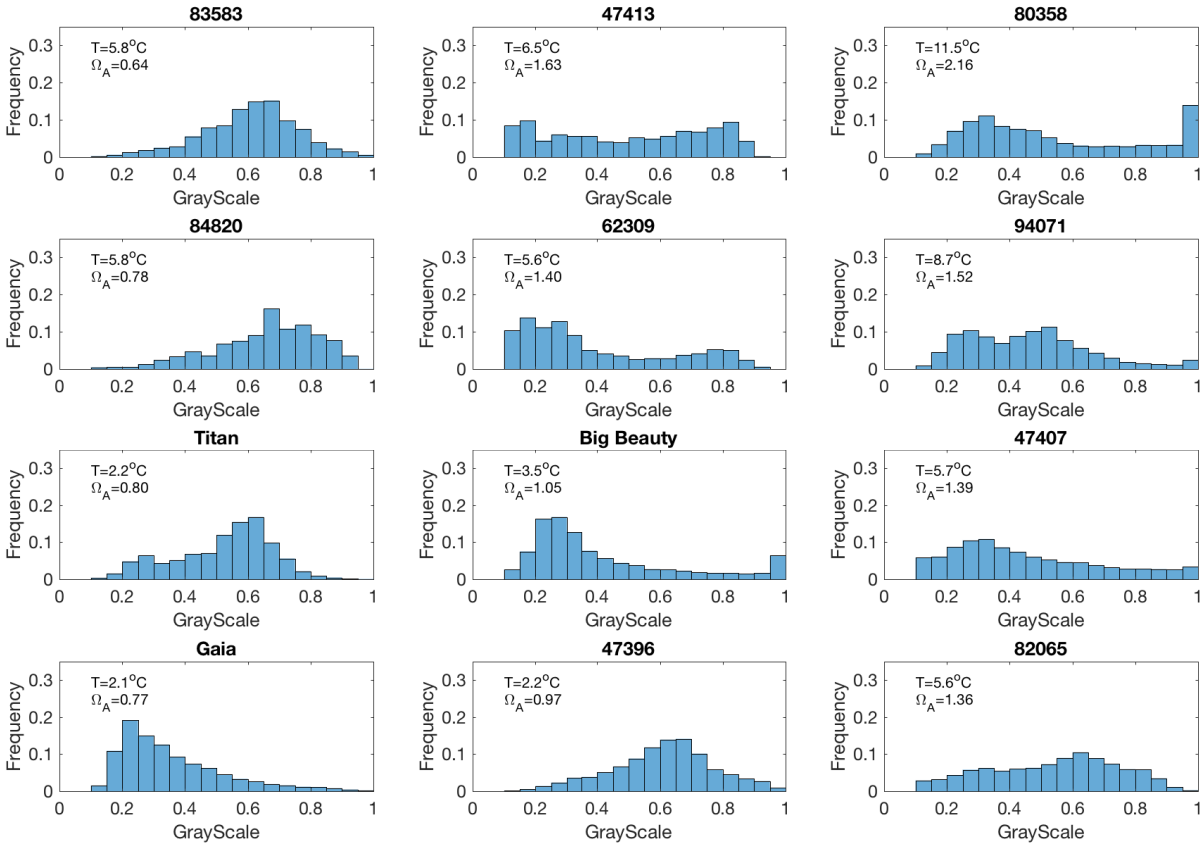

Figure 5-15 Gray scale histograms of pixels in *D.dianthus* skeleton cross section images from Figure 5-14. A gray scale of 0 represents black, while a gray scale of 1 represents white. The black background in the images in Figure 5-14 shows up as a spike below gray scale of 0.1 and is removed from each histogram. The gray scales of all pixels from the original images are normalized by the maximum gray scale value in each image, with the assumption that the whitest parts of the skeletons most likely represent COCs or COC-like materials.

To quantify the potential environmental impact on the texture of coral skeletons, I computed the statistics of the gray scales and compared them against temperature and aragonite saturation state (Figure 5-16). While the mean gray scales show no obvious correlation with temperature or Ω_A, the variance is positively correlated with temperature and Ω_A, and more strongly so with the latter. Although the mean gray scale may be influenced by sample thickness and small changes in lighting conditions when the images were taken on different days, the variance is less susceptible to these artifacts and better reflects true texture changes in the skeletons. There is no statistically significant linear correlation between skewness and temperature or Ω_A, but

the skewness-Ω_A (and temperature) relation shows an interesting structure in that the corals living in a less saturated environment tend to have a more skewed gray scale distribution in either direction. The kurtosis of gray scales is negatively correlated with temperature and Ω_A, also with Ω_A having a stronger correlation. This is partly a result of the lower variance for the corals from undersaturated conditions, which causes extreme values to occur more frequently. These analyses suggest that the ambient aragonite saturation state may impose strong controls on the biomineralization process of *D.dianthus* and thus the texture of the skeletons.

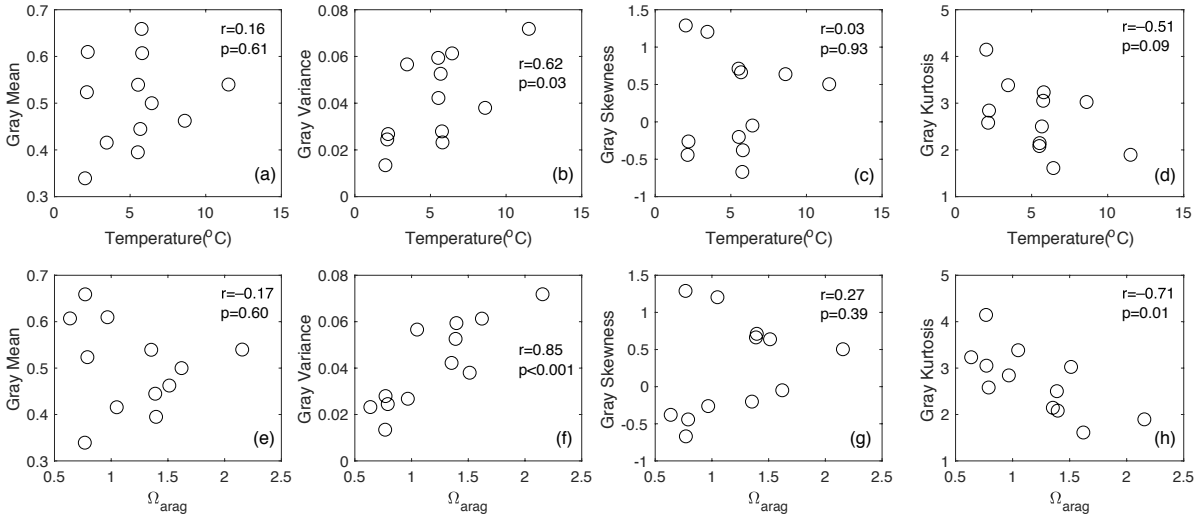

Figure 5-16 Cross plots of gray scale statistics with temperature (a–d) and aragonite saturation state (e–h). From left to right, the statistics are mean, variance, skewness and kurtosis of the pixel gray scales in the images in Figure 5-14, with distributions shown in Figure 5-15. The numbers show the Pearson correlation coefficients and the corresponding p-values.

Since the variance in gray scale is the texture information that is most strongly correlated with temperature and Ω_A, it is interesting to test its correlation with the bulk Me/Ca ratios, as shown in Figure 5-17. We see positive correlations for the gray scale variance with Mg/Ca and Li/Ca, and less so with B/Ca. The gray scale variance is also negatively correlated with Ba/Ca and U/Ca, and shows no clear correlation with Sr/Ca. The correlations for Li/Ca, Mg/Ca and U/Ca can be interpreted as changes in relative fractions of COCs and secondary aragonite, as high variance in gray scale indicates more contribution from COCs and COC-like regions that have higher Li/Ca, Mg/Ca and lower U/Ca. Sr/Ca ratios of COCs are less well-defined relative to the secondary

aragonite, which explains the scatter in the Sr/Ca-gray scale variance correlation (Figure 5-17d). Although COCs have low B/Ca, the B/Ca ratios are not extreme compared to the low B/Ca end member in the secondary aragonite. This may explain the correlation pattern in Figure 5-17b, in which B/Ca stops increasing (with signs of turning around) at high gray scale variance. Ba/Ca ratios in COCs are not well characterized, and the correlation between Ba/Ca and gray scale variance may be a result of their respective correlations with the temperature or carbonate chemistry of the seawater. In sum, we see evidence that the texture and chemical composition of *D.dianthus* skeletons are linked, and both are sensitive to environmental conditions (especially aragonite saturation state), offering a potential explanation for the observed vital effects in Me/Ca ratios in deep-sea corals.

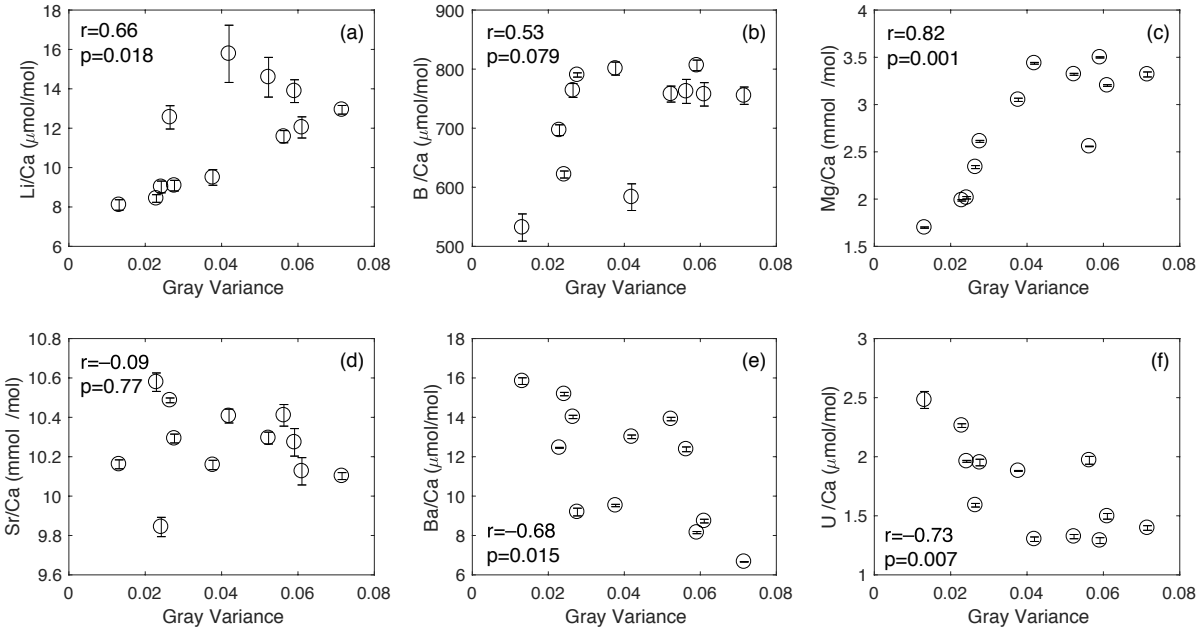

Figure 5-17 Cross plots of Me/Ca ratios in bulk *D.dianthus* samples vs. variance of gray scale in the cross section images. The numbers show the Pearson correlation coefficients and corresponding p-values.

5.5.2 Stable Isotopes and Me/Ca Vital Effects

While the texture changes in coral skeletons can explain the observed Me/Ca vital effects and provide clues to improving paleo-proxies by careful sampling, it still does not offer a

quantitative mechanism for the vital effects. Given the biomineralization model developed in previous chapters, the stable isotope compositions of oxygen and carbon may be the best candidates to quantify the magnitude of the vital effects from the alkalinity pump. Figure 5-18 shows the $\delta^{18}O$ data of the bulk *D.dianthus* samples against temperature. We see that the ranges in $\delta^{18}O$ in these bulk samples are generally a few tenths of a permil (up to 1‰), suggesting substantial averaging of the whole coral skeleton that typically has a 4–5‰ range in $\delta^{18}O$. The $\delta^{18}O$ values of these bulk samples are on average 2.8‰ depeleted from the equilibrium aragonite composition determined by Wang et al. (2013), with similar temperature sensitivity to the equilibrium line. There is significant individual variability on top of the general trend, suggesting that the bulk samples have incorporated different degrees of vital effects from the alkalinity pump (note that spatial variability in seawater $\delta^{18}O$ is also part of the signal, but it is small compared to the full $\delta^{18}O$ variability).

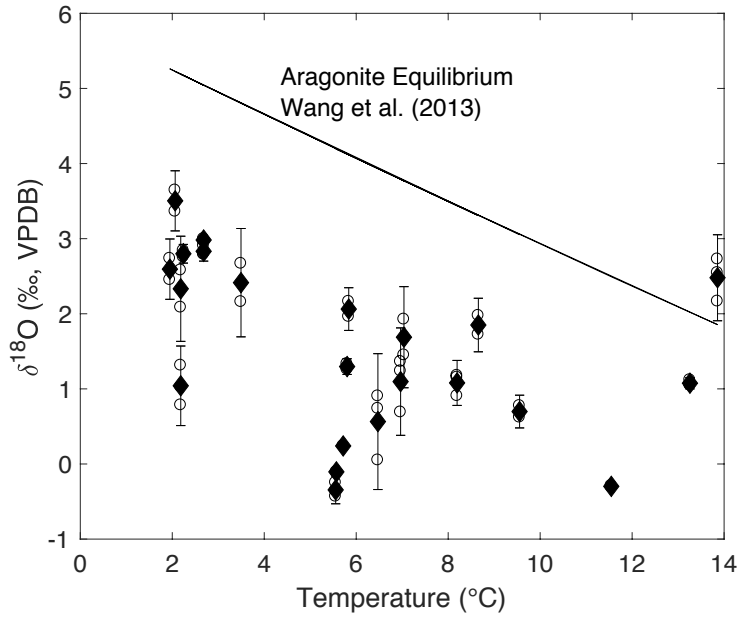

Figure 5-18 $\delta^{18}O$ of bulk *D.dianthus* samples vs. temperature. The open circles are different powder aliquots of the same coral, and the filled diamonds show the mean $\delta^{18}O$ with 2σ standard deviations of the aliquots. The solid line shows equilibrium aragonite composition from Wang et al. (2013), assuming a seawater $\delta^{18}O$ of 0‰ (VSMOW). The bulk coral samples are on average 2.8‰ depleted from the equilibrium line.

In Chapter 3, I used a numerical model to predict the correlations between $\delta^{18}O$ and Me/Ca ratios in individual corals, based on their respective response to the alkalinity pump. Figure 5-19

shows cross plots of Me/Ca ratios and $\delta^{18}O$ of the bulk *D.dianthus* samples. The correlations in the cross plots have convolved environmental changes and vital effects, and are thus not equivalent to correlations within single corals. However, for Me/Ca ratios that showed scattered correlations with temperature and $[CO_3^{2-}]$ such as Li/Ca and Mg/Ca, we see their strong negative correlations with $\delta^{18}O$, consistent with the model predictions at low f_{Ca} values (Figure 3-3). We also see a negative correlation between B/Ca and $\delta^{18}O$ that is weaker but consistent with the direction predicted by the model. Both U/Ca and Ba/Ca are positively correlated with $\delta^{18}O$, with U/Ca having the strongest correlation with $\delta^{18}O$ among all Me/Ca ratios. The direction of the Ba/Ca-$\delta^{18}O$ correlation also agrees with the model prediction, although the correlation is complicated by temperature and changes in $[Ba]_{sw}$. The model does not include U at this stage, due to an incomplete understanding of its aqueous speciation and the incorporation process into the skeletons. If we simply treat it as UO_2^{2+} ions substituting for Ca^{2+}, it may have a distribution coefficient that is similar to Ba^{2+}, given that they both have variations of a factor of 2 (Figure 5-19e, f). The correlation between Sr/Ca and $\delta^{18}O$ may have been most strongly influenced by the convolution of environmental changes and vital effects compared to other elements. However, the subset of corals from Tasmania shows the expected correlation between Sr/Ca and $\delta^{18}O$ from the model.

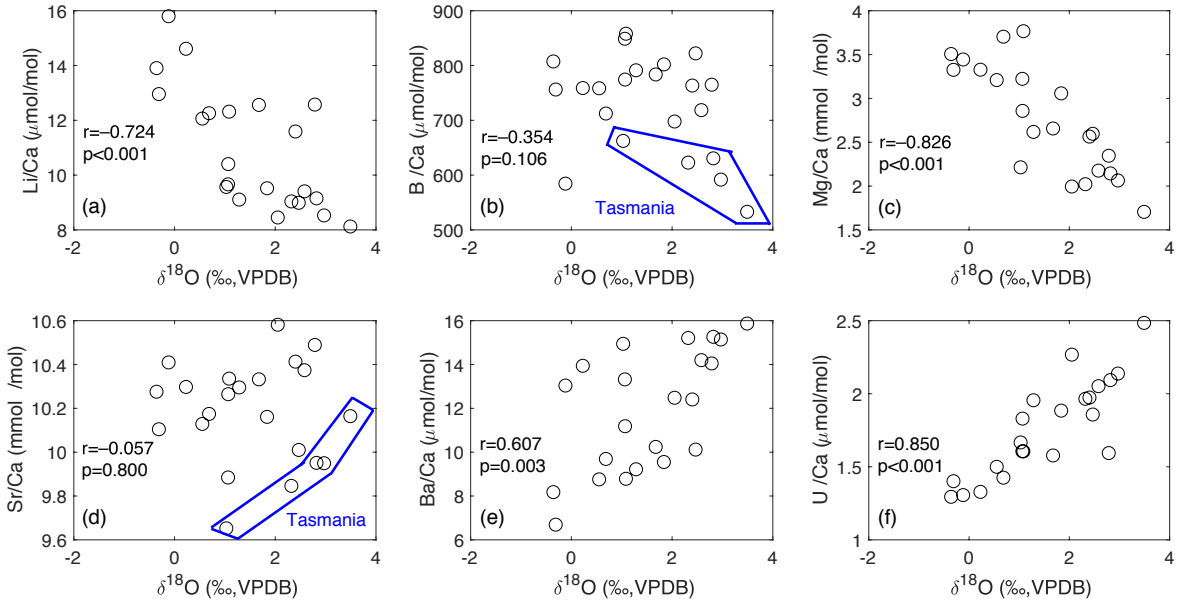

Figure 5-19 Cross plot of Me/Ca ratios vs. $\delta^{18}O$ of *D.dianthus* bulk samples. The numbers show the Pearson correlation coefficients and corresponding p-values. The blue lines in (b) and (d) encircle the five corals collected south of Tasmania.

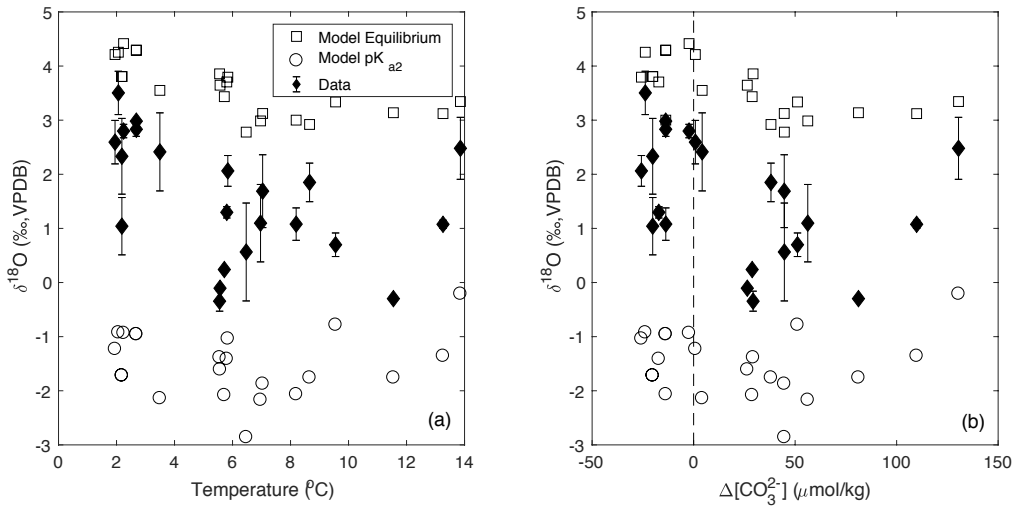

Figure 5-20 Data-model comparison for $\delta^{18}O$ vs. (a) temperature and (b) $\Delta[CO_3^{2-}]$. The $\delta^{18}O$ of seawater for the corals are estimated from the NOAA Global Seawater Oxygen-18 Database (Schmidt, 1999; Bigg & Rohling, 2000). The squares show the equilibrium $\delta^{18}O$ compositions from the model, and the circles show the compositions at pK_{a2} of the DIC system ($\delta^{18}O$-$\delta^{13}C$ kink) in the model. The diamonds show the measured bulk samples with 2σ standard deviations.

To further deconvolve the environmental and vital effects quantitatively, I ran a model simulation for stable isotopes and Me/Ca ratios at the growing conditions of each individual coral. Figure 5-20 shows the measured $\delta^{18}O$ values with respect to the two extremes in the model — the equilibrium $\delta^{18}O$ compositions and the $\delta^{18}O$ compositions at pK_{a2} of the DIC system (also the $\delta^{18}O$-$\delta^{13}C$ kink). We see significant individual variability in terms of the relative positions of the measured $\delta^{18}O$ values between the two extremes, suggesting different amounts of alkalinity pumping and vital effects involved in the Me/Ca ratios. In general, corals from cold and/or undersaturated seawater tend to have $\delta^{18}O$ values closer to equilibrium, while corals from warm and supersaturated seawater can have $\delta^{18}O$ values that span a large range between the two extremes. Figure 5-21 shows the alkalinity pump rates in individual corals calculated from the bulk $\delta^{18}O$ data and the biomineralization model. We see that corals from cold undersaturated seawater tend to have a low and relatively constant alkalinity pump rate, while corals from warm undersaturated seawater tend to have a higher but also relatively constant alkalinity pump rate. In contrast, corals from supersaturated seawater have variable amounts of alkalinity pump from these bulk samples. This is consistent with the stable isotope data for the micromilled samples presented in Chapter 3, as well as the image gray scale analyses in the previous section, and suggests that the degree of alkalinity pumping in deep-sea corals is sensitive to the environmental conditions. It is

more likely for corals in supersaturated seawater to implement a stronger alkalinity pump and produce the skeleton end member with stronger vital effects in its isotopic and Me/Ca compositions. Gagnon et al. (2013) proposed a similar idea to explain the observed carbonate ion effect on Sr/Ca in cultured corals. They hypothesized that corals living in supersaturated seawater can exert alkalinity pumps up to a target pH of pK_{a2}, while corals living in undersaturated seawater can only exert a fixed amount of alkalinity pump, consistent with the $\delta^{18}O$-based pump rates shown in Figure 5-21.

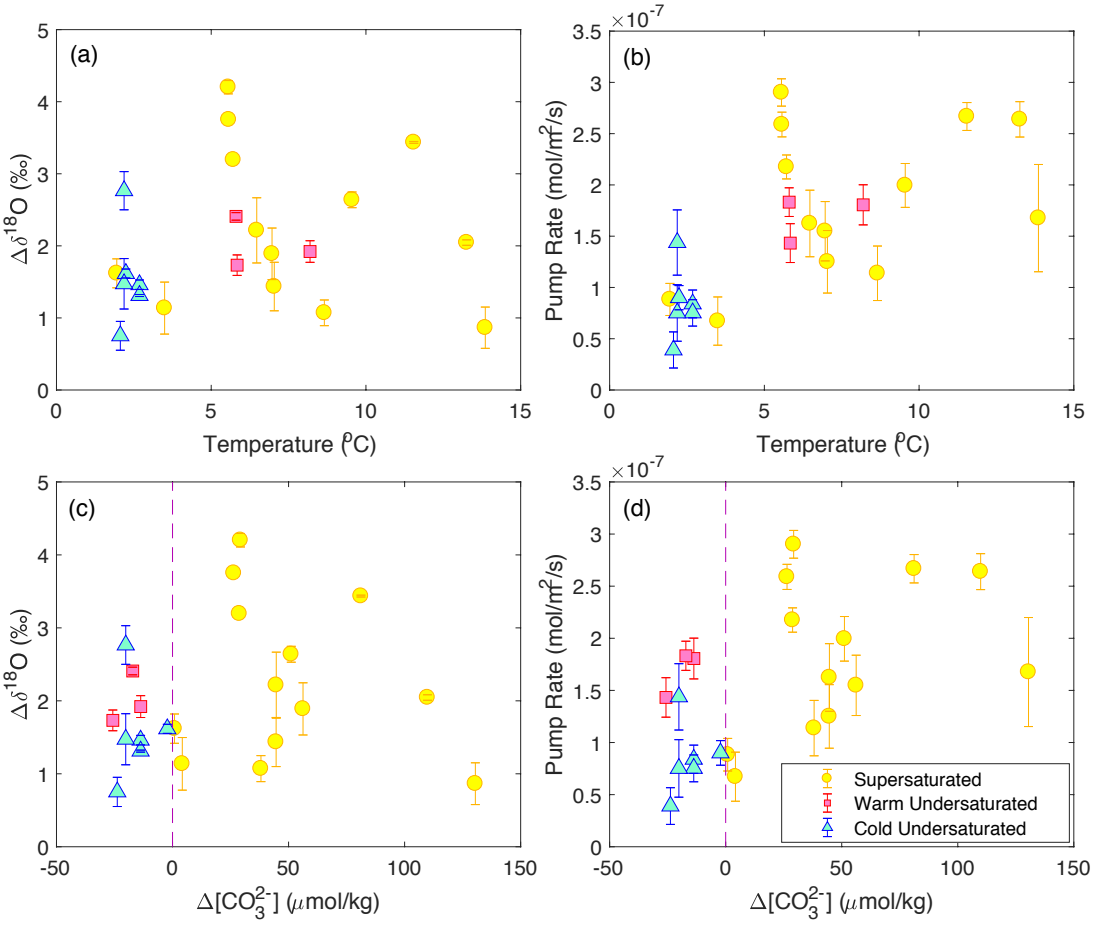

Figure 5-21 Alkalinity pump rate in individual corals derived from measured $\delta^{18}O$ values and the biomineralization model. (a) Difference between measured $\delta^{18}O$ and calculated equilibrium values vs. temperature. (b) Calculated alkalinity pump rates vs. temperature. (c) Difference between measured $\delta^{18}O$ and calculated equilibrium values vs. $\Delta[CO_3^{2-}]$. (d) Calculated alkalinity pump rates vs. $\Delta[CO_3^{2-}]$. The blue triangles represent corals from cold undersaturated seawater. The red squares represent corals from warm undersaturated seawater. The yellow circles represent corals from supersaturated seawater.

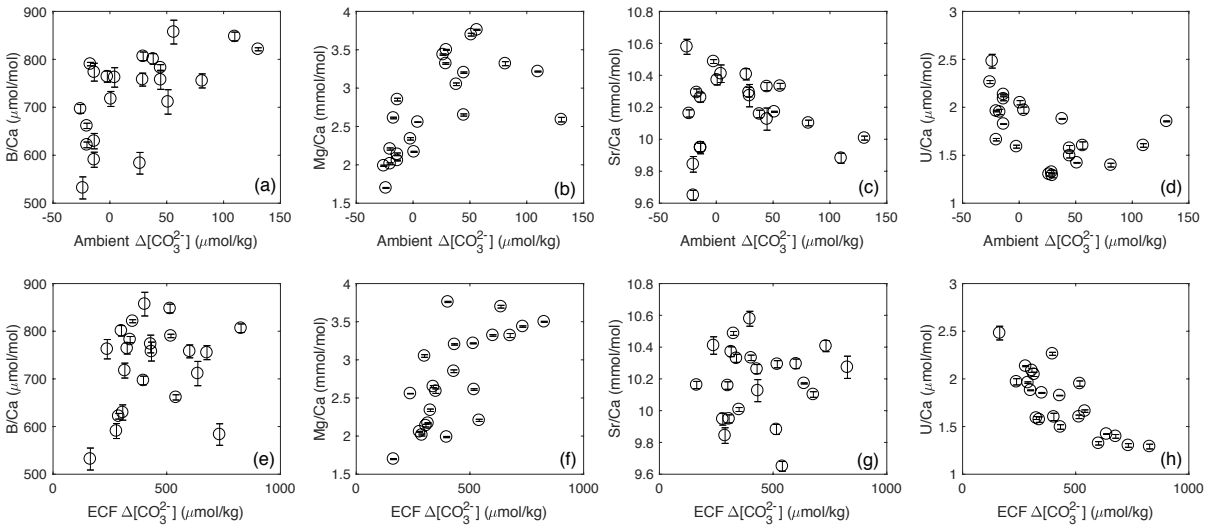

Figure 5-22 Me/Ca ratios vs. $\Delta[CO_3^{2-}]$ in ambient seawater and the ECF. (a–d) Me/Ca ratios vs. $\Delta[CO_3^{2-}]$ in the ambient seawater. (e–h) Me/Ca ratios vs. $\Delta[CO_3^{2-}]$ calculated from the biomineralization model based on the measured $\delta^{18}O$ values.

With the model simulations for individual corals, we can also quantify the carbonate chemistry of the ECF associated with the measured $\delta^{18}O$ values, and investigate how it may influence the interpretation of the Me/Ca ratios. Figure 5-22 provides such an example, in which the measured $\delta^{18}O$ values were used to infer the corresponding alkalinity pump rate in the model for each individual coral, and thus all the carbonate chemistry parameters in the ECF including $[CO_3^{2-}]$ and $\Delta[CO_3^{2-}]$. When the $\Delta[CO_3^{2-}]$ of the ECF from the model is plotted against the measured Me/Ca ratios, some differences are noted compared to the Me/Ca relations with the ambient $\Delta[CO_3^{2-}]$. Most notably, U/Ca is more tightly correlated with ECF $\Delta[CO_3^{2-}]$ compared to the ambient $\Delta[CO_3^{2-}]$, suggesting it is strongly influenced by the biomineralization process. The correlation between Mg/Ca and ECF $\Delta[CO_3^{2-}]$ is also stronger than correlation with ambient $\Delta[CO_3^{2-}]$. For both Mg/Ca and U/Ca, there are data points at high ambient $\Delta[CO_3^{2-}]$ (from Mediterranean Sea) that deviate from the trends defined by other points, which can be accounted for by the $\delta^{18}O$-based correction for the vital effects in the ECF $\Delta[CO_3^{2-}]$, thus increasing the apparent correlations. For Sr/Ca and B/Ca, the correlations with ECF $\Delta[CO_3^{2-}]$ are less clear compared to the ambient $\Delta[CO_3^{2-}]$. It is likely that changes in ECF $\Delta[CO_3^{2-}]$ are associated with changes in the relative fractions of different compositional end members in the coral skeletons. While Mg/Ca and U/Ca changes monotonously from the equilibrium secondary aragonite end

member to a pH-elevated secondary aragonite end member to COCs, both Sr/Ca and B/Ca are observed to change non-monotonously between the end members in previous chapters, with COC compositions not as distinct from the secondary aragonite as Mg/Ca and U/Ca. In particular, we see that Sr/Ca correlates with environmental conditions more strongly than the gray scale texture indices and the stable isotopes, suggesting that it is minimally influenced by the vital effects that change the stable isotope compositions and other Me/Ca ratios of the coral skeletons (except for corals living under extreme conditions like those from Tasmania). Given the relatively small changes in Sr/Ca, it is likely that bulk Sr/Ca samples can sufficiently smooth away the internal variability to produce a robust calibration against temperature, although the current simple model cannot fully predict the measured Sr/Ca-temperature relation (Figure 5-23). For elements with more internal variability (Mg/Ca, Li/Ca, B/Ca, U/Ca), more careful sampling coupled with stable isotope measurements can help constrain the magnitude of vital effects and potentially separate the end members for better tracer calibrations.

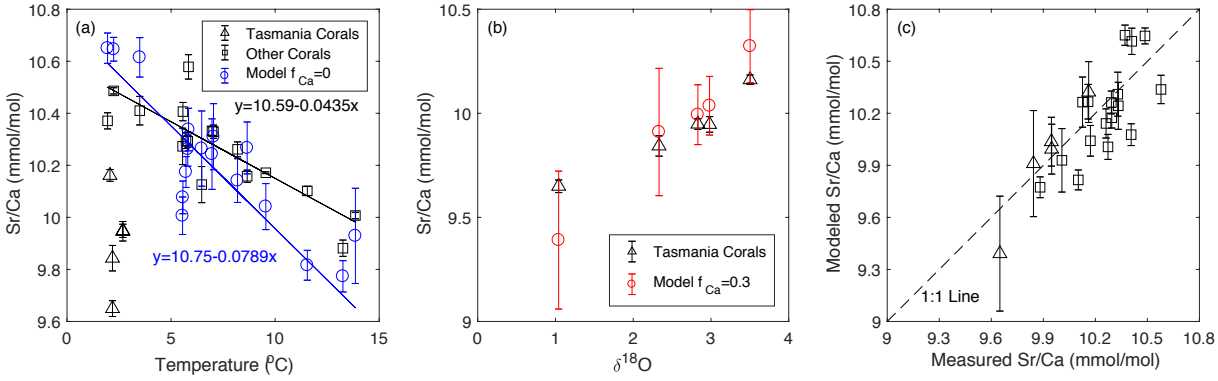

Figure 5-23 Data-model comparison of Sr/Ca in bulk *D.dianthus* samples. (a) Sr/Ca data in *D.dianthus* (black squares and triangles as in Figure 5-7) vs. model predictions (blue circles). The model takes the mean and standard deviations of measured $\delta^{18}O$ in each coral to calculate the corresponding range (2σ) in alkalinity pump rate and Sr/Ca with f_{Ca}=0. This approach tends to predict higher Sr/Ca at lower temperatures and lower Sr/Ca at high temperatures than the data. The model-data difference could be caused by other factors not accounted for in the model such as growth rate dependence of D_{Sr}, aqueous Sr complexation or changes in seawater turnover rates among individual corals. (b) The corals from south of Tasmania do not fall on the Sr/Ca-temperature trend with other corals but have Sr/Ca correlated with $\delta^{18}O$. This can be explained by a pump rate effect with f_{Ca}=0.3. (c) Overall model-data comparison for all corals.

5.6 Conclusions and Outlook

In this chapter, I have reported empirical tracer calibrations with a suite of modern *D.dianthus* specimens from a wide range of environments. Some relatively robust tracer-environment correlations are observed and interpreted in the context of skeletal textures and the biomineralization model. Both Li/Mg and Sr/Ca in bulk *D.dianthus* samples are strongly correlated with temperature. The Li/Mg-temperature relation in *D.dianthus* is consistent with previous calibrations in other corals and *H.elegans*. With a few exceptions from Tasmania, Sr/Ca in *D.dianthus* has the same temperature sensitivity as inorganic aragonite, but lower in absolute value by ~4%. The Sr/Ca-temperature calibration seems to be minimally influenced by variable amounts of alkalinity pumping in individual corals, which may result from relatively small Sr/Ca variability in individual corals that are sufficiently averaged in the bulk samples. Both B/Ca and U/Ca of bulk *D.dianthus* samples are correlated with $\Delta[CO_3^{2-}]$ in the ambient seawater. While the mechanism for the B/Ca-$\Delta[CO_3^{2-}]$ correlation is still unclear, the U/Ca-$\Delta[CO_3^{2-}]$ correlation can be explained by a biomineralization response to the aragonite saturation state in the ambient seawater, as supported by skeletal texture changes and stable isotope analyses. Mg/Ca seems to be influenced by the biomineralization response to the ambient saturation state in a similar way to U/Ca, and the Mg/Ca in *D.dianthus* skeletons mainly reflects the relative fractions of different compositional end members. Ba/Ca is correlated with salinity normalized alkalinity in the ambient seawater, which may be a result of the correlation between alkalinity and seawater [Ba]. Similar to Sr/Ca, Ba/Ca in *D.dianthus* seems to be minimally impacted by vital effects, likely due to the same averaging effect in bulk powder samples. On the other hand, Cd/Ca is strongly influenced by the biomineralization process and shows significant variability among different corals, which casts uncertainty on its applicability as a phosphate or water mass tracer.

So far in this thesis, I have tried to combine empirical observations with the numerical biomineralization model to understand the vital effects in the isotopic, minor and trace element compositions of the aragonitic skeletons of the deep-sea coral *D.dianthus*. The numerical model has been developed to explain all the key features in the stable isotope vital effects. It has also been adapted to explain some Me/Ca correlations and vital effects observed in deep-sea corals over a range of sampling scales. It was the goal of this work that a combination of stable isotope and Me/Ca measurements with the numerical model could help us develop paleo-tracers in deep-sea

corals that are mechanistically well understood from a biomineralization perspective. While the biomineralization model has partial success in explaining the Me/Ca variabilities and their relations to the stable isotopes in individual corals, the interpretations of the Me/Ca data are far from quantitative and satisfactory, and most of the robust Me/Ca tracer calibrations presented in the thesis are still empirical.

There are three aspects of the problem that are worth further exploration. First, some of the model-data comparisons in the thesis are hampered by data quality issues. While SIMS and nanoSIMS measurements have accuracy calibration problems, the bulk samples may be influenced by a sampling bias of the heterogeneous coral skeletons. The micromilled samples could have avoided these disadvantages with the added benefit of coupled stable isotope and Me/Ca measurements of the same small amounts of powder, but the quality of the dataset was compromised due to preparation and analytical problems. Therefore, I still lack a perfect dataset to test all the hypotheses in the model. Second, the current model is still a simple description of the biomineralization and tracer incorporation process. It is likely that many of the minor and trace elements are influenced by more complicated processes, such as aqueous speciation into complexes, interactions with the mineral surface (including the presence of organic templates), and biological manipulations of their concentrations in the ECF. Considerations of these processes may help us better understand the observed Me/Ca values and patterns in coral skeletons. Finally, related to the shortcomings in the model, we do not have a well-established inorganic reference frame for aragonite for many of the minor and trace elements, including their partitioning under equilibrium conditions and kinetic limits at different temperatures. Therefore, it is difficult to compare the empirical tracer calibrations in biogenic aragonites to physicochemical expectations. I am hopeful that more progress can be made on this front in the coming years, given the promising new tracers that are being rapidly developed in corals and other calcifying organisms. Progress in paleo-proxy development has always been made by a combination of empirical calibrations and theoretical models, and it is my hope that the gaps between the two can be further bridged through new knowledge on both fronts.

C h a p t e r 6

Mechanism of Solid-State Clumped Isotope Reordering in Carbonate Minerals from Aragonite Heating Experiments

The content of this chapter has been accepted by *Geochimica et Cosmochimoca Acta*, with the authors and title listed below.

Chen, S., Ryb, U., Piasecki, A.M., Lloyd, M.K., Baker, M.B., & Eiler, J.M. (*2019*). "Mechanism of solid-state clumped isotope reordering from aragonite heating experiments". In: *Geochimica et Cosmochimica Acta*. doi: 10.1016/j.gca.2019.05.018.

Abstract

The clumped isotope compositions of carbonate minerals are subject to alteration at elevated temperatures. Understanding the mechanism of solid-state reordering in carbonate minerals is important in our interpretations of past climates and the thermal history of rocks. The kinetics of solid-state isotope reordering has been previously studied through controlled heating experiments of calcite, dolomite and apatite. Here we further explore this issue through controlled heating experiments on aragonite. We find that Δ_{47} values generally decrease during heating of aragonite, but increase by 0.05–0.15‰ as aragonite starts to transform into calcite. We argue that this finding is consistent with the presence of an intermediate pool of immediately adjacent singly-substituted carbonate ion isotopologues ('pairs'), which back-react to form clumped isotopologues during aragonite to calcite transformation, revealing the existence of kinetically preferred isotope exchange pathways. Our results reinforce the 'reaction-diffusion' model as the mechanism for solid-state clumped isotope reordering in carbonate minerals. Our experiments also reveal that the reordering kinetics in aragonite is faster than in calcite and dolomite, making its clumped isotope composition highly susceptible to alteration during early diagenesis, even before conversion to calcite.

6.1 Introduction

The carbonate 'clumped isotope thermometer' is based on the preferential bonding of ^{13}C and ^{18}O atoms within the same carbonate ion group at low temperatures, which transitions toward a more random isotope distribution among carbonate ions at high temperatures (Wang et al., 2004;

Ghosh et al., 2006; Schauble et al., 2006; Eiler, 2011). Carbonate clumped isotope abundances are reported using the Δ_{47} notation, which is the ratio of the mass 47 isotopologue of CO_2 ($^{13}C^{18}O^{16}O$) to the mass 44 isotopologue ($^{12}C^{16}O_2$) in CO_2 released from a carbonate mineral by acid digestion, normalized to the ratio expected for a stochastic isotope distribution (Wang et al., 2004). The thermometer is interpreted to reflect homogeneous isotope exchange equilibrium between isotopic forms of carbonate ions in the mineral:

$$^{13}C^{18}O^{16}O_2^{2-} + {}^{12}C^{16}O_3^{2-} \Leftrightarrow {}^{12}C^{18}O^{16}O_2^{2-} + {}^{13}C^{16}O_3^{2-} \ (Rxn\ 1)$$

The temperature dependent equilibrium constant for this reaction can constrain the temperature of mineral formation or equilibration, independent of the carbon and/or oxygen isotope composition of the fluid from which the mineral grew, and of the mineral itself (Eiler, 2007; Eiler, 2011). This quality makes this proxy useful for reconstructing Earth-surface temperatures for geological times and locations where the ^{18}O content of the water is not well known (e.g., Thiagarajan et al., 2014; Tripati et al., 2014; Rodriguez-Sanz et al., 2017; Henkes et al., 2018). Carbonate clumped isotope thermometry has also been used to infer temperatures of processes that occur in the shallow crust such as diagenesis (Dennis & Schrag, 2010; Huntington et al., 2011; Cummins et al., 2014; Winkelstern & Lohman, 2016; Ryb & Eiler, 2018) and metamorphism (Ferry et al., 2011; Ryb et al., 2017; Lloyd et al. 2017).

The application of carbonate clumped isotope thermometry to the reconstruction of climate, water $\delta^{18}O$ values, or the thermal histories of rocks is complicated by the alteration of Δ_{47} values at elevated burial temperatures through solid-state reordering of C–O bonds (Passey & Henkes, 2012; Henkes et al., 2014; Stolper & Eiler 2015; Lloyd et al., 2017; Shenton et al., 2015; Gallagher et al., 2017; Lacroix & Niemi, 2019; Ryb et al., 2017; Ingalls, 2019). Previous studies have used controlled heating experiments to constrain the kinetics of solid-state isotope reordering of calcite (Passey & Henkes, 2012; Henkes, et al., 2014; Stolper & Eiler, 2015; Brenner et al., 2018), apatite (Stolper & Eiler, 2015) and dolomite (Lloyd et al., 2018). In these experiments, aliquots of the mineral of interest were held at a constant temperature for different amounts of time to create a time series over which the mineral Δ_{47} values could be observed to gradually approach equilibrium appropriate for that temperature. The rate of change of Δ_{47} values observed in such experiments constrains the kinetics of isotopic re-distribution among carbonate ions in the mineral lattice.

A key finding of these previous experiments is that solid-state alteration of Δ_{47} values in calcite, apatite, and dolomite all follow non-first-order kinetics. This finding has been interpreted as evidence that isotopic reordering is a two-stage process involving two mechanisms with different rate laws. Early in each set of time-series experiments, the rate of change of Δ_{47} values is dominated by a relatively fast process, which sharply transitions to a slower process that controls the remainder of the time series. Passey & Henkes (2012) attributed the initial rapid decrease in Δ_{47} in calcite to rapid diffusion facilitated by initially abundant lattice defects, and suggested the transition to slower kinetics reflects annealing of those defects, reducing their abundance and therefore the overall rate of isotopic re-equilibration. Stolper & Eiler (2015) proposed an alternative reaction-diffusion model to explain the two stages of calcite reordering. This model introduced the concept of 'pairs' and 'singletons.' Whereas a 'clump' is a carbonate group that contains both ^{13}C and ^{18}O, a 'pair' is a set of two adjacent carbonate groups, one of which contains ^{13}C and the other of which contains ^{18}O, while a 'singleton' is any carbonate group that contains either a single ^{13}C or a single ^{18}O, and has as immediate neighbors only carbonate ion units that lack ^{13}C and ^{18}O (i.e., they are all $^{12}C^{16}O_3^{2-}$). Stolper and Eiler (2015) suggested that clumped isotope evolution reflects rapid exchange between 'clumps' and 'pairs' coupled with slow diffusion-controlled separation of 'pairs' into isolated 'singletons' (Figure 6-1a). In this case, the reordering reaction is described by the equation:

$$^{13}C^{18}O^{16}O_2^{2-} + {}^{12}C^{16}O_3^{2-} \overset{k_f/k_b}{\Longleftrightarrow} pair \overset{k_d/k_s}{\Longleftrightarrow} {}^{12}C^{18}O^{16}O_{2,single}^{2-} + {}^{13}C^{16}O_{3,single}^{2-} \quad (Rxn\ 2)$$

where k_f is the forward rate of transformation of a clump and neighboring unsubstituted carbonate ion into a pair, k_b is the rate of back reaction of a pair to form a clump, k_d is the diffusion-controlled rate of separation of pairs to form singletons, and k_s is the rate of diffusion for singletons to remake pairs.

The presence of the intermediate pool of pairs can explain the two stages of clumped isotope reordering as follows (Stolper and Eiler, 2015): the first stage of rapid reaction is dominated by the formation of pairs from clumps through isotope exchange of immediately adjacent neighbors, while the second stage is dominated by diffusion in the crystal lattice. Because the second stage is slower than the first, the region surrounding the initial clumps becomes saturated with pairs of singly-substituted carbonate ion units that have not yet diffused away from

each other; back reaction of this saturated pool of pairs is what buffers the decrease in the Δ_{47} value during the slower, diffusion-limited stage of the time series. Stolper and Eiler (2015) did not offer an atomistic explanation for why the transition from clump to pair is faster than the separation of pairs — intuition might predict these should have the same rate, as both types of reactions involve migration of ^{18}O (and perhaps ^{13}C) from one carbonate ion unit to another. This unresolved aspect of the reaction-diffusion model is one of the inspirations for the present study.

While both the defect-annealing and reaction-diffusion models have been successfully applied to natural samples (Henkes et al., 2014; Shenton et al., 2015; Lloyd et al., 2017; Ryb et al., 2017, Ingalls, 2019), it has been argued that the reaction-diffusion model is favored by the observation that the kinetics of isotopic reordering in optical calcite, brachiopods, and deformed and undeformed natural marbles are indistinguishable from one another (the idea being that these diverse materials might be expected to differ in their initial defect populations; Stolper & Eiler, 2015; Ryb et al., 2017; Lloyd et al., 2018). Nevertheless, there is a strong motivation to establish which of these two interpretations (or perhaps some other not yet proposed) is correct. And, if the reaction-diffusion model is correct, we still must understand why it is that an initial exchange between two adjacent carbonate ion groups is significantly faster than subsequent, but otherwise generally similar exchanges. The answers to these questions will dictate how carbonate clumped isotope measurements are used to reconstruct temperature-time histories of rocks that have been heated during protracted burial in sedimentary basins, and may inspire new tools based on the physical processes that control this phenomenon.

In this study, we re-examine this problem through observations of the kinetics of Δ_{47} changes when aragonite is exposed to elevated temperatures, at either high pressure where aragonite remains stable during heating, or at low pressure where it transforms into calcite over the time scales of our heating experiments. This work was initiated to obtain constraints on the susceptibility of aragonite to clumped-isotope reordering at shallow crustal conditions. However, our initial experimental results made it clear that this process provided an unexpected window on the atomistic mechanisms of the general phenomenon of clumped isotope reordering.

Aragonite is a polymorph of calcium carbonate that is common in nature, despite the fact that it is thermodynamically unstable at Earth surface conditions and readily transforms into calcite

through heating or dissolution-reprecipitation reactions (Jamieson, 1953; Bischoff, 1969; Carlson, 1980; Budd, 1988). Clumped isotope compositions of aragonite follow the same temperature vs. Δ_{47} calibration curve as other carbonate minerals (Ghosh et al., 2006; Thiagarajan et al., 2011; Bonifacie et al., 2017). Clumped isotope compositions of fossil aragonite have been used in paleoclimate reconstructions of the recent ice age (Thiagarajan et al., 2014) and deeper times of the Phanerozoic (Dennis et al., 2013). Given its thermodynamic instability, it has generally been assumed that aragonite found in nature has been unaltered in its elemental and isotopic compositions. Recently, it has been shown in laboratory experiments and natural speleothems that the carbon, oxygen, and clumped isotope compositions can all be altered during the aragonite to calcite phase transition (Zhang et al., 2014; Staudigel & Swart, 2016). In particular, Staudigel & Swart (2016) observed complicated clumped isotope reordering patterns in aragonite heating experiments over a range of temperatures (125–425°C), including unexpected increases in Δ_{47} values during the heating process in certain experiments. These increases in Δ_{47} values are, however, not consistently observed in all their experiments, and are statistically indistinguishable from the previous time step in many cases. The authors noted these complexities but described aragonite reordering with a first order kinetic model. Staudigel & Swart (2016) also noticed that aragonite reordering initiates at lower temperatures than calcite does. However, a systematic decreasing trend in the bulk isotope composition (2.5‰ in $\delta^{18}O$ and 1.5‰ in $\delta^{13}C$) with time was observed in these experiments, suggesting a possible influence of open system exchange that would complicate the interpretation of these data as simply reflecting the solid-state reordering process.

We present new aragonite reordering experiments that reproduce and extend the previously observed complex clumped isotope reordering patterns, and we explain these findings as natural consequences of the reaction-diffusion model in a system undergoing a phase transition. We then test this hypothesis further through experiments in which we manipulate the distributions of clumped, pair, and singleton carbonate groups by preliminary thermal treatments to aragonite and calcite, and then observe the effect of those treatments on the solid-state reordering kinetics of both phases in a second heating experiment (Figure 6-1b,c). We summarize our hypothesis and experimental tests in the reaction-diffusion framework with a fluid-flow analogy in Figure 6-1, which are detailed in the following sections. Our experimental results suggest the presence of an

intermediate pool of pairs in both aragonite and calcite, re-enforcing the reaction-diffusion model of clumped isotope reordering.

6.2 Materials and Methods

6.2.1 Aragonite Samples

The aragonite used in our experiments was obtained from Tazouta, Sefrou Province, Fès-Boulemane, Morocco. It is a fist-sized aggregate of faceted intergrown crystals that are 0.5–1 cm in size. The sample was chosen due to its size, visual homogeneity and low-temperature origin. Replicate analysis (n = 21) of the bulk and clumped isotope composition of the aragonite yields a $\delta^{13}C$ value of 7.53±0.17‰ (VPDB), a $\delta^{18}O$ value of –7.49±0.19‰ (VPDB), and a Δ_{47} value of 0.757±0.028‰ (means and aliquot-to-aliquot standard deviations; all reported Δ_{47} values are given in the absolute reference frame following Dennis et al., 2011). The Δ_{47} value corresponds to a formation temperature of 16±5°C (Dennis et al., 2011). The reported standard deviations of bulk and clumped isotope compositions are higher than the long-term reproducibility of carbonate standards at Caltech (0.03‰ for $\delta^{13}C$, 0.08% for $\delta^{18}O$, 0.02‰ for Δ_{47}), and suggest some natural heterogeneity within our sample. In interpreting our experiment results, we consider a measured isotope composition of a sample significantly different from others only when these differences exceed the internal variabilities in the starting materials.

6.2.2 Aragonite Reordering Experiments

The aragonite crystals were coarsely crushed into ~10 mg fragments (each ~1–2 mm across). The crystals were not further reduced in grain size because we wished to minimize the surface area and therefore any effects of adsorbed water or other surface chemistry. Approximately 20 mg of aragonite fragments were sealed in ¼″ quartz or Pyrex® tubes with 6.6 kPa isotopically distinct CO_2 gas ($\delta^{13}C$ = –11‰, $\delta^{18}O$ = +16‰, VPDB) in the headspace. The CO_2 gas was cryogenically purified with a dry ice-ethanol mixture to remove water vapor. The experiments were carried out under CO_2 atmosphere to minimize decarbonation of the aragonite, as well as to detect whether open-system isotope exchange reactions had occurred.

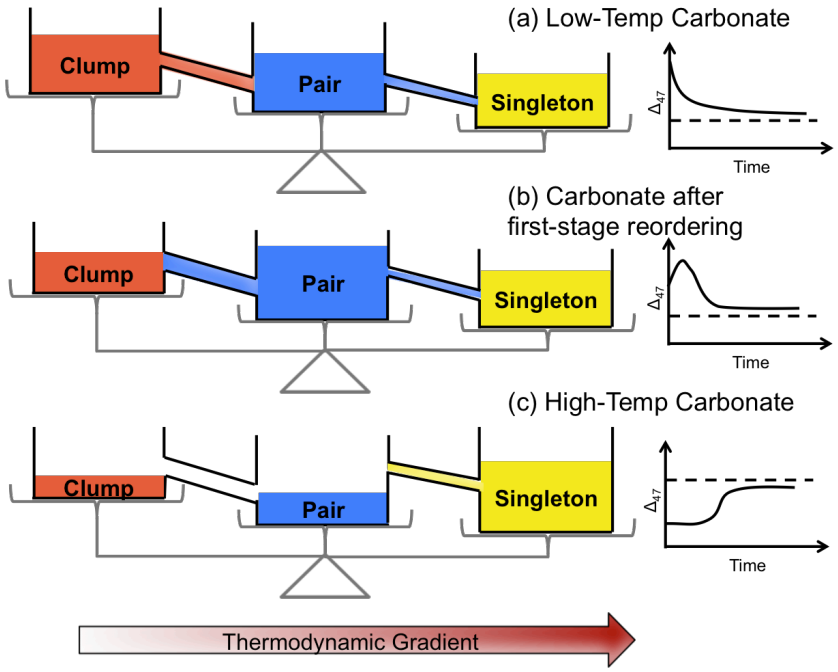

Figure 6-1 A fluid flow analogy to the reaction-diffusion model as applied to different reordering experiments in this study. In the model, there are three pools of isotopically substituted carbonate groups in carbonate minerals: clumps, pairs and singletons, shown as fluids of different colors. The directions of the reactions (fluid flow) depend on two things: the fluid levels and the vertical positions of the tanks. The fluid level corresponds to actual concentrations of these carbonate groups, and the relative base height of the tanks corresponds to the thermodynamic trend. The plots on the right column show expected clumped isotope reordering patterns in a controlled heating experiment based on the abundance of clumps, pairs and singletons in each case. (a) This scenario represents a low-temperature carbonate, like the untreated starting material in the experiment. When exposed to high temperatures, the thermodynamic gradient drives the reaction from clumps to pairs and pairs diffuse away to form singletons, with a decrease in Δ_{47} over time. (b) This scenario represents a mineral that has been heated for a relatively short amount of time. In this case, pairs build up in the mineral at the expense of clumps. The pairs may diffuse to fill the singleton tank, but this process has a higher kinetic limit (thinner tube between blue and yellow), so that the build-up of pairs exceeds the formation of singletons. The pretreated calcite in our experiment may represent this scenario, with pairs building up in excess of equilibrium, and could remake clumps when a higher temperature is imposed. A similar scenario may explain Δ_{47} increases in aragonite as phase transition is triggered. The multi-stage reordering in aragonite is a likely combination of (a) and (b). An analogy for pair-excess created by phase transition may be a shrink in the size of the tank for pairs due to a rearrangement of carbonate ions in the lattices. The difference between the two minerals may also be related to different reaction rates (size of connection rubes), or different responses of the equilibrium pair concentration (vertical position of tanks) to the thermodynamic gradient. (c) This scenario represents the aragonite equilibrated at high temperatures. The equilibration process destroys most clumps and separates pairs into singletons, and the reordering reaction only goes in the reverse direction afterwards at a lower temperature. Clump formation can only happen when excess pairs build up, and a buffering time is expected for an increase in Δ_{47} to be observed.

The tubes containing aragonite and CO_2 were put into a box furnace held at one of several prescribed temperatures (200–500°C). For each temperature, different aragonite samples were heated for different lengths of time to create a time series of clumped isotope reordering. After heating, we weighed each sample and determined the fractions of aragonite and calcite in the samples by X-ray diffraction (XRD) or Raman spectroscopy before isotope compositions were measured. For most samples, the weight loss is <0.3mg before and after heating, and the bulk isotope compositions are within the initial heterogeneities of the starting material, consistent with no decarbonation or open-system exchange (Table 6-1, Figure 6-2c,f). In three of the heating experiments, the aragonite was run in unsealed tubes and thus was exposed to the ambient atmosphere (Table 6-1). As with the sealed tube experiments, no significant decarbonation or open system exchange was observed for these three experiments. The aragonite to calcite phase transition was faster when exposed to the ambient atmosphere (Figure 6-2b,e), but the clumped isotope reordering pattern was similar to the experiments with sealed tubes.

6.2.3 High-Pressure Aragonite Experiment

For this experiment, we used a cylinder cored from a large crystal that comprised a portion of our aragonite sample. The core (260 mg) was loaded into a 0.2″ (outer diameter) Au capsule welded at both ends (for the second weld, the capsule was partially immersed in a water bath to minimize any heating of the aragonite). The capsule was run in a 1/2″ piston cylinder pressure vessel using an assembly that consisted of inner pieces of MgO (dried at 1000°C for ~8 hours), a straight-walled graphite furnace, and an outer sleeve of calcium fluoride. Temperature was monitored and controlled to within 1°C of the set point using a $W_3Re/W_{25}Re$ thermocouple (care was taken to avoid thermocouple oxidation by bleeding N_2 gas into the slot in the thermocouple plate). Run conditions were 1.7 GPa and 600°C and the sample was quenched after 10 days. Based on thermocouple output as a function of time, the sample cooled to room temperature in ~30 s. The experiment was designed to equilibrate the clumped isotope composition (and potentially the concentration of pairs) at high temperature while maintaining aragonite in its stability field. The *P-T* conditions of the experiment were well within the aragonite field based on the $CaCO_3$ *P-T* phase relations compiled by Carlson (1980), and Raman spectroscopy showed that the post-run material

was, indeed, aragonite (Figure 6-3c). Next, an aliquot of this *P-T*-treated aragonite was measured for bulk and clumped isotope composition, while other fragments went through a reordering experiment at 350°C at ambient pressure in a CO_2 atmosphere (see Section 2.2) before isotopic analysis. A 350°C reordering experiment using untreated fragments of the aragonite was carried out in parallel for direct comparison.

6.2.4 Two-Step Calcite Heating Experiment

The two-step calcite heating experiment was designed to test if the complex clumped isotope reordering behavior in aragonite, in particular increases in Δ_{47} during heating, can occur in calcite. An optical calcite (catalog # N21-1) was selected from the Caltech mineral collection for its size, clarity, lack of visible defects or inclusions, and its relatively low-temperature origin. Bulk and clumped isotope analyses (n = 17) yield a $\delta^{13}C$ value of –1.55±0.45‰ (VPDB), a $\delta^{18}O$ value of –16.96±0.30‰ (VPDB) and a Δ_{47} value of 0.586±0.006‰, which corresponds to a temperature of 63±3°C (Bonifacie et al., 2017). While the bulk isotope compositions of this calcite show substantial heterogeneity, the clumped isotope composition is relatively homogeneous. The sample was crushed into 10–30 mg fragments and sealed in quartz tubes with 6.6 kPa purified CO_2 gas that is isotopically distinct ($\delta^{13}C$ = –11‰, $\delta^{18}O$ = +16‰, VPDB) in the headspace. The tubes were initially heated at 450°C for 5 hours, and cooled quickly to room temperature (within ~2 minutes) using a compressed air duster. In the second step of this experiment, the pretreated samples from the first step were heated at 500°C for different time intervals. We repeated this experiment twice to generate a replicate set of samples.

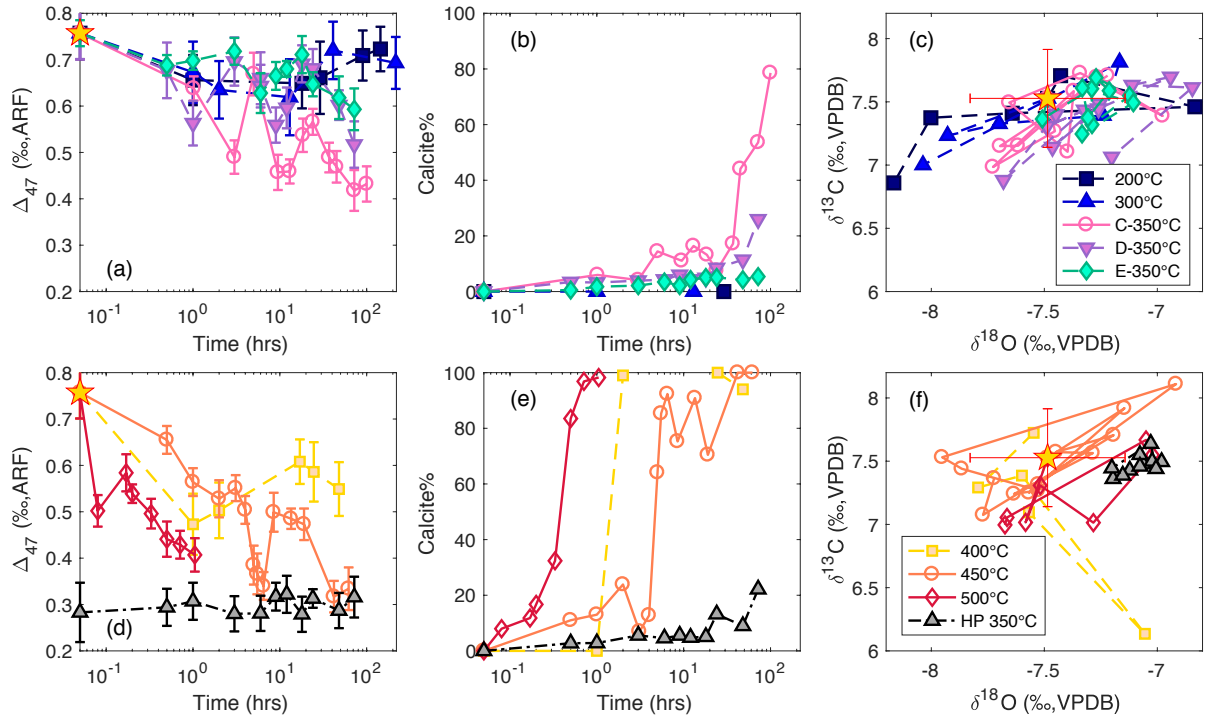

Figure 6-2 Isotope and mineralogy data of the aragonite reordering experiments. Panels (a)-(c) show results of the ambient pressure experiments between 200°C and 350°C, while panels (d)-(f) show results of the ambient pressure experiments between 400°C and 500°C together with the 350°C reordering experiment on the high pressure high temperature (600°C) equilibrated aragonite. (a, d) Clumped isotope composition evolution with time (2σ error bars). The star represents the starting composition of the aragonite. At each temperature, increases in Δ_{47} values of 0.05–0.15‰ during the heating process are observed in the ambient pressure experiments. The black triangles represent the reordering experiment starting with clumped isotope randomized aragonite. Three heating experiments (C-350°C, 450°C, 500°C) were conducted in air (open symbols) while others were conducted in CO_2 atmosphere (filled symbols). (b, e) Percentage of calcite in the samples determined by XRD (200°C, 300°C, 400°C) or Raman spectroscopy (other experiments). There is scatter in the proportions of calcite from the XRD and Raman measurements, but in general there is an increase in calcite% with time in all experiments above 300°C. (c, f) $\delta^{13}C$ and $\delta^{18}O$ values of the reordering experiments. The stars show the initial composition of the aragonite with 2σ standard deviations. The data points are connected in the order of heating time. Most data points scatter within the 2σ range of the initial composition of the aragonite ($\delta^{13}C$ = 7.53±0.17‰ and $\delta^{18}O$ = –7.49±0.19‰), and no systematic trend is observed, suggesting closed system behavior during the reordering experiments.

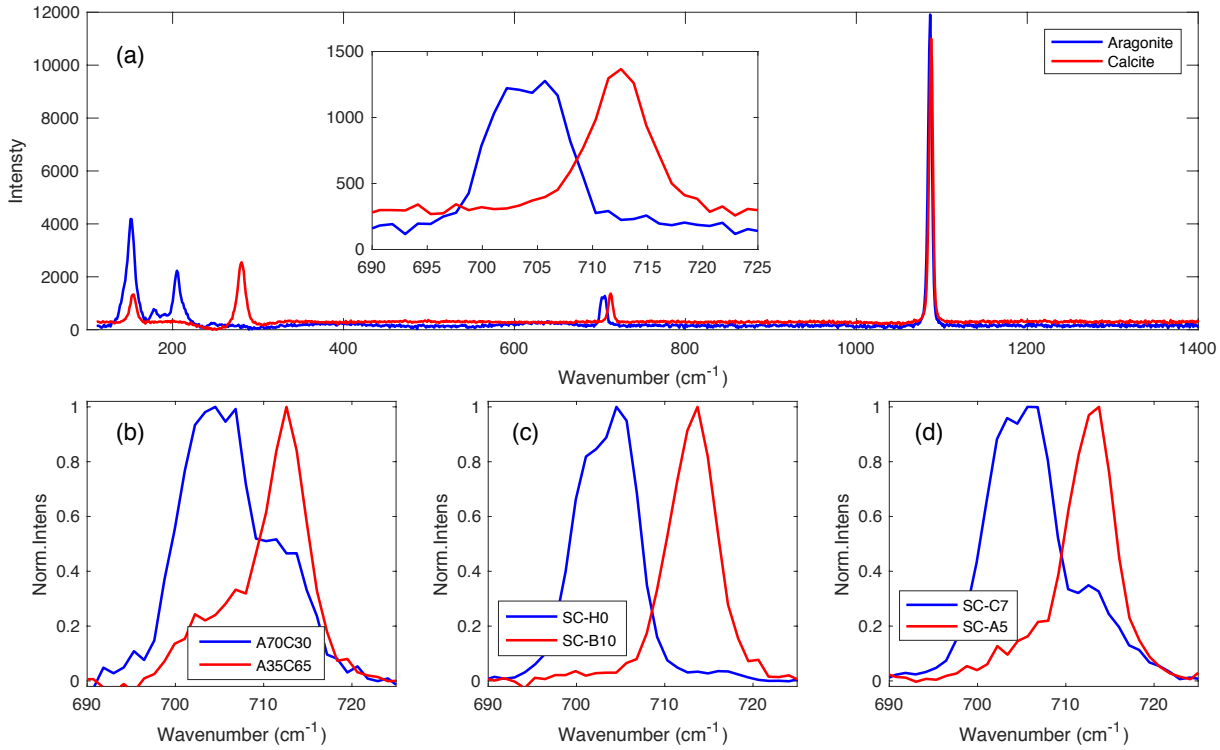

Figure 6-3 Examples of Raman spectra used to determine fractions of aragonite and calcite in the samples. (a) Full spectra of pure aragonite (blue) and calcite (red), with the inset zooming in to the wavenumber range of carbonate ion planar bending mode, used to determine relative abundance of aragonite (704 cm^{-1}) and calcite (713 cm^{-1}) in the samples. (b) Spectra of powder mixtures of aragonite and calcite used as calibration standards. Examples shown here are a 70:30 aragonite:calcite mixture (blue) and a 35:65 aragonite:calcite mixture. (c) Spectra of samples from two experiments. SC-H0 is an aragonite sample whose clumped isotope composition was equilibrated at high temperature (600°C) and high pressure (1.7 GPa). These P-T conditions preserved its aragonite structure. SC-B10 is a sample that has been completely converted to calcite after heating at 450°C for 42 hours. (d) Spectra of samples from two other experiments. SC-C7 was heated at 350°C for 37 hours, and was determined to have 17% calcite by peak area. SC-A5 was heated at 500°C for 30 minutes, and has 85% calcite.

6.2.5 Mineralogy

In order to determine the extent to which aragonite transformed to calcite during the low-pressure, high-temperature experiments, samples were analyzed post-run by XRD or Raman spectroscopy. XRD measurements were performed with a Bruker D2 Phaser benchtop instrument (Cu K_α source) at Caltech. Relative peak areas at specific 2θ angles (30° for calcite, 46° for aragonite) were compared to determine the proportions of aragonite and calcite in the samples,

using an approach similar to Dickinson & McGrath (2001). Relative peak areas were converted to mass fractions with a calibration curve generated from powder mixtures of pure aragonite and calcite. The detection limit of the method is approximately 1% for calcite and 5% for aragonite.

The Raman measurements were performed on a Renishaw M1000 Micro Raman Spectrometer at Caltech. The system uses a solid-state 514.3 nm laser with 100 mW beam power, and the measurements were done with 10% power at 5x magnification (~2 mW on sample) to minimize sample damage and maximize the covered area. Multiple spots (n = 5–10) were measured for each sample to get an average spectrum. Following Dickinson & McGrath (2001), the relative proportions of aragonite and calcite were determined using the scattering peaks for the carbonate ion planar bending mode (704 cm^{-1} for aragonite, 713 cm^{-1} for calcite). Relative peak areas were converted to mass fractions with a calibration constructed from powder mixtures of pure aragonite and calcite (Figure 6-3). The peak areas scale close to 1:1 with mass fractions in the calibration standards. The Raman method was used for most samples because it requires less material than the XRD method we employed, and limited amounts of sample were recovered from each experiment (especially the high-pressure experiment described in Section 2.3). We also viewed the Raman measurement as more robust because of the greater linearity of its calibration trend.

6.2.6 Stable Isotope Measurements

The bulk and clumped isotope compositions of the samples were measured using a Thermo MAT253 isotope ratio mass spectrometer at Caltech. Sample preparation and analysis procedures have been previously described in detail (Ghosh et al., 2006; Guo et al., 2009; Huntington et al., 2009; Passey et al., 2010). In brief, samples (~10 mg) were digested in phosphoric acid at 90°C. Evolved CO_2 gas was purified cryogenically and went through a Porapak Q (50/80 mesh) GC column held at –20°C, and then measured against a reference CO_2 gas. The measurements were standardized to heated (1000°C) and water-equilibrated (25°C) CO_2 gases, and in-house carbonate standards. In the calculation of bulk and clumped isotope compositions, we used the $^{17}O/^{16}O$, $^{18}O/^{16}O$ ratios for VSMOW and the $^{13}C/^{12}C$ ratio for VPDB suggested by Brand et al. (2010), which were found to minimize inter- and intra-laboratory discrepancies in reported Δ_{47} values

(Schauer et al., 2016; Daëron et al., 2016). Measurements and uncertainties were calculated in the absolute reference frame (Dennis et al., 2011) following Daëron et al. (2016).

6.3 Results

6.3.1 Aragonite-Calcite Phase Transition

Given its instability under ambient pressure, aragonite is expected to transform into calcite during our low pressure heating experiments. XRD and Raman spectroscopy measurements confirm this general prediction, although there is significant variation in the reaction progress as a function of time (Figure 6-2b,e). Similar variations in reaction progress were observed in the XRD powder patterns in the aragonite heating experiments of Staudigel & Swart (2016). This is likely related to the phase transition progressing inhomogeneously through the crystal lattice. Nevertheless, the overall pattern of the time and temperature evolution of the reaction is clear: at 200 and 300°C, we observed negligible production of calcite over the course of our experiments. Significant amounts of newly grown calcite were observed at temperatures of 350°C and above. When the samples were exposed to the ambient air (rather than being heated in a pure CO_2 atmosphere), 80% of the aragonite was converted to calcite in 72 hours at 350°C (Experiment SC-C). However, such rapid conversion at this relatively low temperature was atypical; the experiments conducted at 350°C in a CO_2 atmosphere underwent 5–25% conversion after 72 hours (Experiment SC-D, SC-E and SC-H). We conclude that when the reaction proceeds in air, the phase transformation is accelerated, perhaps due to the presence of water vapor. At 400°C and 450°C, aragonite was mostly converted to calcite within 10 hours. At 500°C, nearly complete conversion to calcite was achieved in 40 minutes (Figure 6-2e). Previous studies that conducted in-situ XRD and FTIR characterizations of the aragonite to calcite phase transition show a more rapid conversion over a period of ~10 minutes as the temperature is raised to 400–450°C (Antao & Hassan, 2010; Koga et al., 2013). Other experimental studies have found timescales for the phase transition more similar to what we observe, from minutes to hours above 400°C, depending on the sample origin, grain sizes and the experimental method (Davis & Adams, 1965; Madon & Gillet, 1984; Koga et al., 2013; Staudigel & Swart, 2016). Thus, we find a threshold temperature for

significant phase transition similar to that observed in previous studies, and rates of conversion that lie at the slower end of the spectrum of values reported in previous work. We suspect that the relatively slow rate of the phase transition measured in our experiments is related to the length scale of the techniques we used to characterize crystal structure for most of our experimental products. XRD (used for only a few of our samples) observes structures that are coherent over hundreds to thousands of unit cells (10^{-8}–10^{-7} m), whereas Raman spectroscopy (used for most of our samples) observes structural properties at length scales corresponding to the wavelengths of infrared light (10^{-6} m). As a result, phase transitions detected by Raman spectroscopy might be seen to occur later than those detected by XRD (i.e., assuming phase transformation is structurally coherent over longer length scales as time progresses). This suspicion is supported by the observation that our XRD characterization of the phase transition at 400°C indicated that it was completed in two hours, faster than the 450°C experiment measured by Raman spectroscopy.

6.3.2 Clumped Isotope Reordering of Low-Temperature Aragonite

Given the thermodynamic basis for the carbonate clumped isotope thermometer, it is expected that the Δ_{47} value of a carbonate mineral that initially grows at low-temperature and then is subjected to a higher temperature will monotonically decrease in Δ_{47} until it approaches the new, higher temperature equilibrium state of a lower Δ_{47} value (Figure 6-1a). This behavior was previously observed in calcite, apatite, and dolomite reordering experiments (Passey & Henkes, 2012; Henkes et al., 2014; Stolper & Eiler, 2015; Lloyd et al., 2018; Brenner et al., 2018). The reaction progress of solid-state isotopic reordering we observe in aragonite violates this expectation. Following an initial rapid decrease in Δ_{47}, we observe abrupt increases in Δ_{47}, with amplitudes in the range of 0.05–0.15 ‰, followed by a more gradual decrease in Δ_{47} values toward the thermodynamic equilibrium values (Figure 6-2a,d, Figure 6-4). This complex pattern has amplitudes of initial fall and subsequent rise that are large multiples of our analytical precision, and was observed to be significant and generally homologous in form in all of the experiments in which there was significant contrast between the initial and final equilibrium Δ_{47} values.

In our 350°C experiments conducted in both air (SC-C) and CO_2 (SC-D and SC-E), it is clear that there are two separate increases in Δ_{47} in the first 24 hours, separated by an intermediate ‘dip’, and that both of the increases and all three periods of decrease are statistically well resolved

(Figure 6-2a, 4). There is a suggestion that the 450°C experiment conducted in air could also have two separate periods of increasing Δ_{47}, but the first of them is not clearly resolved from the surrounding pattern of decreasing Δ_{47}. Experiments conducted at higher and lower temperatures have only one increase in Δ_{47} during the reordering process.

For most series of experiments conducted at one temperature, the first (or only) increase in Δ_{47} observed mid-way through the heating period occurred at the initial stage of the phase transition, i.e., the sample contained less than 20% calcite as determined by XRD or Raman spectroscopy (Figure 6-4). However, as the proportion of calcite increases (i.e., >20%), the Δ_{47} values decrease again with further heating. Because the timing of the first appearance of calcite and time-evolution in the calcite/aragonite ratio are somewhat irregular in detail, it is not always clear how the rate and direction of change in Δ_{47} relates to the progress of the aragonite to calcite phase transition. However, when we plot the percentage of calcite vs. the Δ_{47} value (a bulk measurement of both aragonite and calcite), it is clear that increases in Δ_{47} occur early in the progress of the aragonite to calcite transition (Figure 6-4). In summary, the reorganization of ^{13}C and ^{18}O (i.e., changes in Δ_{47} value) that occurs when aragonite is heated can be described as a (at least) three-stage process: initial destruction of ^{13}C–^{18}O bonds (decrease in Δ_{47}), followed by a re-formation of ^{13}C–^{18}O bonds (increase in Δ_{47}), followed by a monotonic decay in ^{13}C–^{18}O bonds until the high temperature equilibrium Δ_{47} value is reached. As noted above, in some experiments, a second cycle of increase and subsequent decrease in Δ_{47} is observed. The stage or stages of heating during which ^{13}C-^{18}O bonds re-form is both a strong departure from thermodynamic equilibrium at the conditions of the experiment, and clearly first occurs during the early stage of aragonite to calcite transition. This pattern is reproducible across a temperature range of more than 100°C. We also note that the Δ_{47} values approach equilibrium at rates that are statistically indistinguishable from the calcite reordering experiments (Passey & Henkes, 2012; Henkes et al., 2014; Stolper & Eiler, 2015) after most of the aragonite has been converted to calcite.

Table 6-1 Data from Aragonite and Calcite Clumped Isotope Reordering Experiments

Sample	Temp (°C)	Heat Time (hrs)	$\delta^{13}C$ (‰,VPDB)[e]	$\delta^{18}O$ (‰,VPDB)[e]	Calcite%[f]	Δ_{47} (‰,ARF)[g]
SC-A2[a]	500	0.71	7.055±0.005	–7.665±0.014	97	0.429±0.015
SC-A3	500	0.33	7.548±0.002	–7.022±0.017	32	0.496±0.016
SC-A4	500	0.17	7.308±0.003	–7.518±0.010	12	0.584±0.020
SC-A5	500	0.50	7.668±0.004	–7.050±0.016	85	0.441±0.019
SC-A6	500	0.20	7.014±0.004	–7.283±0.010	17	0.539±0.010
SC-A7	500	1.05	6.996±0.004	–7.674±0.007	98	0.407±0.018
SC-A8	500	0.08	7.016±0.005	–7.583±0.008	8	0.502±0.017
SC-B1	450	1	7.250±0.003	–7.568±0.004	13	0.564±0.015
SC-B2	450	19	7.706±0.002	–7.193±0.009	70	0.473±0.017
SC-B4	450	8.5	7.564±0.003	–7.285±0.009	75	0.499±0.021
SC-B5	450	2	7.316±0.002	–7.527±0.009	24	0.528±0.020
SC-B6	450	3.1	8.110±0.002	–6.917±0.006	7	0.551±0.014
SC-B7	450	6.5	7.241±0.004	–7.634±0.008	92	0.340±0.015
SC-B9	450	13.5	7.572±0.004	–7.448±0.009	91	0.485±0.011
SC-B10	450	42	7.075±0.005	–7.771±0.004	100	0.317±0.017
SC-B11	450	4	7.531±0.003	–7.952±0.008	13	0.504±0.015
SC-B12	450	0.5	7.919±0.003	–7.145±0.006	11	0.655±0.015
SC-B13	450	5	7.440±0.003	–7.865±0.010	64	0.385±0.021
SC-B14	450	62	7.364±0.003	–7.722±0.007	100	0.334±0.023
SC-B15	450	5.5	7.269±0.003	–7.527±0.013	85	0.366±0.022
SC-C2[b]	350	5	7.585±0.002	–7.370±0.010	14	0.669±0.023
SC-C3	350	13	7.494±0.003	–7.655±0.006	16	0.459±0.013
SC-C4	350	1.02	7.268±0.003	–7.453±0.006	6	0.638±0.013
SC-C5	350	3	6.985±0.003	–7.727±0.004	4	0.490±0.018
SC-C6	350	18.5	7.728±0.005	–7.341±0.017	13	0.537±0.018
SC-C7	350	37	7.696±0.003	–7.268±0.006	17	0.489±0.016
SC-C8	350	45	7.153±0.002	–7.616±0.010	44	0.469±0.017
SC-C9	350	24	7.389±0.002	–6.976±0.010	8	0.566±0.014
SC-C10	350	72	7.150±0.003	–7.696±0.014	54	0.418±0.022
SC-C11	350	9.5	7.105±0.003	–7.397±0.011	11	0.457±0.019
SC-C12	350	100	7.707±0.004	–7.220±0.016	79	0.432±0.019
SC-D1[b]	350	9	7.142±0.008	–7.464±0.012	6	0.559±0.019
SC-D2	350	1	6.880±0.007	–7.681±0.011	3	0.563±0.024
SC-D3	350	3	7.436±0.010	–7.323±0.014	4	0.696±0.026
SC-D4b	350	18	7.697±0.006	–6.942±0.007	5	0.691±0.020
SC-D5	350	0.5	7.400±0.008	–7.449±0.011	3	0.677±0.030
SC-D6	350	48	7.613±0.004	–6.845±0.008	11	0.602±0.016
SC-D7	350	72	7.064±0.008	–7.202±0.013	26	0.517±0.025
SC-D8	350	6	7.306±0.007	–7.489±0.011	4	0.660±0.028
SC-D8b	350	6	7.483±0.006	–7.257±0.008	4	0.643±0.023
SC-D9	350	24	7.632±0.007	–7.112±0.011	8	0.681±0.021

SC-D10	350	12	7.446±0.004	–7.260±0.007	4	0.596±0.022
SC-E1	350	6	7.549±0.004	–7.123±0.005	3	0.628±0.018
SC-E2	350	9	7.691±0.010	–7.271±0.004	2	0.665±0.015
SC-E3	350	1	7.604±0.002	–7.290±0.004	2	0.698±0.012
SC-E4	350	3	7.320±0.002	–7.289±0.005	2	0.718±0.014
SC-E5	350	18	7.375±0.002	–7.307±0.006	5	0.711±0.017
SC-E6	350	0.5	7.364±0.003	–7.509±0.006	1	0.688±0.012
SC-E7	350	48	7.493±0.005	–7.106±0.004	4	0.618±0.019
SC-E8	350	72	7.246±0.002	–7.333±0.003	5	0.593±0.019
SC-E9	350	24	7.610±0.004	–7.332±0.007	5	0.647±0.013
SC-E10	350	12	7.588±0.004	–7.213±0.003	4	0.680±0.013
SC-H0[c]	350	0	7.428±0.046	–7.122±0.049	0	0.283±0.016
SC-H1b	350	9	7.361±0.004	–7.196±0.005	6	0.317±0.015
SC-H2b	350	72	7.445±0.004	–7.201±0.009	22	0.316±0.022
SC-H3	350	48	7.639±0.004	–7.029±0.008	9	0.287±0.019
SC-H4	350	1	7.477±0.006	–7.062±0.009	3	0.307±0.020
SC-H5	350	18	7.459±0.005	–7.077±0.008	5	0.279±0.019
SC-H6	350	0.5	7.495±0.005	–6.981±0.008	3	0.294±0.020
SC-H7	350	12	7.388±0.008	–7.153±0.012	5	0.322±0.020
SC-H8	350	3	7.551±0.005	–7.077±0.009	6	0.280±0.019
SC-H9	350	6	7.499±0.005	–7.023±0.008	5	0.281±0.019
SC-H10	350	24	7.440±0.006	–7.006±0.008	13	0.313±0.010
AP-1	200	1	7.707±0.004	–7.428±0.012		0.656±0.027
AP-7	200	18	7.461±0.005	–6.834±0.010		0.649±0.027
AP-15	200	29	7.410±0.004	–7.642±0.008	0	0.661±0.039
AP-C3	200	90	7.374±0.002	–8.002±0.005		0.709±0.027
AP-C1	200	144	6.859±0.003	–8.166±0.004		0.723±0.024
AP-4	300	1	7.233±0.006	–7.928±0.011	0	0.673±0.033
AP-L	300	2	7.327±0.004	–7.700±0.010		0.635±0.031
AP-2	300	13	7.392±0.005	–7.240±0.010	0	0.619±0.041
AP-10	300	41	7.813±0.004	–7.167±0.010		0.720±0.031
AP-D6	300	216	7.001±0.003	–8.037±0.006		0.693±0.028
AP-G	400	1	7.096±0.004	–7.568±0.009	0	0.473±0.009
AP-B4	400	2	6.135±0.005	–7.055±0.010	99	0.503±0.033
AP-E	400	17	7.386±0.004	–7.599±0.006		0.608±0.030
AP-B2	400	24.6	7.292±0.005	–7.793±0.011	1	0.586±0.032
AP-B11	400	48	7.724±0.007	–7.547±0.015	94	0.549±0.029
N21-1a1[d]	500	0	–1.381±0.028	–16.788±0.080	100	0.474±0.015
N21-1a2	500	0	–1.168±0.068	–16.894±0.030	100	0.426±0.017
N21-1b1	500	0.25	–1.658±0.026	–17.205±0.101	100	0.503±0.018
N21-1b2	500	0.25	–2.296±0.025	–16.641±0.030	100	0.498±0.008
N21-1c1	500	0.5	–1.592±0.048	–17.049±0.134	100	0.424±0.014
N21-1c2	500	0.5	–1.802±0.008	–16.705±0.030	100	0.468±0.007
N21-1d1	500	0.75	–1.879±0.025	–16.936±0.081	100	0.443±0.019

N21-1d2	500	0.75	–1.391±0.036	–17.176±0.030	100	0.439±0.001
N21-1e1	500	3	–1.549±0.026	–16.860±0.124	100	0.361±0.012
N21-1e2	500	3	–2.394±0.020	–16.803±0.030	100	0.406±0.011

a. Shaded rows represent heating experiments in ambient atmosphere without CO_2 in the headspace.
b. Both SC-C and SC-D experiments were conducted at 350°C, and are labeled C-350°C and D-350°C in the figures.
c. The SC-H series are reordering experiments with the clumped isotope randomized aragonite, H0 represents the composition after the 10-day high-pressure equilibration at 600°C (average of 2 aliquots). The SC-H series and SC-D series were done at the same time under the same conditions.
d. The N21-1 series are data from the two-step calcite reordering experiment. The experiment was replicated on two sets of samples. Samples N21-1a1 and N21-1a2 represent the composition after the first step of heating at 450°C for 5 hours.
e. Reported as internal standard errors (1σ).
f. Mass fraction of calcite was determined with XRD for AP samples, and with Raman spectroscopy for SC samples.
g. The Δ_{47} errors are total standard errors (1 SE) calculated following Daëron et al. (2016).

Table 6-2 A Summary of Two-Stage Calcite Reordering Models Presented in Figure 6-5

Model	Tuned Variable[a]	Variable Value Relative to Original Model[b]	Timing of 2nd-Stage Δ_{47} Increase (min)	Magnitude of Δ_{47} Increase (‰)
0	None	Original	N/A	None
1	(k_f, k_d)	(2, 0.5)	5	0.001
2	A	1.6	3	0.0003
3	(A, d_i)	(1.6, 0.99985)	6	0.0005
4	(A, d_i, k_f, k_d)	(6, 0.99918, 2, 2)	13	0.03

a. For the tuned variables, k_f and k_d represent the rate constants for isotope exchange in Rxn 2. 'A' represents the temperature sensitivity of the equilibrium pair concentration presented in the reaction-diffusion model of Stolper & Eiler (2015), following the equation:

$$\ln [pair]_{eqm}(T)/[pair]_{random} = A/T.$$

The variable 'd_i' represents an additional variable introduced to account for potential differences in initial pair concentration of different calcite minerals, and to better fit the data of the first-stage of reordering in our experiment. In Model-3 and Model-4, $[pair]_{initial} = d_i[pair]_{eqm}$.
b. Values represent a multiplication factor applied to the original reaction-diffusion model parameters.

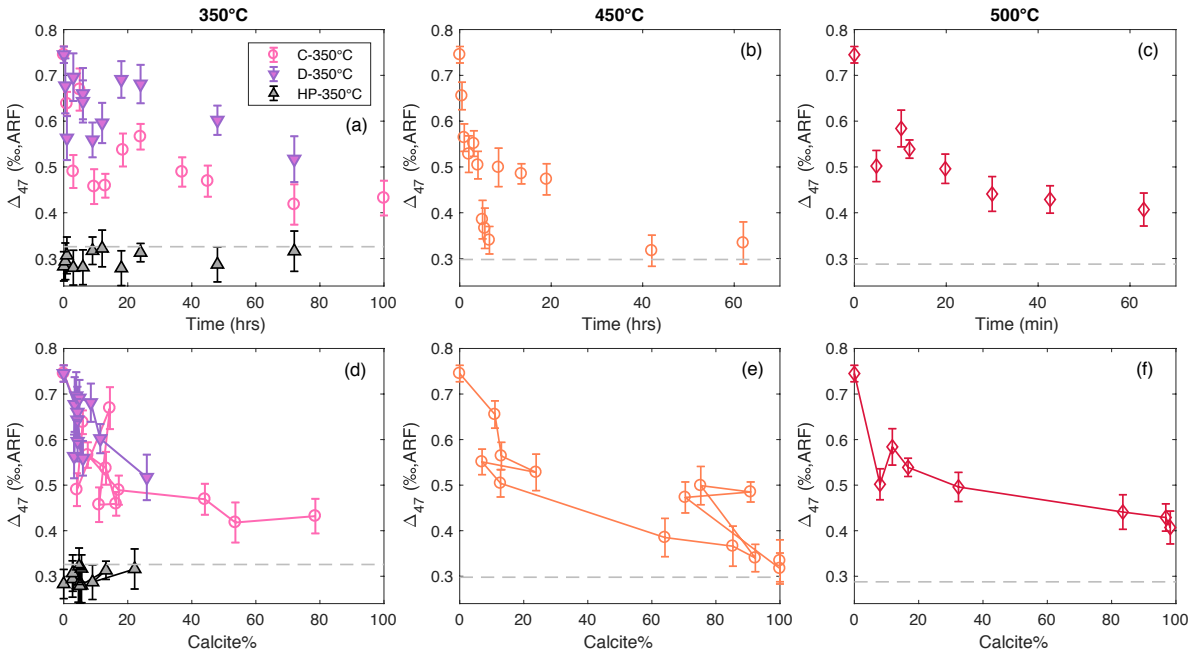

Figure 6-4 Clumped isotope reordering paths with time (a-c) and percentage of calcite (d-f) in the sample for the experiments at 350°C, 450°C, and 500°C. The lines in panels (d-f) connect points in the order of increasing running time. There are apparent reversals in calcite% with time in panels (d) and (e), which represent noise in the phase transition data at 350°C and 450°C. These reversals are more pronounced for experiments conducted in air (C-350°C and 450°C). Increases in Δ_{47} of 0.05–0.15‰ can be observed during each of the experiments, generally in the range of 0–20% phase transition. The experiments at 350°C (C with ambient atmosphere, D and HP with CO_2 atmosphere) have slightly different magnitudes of Δ_{47} reordering with time, but the reordering paths are similar when calcite% is used as the x-axis, suggesting the reordering kinetics is related to the rate of phase transition. The gray triangles are reordering experiments at 350°C with the clumped isotope randomized aragonite. The dashed lines mark the equilibrium Δ_{47} values at 350°C, 450°C ad 500°C respectively (Bonifacie et al., 2017). Note that the x-axis for the 500°C experiment in panel (c) is in minutes.

6.3.3 Clumped Isotope Reordering of High-Temperature-Equilibrated Aragonite

The aragonite heated at 600°C at high-pressure for 10 days achieved a clumped isotope composition (Δ_{47} = 0.283±0.016‰) that is within error of the expected equilibrium at 600°C (Δ_{47_eqm} = 0.273±0.021‰, Bonifacie et al., 2017) (Note that $\delta^{13}C$ and $\delta^{18}O$ of this material are similar to other samples of the starting material: 7.43‰ and –7.12‰, VPDB, respectively; Figure 6-2f). When this pretreated aragonite was subsequently subjected to a second stage of heating at 350°C in a CO_2 atmosphere, the Δ_{47} increased slightly over the course of 72 hours to the somewhat

higher Δ_{47} value expected for equilibrium at 350°C, accompanied by 22% conversion of aragonite to calcite (Figure 6-2d,e, Figure 6-4a,d). The amount of phase transition is similar to the untreated low-temperature aragonite going through the same reordering experiment, but we see no evidence for a sharp rise in Δ_{47} in the middle of the second heating period, as occurred when non-pre-treated aragonite was subjected to this same low-pressure heating schedule (Figure 6-4a,d). A key feature of the high P-T treatment performed on this sample is that it involved a time-at-temperature sufficiently prolonged such that the reaction-diffusion model would predict complete mutual equilibration of all three populations of isotopic species: clumps, pairs and singletons (Figure 6-1c). This series of experiments demonstrates that the anomalous rise in Δ_{47} associated with conversion of aragonite to calcite does not occur in materials that have already attained a fully equilibrated high-temperature isotopic structure due to a long, high-temperature 'soak'; that is, this phenomenon requires that the aragonite to calcite transition takes place in a material that has experienced a sharp drop in Δ_{47} within the previous few hours. This finding also indicates that the increase in Δ_{47} does not arise through a kinetic isotope effect associated with the aragonite to calcite transition (i.e., a dependence of the rate of phase transition on the isotopic composition of the carbonate groups).

6.3.4 Clumped Isotope Reordering in a Two-Step Calcite Experiment

After we subjected two samples of calcite to a first heating treatment of 450°C for 5 hours, their Δ_{47} values dropped from 0.586‰ to 0.474‰ and 0.426‰, respectively, without significant changes in their bulk $\delta^{13}C$ or $\delta^{18}O$ (Table 6-1, Figure 6-5). When each of these pre-heated calcites were subjected to a second heat treatment at 500˚C, their Δ_{47} values increased by 0.03–0.06‰ in the first 15 minutes of the second heating treatment, before decreasing again afterwards. Interpretation of this experiment must be equivocal as the variations in Δ_{47} that we observe are near the 2 standard error limit of significance. Nevertheless, both experimental series suggest that it is possible to subject calcite to a heating schedule that creates subtle but resolvable increases in Δ_{47} in the absence of a phase transition. The specific heating schedule we selected to create this effect was based on a prediction of the reaction-diffusion model, and this experiment is important to our efforts below to interpret and generalize the more pronounced Δ_{47} increases we observe during the aragonite to calcite transition.

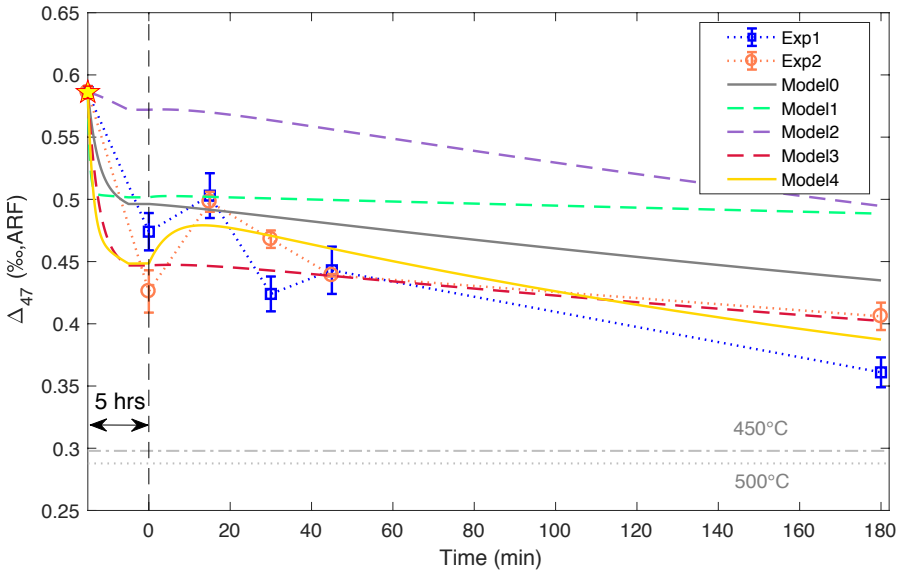

Figure 6-5 Clumped isotope reordering in the two-step calcite heating experiment compared to simulations from the reaction-diffusion model (Stolper & Eiler, 2015). The squares and circles (connected by dotted lines) are replicate reordering experiments at 500°C (second step), to the calcite that was pretreated by heating at 450°C for 5 hours (first step). The star marks the initial composition of the calcite. The vertical line separates the two steps. To the left of the line is the Δ_{47} change with the pretreatment at 450°C for 5 hours (time is not to scale with the second step on the x-axis). The Δ_{47} value at time zero represents the composition after the pretreatment. The dash-dot and dotted horizontal lines mark the thermodynamic equilibrium values at 450°C and 500°C (Bonifacie et al., 2017). In both 500°C reordering experiments, the Δ_{47} values increased by 0.03–0.06‰ after 15 minutes of the second stage, before decreasing toward equilibrium. The solid and dashed curves are model outputs from the reaction-diffusion model with different parameter combinations. The model parameters for each case are listed in Table 6-2. Significant changes to the original model parameters in Stolper & Eiler (2015) are required to generate a curve that fits the data with a well-resolved Δ_{47} increase at the beginning of the second stage (solid gold curve).

6.4 Discussion

The formation of excess ^{13}C–^{18}O bonds (producing an increase in Δ_{47}) during high-temperature transformation of aragonite to calcite is a significant, reproducible observation of this study and appears to act opposite to thermodynamic driving forces. Yet it is also not a kinetic isotope effect associated with some elementary step of the phase transformation, as no such isotopic reordering is observed when aragonite is allowed to achieve a fully equilibrated high-temperature isotopic structure prior to transformation to calcite. This phenomenon has not only

been reproduced in our experiments, but also resembles the similar (though less regular) findings of previous heating experiments performed on aragonites of different origins (Staudigel & Swart, 2016). Moreover, we see suggestive evidence that the same phenomenon can be made to occur in calcite without any phase transformation, provided the calcite is subjected to a specific heating schedule. We find no evidence that any of these effects are accompanied by changes in bulk isotopic content ($\delta^{13}C$ and $\delta^{18}O$) that might provide evidence for open system reactions. We suggest that this behavior is an integral feature of solid-state isotopic reordering in carbonate minerals that needs to be incorporated in future reordering models.

In the following discussion, we describe how this behavior can be conceptually explained by the reaction-diffusion model of Stolper & Eiler (2015). We also discuss the new insights these findings provide regarding the kinetics of atomic mobility within carbonates and the kinetics of the aragonite to calcite transition. Finally, we use these results to support the presence and significance of pairs in carbonate minerals, and to generalize the reaction-diffusion mechanism across carbonate minerals.

6.4.1 The Reaction-Diffusion Model and High-Temperature Formation of Excess ^{13}C–^{18}O Bonds

Increases in Δ_{47} during a high-temperature heating step are a previously unrecognized prediction of the reaction-diffusion model of Stolper and Eiler (2015). Specifically, we now recognize that this phenomenon is a natural consequence of the fact that disproportionation of clumps to form pairs leads to a brief period of time (typically hours at the temperatures of our experiments) when the pairs have not yet diffused apart to form singletons and have the potential to back-react to re-form clumps (Figure 6-1b).

Stolper and Eiler (2015) proposed the reaction-diffusion model as a way of explaining the kink in the time evolution of decreasing Δ_{47} values; specifically, they suggested that this feature marks the time when the rate of net formation of pairs by breakdown of clumps is nearly balanced by the rate of diffusive separation of pairs to form singletons.

We observe several low-pressure time-series where Δ_{47} values rise sharply during the aragonite to calcite transition, with amplitudes of 0.13–0.18‰, or roughly 30–40% of the contrast between the initial Δ_{47} value and the Δ_{47} value the carbonate would have after fully equilibrating at

the temperature of the experiment. Interpreted in the context of the reaction-diffusion model, this implies that the reaction of a clump to form a pair largely reverses at the onset of the aragonite to calcite transition (i.e., 50–80% of clumps destroyed during the earliest stage of heating temporarily re-form). For experiments with two separate Δ_{47} increases at 350°C, the second increase is almost a quantitative reversal of the previous drop in Δ_{47}.

Perhaps the strongest argument that an intermediate pool of pairs is required to drive Δ_{47} increases at high temperatures comes from the lack of a Δ_{47} rise when aragonite is given a long, very high temperature, high pressure 'soak' before the aragonite to calcite transition (see section 3.3 above). This experiment indicates that the sharp increases in Δ_{47} are only a feature of aragonite that undergoes transformation to calcite immediately (within minutes to hours) after its Δ_{47} has decreased in response to heating.

This can be understood as a consequence of the pair mechanism: For all of our experiments involving a single, low-pressure stage of heating, clumps are transformed to pairs early in the experiment, but those pairs have not had enough time to diffusively separate to form singletons, so they are present as a potentially reactive pool of excess pairs when the phase transformation occurs (Figure 6-1b). In aragonite that has undergone long, high-temperature, high-pressure heating, the pool of pairs has been depleted through diffusion to form singletons, removing that pool of excess pairs (Figure 6-1c).

We hypothesize that the reformation of clumps from an over-abundant pool of pairs is associated with the rearrangement of carbonate ions in the crystal lattice on the unit-cell scale. Several models have been proposed to describe the atomistic mechanism of the aragonite-calcite phase transition. Previous studies agree that this solid-state transition involves displacement of calcium layers relative to carbonate layers, and 30° rotations of carbonate groups (Madon & Gillet, 1984; Antao & Hassan, 2010; Miyake & Kawano, 2010). The rotation of carbonate groups converts the 9-coordinated aragonite structure to the 6-coordinated calcite structure, and clearly involves reorganization of Ca–O bonds (Madon & Gillet, 1984; Miyake & Kawano, 2010). However, prior studies did not specify whether this reorganization of the geometries of carbonate ions is accomplished by the breaking and re-forming of C–O bonds or simply involves motions of

carbonate ions with respect to one another. Our findings that the aragonite-to-calcite reaction is accompanied by a large change in ^{13}C–^{18}O ordering suggests that the first possibility is the case.

Each O atom in the aragonite lattice has up to eight nearest neighbor O atoms (i.e., those that can be reached in a straight line, omitting those that share the moving atom's own carbonate ion unit, and noting that some sites that are 'adjacent' by this definition are much closer than others; Figure 6-6a). Thus, if the clump-to-pair transition involved purely random movement of O atoms from one carbonate ion unit to a randomly-selected neighbor, and that the aragonite to calcite transition was accompanied by a second random exchange of an O atom with one of its set of possible 'straight line' nearest neighbors, it should only be possible to recover a small fraction of the original clumped isotope signature (i.e., most ^{18}O atoms that make the first jump away from a clump will not return to their original carbonate ion unit on their second jump; nor are they likely to reach another ^{13}C atom on making a second jump). The fact that most of the Δ_{47} signature that was initially lost is recovered suggests that the transition from clumps to pairs preferentially involves O exchange between only one (or perhaps two) of the possible nearest neighbor pairs, and that the aragonite to calcite transformation is accompanied by an O exchange that takes advantage of that same preferred oxygen site or sites. This might be expected if one of the possible pathways for exchanging an O atom between two carbonate groups has a lower activation energy than any of the other possible exchange mechanisms, and so occurs at a higher rate. In the 9-coordinated aragonite structure, there are five different Ca–O bonds and two non-equivalent oxygen sites, O1 and O2 (Figure 6-6a; Antao & Hassan, 2010; Ye et al., 2012). The strengths of the Ca–O and C–O bonds for these two oxygen sites are different, which we anticipate could give rise to different activation energies of the various possible oxygen exchange pathways. In particular, the three exchange pathways labeled in Figure 6-6a involve breaking the weakest bonds in the aragonite structure and, we suggest, could be energetically favorable. Two of these three pathways involve an O1–O2 exchange (pathways 2 and 3 in Figure 6-6a). After exchange through these two pathways, the aragonite-calcite phase transition would keep the singly-substituted carbonate groups in neighboring positions (i.e., remaining as pairs) as shown in Figure 6-6b. We suggest that quantitative conversion of pairs to clumps can be explained as a two-step mechanism: 1) initial preferential conversion of clumps to pairs along the O1–O2 exchange pathway, followed by 2) forced exchange of O1–O2 oxygen atoms during the aragonite to calcite phase transition. This

hypothesis is an attractive target for future molecular dynamic models of the kinetics of the $CaCO_3$ phase transition and solid-state clumped isotope reordering.

We also draw attention to the fact that the rise in Δ_{47} that accompanies the aragonite to calcite transition is observed at approximately the time when XRD or Raman evidence for calcite formation is first observed, but well before complete conversion of aragonite to calcite (by which time Δ_{47} has fallen again). It would be rational to argue that this is just the behavior expected if the rise in Δ_{47} reflects a kinetic isotope effect associated with the transition (i.e., a dependence of its rate on the isotopic content of the reacting carbonate ions). However, our experiment performed on aragonite that had been isotopically equilibrated at high pressure shows this is not the case. Isotope exchange between adjacent carbonate ion units happens over atomic length scales (10^{-10} m), whereas XRD and Raman observe structures that are coherent over much longer length scales (10^{-8}–10^{-6} m). A comparison of the apparent rates of these three measurements of the aragonite to calcite transition at different spatial scales is shown in an Arrhenius plot (Figure 6-7). We see that over our experimental temperature range, the rate of initial clump-to-pair conversion in aragonite is faster by an order of magnitude than the rate of XRD determined phase transition, which is in turn an order of magnitude faster than the rate of phase transition estimated by Raman spectroscopy over our experimental temperature range. We suggest that the structural rearrangements involved in the aragonite to calcite transition begin at short length scales and only gradually does the calcite structure become coherent to longer length scales; furthermore, we argue that the clumped isotope composition is sensitive to the earliest, shortest length scale re-arrangements, while XRD and Raman are sensitive to structural re-organization on increasingly longer length scales.

The trend in Figure 6-7 for the rate of clumped isotope reordering in aragonite is not a straight line. This observation suggests that clumped isotope reordering may occur through two or more separate steps that differ in activation energies. This finding may offer insight into why we sometimes see two separate rises in Δ_{47} over the course of the aragonite to calcite transition. The two separate increases in Δ_{47} at 350°C may reflect the fact that we can see two separate steps in a complex bond reordering process because the phase transition is slow, letting us observe isotopic evolution over a gradually spreading conversion of aragonite to calcite; by this interpretation, no clear evidence for two Δ_{47} rises is seen at higher temperatures simply because the phase transition progresses too quickly relative to our sampling interval.

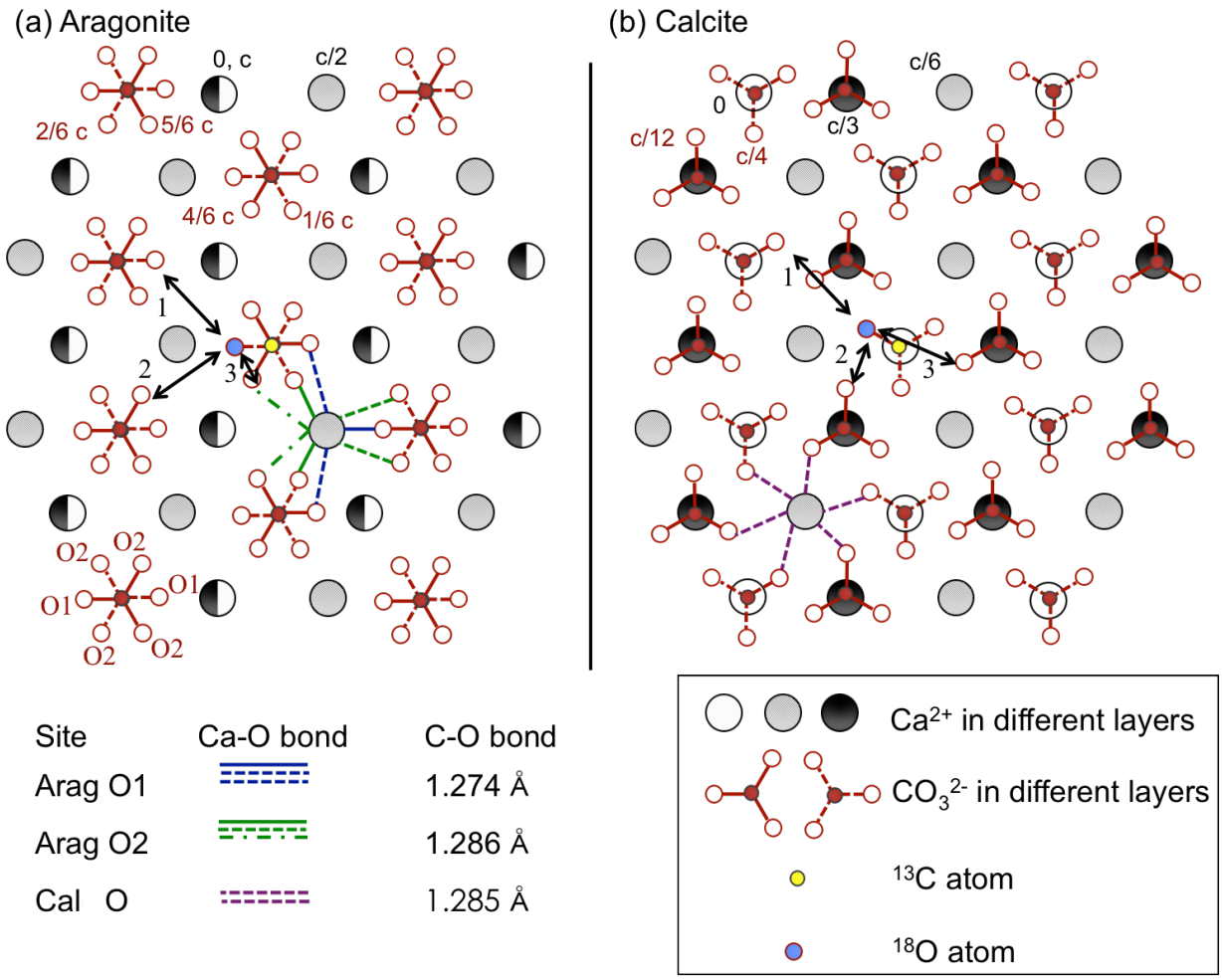

Figure 6-6 Comparison of aragonite and calcite mineral structures. The structures are presented as projections along the c-axis of the minerals, modified from Madon & Gillet (1984). The positions of Ca^{2+} and CO_3^{2-} along the c-axis are marked in the top two rows of the projected structures. The half filled Ca^{2+} ions in (a) represent overlapping layers at position 0 and c along the c-axis. The ^{18}O and ^{13}C atoms are marked by a different color, and are bonded here as a clumped isotopologue. The blue, green and purple lines show the Ca–O bond in the minerals. While all Ca–O bonds in calcite are equivalent, there are five different Ca–O bonds in the 9-coordinated aragonite structure, which gives rise to two non-equivalent oxygen sites O1 and O2. The length of the C–O bonds associated with O1 and O2 sites are listed in the lower left portion of the figure. O1 is more loosely bonded to Ca^{2+} with a slightly stronger C–O bond. In panel (a), the double headed arrows show 3 different pathways for possible preferential oxygen exchange pathways that involve breaking the fewest and weakest bonds. Pathway 1 is an O1-O1 exchange, while pathways 2 and 3 are O1-O2 exchange. In panel (b), the arrows show the same exchange pathways as in (a) after the mineral structure is rearranged. The O1-O2 exchange pathways in (a) have pairs remaining in neighboring positions after the phase transition in (b), and may cause the Δ_{47} increases observed during phase transition by a forced back-exchange.

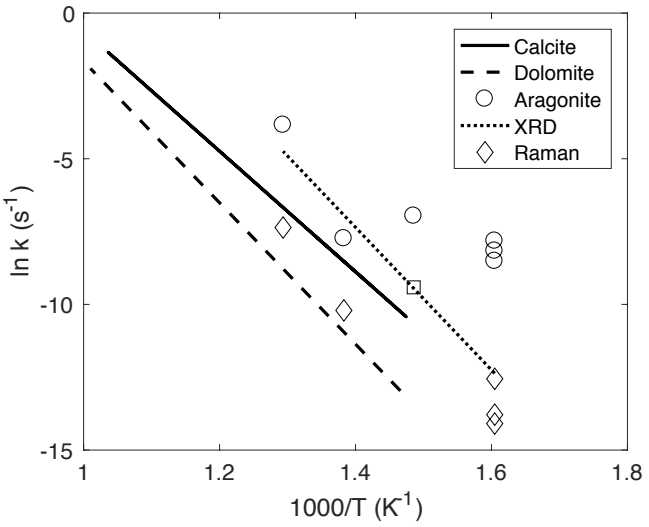

Figure 6-7 Arrhenius plot of clumped isotope reordering and $CaCO_3$ phase transition kinetics. The solid and dashed line represents the rate constants of clump-to-pair conversion (k_f in Rxn 2) calculated from calcite (Stolper & Eiler, 2015) and dolomite (Lloyd et al., 2018) reordering experiments. The circles represent rate constants (k_f) for aragonite estimated by fitting the first stage of Δ_{47} decrease (before the first Δ_{47} increase as phase transition in triggered) in the experimental data with the reaction-diffusion framework. Clumped isotope reordering in aragonite is faster than calcite and dolomite. The dotted line represents rates of aragonite-calcite phase transition at 1 atm calculated from XRD measurements by Davis & Adams (1965). The estimated rate of phase transition measured by XRD in our 400°C experiment (square) is consistent with the literature values. The diamonds represent rates of phase transition measured by Raman spectroscopy in our experiments. Detection of the phase transition by Raman spectroscopy postdates XRD measurements, and the rate of the aragonite to calcite transition as determined using either method is slower than the rate of the clumped isotope reordering reactions in aragonite. The rate constants for phase transition are estimated by $k = 1/\tau$, where τ is the e-folding time (63.2% reaction progress) of the transition. An exponential curve was fit to the noisy reaction progress data to estimate the rate of phase transition.

In summary, we explain the complex evolution in Δ_{47} values observed when an aragonite that formed at a low temperature converts to calcite at a high temperature as an interplay between the mechanisms of isotope exchange between clumps, pairs and singletons on one hand and the dynamics of the aragonite-calcite phase transition on the other. The initial reduction in Δ_{47} that occurs when aragonite is first heated, but has not yet reacted to form detectable calcite is an exchange between the clumped and unsubstituted carbonate ions to build up pairs in the aragonite lattice. This initial exchange preferentially occurs by an exchange of oxygen between only one (or perhaps two) of the several possible pairs of nearest-neighbor O sites. The subsequent rise in Δ_{47} marks the first detectable stage of conversion of aragonite to calcite, which is associated not only

with re-alignment of carbonate ion units, but also with the breaking and re-forming of C–O bonds. The first of these bond breaking and re-forming events takes advantage of the same low activation energy pathway that is the preferred mechanism of clumped isotope reordering. Thus, the O atom exchange that is forced by the phase transition effectively reverses any immediately preceding conversion of clumps to pairs. The only exception to this pattern is seen when aragonite is allowed to isotopically equilibrate at high temperatures before conversion to calcite, which we take as evidence for slower diffusion-limited separation of pairs to form randomly distributed singletons. We suggest that the observation of two separate periods of increasing Δ_{47} when low-temperature aragonite is converted to calcite at 350°C indicates that this structural re-organization occurs through two or more steps that differ in their rates, but that are only clearly observed when phase transformation is slow yet goes to completion (conditions that are not both met at significantly higher or lower temperatures).

6.4.2 Back-reaction of pairs during sharp temperature changes

Our two-step calcite heating experiments were designed to generate pair excesses and drive back-reactions to re-form clumps in the absence of a phase transformation (Figure 6-1b). During the first stage of the experiments, the samples were heated at 450°C for 5 hours. According to the kinetic parameters derived in Stolper & Eiler (2015), these temperature-time conditions should have allowed the clumps-to-pairs reaction to go nearly to completion. In contrast, the diffusion-limited separation of pairs to form singletons should not yet have progressed to a significant extent. Thus, a pair excess should have existed at this point. The samples were then exposed to a higher temperature of 500°C, which lowers the equilibrium pair concentration, increasing the driving force for pairs to either separate or back-react to form clumps.

The magnitude of the change in Δ_{47} predicted by the reaction-diffusion model for this heating history depends on the excesses above a random distribution for both clumps and pairs prior to any heating (i.e., when the studied sample first crystallized), and the temperature dependence of the equilibrium concentrations for clumps and pairs. These quantities are relatively well known for the clumped isotope species, but are essentially unverified assumptions in the case of pairs. If we adopt the assumed values by Stolper and Eiler (2015) for pairs, and adjust their estimated values for the rate constants, k_f, k_d in Rxn 2 within their stated uncertainties, the model

can predict a rise in Δ_{47} during the second stage of this heating experiment (Model-1 in Figure 6-5) that is similar in timing to the rises we observe, but so muted in amplitude that it could not be measured with current analytical methods (whereas we reproducibly observe an effect several times of analytical precision). We constructed several alternative model predictions of the consequences of our experimental heating schedule by increasing the temperature sensitivity of the pair excess by a factor of 6 relative to the value assumed by Stolper and Eiler (2015) (Model-4 in Figure 6-5). A model that closely matches the rate of Δ_{47} decrease in this experiment also requires adjustment of the initial pair concentration, by a few parts in 10^4 (see Table 6-2 and Figure 6-5). These modifications demonstrate the capacity of the reaction-diffusion model to generate temporary increases in Δ_{47}, but show that quantitatively fitting experimental data requires tuning the parameters that define the abundances and behavior of pairs—parameters that are, at present, poorly constrained. For this reason, we consider this set of experiments and the calculations discussed above to provide only suggestive evidence regarding the underlying mechanism that produces the anomalous Δ_{47} rises in calcite during the two-stage heating process.

Despite the complexities in and assumptions of the model required to explain the significant Δ_{47} increases, the experimental observations are important for two reasons: 1) they show that anomalous increases in Δ_{47} can occur during heating in the absence of a phase transformation; and 2) they confirm a peculiar prediction of the reaction-diffusion model that arises from the hypothesized existence and properties of pairs. It remains true that we have no direct observations of pairs (nor can we think of a way in which they could be observed with meaningful precision). However, these results suggest that the dynamics of interconversion of clumps, pairs and singletons could be universal to the solid-state isotopic reordering of carbonate minerals (and perhaps other molecular salts).

We could not think of a way that the defect-annealing mechanism would be predicted to drive a Δ_{47} increase during heating, against the thermodynamic driving force. Our expectation is that the defect density in a crystal changes the rate of diffusion and thus the time it takes to reach equilibrium, but not the direction of clumped isotope evolution. We observed Δ_{47} reversals against thermodynamic trends in both the aragonite-calcite phase transition and the two-stage calcite heating experiments. While the former may involve creation of new defects as the crystal structure is rearranged, we do not expect significant changes in the number of defects in the same calcite

over a short period of time (15 minutes) as the temperature is raised by 50°C. Only the presence of an intermediate pool of pairs can possibly cause the observed clumped isotope reversals.

We also note that the observed Δ_{47} increases in calcite are expected only for specific heating pathways, have been observed only for the experiments discussed here, and are of secondary importance to the overall reordering trend. The original pair-diffusion model parameters in Stolper & Eiler (2015) still predict the general trend of our calcite data better than the variety of other parameters that generate Δ_{47} increases (Figure 6-5), as well as for calcite under a wide range of experimental and geological thermal histories.

6.4.3 Differences Between Aragonite and Calcite in Reordering Kinetics

While the reaction-diffusion reordering mechanism can conceptually explain the complicated clumped isotope reordering pattern in aragonite, it should be noted that the kinetics of clumped isotope reordering in aragonite are distinct from calcite, even in the absence of the aragonite to calcite phase transformation. In our experiments, aragonite clumped isotope reordering is triggered at temperatures much lower than those for calcite. No clumped isotope reordering was observed for calcite up to temperatures of 380°C (Passey & Henkes, 2012; Stolper & Eiler, 2015). In contrast, we see aragonite reordering take place at temperatures as low as 200°C in our experiments, and significant reordering has been observed at even lower temperatures (125°C–175°C) by others (Staudigel & Swart, 2016). Given the complicated reordering pathways and the interplay with the phase transformation, it is challenging to estimate accurate rate constants for clumped isotope reordering in aragonite with the existing data. Using the reaction-diffusion model to fit the data, the initial stage of rapid Δ_{47} decrease by clump-pair conversion in aragonite requires a rate constant (k_f in Rxn 2) that is 1–2 orders of magnitude larger than that in calcite (Figure 6-7). Large uncertainties remain with these estimates due to the scarcity of data points before the phase transition is triggered to cause a reversal in Δ_{47}. We expect time series experiments of aragonite reordering at high pressure (in its stability field) to provide better estimates of the rate constants. However, it is a robust observation in our experiments that when an aragonite-calcite phase transition is involved, the time it takes for the mineral to reach clumped isotope equilibrium is much shorter than for calcite (Figure 6-4). For example, it took 500 hours for calcite to reach equilibrium at 430°C (Stolper & Eiler, 2015), while the equilibrium composition was reached in 42

hours in our 450°C experiment as aragonite was converted to calcite (Figure 6-4). As a result, aragonite's initial clumped isotope composition is predicted to alter at much lower temperatures than that of calcite and dolomite (Stolper & Eiler, 2015; Lloyd et al., 2018), making it highly susceptible to moderate heating during early diagenesis. The Δ_{47} increases during heating and phase transition may further complicate the interpretation of clumped isotope compositions of aragonite and aragonite-derived calcite in sedimentary basin settings. Because unit-cell-scale transformations of aragonite to calcite can artificially raise Δ_{47} values, carbonate materials with 'cold' clumped isotope temperatures that appear to be pristine, unmodified aragonite (based on XRD and Raman spectroscopy) may be indistinguishable from aragonite that experienced moderate heating, partially-reordered in the solid-state, and partially transformed to calcite at a scale finer than the above conventional techniques can detect. However, our reordering experiments make it possible to better constrain a quantitative model of clumped isotope reordering in carbonate minerals in general, and potentially will allow a more complete understanding of the temperature history of natural carbonates measured using clumped isotopes.

Because aragonite and calcite have the same chemical composition, the difference in reordering kinetics is likely a result of structural differences between the two minerals. We surmise that the rate of isotope exchange in the solid-state is determined by the bonding environment of atoms in the crystal lattice. Aragonite has a more tightly compacted structure compared to calcite, and the shortest pathway between oxygen atoms in neighboring carbonate groups is smaller in aragonite than in calcite. Nevertheless, certain Ca–O and C–O bonds in aragonite are longer and thus weaker in aragonite than in calcite (Antao & Hassan, 2010; Ye et al., 2012). As a result, the pairs in aragonite that originate from disproportionation of a clump may have a lower energetic barrier to form (and to exchange back to the clumped species, in the event that a phase transformation forces an oxygen exchange between neighboring pairs). The bonding environment of oxygen atoms is also less symmetric in aragonite than calcite (Figure 6-6), which may create multiple pools of pairs at the non-equivalent oxygen sites; we speculate that this diversity of O bonding environments may be related to the fact that we observe two separate Δ_{47} increases when the aragonite to calcite transformation occurs at 350 ˚C. The factors controlling these elementary kinetic steps could be further investigated by performing reordering experiments of other carbonate minerals of both calcite-type (e.g., siderite, rhodochrosite) and aragonite-type (e.g., strontianite,

witherite) structures, as well as developing molecular dynamic models of solid-state isotope exchange.

6.5 Conclusions

We conducted a series of isotopic reordering experiments in aragonite at different temperatures and observed complicated patterns of decreasing and increasing Δ_{47} values. In general, the reordering pathway can be described as a series of steps in which Δ_{47} initially drops sharply, then rises sharply at the onset of conversion of aragonite to calcite, and finally falls asymptotically toward the high-temperature equilibrium value. We propose that this pattern can be explained with the reaction-diffusion reordering mechanism associated with the aragonite-calcite phase transition. We tested the hypothesis with a reordering experiment on an aragonite sample whose isotopic structure (clumps, pairs and singletons) was equilibrated at high temperature and pressure. The lack of an abrupt rise in Δ_{47} when this sample was subsequently converted to calcite suggests that such Δ_{47} increases require pools of excess pairs. We further tested the presence of pairs in carbonates in general by conducting a two-step calcite heating experiment. After a pretreatment aimed at increasing pair concentrations in calcite, a small, but statistically significant rise in Δ_{47} was reproduced during the second stage of the experiment. These experiments suggest a general mechanism of clumped isotope reordering based on the reaction-diffusion model that can be applied to different carbonate minerals.

Although the mechanism of clumped isotope reordering in aragonite and calcite may be similar, the kinetics of the reordering reactions is different for the two minerals. Clumped isotope compositions of aragonite are highly susceptible to reordering at moderate heating, and the reordering kinetics is much faster than in calcite and dolomite. This must be taken into account when applying the clumped isotope thermometer to natural aragonite that has gone through early diagenesis. The lower activation energy of clumped isotope reordering in aragonite as compared to calcite may be related to the bonding environment of the oxygen atoms in the crystal lattice associated with its structure. Factors determining the kinetics of isotope exchange in carbonate

minerals could be further investigated by reordering experiments of other carbonate minerals, as well as molecular dynamic models of the mobility of different isotopes through crystal structures.

BIBLIOGRAPHY

Chapter 1

Adkins, J.F. (1998). Deep-sea corals: a new oceanic archive. MIT-WHOI Joint Program Thesis.

Adkins, J. F. (2013). The role of deep ocean circulation in setting glacial climates. *Paleoceanography, 28*, https://doi.org/10.1002/palo.20046

Adkins, J. F., Boyle, E. A., Curry, W. B., & Lutringer, A. (2003). Stable isotopes in deep-sea corals and a new mechanism for "vital effects." *Geochimica et Cosmochimica Acta*, *67*(6), 1129–1143. https://doi.org/10.1016/S0016-7037(02)01203-6

Adkins, J. F., Cheng, H., Boyle, E. A., Druffel, E. R. M., & Edwards, R. L. (1998). Deep-Sea Coral Evidence for Rapid Change in Ventilation of the Deep North Atlantic 15,400 Years Ago. *Science, 280*(5364). 725-728. https://doi.org/10.1126/science.280.5364.725

Adkins, J. F., Griffin, S., Kashgarian, M., Cheng, H., Druffel, E. R. M., Boyle, E. A., Edwards, R. L., Shen, C.-C. (2002). Radiocarbon dating of deep-sea corals. *Radiocarbon, 44*, 567-580.

Adkins, J. F., Henderson, G. M., Wang, S. L., O'Shea, S., & Mokadem, F. (2004). Growth rates of the deep-sea scleractinia *Desmophyllum cristagalli* and *Enallopsammia rostrata*. *Earth and Planetary Science Letters, 227*(3–4). 481-490. http://dx.doi.org/10.1016/j.epsl.2004.08.022

Al-Horani, F. A., Al-Moghrabi, S. M., & de Beer, D. (2003). The mechanism of calcification and its relation to photosynthesis and respiration in the scleractinian coral *Galaxea fascicularis*. *Marine Biology, 142*(3). 419-426. https://doi.org/10.1007/s00227-002-0981-8

Anagnostou, E., Huang, K. F., You, C. F., Sikes, E. L., & Sherrell, R. M. (2012). Evaluation of boron isotope ratio as a pH proxy in the deep sea coral *Desmophyllum dianthus*: Evidence of physiological pH adjustment. *Earth and Planetary Science Letters, 349–350*, 251-260. http://dx.doi.org/10.1016/j.epsl.2012.07.006

Anagnostou, E., Sherrell, R. M., Gagnon, A., LaVigne, M., Field, M. P., & McDonough, W. F. (2011). Seawater nutrient and carbonate ion concentrations recorded as P/Ca, Ba/Ca, and U/Ca in the deep-sea coral Desmophyllum dianthus. *Geochimica et Cosmochimica Acta, 75*(9). 2529-2543. http://dx.doi.org/10.1016/j.gca.2011.02.019

Anand, P., Elderfield, H., & Conte, M. H. (2003). Calibration of Mg/Ca thermometry in planktonic foraminifera from a sediment trap time series. *Paleoceanography*, 18(2). https://doi.org/10.1029/2002PA000846

Bemis, B. E., Spero, H. J., Bijma, J., & Lea, D. W. (1998). Reevaluation of the oxygen isotopic composition of planktonic foraminifera: Experimental results and revised paleotemperature equations. *Paleoceanography, 13*, 150-160. https://doi.org/10.1029/98PA00070

Bentov, S., & Erez, J. (2006). Impact of biomineralization processes on the Mg content of foraminiferal shells: A biological perspective. Geochemistry, Geophysics, Geosystems, 7(1). https://doi.org/10.1029/2005GC001015

Blamart, D., Rollion-Bard, C., Cuif, J.-P., Juillet-Leclerc, A., Lutringer, A., van Weering, T. C. E., & Henriet, J.-P. (2005). C and O isotopes in a deep-sea coral (Lophelia pertusa) related to skeletal microstructure. In A. Freiwald & J. M. Roberts (Eds.), Cold-Water Corals and Ecosystems (pp. 1005–1020). https://doi.org/10.1007/3-540-27673-4_50

Blamart, D., Rollion-Bard, C., Meibom, A., Cuif, J. P., Juillet-Leclerc, A., & Dauphin, Y. (2007). Correlation of boron isotopic composition with ultrastructure in the deep-sea coral *Lophelia pertusa*: Implications for biomineralization and paleo-pH. *Geochemistry, Geophysics, Geosystems, 8*(12). https://doi.org/10.1029/2007GC001686

Broecker, W. S. (1982). Glacial to interglacial changes in ocean chemistry. *Progress in Oceanography*, 11(2), 151–197. https://doi.org/10.1016/0079-6611(82)90007-6

Broecker, W. S., & Peng, T.-H. (1987). The role of $CaCO_3$ compensation in the glacial to interglacial atmospheric CO_2 change. *Global Biogeochemical Cycles*, 1(1), 15–29. https://doi.org/10.1029/GB001i001p00015

Bryan, S. P., & Marchitto, T. M. (2008). Mg/Ca–temperature proxy in benthic foraminifera: New calibrations from the Florida Straits and a hypothesis regarding Mg/Li. *Paleoceanography, 23*(2). https://doi.org/10.1029/2007PA001553

Case, D. H., Robinson, L. F., Auro, M. E., & Gagnon, A. C. (2010). Environmental and biological controls on Mg and Li in deep-sea scleractinian corals. *Earth and Planetary Science Letters, 300*(3–4). 215-225. http://dx.doi.org/10.1016/j.epsl.2010.09.029

Cheng, H., Adkins, J., Edwards, R. L., & Boyle, E. A. (2000). U-Th dating of deep-sea corals. *Geochimica et Cosmochimica Acta, 64*(14). 2401-2416. http://dx.doi.org/10.1016/S0016-7037(99)00422-6

Cohen, A., Owens, K. E., Layne, G., & Shimizu, N. (2002). The effect of algal symbionts on the accuracy of Sr/Ca paleotemperatures from coral. *Science, 296*, 331-333. https://doi.org/10.1126/science.1069330

Correge, T. (2006). Sea surface temperature and salinity reconstruction from coral geochemical tracers. *Paleoceanography Paleoclimatology Paleoecology, 232*, 408-428. https://doi.org/10.1016/j.palaeo.2005.10.014

Cuif, J.-P., & Dauphin, Y. (2005). The two-step mode of growth in the scleractinian coral skeletons from the micrometre to the overall scale. *Journal of Structural Biology, 150*(3). 319-331. https://doi.org/10.1016/j.jsb.2005.03.004

Eltgroth, S. F., Adkins, J. F., Robinson, L. F., Southon, J., & Kashgarian, M. (2006). A deep-sea coral record of North Atlantic radiocarbon through the Younger Dryas: Evidence for intermediate water/deepwater reorganization. *Paleoceanography*, 21(4). https://doi.org/10.1029/2005PA001192

Emiliani, C., Hudson, J. H., Shinn, E., & George, R. Y. (1978). Oxygen and carbon isotopic growth record in a reef coral from the Florida Keys and a deep-sea coral from Blake Plateau. *Science, 202*, 627-629. https://doi.org/10.1126/science.202.4368.627

Foster, G. L. (2008). Seawater pH, pCO_2 and $[CO_3^{2-}]$ variations in the Caribbean Sea over the last 130 kyr: A boron isotope and B/Ca study of planktic foraminifera. *Earth and Planetary Science Letters*, 271(1), 254–266. https://doi.org/10.1016/j.epsl.2008.04.015

Gaetani, G. A., Cohen, A. L., Wang, Z., & Crusius, J. (2011). Rayleigh-based, multi-element coral thermometry: A biomineralization approach to developing climate proxies. Geochimica et Cosmochimica Acta, 75(7), 1920–1932. https://doi.org/10.1016/j.gca.2011.01.010

Gagnon, A. C., Adkins, J. F., Fernandez, D. P., & Robinson, L. F. (2007). Sr/Ca and Mg/Ca vital effects correlated with skeletal architecture in a scleractinian deep-sea coral and the role of Rayleigh fractionation. *Earth and Planetary Science Letters*, *261*(1), 280–295. https://doi.org/10.1016/j.epsl.2007.07.013

Gagnon, A. C., Adkins, J. F., & Erez, J. (2012). Seawater transport during coral

biomineralization. *Earth and Planetary Science Letters, 329–330*, 150-161. http://dx.doi.org/10.1016/j.epsl.2012.03.005

Gladfelter, E. H. (1982). Skeletal development in *Acropora cervicornis*: I. Patterns of calcium carbonate accretion in the axial corallite. *Coral Reefs, 1*(1), 45-51. https://doi.org/10.1007/BF00286539

Hain, M., D. M. Sigman, and G. H. Haug (2010). Carbon dioxide effects of Antarctic stratification, North Atlantic Intermediate Water formation, and subantarctic nutrient drawdown during the last ice age: Diagnosis and synthesis in a geochemical box model. *Global Biogeochemical Cycles, 24*, https://doi.org/10.1029/2010GB003790

Hemsing, F., Hsieh, Y.-T., Bridgestock, L., Spooner, P. T., Robinson, L. F., Frank, N., & Henderson, G. M. (2018). Barium isotopes in cold-water corals. *Earth and Planetary Science Letters, 491*, 183–192. https://doi.org/10.1016/j.epsl.2018.03.040

Henehan, M. J., Rae, J. W. B., Foster, G. L., Erez, J., Prentice, K. C., Kucera, M., Bostock, H. C., Martinez-Boti. M. A., Milton, J. A., Wilson, P. A., Marshall, B.J., & Elliott, T. (2013). Calibration of the boron isotope proxy in the planktonic foraminifera Globigerinoides ruber for use in palaeo-CO2 reconstruction. *Earth and Planetary Science Letters, 364*, 111–122. https://doi.org/10.1016/j.epsl.2012.12.029

Hines, S. K. V., Southon, J. R., & Adkins, J. F. (2015). A high-resolution record of Southern Ocean intermediate water radiocarbon over the past 30,000 years. *Earth and Planetary Science Letters*, *432*, 46–58. https://doi.org/10.1016/j.epsl.2015.09.038

Hönisch, B., Hemming, N. G., Grottoli, A. G., Amat, A., Hanson, G. N., & Bijma, J. (2004). Assessing scleractinian corals as recorders for paleo-pH: Empirical calibration and vital effects. *Geochimica et Cosmochimica Acta*, 68(18), 3675–3685. https://doi.org/10.1016/j.gca.2004.03.002

Knox, F., and M. McElroy (1984). Changes in atmospheric CO2: influence of biota at high latitudes. *J. Geophys. Res., 89*, 4629-4637. https://doi.org/10.1029/JD089iD03p04629

Krief, S., Hendy, E. J., Fine, M., Yam, R., Meibom, A., Foster, G. L., & Shemesh, A. (2010). Physiological and isotopic responses of scleractinian corals to ocean acidification. *Geochimica et Cosmochimica Acta*, *74*(17), 4988–5001. https://doi.org/10.1016/j.gca.2010.05.023

Lea, D. W. (1993). Constraints on the alkalinity and circulation of glacial circumpolar deep water from benthic foraminiferal barium. *Global Biogeochemical Cycles*, *7*(3), 695–710. https://doi.org/10.1029/93GB01536

Lea, D. W., Mashiotta, T. A., & Spero, H. J. (1999). Controls on magnesium and strontium uptake in planktonic foraminifera determined by live culturing. *Geochimica et Cosmochimica Acta*, *63*(16), 2369–2379. https://doi.org/10.1016/S0016-7037(99)00197-0

Marchitto, T. M., Curry, W. B., Lynch-Stieglitz, J., Bryan, S. P., Cobb, K. M., & Lund, D. C. (2014). Improved oxygen isotope temperature calibrations for cosmopolitan benthic foraminifera. *Geochimica et Cosmochimica Acta*, 130, 1–11. https://doi.org/10.1016/j.gca.2013.12.034

McConnaughey, T. A. (1989a). ^{13}C and ^{18}O isotopic disequilibrium in biological carbonates: I. Patterns. *Geochimica et Cosmochimica Acta, 53*, 151-162. https://doi.org/10.1016/0016-7037(89)90282-2

McConnaughey, T. A. (1989b). ^{13}C and ^{18}O isotopic disequilibrium in biological carbonates: II. In vitro simulation of kinetic isotope effects. *Geochim. Cosmochim. Acta, 53*, 163-171.

https://doi.org/10.1016/0016-7037(89)90283-4
McCulloch, M., Trotter, J., Montagna, P., Falter, J., Dunbar, R., Freiwald, A., Försterra, G., López Correa, M., Maier, C., Rüggeberg, A., & Taviani, M. (2012). Resilience of cold-water scleractinian corals to ocean acidification: Boron isotopic systematics of pH and saturation state up-regulation. *Geochimica et Cosmochimica Acta, 87*, 21-34. https://doi.org/10.1016/j.gca.2012.03.027
Raddatz, J., Rüggeberg, A., Flögel, S., Hathorne, E. C., Liebetrau, V., Eisenhauer, A., & Dullo, W. C. (2014). The influence of seawater pH on U / Ca ratios in the scleractinian cold-water coral *Lophelia pertusa*. *Biogeosciences, 11*(7). 1863-1871. https://doi.org/10.5194/bg-11-1863-2014
Rae, J. W. B., Burke, A., Robinson, L. F., Adkins, J. F., Chen, T., Cole, C., Greenop, R., Li, T., Littley, E. F. M., Nita, D. C., Stewart, J. A., & Taylor, B. J. (2018). CO_2 storage and release in the deep Southern Ocean on millennial to centennial timescales. *Nature*, *562*(7728), 569–573. https://doi.org/10.1038/s41586-018-0614-0
Robinson, L. F., Adkins, J. F., Fernandez, D. P., Burnett, D. S., Wang, S.-L., Gagnon, A. C., & Krakauer, N. (2006). Primary U distribution in scleractinian corals and its implications for U series dating. *Geochemistry, Geophysics, Geosystems*, *7*(5). https://doi.org/10.1029/2005GC001138
Robinson, L., Adkins, J. F., Keigwin, L. D., Southon, J., Fernandez, D. P., Wang, S.-L., & Scheirer, D. S. (2005). Radiocarbon variability in the Western North Atlantic during the last deglaciation. *Science, 310*, 1469-1473. https://doi.org/10.1126/science.1114832
Rollion-Bard, C., Blamart, D., Cuif, J.-P., & Dauphin, Y. (2010). In situ measurements of oxygen isotopic composition in deep-sea coral, Lophelia pertusa: Re-examination of the current geochemical models of biomineralization. *Geochimica et Cosmochimica Acta, 74*(4). 1338-1349. https://doi.org/10.1016/j.gca.2009.11.011
Rollion-Bard, C., Chaussidon, M., & France-Lanord, C. (2003). pH control on oxygen isotopic composition of symbiotic corals. *Earth and Planetary Science Letters, 215*, 275-288. https://doi.org/10.1016/S0012-821X(03)00391-1
Sarmiento, J. L., and J. R. Toggweiler (1984). A new model for the role of the oceans in determining atmospheric pCO_2, *Nature, 308*, 621-624. https://doi.org/10.1038/308621a0
Shackleton, N. J., & Opdyke, N. D. (1973). Oxygen isotope and palaeomagnetic stratigraphy of Equatorial Pacific core V28-238: Oxygen isotope temperatures and ice volumes on a 105 year and 106 year scale. *Quaternary Research*, *3*(1), 39–55. https://doi.org/10.1016/0033-5894(73)90052-5
Siegenthaler, U., and T. Wenk (1984). Rapid atmospheric CO_2 variations and ocean circulation. *Nature, 308*, 624-625. https://doi.org/10.1038/308624a0
Sigman, D., and E. A. Boyle (2000). Glacial/Interglacial variations in atmospheric carbon dioxide. *Nature, 407*, 859-869. https://doi.org/10.1038/35038000
Sigman, D., M. Hain, and G. H. Haug (2010). The polar ocean and glacial cycles in atmospheric CO_2 concentration. *Nature, 466*, 47-55. https://doi.org/10.1038/nature09149
Sinclair, D. J., & Risk, M. J. (2006). A numerical model of trace-element coprecipitation in a physicochemical calcification system: Application to coral biomineralization and trace-element 'vital effects.' *Geochimica et Cosmochimica Acta, 70*(15), 3855–3868. https://doi.org/10.1016/j.gca.2006.05.019
Spooner, P. T., Robinson, L. F., Hemsing, F., Morris, P., & Stewart, J. A. (2018). Extended calibration of cold-water coral Ba/Ca using multiple genera and co-located measurements

of dissolved barium concentration. *Chemical Geology, 499*, 100–110. https://doi.org/10.1016/j.chemgeo.2018.09.012

Stewart, J. A., Anagnostou, E., & Foster, G. L. (2016). An improved boron isotope pH proxy calibration for the deep-sea coral Desmophyllum dianthus through sub-sampling of fibrous aragonite. *Chemical Geology*, *447*, 148–160. https://doi.org/10.1016/j.chemgeo.2016.10.029

Thiagarajan, N., Adkins, J., & Eiler, J. (2011). Carbonate clumped isotope thermometry of deep-sea corals and implications for vital effects. *Geochimica et Cosmochimica Acta, 75*(16). 4416-4425. http://dx.doi.org/10.1016/j.gca.2011.05.004

Thiagarajan, N., Subhas, A. V., Southon, J. R., Eiler, J. M., & Adkins, J. F. (2014). Abrupt pre-Bolling-Allerod warming and circulation changes in the deep ocean. *Nature, 511*(7507). 75-78. https://doi.org/10.1038/nature13472

Toggweiler, J. R. (1999). Variation of atmospheric CO_2 by ventilation of the ocean's deepest water, *Paleoceanography, 14*, 571-588. https://doi.org/10.1029/1999PA900033

Toyofuku, T., Matsuo, M. Y., de Nooijer, L. J., Nagai, Y., Kawada, S., Fujita, K., Reinchart, G., Nomaki, H., Tsuchiya, M., Sakaguchi, H., & Kitazato, H. (2017). Proton pumping accompanies calcification in foraminifera. *Nature Communications, 8*, 14145. https://doi.org/10.1038/ncomms14145

van de Flierdt, T., Robinson, L. F., & Adkins, J. F. (2010). Deep-sea coral aragonite as a recorder for the neodymium isotopic composition of seawater. *Geochimica et Cosmochimica Acta, 74*(21). 6014-6032. http://dx.doi.org/10.1016/j.gca.2010.08.001

Venn, A., Tambutté, E., Holcomb, M., Allemand, D., & Tambutté, S. (2011). Live Tissue Imaging Shows Reef Corals Elevate pH under Their Calcifying Tissue Relative to Seawater. *PLOS ONE, 6*(5). e20013. https://doi.org/10.1371/journal.pone.0020013

Wang, X. T., Prokopenko, M. G., Sigman, D. M., Adkins, J. F., Robinson, L. F., Ren, H., Oleynik, S., Williams, B., & Haug, G. H. (2014). Isotopic composition of carbonate-bound organic nitrogen in deep-sea scleractinian corals: A new window into past biogeochemical change. *Earth and Planetary Science Letters, 400*, 243–250. https://doi.org/10.1016/j.epsl.2014.05.048

Wang, X. T., Sigman, D. M., Prokopenko, M. G., Adkins, J. F., Robinson, L. F., Hines, S. K., Chai, J., Studer, A. S., Martinez-Garcia, A., Chen, T., & Haug, G. H. (2017). Deep-sea coral evidence for lower Southern Ocean surface nitrate concentrations during the last ice age. *Proceedings of the National Academy of Sciences, 114*(13), 3352–3357. https://doi.org/10.1073/pnas.1615718114

Watkins, J. M., & Hunt, J. D. (2015). A process-based model for non-equilibrium clumped isotope effects in carbonates. *Earth and Planetary Science Letters, 432*, 152-165. https://doi.org/10.1016/j.epsl.2015.09.042

Watkins, J. M., Hunt, J. D., Ryerson, F. J., & DePaolo, D. J. (2014). The influence of temperature, pH, and growth rate on the δ18O composition of inorganically precipitated calcite. *Earth and Planetary Science Letters, 404*, 332-343. http://dx.doi.org/10.1016/j.epsl.2014.07.036

Watkins, J. M., Nielsen, L. C., Ryerson, F. J., & DePaolo, D. J. (2013). The influence of kinetics on the oxygen isotope composition of calcium carbonate. *Earth and Planetary Science Letters, 375*, 349-360. http://dx.doi.org/10.1016/j.epsl.2013.05.054

Weber, J. N., & Woodhead, P. M. J. (1972). Temperature dependence of oxygen-18 concentration in reef coral carbonates. *Journal of Geophysical Research (1896-1977),*

77(3), 463–473. https://doi.org/10.1029/JC077i003p00463

Wilson, D. J., Crocket, K. C., Flierdt, T. van de, Robinson, L. F., & Adkins, J. F. (2014). Dynamic intermediate ocean circulation in the North Atlantic during Heinrich Stadial 1: A radiocarbon and neodymium isotope perspective. *Paleoceanography, 29*(11), 1072–1093. https://doi.org/10.1002/2014PA002674

Wilson, D. J., van de Flierdt, T., & Adkins, J. F. (2017). Lead isotopes in deep-sea coral skeletons: Ground-truthing and a first deglacial Southern Ocean record. *Geochimica et Cosmochimica Acta, 204*, 350–374. https://doi.org/10.1016/j.gca.2017.01.052

Zoccola, D., Tambutté, E., Kulhanek, E., Puverel, S., Scimeca, J.-C., Allemand, D., & Tambutté, S. (2004). Molecular cloning and localization of a PMCA P-type calcium ATPase from the coral Stylophora pistillata. *Biochimica Et Biophysica Acta, 1663*(1–2), 117–126. https://doi.org/10.1016/j.bbamem.2004.02.010

Chapter 2

Addadi, L., Raz, S., & Weiner, S. (2003). Taking Advantage of Disorder: Amorphous Calcium Carbonate and Its Roles in Biomineralization. *Advanced Materials, 15*(12), 959-970. https://doi.org/10.1002/adma.200300381

Adkins, J. F., Boyle, E. A., Curry, W. B., & Lutringer, A. (2003). Stable isotopes in deep-sea corals and a new mechanism for "vital effects." *Geochimica et Cosmochimica Acta*, *67*(6), 1129–1143. https://doi.org/10.1016/S0016-7037(02)01203-6

Adkins, J. F., Griffin, S., Kashgarian, M., Cheng, H., Druffel, E. R. M., Boyle, E. A., Edwards, R.L., Shen, C.-C. (2002). Radiocarbon dating of deep-sea corals. *Radiocarbon, 44*, 567-580.

Al-Horani, F. A., Al-Moghrabi, S. M., & de Beer, D. (2003). The mechanism of calcification and its relation to photosynthesis and respiration in the scleractinian coral *Galaxea fascicularis*. *Marine Biology, 142*(3), 419-426. https://doi.org/10.1007/s00227-002-0981-8

Allison, N., Cohen, I., Finch, A. A., Erez, J., & Tudhope, A. W. (2014). Corals concentrate dissolved inorganic carbon to facilitate calcification. *Nature Communications, 5*, 5741. https://doi.org/10.1038/ncomms6741

Beck, W. C., Grossman, E. L., & Morse, J. W. (2005). Experimental studies of oxygen isotope fractionation in the carbonic acid system at 15°, 25°, and 40°C. *Geochimica et Cosmochimca Acta, 69*, 3493-3503. https://doi.org/10.1016/j.gca.2005.02.003

Bertucci, A., Moya, A., Tambutté, S., Allemand, D., Supuran, C. T., & Zoccola, D. (2013). Carbonic anhydrases in anthozoan corals—A review. *Bioorganic & Medicinal Chemistry, 21*(6), 1437-1450. http://dx.doi.org/10.1016/j.bmc.2012.10.02

Bertucci, A., Tambutté, S., Supuran, C. T., Allemand, D., & Zoccola, D. (2011). A New Coral Carbonic Anhydrase in *Stylophora pistillata*. *Marine Biotechnology, 13*(5), 992-1002. https://doi.org/10.1007/s10126-011-9363-x

Bertucci, A., Zoccola, D., Tambutté, S., Vullo, D., & Supuran, C. T. (2010). Carbonic anhydrase activators. The first activation study of a coral secretory isoform with amino acids and amines. *Bioorganic & Medicinal Chemistry, 18*(6), 2300-2303. https://doi.org/10.1016/j.bmc.2010.01.059

Blamart, D., Rollion-Bard, C., Meibom, A., Cuif, J. P., Juillet-Leclerc, A., & Dauphin, Y. (2007). Correlation of boron isotopic composition with ultrastructure in the deep-sea

coral *Lophelia pertusa*: Implications for biomineralization and paleo-pH. *Geochemistry, Geophysics, Geosystems, 8*(12). https://doi.org/10.1029/2007GC001686

Cai, W.-J., Ma, Y., Hopkinson, B. M., Grottoli, A. G., Warner, M. E., Ding, Q., Hu, X., Yuan, X., Schoepf,.V., Xu, H., Han, C., Melman, T.F., Hoadley, K.D., Pettay, D.T., Matsui, Y., Baumann, J.H., Levas, S., Ying, Y., & Wang, Y. (2016). Microelectrode characterization of coral daytime interior pH and carbonate chemistry. *Nature Communications, 7*, 11144. https://doi.org/10.1038/ncomms11144

Case, D. H., Robinson, L. F., Auro, M. E., & Gagnon, A. C. (2010). Environmental and biological controls on Mg and Li in deep-sea scleractinian corals. *Earth and Planetary Science Letters*, *300*(3), 215–225. https://doi.org/10.1016/j.epsl.2010.09.029

Cuif, J.-P., & Dauphin, Y. (2005). The two-step mode of growth in the scleractinian coral skeletons from the micrometre to the overall scale. *Journal of Structural Biology, 150*(3), 319-331. https://doi.org/10.1016/j.jsb.2005.03.004

De Yoreo, J. J., Wierzbicki, A., & Dove, P. M. (2007). New insights into mechanisms of biomolecular control on growth of inorganic crystals. *CrystEngComm, 9*(12), 1144-1152. https://doi.org/10.1039/B713006F

Demény, A., Németh, P., Czuppon, G., Leél-Őssy, S., Szabó, M., Judik, K., Németh, T., Stieber, J. (2016). Formation of amorphous calcium carbonate in caves and its implications for speleothem research. *Scientific Reports, 6*, 39602. https://doi.org/10.1038/srep39602.

Emiliani, C., Hudson, J. H., Shinn, E. A., & George, R. Y. (1978). Oxygen and Carbon Isotopic Growth Record in a Reef Coral from the Florida Keys and a Deep-Sea Coral from Blake Plateau. *Science, 202*(4368), 627-629. https://doi.org/10.1126/science.202.4368.627

Gabitov, R. I. (2013). Growth-rate induced disequilibrium of oxygen isotopes in aragonite: An in situ study. *Chemical Geology, 351*, 268-275. https://doi.org/10.1016/j.chemgeo.2013.05.015

Gabitov, R. I., Watson, E. B., & Sadekov, A. (2012). Oxygen isotope fractionation between calcite and fluid as a function of growth rate and temperature: An in situ study. *Chemical Geology, 306–307*, 92-102. https://doi.org/10.1016/j.chemgeo.2012.02.021

Gagnon, A. C., Adkins, J. F., Fernandez, D. P., & Robinson, L. F. (2007). Sr/Ca and Mg/Ca vital effects correlated with skeletal architecture in a scleractinian deep-sea coral and the role of Rayleigh fractionation. *Earth and Planetary Science Letters*, *261*(1), 280–295. https://doi.org/10.1016/j.epsl.2007.07.013

Gagnon, A. C., Adkins, J. F., & Erez, J. (2012). Seawater transport during coral biomineralization. *Earth and Planetary Science Letters, 329–330*, 150-161. http://dx.doi.org/10.1016/j.epsl.2012.03.005

Gago-Duport, L., Briones, M. J. I., Rodríguez, J. B., & Covelo, B. (2008). Amorphous calcium carbonate biomineralization in the earthworm's calciferous gland: Pathways to the formation of crystalline phases. *Journal of Structural Biology, 162*(3), 422-435. https://doi.org/10.1016/j.jsb.2008.02.007.

Gladfelter, E. H. (1982). Skeletal development in *Acropora cervicornis*: I. Patterns of calcium carbonate accretion in the axial corallite. *Coral Reefs, 1*(1), 45-51. https://doi.org/10.1007/BF00286539

Gong, Y. U. T., Killian, C. E., Olson, I. C., Appathurai, N. P., Amasino, A. L., Martin, M. C., Holt, L.J., Wilt, F.H., & Gilbert, P. U. P. A. (2012). Phase transitions in biogenic amorphous calcium carbonate. *Proceedings of the National Academy of Sciences, 109*(16), 6088-6093. https://doi.org/10.1073/pnas.1118085109

Goreau, T. F. (1959). Thy physiology of skeleton formation in corals. I. A method for measuring the rate of calcium deposition by corals under different conditions. *The Biological Bulletin, 116*(1), 59-75. https://doi.org/10.2307/1539156

Hentunen, T. A., Härkönen, P. L., & Väänänen, H. K. (2000). Carbonic anhydrases in calcified tissues. In W. R. Chegwidden, N. D. Carter & Y. H. Edwards (Eds.), *The Carbonic Anhydrases: New Horizons* (pp. 491-497). Basel: Birkhäuser Basel.

Hermoso, M., Horner, T. J., Minoletti, F., & Rickaby, R. E. M. (2014). Constraints on the vital effect in coccolithophore and dinoflagellate calcite by oxygen isotopic modification of seawater. *Geochimica et Cosmochimica Acta, 141*, 612-627. https://doi.org/10.1016/j.gca.2014.05.002

Hermoso, M., Minoletti, F., Aloisi, G., Bonifacie, M., McClelland, H. L. O., Labourdette, N., Renforth, P., Chaduteau, C., Rickaby, R. E. M. (2016). An explanation for the ^{18}O excess in Noelaerhabdaceae coccolith calcite. *Geochimica et Cosmochimica Acta, 189*, 132-142. https://doi.org/10.1016/j.gca.2016.06.016

Hopkinson, B. M., Tansik, A. L., & Fitt, W. K. (2015). Internal carbonic anhydrase activity in the tissue of scleractinian corals is sufficient to support proposed roles in photosynthesis and calcification. *The Journal of Experimental Biology, 218*(13), 2039-2048. https://doi.org/10.1242/jeb.118182

Jacob, D. E., Soldati, A. L., Wirth, R., Huth, J., Wehrmeister, U., & Hofmeister, W. (2008). Nanostructure, composition and mechanisms of bivalve shell growth. *Geochimica et Cosmochimica Acta, 72*(22), 5401-5415. https://doi.org/10.1016/j.gca.2008.08.019

Johnson, K. S. (1982). Carbon dioxide hydration and dehydration kinetics in seawater. *Limnology and Oceanography, 27*(5), 849-855. https://doi.org/10.4319/lo.1982.27.5.0849

Juillet-Leclerc, A., & Reynaud, S. (2010). Light effects on the isotopic fractionation of skeletal oxygen and carbon in the cultured zooxanthellate coral, *Acropora*: implications for coral-growth rates. *Biogeosciences, 7*(3), 893-906. https://doi.org/10.5194/bg-7-893-2010

Keith, M. L., & Weber, J. N. (1965). Systematic Relationships between Carbon and Oxygen Isotopes in Carbonates Deposited by Modern Corals and Algae. *Science, 150*(3695), 498-501. https://doi.org/10.1126/science.150.3695.498

Kim, S.-T., & O'Neil, J. R. (1997). Equilibrium and nonequilibrium oxygen isotope effects in synthetic carbonates. *Geochemica et Cosmochimica Acta, 61*, 3461-3475. https://doi.org/10.1016/S0016-7037(97)00169-5

Land, L. S., Lang, J. C., & Barnes, D. J. (1977). On the stable carbon and oxygen isotopic composition of some shallow water, ahermatypic, scleractinian coral skeletons. *Geochimica et Cosmochimica Acta, 41*, 169-172. https://doi.org/10.1016/0016-7037(77)90197-1

Marlier, J. F., & O'Leary, M. H. (1984). Carbon kinetic isotope effects on the hydration of carbon dioxide and the dehydration of bicarbonate ion. *Journal of the American Chemical Society, 106*(18), 5054-5057. https://doi.org/10.1021/ja00330a003

Mass, T., Drake, J. L., Peters, E. C., Jiang, W., & Falkowski, P. G. (2014). Immunolocalization of skeletal matrix proteins in tissue and mineral of the coral *Stylophora pistillata*. *Proceedings of the National Academy of Sciences, 111*(35), 12728-12733. https://doi.org/10.1073/pnas.1408621111

McConnaughey, T. A. (1989a). ^{13}C and ^{18}O isotopic disequilibrium in biological carbonates: I. Patterns. *Geochimica et Cosmochimica Acta, 53*, 151-162. https://doi.org/10.1016/0016-7037(89)90282-2

McConnaughey, T. A. (1989b). ^{13}C and ^{18}O isotopic disequilibrium in biological carbonates: II. In vitro simulation of kinetic isotope effects. *Geochim. Cosmochim. Acta, 53*, 163-171. https://doi.org/10.1016/0016-7037(89)90283-4

McCrea, J. M. (1950). On the isotopic chemistry of carbonates and a paleotemperature scale. *Journal of Chemical Physics, 18*, 849-857. https://doi.org/10.1063/1.1747785

McCulloch, M., Trotter, J., Montagna, P., Falter, J., Dunbar, R., Freiwald, A., Försterra, G., López Correa, M., Maier, C., Rüggeberg, A., & Taviani, M. (2012). Resilience of cold-water scleractinian corals to ocean acidification: Boron isotopic systematics of pH and saturation state up-regulation. *Geochimica et Cosmochimica Acta, 87*, 21-34. https://doi.org/10.1016/j.gca.2012.03.027

Moya, A., Tambutté, S., Bertucci, A., Tambutté, E., Lotto, S., Vullo, D., Supuran, C.T., Allemand, D., & Zoccola, D. (2008). Carbonic Anhydrase in the Scleractinian Coral Stylophora pistillata: characterization, localization, and role in biomineralization. *Journal of Biological Chemistry, 283*(37), 25475-25484. https://doi.org/10.1074/jbc.M804726200

O'Leary, M. H. (1984). Measurement of the isotope fractionation associated with diffusion of carbon dioxide in aqueous solution. *The Journal of Physical Chemistry, 88*(4), 823-825. https://doi.org/10.1021/j150648a041

O'Leary, M. H., Madhavan, S., & Paneth, P. (1992). Physical and chemical basis of carbon isotope fractionation in plants. *Plant, Cell & Environment, 15*(9), 1099-1104. https://doi.org/10.1111/j.1365-3040.1992.tb01660.x

Robinson, L. F., Adkins, J. F., Fernandez, D. P., Burnett, D. S., Wang, S. L., Gagnon, A. C., & Krakauer, N. (2006). Primary U distribution in scleractinian corals and its implications for U series dating. *Geochemistry, Geophysics, Geosystems, 7*, Q05022. https://doi.org/10.1029/2005GC001138

Rollion-Bard, C., Blamart, D., Cuif, J.-P., & Dauphin, Y. (2010). In situ measurements of oxygen isotopic composition in deep-sea coral, Lophelia pertusa: Re-examination of the current geochemical models of biomineralization. *Geochimica et Cosmochimica Acta, 74*(4), 1338-1349. https://doi.org/10.1016/j.gca.2009.11.011

Rollion-Bard, C., Chaussidon, M., & France-Lanord, C. (2003). pH control on oxygen isotopic composition of symbiotic corals. *Earth and Planetary Science Letters, 215*, 275-288. https://doi.org/10.1016/S0012-821X(03)00391-1

Romanek, C. S., Grossman, E. L., & Morse, J. W. (1992). Carbon isotopic fractionation in synthetic aragonite and calcite: Effects of temperature and precipitation rate. *Geochimica et Cosmochimica Acta, 56*(1), 419-430. http://dx.doi.org/10.1016/0016-7037(92)90142-6

Romanek, C. S., Morse, J. W., & Grossman, E. L. (2011). Aragonite Kinetics in Dilute Solutions. *Aquatic Geochemistry, 17*(4), 339. https://doi.org/10.1007/s10498-011-9127-2

Spero, H. J., Bijma, J., Lea, D. W., & Bemis, B. E. (1997). Effect of seawater carbonate concentration on foraminiferal carbon and oxygen isotopes. *Nature, 390*, 497-500. https://doi.org/10.1038/37333

Sültemeyer, D., & Rinast, K.-A. (1996). The CO_2 permeability of the plasma membrane of *Chlamydomonas reinhardtii*: mass-spectrometric ^{18}O-exchange measurements from $^{13}C^{18}O_2$ in suspensions of carbonic anhydrase-loaded plasma-membrane vesicles. *Planta, 200*(3), 358-368. https://doi.org/10.1007/BF00200304

Tambutté, S., Tambutté, E., Zoccola, D., Caminiti, N., Lotto, S., Moya, A., Allemand, D., & Adkins, J. (2007). Characterization and role of carbonic anhydrase in the calcification process of the azooxanthellate coral *Tubastrea aurea*. *Marine Biology, 151*(1), 71-83.

https://doi.org/10.1007/s00227-006-0452-8

Tambutté, S., Holcomb, M., Ferrier-Pagès, C., Reynaud, S., Tambutté, É., Zoccola, D., & Allemand, D. (2011). Coral biomineralization: From the gene to the environment. *Journal of Experimental Marine Biology and Ecology, 408*(1–2), 58-78. http://dx.doi.org/10.1016/j.jembe.2011.07.026

Tambutté, E., Tambutté, S., Segonds, N., Zoccola, D., Venn, A., Erez, J., & Allemand, D. (2012). Calcein labelling and electrophysiology: insights on coral tissue permeability and calcification. *Proceedings of the Royal Society B: Biological Sciences, 279*(1726), 19-27. https://doi.org/10.1098/rspb.2011.0733

Uchikawa, J., & Zeebe, R. E. (2012). The effect of carbonic anhydrase on the kinetics and equilibrium of the oxygen isotope exchange in the CO_2–H_2O system: Implications for $\delta^{18}O$ vital effects in biogenic carbonates. *Geochimica et Cosmochimica Acta, 95*, 15-34. http://dx.doi.org/10.1016/j.gca.2012.07.022

Urey, H. C. (1947). The thermodynamic properties of isotopic substances. *J. Chem. Soc., 1947*, 562-581. https://doi.org/10.1039/JR9470000562

Usdowski, E., & Hoefs, J. (1993). Oxygen isotope exchange between carbonic acid, bicarbonate, and water: a re-examination of the data of McCrea (1950) and an expression for the overall partitioning of oxygen isotopes between the carbonate species and water. *Geochimica et Cosmochimica Acta, 57*, 3815-3818. https://doi.org/10.1016/0016-7037(93)90159-T

Venn, A., Tambutté, E., Holcomb, M., Allemand, D., & Tambutté, S. (2011). Live Tissue Imaging Shows Reef Corals Elevate pH under Their Calcifying Tissue Relative to Seawater. *PLOS ONE, 6*(5), e20013. https://doi.org/10.1371/journal.pone.0020013

Vergnaud Grazzini, C. (1976). Non-equilibrium isotopic compositions of shells of planktonic foraminifera in the Mediterranean sea. *Palaeogeography, Palaeoclimatology, Palaeoecology, 20*(4), 263-276. http://dx.doi.org/10.1016/0031-0182(76)90007-9

Vinot-Bertouille, A.-C., & Duplessy, J.-C. (1973). Individual isotopic fractionation of carbon and oxygen in benthic foraminifera. *Earth and Planetary Science Letters, 18*(2), 247-252. http://dx.doi.org/10.1016/0012-821X(73)90063-0

Von Euw, S., Zhang, Q., Manichev, V., Murali, N., Gross, J., Feldman, L. C., Gustafsson, T., Flach, C., Mendelsohn, R., & Falkowski, P. G. (2017). Biological control of aragonite formation in stony corals. *Science, 356*(6341), 933-938. https://doi.org/10.1126/science.aam6371

Wall, M., Ragazzola, F., Foster, L. C., Form, A., & Schmidt, D. N. (2015). pH up-regulation as a potential mechanism for the cold-water coral *Lophelia pertusa* to sustain growth in aragonite undersaturated conditions. *Biogeosciences, 12*(23), 6869-6880. https://doi.org/10.5194/bg-12-6869-2015

Wang, Z., Gaetani, G., Liu, C., & Cohen, A. (2013). Oxygen isotope fractionation between aragonite and seawater: Developing a novel kinetic oxygen isotope fractionation model. *Geochimica et Cosmochimica Acta, 117*, 232-251. https://doi.org/10.1016/j.gca.2013.04.025

Watkins, J. M., & Hunt, J. D. (2015). A process-based model for non-equilibrium clumped isotope effects in carbonates. *Earth and Planetary Science Letters, 432*, 152-165. https://doi.org/10.1016/j.epsl.2015.09.042

Watkins, J. M., Hunt, J. D., Ryerson, F. J., & DePaolo, D. J. (2014). The influence of temperature, pH, and growth rate on the $\delta^{18}O$ composition of inorganically precipitated

calcite. *Earth and Planetary Science Letters, 404*, 332-343. http://dx.doi.org/10.1016/j.epsl.2014.07.036

Watkins, J. M., Nielsen, L. C., Ryerson, F. J., & DePaolo, D. J. (2013). The influence of kinetics on the oxygen isotope composition of calcium carbonate. *Earth and Planetary Science Letters, 375*, 349-360. http://dx.doi.org/10.1016/j.epsl.2013.05.054

Weber, J. N., & Raup, D. M. (1966). Fractionation of the stable isotopes of carbon and oxygen in marine calcareous organisms—the Echinoidea. Part I. Variation of C13 and O18 content within individuals. *Geochimica et Cosmochimica Acta, 30*(7), 681-703. http://dx.doi.org/10.1016/0016-7037(66)90097-4

Weber, J. N., & Woodhead, P. M. J. (1970). Carbon and oxygen isotope fractionation in the skeletal carbonate of reef-building corals. *Chemical Geology, 6*, 93-117. https://doi.org/10.1016/0009-2541(70)90009-4

Zeebe, R. (1999). An explanation of the effect of seawater carbonate concentration on foraminiferal oxygen isotopes. *Geochimica et Cosmochimica Acta, 63*, 2001-2007. https://doi.org/10.1016/S0016-7037(99)00091-5

Zeebe, R. E. (2014). Kinetic fractionation of carbon and oxygen isotopes during hydration of carbon dioxide. *Geochimica et Cosmochimica Acta, 139*, 540-552. http://dx.doi.org/10.1016/j.gca.2014.05.005

Zeebe, R. E., Bijma, J., & Wolf-Gladrow, D. A. (1999). A diffusion-reaction model of carbon isotope fractionation in foraminifera. *Marine Chemistry, 64*(3), 199-227. https://doi.org/10.1016/S0304-4203(98)00075-9

Zeebe, R. E., & Sanyal, A. (2002). Comparison of two potential strategies of planktonic foraminifera for house building: Mg^{2+} or H^{+} removal? *Geochimica et Cosmochimica Acta, 66*(7), 1159-1169. https://doi.org/10.1016/S0016-7037(01)00852-3

Zeebe, R. E., & Wolf-Gladrow, D. (2001). *CO_2 in seawater: equilibrium, kinetics, isotopes* (Vol. 65). Amsterdam: Elsevier.

Zhang, J., Quay, P. D., & Wilbur, D. O. (1995). Carbon isotope fractionation during gas-water exchange and dissolution of CO_2. *Geochimica et Cosmochimica Acta, 59*, 107-114. https://doi.org/10.1016/0016-7037(95)91550-D

Zoccola, D., Tambutté, E., Kulhanek, E., Puverel, S., Scimeca, J.-C., Allemand, D., & Tambutté, S. (2004). Molecular cloning and localization of a PMCA P-type calcium ATPase from the coral Stylophora pistillata. *Biochimica et Biophysica Acta (BBA) - Biomembranes, 1663*(1), 117-126. https://doi.org/10.1016/j.bbamem.2004.02.010

Chapter 3

Adkins, J.F. (1998). Deep-sea corals: a new oceanic archive. Ph.D. Thesis. MIT-WHOI, 98-07.

Adkins, J. F., Boyle, E. A., Curry, W. B., & Lutringer, A. (2003). Stable isotopes in deep-sea corals and a new mechanism for "vital effects." *Geochimica et Cosmochimica Acta*, *67*(6), 1129–1143. https://doi.org/10.1016/S0016-7037(02)01203-6

Adkins, Jess F., McIntyre, K., & Schrag, D. P. (2002). The Salinity, Temperature, and δ18O of the Glacial Deep Ocean. *Science*, *298*(5599), 1769–1773. https://doi.org/10.1126/science.1076252

Alibert, C., & McCulloch, M. T. (1997). Strontium/calcium ratios in modern porites corals From the Great Barrier Reef as a proxy for sea surface temperature: Calibration of the

thermometer and monitoring of ENSO. *Paleoceanography*, *12*(3), 345–363. https://doi.org/10.1029/97PA00318

Allen, K. A., Hönisch, B., Eggins, S. M., & Rosenthal, Y. (2012). Environmental controls on B/Ca in calcite tests of the tropical planktic foraminifer species Globigerinoides ruber and Globigerinoides sacculifer. *Earth and Planetary Science Letters*, *351–352*, 270–280. https://doi.org/10.1016/j.epsl.2012.07.004

Allison, N., Cohen, I., Finch, A. A., Erez, J., & Tudhope, A. W. (2014). Corals concentrate dissolved inorganic carbon to facilitate calcification. *Nature Communications*, *5*, 5741. https://doi.org/10.1038/ncomms6741

Allison, N., & Finch, A. A. (2004). High-resolution Sr/Ca records in modern Porites lobata corals: Effects of skeletal extension rate and architecture. *Geochemistry, Geophysics, Geosystems*, *5*(5). https://doi.org/10.1029/2004GC000696

Anagnostou, E., Huang, K.-F., You, C.-F., Sikes, E. L., & Sherrell, R. M. (2012). Evaluation of boron isotope ratio as a pH proxy in the deep sea coral Desmophyllum dianthus: Evidence of physiological pH adjustment. *Earth and Planetary Science Letters*, *349–350*, 251–260. https://doi.org/10.1016/j.epsl.2012.07.006

Anagnostou, Eleni, Sherrell, R. M., Gagnon, A., LaVigne, M., Field, M. P., & McDonough, W. F. (2011). Seawater nutrient and carbonate ion concentrations recorded as P/Ca, Ba/Ca, and U/Ca in the deep-sea coral Desmophyllum dianthus. *Geochimica et Cosmochimica Acta*, *75*(9), 2529–2543. https://doi.org/10.1016/j.gca.2011.02.019

Anand, P., Elderfield, H., & Conte, M. H. (2003). Calibration of Mg/Ca thermometry in planktonic foraminifera from a sediment trap time series. *Paleoceanography*, *18*(2). https://doi.org/10.1029/2002PA000846

Balan, E., Noireaux, J., Mavromatis, V., Saldi, G. D., Montouillout, V., Blanchard, M., Pietrucci, F., Gervais, C., Rustad, J. R., Schott, J., & Gaillardet, J. (2018). Theoretical isotopic fractionation between structural boron in carbonates and aqueous boric acid and borate ion. *Geochimica et Cosmochimica Acta*, *222*, 117–129. https://doi.org/10.1016/j.gca.2017.10.017

Balan, E., Pietrucci, F., Gervais, C., Blanchard, M., Schott, J., & Gaillardet, J. (2016). First-principles study of boron speciation in calcite and aragonite. *Geochimica et Cosmochimica Acta*, *193*, 119–131. https://doi.org/10.1016/j.gca.2016.07.026

Barnola, J. M., Raynaud, D., Korotkevich, Y. S., & Lorius, C. (1987). Vostok ice core provides 160,000-year record of atmospheric CO 2. *Nature*, *329*(6138), 408–414. https://doi.org/10.1038/329408a0

Beck, J. W., Edwards, R. L., Ito, E., Taylor, F. W., Recy, J., Rougerie, F., Joannot, P., & Henin, C. (1992). Sea-surface temperature from coral skeletal strontium/calcium ratios. *Science*, *257*(5070), 644–647. https://doi.org/10.1126/science.257.5070.644

Branson, O., Kaczmarek, K., Redfern, S. A. T., Misra, S., Langer, G., Tyliszczak, T., Bijma, J., & Elderfield, H. (2015). The coordination and distribution of B in foraminiferal calcite. *Earth and Planetary Science Letters*, *416*, 67–72. https://doi.org/10.1016/j.epsl.2015.02.006

Broecker, W. S., & Peng, T.-H. (1987). The role of CaCO3 compensation in the glacial to interglacial atmospheric CO2 change. *Global Biogeochemical Cycles*, *1*(1), 15–29. https://doi.org/10.1029/GB001i001p00015

Bryan, S. P., & Marchitto, T. M. (2008). Mg/Ca–temperature proxy in benthic foraminifera: New calibrations from the Florida Straits and a hypothesis regarding Mg/Li. *Paleoceanography*, *23*(2). https://doi.org/10.1029/2007PA001553

Case, D. H., Robinson, L. F., Auro, M. E., & Gagnon, A. C. (2010). Environmental and biological controls on Mg and Li in deep-sea scleractinian corals. *Earth and Planetary Science Letters*, *300*(3), 215–225. https://doi.org/10.1016/j.epsl.2010.09.029

Chappell, J., & Shackleton, N. J. (1986). Oxygen isotopes and sea level. *Nature*, *324*(6093), 137–140. https://doi.org/10.1038/324137a0

Cohen, A. L., Gaetani, G. A., Lundälv, T., Corliss, B. H., & George, R. Y. (2006). Compositional variability in a cold-water scleractinian, Lophelia pertusa: New insights into "vital effects." *Geochemistry, Geophysics, Geosystems*, *7*(12). https://doi.org/10.1029/2006GC001354

Cohen, A. L., McCorkle, D. C., Putron, S. de, Gaetani, G. A., & Rose, K. A. (2009). Morphological and compositional changes in the skeletons of new coral recruits reared in acidified seawater: Insights into the biomineralization response to ocean acidification. *Geochemistry, Geophysics, Geosystems*, *10*(7). https://doi.org/10.1029/2009GC002411

Cohen, A. L., Owens, K. E., Layne, G. D., & Shimizu, N. (2002). The Effect of Algal Symbionts on the Accuracy of Sr/Ca Paleotemperatures from Coral. *Science*, *296*(5566), 331–333. https://doi.org/10.1126/science.1069330

Cutler, K. B., Edwards, R. L., Taylor, F. W., Cheng, H., Adkins, J., Gallup, C. D., Cutler, P. M., Burr, G. S., & Bloom, A. L. (2003). Rapid sea-level fall and deep-ocean temperature change since the last interglacial period. *Earth and Planetary Science Letters*, *206*(3), 253–271. https://doi.org/10.1016/S0012-821X(02)01107-X

DeCarlo, T. M., Gaetani, G. A., Cohen, A. L., Foster, G. L., Alpert, A. E., & Stewart, J. A. (2016). Coral Sr-U thermometry. *Paleoceanography*, *31*(6), 626–638. https://doi.org/10.1002/2015PA002908

Dettman, D. L., & Lohmann, K. C. (1995). Microsampling carbonates for stable isotope and minor element analysis; physical separation of samples on a 20 micrometer scale. *Journal of Sedimentary Research*, *65*(3a), 566–569. https://doi.org/10.1306/D426813F-2B26-11D7-8648000102C1865D

Dietzel, M., Gussone, N., & Eisenhauer, A. (2004). Co-precipitation of Sr2+ and Ba2+ with aragonite by membrane diffusion of CO2 between 10 and 50 °C. *Chemical Geology*, *203*(1), 139–151. https://doi.org/10.1016/j.chemgeo.2003.09.008

D'Olivo, J. P., & McCulloch, M. T. (2017). Response of coral calcification and calcifying fluid composition to thermally induced bleaching stress. *Scientific Reports*, *7*(1), 2207. https://doi.org/10.1038/s41598-017-02306-x

Eiler, J. M. (2011). Paleoclimate reconstruction using carbonate clumped isotope thermometry. *Quaternary Science Reviews*, *30*(25), 3575–3588. https://doi.org/10.1016/j.quascirev.2011.09.001

Elderfield, H., Bertram, C. J., & Erez, J. (1996). A biomineralization model for the incorporation of trace elements into foraminiferal calcium carbonate. *Earth and Planetary Science Letters*, *142*(3), 409–423. https://doi.org/10.1016/0012-821X(96)00105-7

Elderfield, H., Ferretti, P., Greaves, M., Crowhurst, S., McCave, I. N., Hodell, D., & Piotrowski, A. M. (2012). Evolution of Ocean Temperature and Ice Volume Through the Mid-Pleistocene Climate Transition. *Science*, *337*(6095), 704–709. https://doi.org/10.1126/science.1221294

Elderfield, H., Yu, J., Anand, P., Kiefer, T., & Nyland, B. (2006). Calibrations for benthic foraminiferal Mg/Ca paleothermometry and the carbonate ion hypothesis. *Earth and Planetary Science Letters*, *250*(3), 633–649. https://doi.org/10.1016/j.epsl.2006.07.041

Emiliani, C. (1955). Pleistocene Temperatures. *The Journal of Geology*, *63*(6), 538–578. https://doi.org/10.1086/626295

Farmer, J. R., Branson, O., Uchikawa, J., Penman, D. E., Hönisch, B., & Zeebe, R. E. (2019). Boric acid and borate incorporation in inorganic calcite inferred from B/Ca, boron isotopes and surface kinetic modeling. *Geochimica et Cosmochimica Acta*, *244*, 229–247. https://doi.org/10.1016/j.gca.2018.10.008

Foster, G. L. (2008). Seawater pH, pCO2 and [CO_3^{2-}] variations in the Caribbean Sea over the last 130 kyr: A boron isotope and B/Ca study of planktic foraminifera. *Earth and Planetary Science Letters*, *271*(1), 254–266. https://doi.org/10.1016/j.epsl.2008.04.015

Gabitov, R. I., Gaetani, G. A., Watson, E. B., Cohen, A. L., & Ehrlich, H. L. (2008). Experimental determination of growth rate effect on U6+ and Mg2+ partitioning between aragonite and fluid at elevated U6+ concentration. *Geochimica et Cosmochimica Acta*, *72*(16), 4058–4068. https://doi.org/10.1016/j.gca.2008.05.047

Gabitov, Rinat I., Rollion-Bard, C., Tripati, A., & Sadekov, A. (2014). In situ study of boron partitioning between calcite and fluid at different crystal growth rates. *Geochimica et Cosmochimica Acta*, *137*, 81–92. https://doi.org/10.1016/j.gca.2014.04.014

Gaetani, G. A., & Cohen, A. L. (2006). Element partitioning during precipitation of aragonite from seawater: A framework for understanding paleoproxies. *Geochimica et Cosmochimica Acta*, *70*(18), 4617–4634. https://doi.org/10.1016/j.gca.2006.07.008

Gaetani, G. A., Cohen, A. L., Wang, Z., & Crusius, J. (2011). Rayleigh-based, multi-element coral thermometry: A biomineralization approach to developing climate proxies. *Geochimica et Cosmochimica Acta*, *75*(7), 1920–1932. https://doi.org/10.1016/j.gca.2011.01.010

Gagnon, A. C., Adkins, J. F., & Erez, J. (2012). Seawater transport during coral biomineralization. *Earth and Planetary Science Letters*, *329–330*, 150–161. https://doi.org/10.1016/j.epsl.2012.03.005

Gagnon, A. C., Adkins, J. F., Erez, J., Eiler, J. M., & Guan, Y. (2013). Sr/Ca sensitivity to aragonite saturation state in cultured subsamples from a single colony of coral: Mechanism of biomineralization during ocean acidification. *Geochimica et Cosmochimica Acta*, *105*, 240–254. https://doi.org/10.1016/j.gca.2012.11.038

Gagnon, A. C., Adkins, J. F., Fernandez, D. P., & Robinson, L. F. (2007). Sr/Ca and Mg/Ca vital effects correlated with skeletal architecture in a scleractinian deep-sea coral and the role of Rayleigh fractionation. *Earth and Planetary Science Letters*, *261*(1), 280–295. https://doi.org/10.1016/j.epsl.2007.07.013

Ghosh, P., Adkins, J., Affek, H., Balta, B., Guo, W., Schauble, E. A., Schrag, D., & Eiler, J. M. (2006). 13C–18O bonds in carbonate minerals: A new kind of paleothermometer. *Geochimica et Cosmochimica Acta*, *70*(6), 1439–1456. https://doi.org/10.1016/j.gca.2005.11.014

Gray, W. R., Weldeab, S., Lea, D. W., Rosenthal, Y., Gruber, N., Donner, B., & Fischer, G. (2018). The effects of temperature, salinity, and the carbonate system on Mg/Ca in Globigerinoides ruber (white): A global sediment trap calibration. *Earth and Planetary Science Letters*, *482*, 607–620. https://doi.org/10.1016/j.epsl.2017.11.026

Guilderson, T. P., Fairbanks, R. G., & Rubenstone, J. L. (1994). Tropical Temperature Variations Since 20,000 Years Ago: Modulating Interhemispheric Climate Change. *Science*, *263*(5147), 663–665. https://doi.org/10.1126/science.263.5147.663

Hemming, N. G., & Hanson, G. N. (1992). Boron isotopic composition and concentration in modern marine carbonates. *Geochimica et Cosmochimica Acta*, *56*(1), 537–543. https://doi.org/10.1016/0016-7037(92)90151-8

Holcomb, M., DeCarlo, T. M., Gaetani, G. A., & McCulloch, M. (2016). Factors affecting B/Ca ratios in synthetic aragonite. *Chemical Geology*, *437*, 67–76. https://doi.org/10.1016/j.chemgeo.2016.05.007

Hönisch, B., Hemming, N. G., Grottoli, A. G., Amat, A., Hanson, G. N., & Bijma, J. (2004). Assessing scleractinian corals as recorders for paleo-pH: Empirical calibration and vital effects. *Geochimica et Cosmochimica Acta*, *68*(18), 3675–3685. https://doi.org/10.1016/j.gca.2004.03.002

Hönisch, Bärbel, & Hemming, N. G. (2004). Ground-truthing the boron isotope-paleo-pH proxy in planktonic foraminifera shells: Partial dissolution and shell size effects. *Paleoceanography*, *19*(4). https://doi.org/10.1029/2004PA001026

Hönisch, Bärbel, & Hemming, N. G. (2005). Surface ocean pH response to variations in pCO2 through two full glacial cycles. *Earth and Planetary Science Letters*, *236*(1), 305–314. https://doi.org/10.1016/j.epsl.2005.04.027

Hostetler, S. W., & Mix, A. C. (1999). Reassessment of ice-age cooling of the tropical ocean and atmosphere. *Nature*, *399*(6737), 673–676. https://doi.org/10.1038/21401

Imbrie, J., van Donk, J., & Kipp, N. G. (1973). Paleoclimatic investigation of a late Pleistocene Caribbean deep-sea core: Comparison of isotopic and faunal methods. *Quaternary Research*, *3*(1), 10–38. https://doi.org/10.1016/0033-5894(73)90051-3

Inoue, M., Suwa, R., Suzuki, A., Sakai, K., & Kawahata, H. (2011). Effects of seawater pH on growth and skeletal U/Ca ratios of Acropora digitifera coral polyps. *Geophysical Research Letters*, *38*(12). https://doi.org/10.1029/2011GL047786

Kinsman, D. J. J., & Holland, H. D. (1969). The co-precipitation of cations with CaCO3—IV. The co-precipitation of Sr2+ with aragonite between 16° and 96°C. *Geochimica et Cosmochimica Acta*, *33*(1), 1–17. https://doi.org/10.1016/0016-7037(69)90089-1

Klochko, K., Cody, G. D., Tossell, J. A., Dera, P., & Kaufman, A. J. (2009). Re-evaluating boron speciation in biogenic calcite and aragonite using 11B MAS NMR. *Geochimica et Cosmochimica Acta*, *73*(7), 1890–1900. https://doi.org/10.1016/j.gca.2009.01.002

Lea, D., & Boyle, E. (1989). Barium content of benthic foraminifera controlled by bottom-water composition. *Nature*, *338*(6218), 751–753. https://doi.org/10.1038/338751a0

Lea, D. W. (1993). Constraints on the alkalinity and circulation of glacial circumpolar deep water from benthic foraminiferal barium. *Global Biogeochemical Cycles*, *7*(3), 695–710. https://doi.org/10.1029/93GB01536

Lea, D. W., Mashiotta, T. A., & Spero, H. J. (1999). Controls on magnesium and strontium uptake in planktonic foraminifera determined by live culturing. *Geochimica et Cosmochimica Acta*, *63*(16), 2369–2379. https://doi.org/10.1016/S0016-7037(99)00197-0

Lear, C. H., Rosenthal, Y., & Slowey, N. (2002). Benthic foraminiferal Mg/Ca-paleothermometry: a revised core-top calibration. *Geochimica et Cosmochimica Acta*, *66*(19), 3375–3387. https://doi.org/10.1016/S0016-7037(02)00941-9

Marchitto, T. M., Bryan, S. P., Doss, W., McCulloch, M. T., & Montagna, P. (2018). A simple biomineralization model to explain Li, Mg, and Sr incorporation into aragonitic foraminifera and corals. *Earth and Planetary Science Letters*, *481*, 20–29. https://doi.org/10.1016/j.epsl.2017.10.022

Marriott, C. S., Henderson, G. M., Belshaw, N. S., & Tudhope, A. W. (2004). Temperature dependence of δ7Li, δ44Ca and Li/Ca during growth of calcium carbonate. *Earth and Planetary Science Letters*, *222*(2), 615–624. https://doi.org/10.1016/j.epsl.2004.02.031

Martínez-Botí, M. A., Marino, G., Foster, G. L., Ziveri, P., Henehan, M. J., Rae, J. W. B., Mortyn, P. G., & Vance, D. (2015). Boron isotope evidence for oceanic carbon dioxide leakage during the last deglaciation. *Nature*, *518*(7538), 219–222. https://doi.org/10.1038/nature14155

Mashiotta, T. A., Lea, D. W., & Spero, H. J. (1999). Glacial–interglacial changes in Subantarctic sea surface temperature and δ18O-water using foraminiferal Mg. *Earth and Planetary Science Letters*, *170*(4), 417–432. https://doi.org/10.1016/S0012-821X(99)00116-8

Mavromatis, V., Montouillout, V., Noireaux, J., Gaillardet, J., & Schott, J. (2015). Characterization of boron incorporation and speciation in calcite and aragonite from co-precipitation experiments under controlled pH, temperature and precipitation rate. *Geochimica et Cosmochimica Acta*, *150*, 299–313. https://doi.org/10.1016/j.gca.2014.10.024

McConnaughey, T. (1989). 13C and 18O isotopic disequilibrium in biological carbonates: I. Patterns. *Geochimica et Cosmochimica Acta*, *53*(1), 151–162. https://doi.org/10.1016/0016-7037(89)90282-2

McCulloch, M. T., D'Olivo, J. P., Falter, J., Holcomb, M., & Trotter, J. A. (2017). Coral calcification in a changing World and the interactive dynamics of pH and DIC upregulation. *Nature Communications*, *8*, 15686. https://doi.org/10.1038/ncomms15686

Meibom, A., Cuif, J.-P., Houlbreque, F., Mostefaoui, S., Dauphin, Y., Meibom, K. L., & Dunbar, R. (2008). Compositional variations at ultra-structure length scales in coral skeleton. *Geochimica et Cosmochimica Acta*, *72*(6), 1555–1569. https://doi.org/10.1016/j.gca.2008.01.009

CLIMAP Members. (1976). The Surface of the Ice-Age Earth. *Science*, *191*(4232), 1131–1137. https://doi.org/10.1126/science.191.4232.1131

Mollica, N. R., Guo, W., Cohen, A. L., Huang, K.-F., Foster, G. L., Donald, H. K., & Solow, A. R. (2018). Ocean acidification affects coral growth by reducing skeletal density. *Proceedings of the National Academy of Sciences*, *115*(8), 1754–1759. https://doi.org/10.1073/pnas.1712806115

Montagna, P., McCulloch, M., Douville, E., López Correa, M., Trotter, J., Rodolfo-Metalpa, R., Dissard, D., Ferrier-Pagès, C., Frank, N., Freiwald, A., Goldstein, S., Mazzoli, C., Reynaud, S., Rüggeberg, A., Russo, S., & Taviani, M. (2014). Li/Mg systematics in scleractinian corals: Calibration of the thermometer. *Geochimica et Cosmochimica Acta*, *132*, 288–310. https://doi.org/10.1016/j.gca.2014.02.005

Mucci, A., Canuel, R., & Zhong, S. (1989). The solubility of calcite and aragonite in sulfate-free seawater and the seeded growth kinetics and composition of the precipitates at 25°C. *Chemical Geology*, *74*(3), 309–320. https://doi.org/10.1016/0009-2541(89)90040-5

Petit, J. R., Jouzel, J., Raynaud, D., Barkov, N. I., Barnola, J.-M., Basile, I., Bender, M., Chappellaz, J., Davis, M., Delaygue, G., Delmotte, M., Kotlyakov, V. M., Legrand, M., Lipenkov, V. Y., Lorius, C., Pépin, L., Ritz, C., Saltzman, E., & Stievenard, M. (1999).

Climate and atmospheric history of the past 420,000 years from the Vostok ice core, Antarctica. *Nature*, *399*(6735), 429–436. https://doi.org/10.1038/20859

Raddatz, J., Liebetrau, V., Rüggeberg, A., Hathorne, E., Krabbenhöft, A., Eisenhauer, A., Böhm, F., Vollstaedt, H., Fietzke, J., López Correa, M., Freiwald, A., & Dullo, W.-C. (2013). Stable Sr-isotope, Sr/Ca, Mg/Ca, Li/Ca and Mg/Li ratios in the scleractinian cold-water coral *Lophelia pertusa*. *Chemical Geology*, *352*, 143–152. https://doi.org/10.1016/j.chemgeo.2013.06.013

Rae, J. W. B., Burke, A., Robinson, L. F., Adkins, J. F., Chen, T., Cole, C., Greenop, R., Li, T., Littley, E. F. M., Nita, D. C., Stewart, J. A., & Taylor, B. J. (2018). CO_2 storage and release in the deep Southern Ocean on millennial to centennial timescales. *Nature*, *562*(7728), 569–573. https://doi.org/10.1038/s41586-018-0614-0

Rae, James W. B., Foster, G. L., Schmidt, D. N., & Elliott, T. (2011). Boron isotopes and B/Ca in benthic foraminifera: Proxies for the deep ocean carbonate system. *Earth and Planetary Science Letters*, *302*(3), 403–413. https://doi.org/10.1016/j.epsl.2010.12.034

Reynaud, S., Ferrier-Pagès, C., Meibom, A., Mostefaoui, S., Mortlock, R., Fairbanks, R., & Allemand, D. (2007). Light and temperature effects on Sr/Ca and Mg/Ca ratios in the scleractinian coral Acropora sp. *Geochimica et Cosmochimica Acta*, *71*(2), 354–362. https://doi.org/10.1016/j.gca.2006.09.009

Rind, D., & Peteet, D. (1985). Terrestrial conditions at the Last Glacial Maximum and CLIMAP sea-surface temperature estimates: Are they consistent? *Quaternary Research*, *24*(1), 1–22. https://doi.org/10.1016/0033-5894(85)90080-8

Robinson, L. F., Adkins, J. F., Fernandez, D. P., Burnett, D. S., Wang, S.-L., Gagnon, A. C., & Krakauer, N. (2006). Primary U distribution in scleractinian corals and its implications for U series dating. *Geochemistry, Geophysics, Geosystems*, *7*(5). https://doi.org/10.1029/2005GC001138

Rollion-Bard, C., Blamart, D., Trebosc, J., Tricot, G., Mussi, A., & Cuif, J.-P. (2011). Boron isotopes as pH proxy: A new look at boron speciation in deep-sea corals using 11B MAS NMR and EELS. *Geochimica et Cosmochimica Acta*, *75*(4), 1003–1012. https://doi.org/10.1016/j.gca.2010.11.023

Rosenthal, Y., Field, M. P., & Sherrell, R. M. (1999). Precise determination of element/calcium ratios in calcareous samples using sector field inductively coupled plasma mass spectrometry. *Analytical Chemistry*, *71*(15), 3248–3253. https://doi.org/10.1021/ac981410x

Rosenthal, Yair, Boyle, E. A., & Slowey, N. (1997). Temperature control on the incorporation of magnesium, strontium, fluorine, and cadmium into benthic foraminiferal shells from Little Bahama Bank: Prospects for thermocline paleoceanography. *Geochimica et Cosmochimica Acta*, *61*(17), 3633–3643. https://doi.org/10.1016/S0016-7037(97)00181-6

Rosenthal, Yair, Lear, C. H., Oppo, D. W., & Linsley, B. K. (2006). Temperature and carbonate ion effects on Mg/Ca and Sr/Ca ratios in benthic foraminifera: Aragonitic species Hoeglundina elegans. *Paleoceanography*, *21*(1). https://doi.org/10.1029/2005PA001158

Sachs, H. M., Webb, T., & Clark, D. R. (1977). Paleoecological Transfer Functions. *Annual Review of Earth and Planetary Sciences*, *5*(1), 159–178. https://doi.org/10.1146/annurev.ea.05.050177.001111

Sanyal, A., Hemming, N. G., Hanson, G. N., & Broecker, W. S. (1995). Evidence for a higher pH in the glacial ocean from boron isotopes in foraminifera. *Nature*, *373*(6511), 234–236. https://doi.org/10.1038/373234a0

Schrag, D. P. (1999). Rapid analysis of high-precision Sr/Ca ratios in corals and other marine carbonates. *Paleoceanography*, *14*(2), 97–102. https://doi.org/10.1029/1998PA900025

Schrag, D. P., Adkins, J. F., McIntyre, K., Alexander, J. L., Hodell, D. A., Charles, C. D., & McManus, J. F. (2002). The oxygen isotopic composition of seawater during the Last Glacial Maximum. *Quaternary Science Reviews*, *21*(1), 331–342. https://doi.org/10.1016/S0277-3791(01)00110-X

Schrag, D. P., Hampt, G., & Murray, D. W. (1996). Pore Fluid Constraints on the Temperature and Oxygen Isotopic Composition of the Glacial Ocean. *Science*, *272*(5270), 1930–1932. https://doi.org/10.1126/science.272.5270.1930

Shackleton, N. (1967). Oxygen Isotope Analyses and Pleistocene Temperatures Re-assessed. *Nature*, *215*(5096), 15–17. https://doi.org/10.1038/215015a0

Stewart, J. A., Anagnostou, E., & Foster, G. L. (2016). An improved boron isotope pH proxy calibration for the deep-sea coral Desmophyllum dianthus through sub-sampling of fibrous aragonite. *Chemical Geology*, *447*, 148–160. https://doi.org/10.1016/j.chemgeo.2016.10.029

Uchikawa, J., Harper, D. T., Penman, D. E., Zachos, J. C., & Zeebe, R. E. (2017). Influence of solution chemistry on the boron content in inorganic calcite grown in artificial seawater. *Geochimica et Cosmochimica Acta*, *218*, 291–307. https://doi.org/10.1016/j.gca.2017.09.016

Uchikawa, J., Penman, D. E., Zachos, J. C., & Zeebe, R. E. (2015). Experimental evidence for kinetic effects on B/Ca in synthetic calcite: Implications for potential B(OH)4− and B(OH)3 incorporation. *Geochimica et Cosmochimica Acta*, *150*, 171–191. https://doi.org/10.1016/j.gca.2014.11.022

Yu, J., & Elderfield, H. (2007). Benthic foraminiferal B/Ca ratios reflect deep water carbonate saturation state. *Earth and Planetary Science Letters*, *258*(1), 73–86. https://doi.org/10.1016/j.epsl.2007.03.025

Yu, J., Foster, G. L., Elderfield, H., Broecker, W. S., & Clark, E. (2010). An evaluation of benthic foraminiferal B/Ca and δ11B for deep ocean carbonate ion and pH reconstructions. *Earth and Planetary Science Letters*, *293*(1), 114–120. https://doi.org/10.1016/j.epsl.2010.02.029

Chapter 4

Adkins, J. F., Henderson, G. M., Wang, S.-L., O'Shea, S., & Mokadem, F. (2004). Growth rates of the deep-sea scleractinia Desmophyllum cristagalli and Enallopsammia rostrata. *Earth and Planetary Science Letters*, *227*(3), 481–490. https://doi.org/10.1016/j.epsl.2004.08.022

Allison, N. (1996). Comparative determinations of trace and minor elements in coral aragonite by ion microprobe analysis, with preliminary results from Phuket, southern Thailand. *Geochimica et Cosmochimica Acta*, *60*(18), 3457–3470. https://doi.org/10.1016/0016-7037(96)00171-8

Allison, Nicola, Finch, A. A., Newville, M., & Sutton, S. R. (2005). Strontium in coral aragonite: 3. Sr coordination and geochemistry in relation to skeletal architecture. *Geochimica et Cosmochimica Acta*, *69*(15), 3801–3811. https://doi.org/10.1016/j.gca.2005.01.026

Bentov, S., & Erez, J. (2006). Impact of biomineralization processes on the Mg content of foraminiferal shells: A biological perspective. *Geochemistry, Geophysics, Geosystems*, *7*(1). https://doi.org/10.1029/2005GC001015

Blamart, D., Rollion-Bard, C., Meibom, A., Cuif, J.-P., Juillet-Leclerc, A., & Dauphin, Y. (2007). Correlation of boron isotopic composition with ultrastructure in the deep-sea coral Lophelia pertusa: Implications for biomineralization and paleo-pH. *Geochemistry, Geophysics, Geosystems*, *8*(12). https://doi.org/10.1029/2007GC001686

Bontognali, T. R. R., Sessions, A. L., Allwood, A. C., Fischer, W. W., Grotzinger, J. P., Summons, R. E., & Eiler, J. M. (2012). Sulfur isotopes of organic matter preserved in 3.45-billion-year-old stromatolites reveal microbial metabolism. *Proceedings of the National Academy of Sciences*, *109*(38), 15146–15151. https://doi.org/10.1073/pnas.1207491109

Brinza, L., Schofield, P. F., Hodson, M. E., Weller, S., Ignatyev, K., Geraki, K., Quinn, P. D., & Mosselmans, J. F. W. (2014). Combining μXANES and μXRD mapping to analyze the heterogeneity in calcium carbonate granules excreted by the earthworm *Lumbricus terrestris*. *Journal of Synchrotron Radiation*, 21. 235-241.

Bryan, S. P., & Marchitto, T. M. (2008). Mg/Ca–temperature proxy in benthic foraminifera: New calibrations from the Florida Straits and a hypothesis regarding Mg/Li. *Paleoceanography*, *23*(2). https://doi.org/10.1029/2007PA001553

Case, D. H., Robinson, L. F., Auro, M. E., & Gagnon, A. C. (2010). Environmental and biological controls on Mg and Li in deep-sea scleractinian corals. *Earth and Planetary Science Letters*, *300*(3), 215–225. https://doi.org/10.1016/j.epsl.2010.09.029

Cohen, A. L., Gaetani, G. A., Lundälv, T., Corliss, B. H., & George, R. Y. (2006). Compositional variability in a cold-water scleractinian, Lophelia pertusa: New insights into "vital effects." *Geochemistry, Geophysics, Geosystems*, *7*(12). https://doi.org/10.1029/2006GC001354

Cusack, M., & Freer, A. (2008). Biomineralization: Elemental and Organic Influence in Carbonate Systems. *Chemical Reviews*, *108*(11), 4433–4454. https://doi.org/10.1021/cr078270o

Fallon, S. J., McCulloch, M. T., van Woesik, R., & Sinclair, D. J. (1999). Corals at their latitudinal limits: laser ablation trace element systematics in Porites from Shirigai Bay, Japan. *Earth and Planetary Science Letters*, *172*(3), 221–238. https://doi.org/10.1016/S0012-821X(99)00200-9

Farfan, G. A., Apprill, A., Webb, S. M., & Hansel, C. M. (2018). Coupled X-ray Fluorescence and X-ray Absorption Spectroscopy for Microscale Imaging and Identification of Sulfur Species within Tissues and Skeletons of Scleractinian Corals. *Analytical Chemistry*, *90*(21), 12559–12566. https://doi.org/10.1021/acs.analchem.8b02638

Farre, B., Cuif, J.-P., & Dauphin, Y. (2010). Occurrence and diversity of lipids in modern coral skeletons. *Zoology (Jena, Germany)*, *113*(4), 250–257. https://doi.org/10.1016/j.zool.2009.11.004

Fehrenbacher, J. S., Russell, A. D., Davis, C. V., Gagnon, A. C., Spero, H. J., Cliff, J. B., Zhu, Z., & Martin, P. (2017). Link between light-triggered Mg-banding and chamber

formation in the planktic foraminifera *Neogloboquadrina dutertrei*. *Nature Communications*, *8*, 15441. https://doi.org/10.1038/ncomms15441

Finch, A. A., & Allison, N. (2008). Mg structural state in coral aragonite and implications for the paleoenvironmental proxy. *Geophysical Research Letters*, *35*(8). https://doi.org/10.1029/2008GL033543

Finch, A. A., Allison, N., Sutton, S. R., & Newville, M. (2003). Strontium in coral aragonite: 1. Characterization of Sr coordination by extended absorption X-ray fine structure. *Geochimica et Cosmochimica Acta*, *67*(6), 1197–1202. https://doi.org/10.1016/S0016-7037(02)01224-3

Foster, L. C., Allison, N., Finch, A. A., & Andersson, C. (2009). Strontium distribution in the shell of the aragonite bivalve Arctica islandica. *Geochemistry, Geophysics, Geosystems*, *10*(3). https://doi.org/10.1029/2007GC001915

Gabitov, R. I., Gaetani, G. A., Watson, E. B., Cohen, A. L., & Ehrlich, H. L. (2008). Experimental determination of growth rate effect on U6+ and Mg2+ partitioning between aragonite and fluid at elevated U6+ concentration. *Geochimica et Cosmochimica Acta*, *72*(16), 4058–4068. https://doi.org/10.1016/j.gca.2008.05.047

Gabitov, R. I., Gagnon, A. C., Guan, Y., Eiler, J. M., & Adkins, J. F. (2013). Accurate Mg/Ca, Sr/Ca, and Ba/Ca ratio measurements in carbonates by SIMS and NanoSIMS and an assessment of heterogeneity in common calcium carbonate standards. *Chemical Geology*, *356*, 94–108. https://doi.org/10.1016/j.chemgeo.2013.07.019

Gaetani, G. A., & Cohen, A. L. (2006). Element partitioning during precipitation of aragonite from seawater: A framework for understanding paleoproxies. *Geochimica et Cosmochimica Acta*, *70*(18), 4617–4634. https://doi.org/10.1016/j.gca.2006.07.008

Gaetani, G. A., Cohen, A. L., Wang, Z., & Crusius, J. (2011). Rayleigh-based, multi-element coral thermometry: A biomineralization approach to developing climate proxies. *Geochimica et Cosmochimica Acta*, *75*(7), 1920–1932. https://doi.org/10.1016/j.gca.2011.01.010

Gagnon, A. C., Adkins, J. F., & Erez, J. (2012). Seawater transport during coral biomineralization. *Earth and Planetary Science Letters*, *329–330*, 150–161. https://doi.org/10.1016/j.epsl.2012.03.005

Gagnon, A. C., Adkins, J. F., Fernandez, D. P., & Robinson, L. F. (2007). Sr/Ca and Mg/Ca vital effects correlated with skeletal architecture in a scleractinian deep-sea coral and the role of Rayleigh fractionation. *Earth and Planetary Science Letters*, *261*(1), 280–295. https://doi.org/10.1016/j.epsl.2007.07.013

Gong, Y. U. T., Killian, C. E., Olson, I. C., Appathurai, N. P., Amasino, A. L., Martin, M. C., Holt, L. J., Wilt, F. H., & Gilbert, P. U. P. A. (2012). Phase transitions in biogenic amorphous calcium carbonate. *Proceedings of the National Academy of Sciences*, *109*(16), 6088–6093. https://doi.org/10.1073/pnas.1118085109

Gothmann, A. M., Stolarski, J., Adkins, J. F., Schoene, B., Dennis, K. J., Schrag, D. P., Mazur, M., & Bender, M. L. (2015). Fossil corals as an archive of secular variations in seawater chemistry since the Mesozoic. *Geochimica et Cosmochimica Acta*, *160*, 188–208. https://doi.org/10.1016/j.gca.2015.03.018

Greegor, R. B., Pingitore, N. E., & Lytle, F. W. (1997). Strontianite in Coral Skeletal Aragonite. *Science*, *275*(5305), 1452–1454. https://doi.org/10.1126/science.275.5305.1452

Guilderson, T. P., McCarthy, M. D., Dunbar, R. B., Englebrecht, A., & Roark, E. B. (2013). Late Holocene variations in Pacific surface circulation and biogeochemistry inferred from

proteinaceous deep-sea corals. *Biogeosciences*, *10*(9), 6019–6028. https://doi.org/10.5194/bg-10-6019-2013

Holcomb, M., DeCarlo, T. M., Gaetani, G. A., & McCulloch, M. (2016). Factors affecting B/Ca ratios in synthetic aragonite. *Chemical Geology*, *437*, 67–76. https://doi.org/10.1016/j.chemgeo.2016.05.007

Holcomb, Michael, Cohen, A. L., Gabitov, R. I., & Hutter, J. L. (2009). Compositional and morphological features of aragonite precipitated experimentally from seawater and biogenically by corals. *Geochimica et Cosmochimica Acta*, *73*(14), 4166–4179. https://doi.org/10.1016/j.gca.2009.04.015

Jochum, K. P., Stoll, B., Herwig, K., Willbold, M., Hofmann, A. W., Amini, M., … Woodhead, J. D. (2006). MPI-DING reference glasses for in situ microanalysis: New reference values for element concentrations and isotope ratios. *Geochemistry, Geophysics, Geosystems*, *7*(2). https://doi.org/10.1029/2005GC001060

John, S. G., & Adkins, J. F. (2010). Analysis of dissolved iron isotopes in seawater. *Marine Chemistry*, *119*(1), 65–76. https://doi.org/10.1016/j.marchem.2010.01.001

Kita, N. T., Ushikubo, T., Fu, B., & Valley, J. W. (2009). High precision SIMS oxygen isotope analysis and the effect of sample topography. *Chemical Geology*, *264*(1), 43–57. https://doi.org/10.1016/j.chemgeo.2009.02.012

Kunioka, D., Shirai, K., Takahata, N., Sano, Y., Toyofuku, T., & Ujiie, Y. (2006). Microdistribution of Mg/Ca, Sr/Ca, and Ba/Ca ratios in Pulleniatina obliquiloculata test by using a NanoSIMS: Implication for the vital effect mechanism. *Geochemistry, Geophysics, Geosystems*, *7*(12). https://doi.org/10.1029/2006GC001280

LaVigne, M., Field, M. P., Anagnostou, E., Grottoli, A. G., Wellington, G. M., & Sherrell, R. M. (2008). Skeletal P/Ca tracks upwelling in Gulf of Panamá coral: Evidence for a new seawater phosphate proxy. *Geophysical Research Letters*, *35*(5). https://doi.org/10.1029/2007GL031926

MacRae, N. D. (1995). Secondary-ion mass spectrometry and geology. *The Canadian Mineralogist*, *33*(2), 219–236.

Marchitto, T. M., Bryan, S. P., Doss, W., McCulloch, M. T., & Montagna, P. (2018). A simple biomineralization model to explain Li, Mg, and Sr incorporation into aragonitic foraminifera and corals. *Earth and Planetary Science Letters*, *481*, 20–29. https://doi.org/10.1016/j.epsl.2017.10.022

Mass, T., Giuffre, A. J., Sun, C.-Y., Stifler, C. A., Frazier, M. J., Neder, M., Tamura, N., Stan, C. V., Marcus, M. A., & Gilbert, P. U. P. A. (2017). Amorphous calcium carbonate particles form coral skeletons. *Proceedings of the National Academy of Sciences*, *114*(37), E7670–E7678. https://doi.org/10.1073/pnas.1707890114

Meibom, A., Cuif, J.-P., Hillion, F., Constantz, B. R., Juillet-Leclerc, A., Dauphin, Y., Watanabe, T., & Dunbar, R. B. (2004). Distribution of magnesium in coral skeleton. *Geophysical Research Letters*, *31*(23). https://doi.org/10.1029/2004GL021313

Meibom, A., Cuif, J.-P., Houlbreque, F., Mostefaoui, S., Dauphin, Y., Meibom, K. L., & Dunbar, R. (2008). Compositional variations at ultra-structure length scales in coral skeleton. *Geochimica et Cosmochimica Acta*, *72*(6), 1555–1569. https://doi.org/10.1016/j.gca.2008.01.009

Meibom, A., Mostefaoui, S., Cuif, J.-P., Dauphin, Y., Houlbreque, F., Dunbar, R., & Constantz, B. (2007). Biological forcing controls the chemistry of reef-building coral skeleton. *Geophysical Research Letters*, *34*(2). https://doi.org/10.1029/2006GL028657

Oehler, D. Z., Robert, F., Walter, M. R., Sugitani, K., Meibom, A., Mostefaoui, S., & Gibson, E. K. (2010). Diversity in the Archean biosphere: new insights from NanoSIMS. *Astrobiology*, *10*(4), 413–424. https://doi.org/10.1089/ast.2009.0426

Paris, G., Fehrenbacher, J. S., Sessions, A. L., Spero, H. J., & Adkins, J. F. (2014). Experimental determination of carbonate-associated sulfate δ34S in planktonic foraminifera shells. *Geochemistry, Geophysics, Geosystems*, *15*(4), 1452–1461. https://doi.org/10.1002/2014GC005295

Polerecky, L., Adam, B., Milucka, J., Musat, N., Vagner, T., & Kuypers, M. M. M. (2012). Look@NanoSIMS--a tool for the analysis of nanoSIMS data in environmental microbiology. *Environmental Microbiology*, *14*(4), 1009–1023. https://doi.org/10.1111/j.1462-2920.2011.02681.x

Politi, Y., Metzler, R. A., Abrecht, M., Gilbert, B., Wilt, F. H., Sagi, I., Addadi, L., Weiner, S., & Gilbert, P. U. P. A. (2008). Transformation mechanism of amorphous calcium carbonate into calcite in the sea urchin larval spicule. *Proceedings of the National Academy of Sciences*, *105*(45), 17362–17366. https://doi.org/10.1073/pnas.0806604105

Reed, S. J. B. (1984). Geological Applications of SIMS. In A. Benninghoven, J. Okano, R. Shimizu, & H. W. Werner (Eds.), *Secondary Ion Mass Spectrometry SIMS IV* (pp. 451–455). Springer Berlin Heidelberg.

Robinson, L. F., Adkins, J. F., Fernandez, D. P., Burnett, D. S., Wang, S.-L., Gagnon, A. C., & Krakauer, N. (2006). Primary U distribution in scleractinian corals and its implications for U series dating. *Geochemistry, Geophysics, Geosystems*, *7*(5). https://doi.org/10.1029/2005GC001138

Rollion-Bard, C., & Blamart, D. (2015). Possible controls on Li, Na, and Mg incorporation into aragonite coral skeletons. *Chemical Geology*, *396*, 98–111. https://doi.org/10.1016/j.chemgeo.2014.12.011

Rollion-Bard, C., Blamart, D., Cuif, J.-P., & Dauphin, Y. (2010). In situ measurements of oxygen isotopic composition in deep-sea coral, Lophelia pertusa: Re-examination of the current geochemical models of biomineralization. *Geochimica et Cosmochimica Acta*, *74*(4), 1338–1349. https://doi.org/10.1016/j.gca.2009.11.011

Rollion-Bard, C., Chaussidon, M., & France-Lanord, C. (2003). pH control on oxygen isotopic composition of symbiotic corals. *Earth and Planetary Science Letters*, *215*(1), 275–288. https://doi.org/10.1016/S0012-821X(03)00391-1

Sherwood, O. A., Heikoop, J. M., Scott, D. B., Risk, M. J., Guilderson, T. P., & McKinney, R. A. (2005). Stable isotopic composition of deep-sea gorgonian corals Primnoa spp.: a new archive of surface processes. *Marine Ecology Progress Series*, *301*, 135–148. https://doi.org/10.3354/meps301135

Shimizu, N., & Hart, S. R. (1982). Applications of the Ion Microprobe to Geochemistry and Cosmochemistry. *Annual Review of Earth and Planetary Sciences*, *10*(1), 483–526. https://doi.org/10.1146/annurev.ea.10.050182.002411

Sinclair, D. J. (2005). Correlated trace element "vital effects" in tropical corals: A new geochemical tool for probing biomineralization. *Geochimica et Cosmochimica Acta*, *69*(13), 3265–3284. https://doi.org/10.1016/j.gca.2005.02.030

Slodzian, G., Lorin, J. C., & Havette, A. (1980). Isotopic effect on the ionization probabilities in secondary ion emission. *Journal de Physique Lettres*, *41*(23), 555–558. https://doi.org/10.1051/jphyslet:019800041023055500

Tamenori, Y., Yoshimura, T., Luan, N. T., Hasegawa, H., Suzuki, A., Kawahata, H., & Iwasaki, N. (2014). Identification of the chemical form of sulfur compounds in the Japanese pink coral (Corallium elatius) skeleton using μ-XRF/XAS speciation mapping. *Journal of Structural Biology*, *186*(2), 214–223. https://doi.org/10.1016/j.jsb.2014.04.001

Vigier, N., Rollion-Bard, C., Levenson, Y., & Erez, J. (2015). Lithium isotopes in foraminifera shells as a novel proxy for the ocean dissolved inorganic carbon (DIC). *Comptes Rendus Geoscience*, *347*(1), 43–51. https://doi.org/10.1016/j.crte.2014.12.001

Wacey, D., Gleeson, D., & Kilburn, M. R. (2010). Microbialite taphonomy and biogenicity: new insights from NanoSIMS. *Geobiology*, *8*(5), 403–416. https://doi.org/10.1111/j.1472-4669.2010.00251.x

Wang, X. T., Prokopenko, M. G., Sigman, D. M., Adkins, J. F., Robinson, L. F., Ren, H., Oleynik, S., Williams, B., & Haug, G. H. (2014). Isotopic composition of carbonate-bound organic nitrogen in deep-sea scleractinian corals: A new window into past biogeochemical change. *Earth and Planetary Science Letters*, *400*, 243–250. https://doi.org/10.1016/j.epsl.2014.05.048

Weber, P. K., Bacon, C. R., Hutcheon, I. D., Ingram, B. L., & Wooden, J. L. (2005). Ion microprobe measurement of strontium isotopes in calcium carbonate with application to salmon otoliths. *Geochimica et Cosmochimica Acta*, *69*(5), 1225–1239. https://doi.org/10.1016/j.gca.2004.05.051

York, D., Evensen, N. M., Martínez, M. L., & De Basabe Delgado, J. (2004). Unified equations for the slope, intercept, and standard errors of the best straight line. *American Journal of Physics*, *72*(3), 367–375. https://doi.org/10.1119/1.1632486

Chapter 5

Adkins, J.F. (1998). Deep-sea corals: a new oceanic archive. Ph.D. Thesis. MIT-WHOI, 98-07.

Adkins, J. F., Boyle, E. A., Curry, W. B., & Lutringer, A. (2003). Stable isotopes in deep-sea corals and a new mechanism for "vital effects." *Geochimica et Cosmochimica Acta*, *67*(6), 1129–1143. https://doi.org/10.1016/S0016-7037(02)01203-6

Adkins, Jess F., Cheng, H., Boyle, E. A., Druffel, E. R. M., & Edwards, R. L. (1998). Deep-Sea Coral Evidence for Rapid Change in Ventilation of the Deep North Atlantic 15,400 Years Ago. *Science*, *280*(5364), 725–728. https://doi.org/10.1126/science.280.5364.725

Allen, K. A., Hönisch, B., Eggins, S. M., Haynes, L. L., Rosenthal, Y., & Yu, J. (2016). Trace element proxies for surface ocean conditions: A synthesis of culture calibrations with planktic foraminifera. *Geochimica et Cosmochimica Acta*, *193*, 197–221. https://doi.org/10.1016/j.gca.2016.08.015

Allen, K. A., Hönisch, B., Eggins, S. M., & Rosenthal, Y. (2012). Environmental controls on B/Ca in calcite tests of the tropical planktic foraminifer species Globigerinoides ruber and Globigerinoides sacculifer. *Earth and Planetary Science Letters*, *351–352*, 270–280. https://doi.org/10.1016/j.epsl.2012.07.004

Allison, N., Cohen, I., Finch, A. A., Erez, J., & Tudhope, A. W. (2014). Corals concentrate dissolved inorganic carbon to facilitate calcification. *Nature Communications*, *5*, 5741. https://doi.org/10.1038/ncomms6741

Anagnostou, E., Sherrell, R. M., Gagnon, A., LaVigne, M., Field, M. P., & McDonough, W. F. (2011). Seawater nutrient and carbonate ion concentrations recorded as P/Ca, Ba/Ca, and

U/Ca in the deep-sea coral Desmophyllum dianthus. *Geochimica et Cosmochimica Acta*, *75*(9), 2529–2543. https://doi.org/10.1016/j.gca.2011.02.019

Beck, J. W., Edwards, R. L., Ito, E., Taylor, F. W., Recy, J., Rougerie, F., Joannot, P., & Henin, C. (1992). Sea-surface temperature from coral skeletal strontium/calcium ratios. *Science*, *257*(5070), 644–647. https://doi.org/10.1126/science.257.5070.644

Bentov, S., & Erez, J. (2006). Impact of biomineralization processes on the Mg content of foraminiferal shells: A biological perspective. *Geochemistry, Geophysics, Geosystems*, *7*(1). https://doi.org/10.1029/2005GC001015

Bigg, G. R., & Rohling, E. J. (2000). An oxygen isotope data set for marine waters. *Journal of Geophysical Research: Oceans*, *105*(C4), 8527–8535. https://doi.org/10.1029/2000JC900005

Boyle, E. A., Sclater, F., & Edmond, J. M. (1976). On the marine geochemistry of cadmium. *Nature*, *263*(5572), 42. https://doi.org/10.1038/263042a0

Boyle, Edward A. (1988). Cadmium: Chemical tracer of deepwater paleoceanography. *Paleoceanography*, *3*(4), 471–489. https://doi.org/10.1029/PA003i004p00471

Boyle, E. A. (1992). Cadmium and $\delta^{13}C$ Paleochemical ocean distributions during the Stage 2 glacial maximum. *Annual Review of Earth and Planetary Sciences*, *20*(1), 245–287. https://doi.org/10.1146/annurev.ea.20.050192.001333

Boyle, Edward A., & Keigwin, L. D. (1982). Deep Circulation of the North Atlantic over the Last 200,000 Years: Geochemical Evidence. *Science*, *218*(4574), 784–787. https://doi.org/10.1126/science.218.4574.784

Bryan, S. P., & Marchitto, T. M. (2008). Mg/Ca–temperature proxy in benthic foraminifera: New calibrations from the Florida Straits and a hypothesis regarding Mg/Li. *Paleoceanography*, *23*(2). https://doi.org/10.1029/2007PA001553

Case, D. H., Robinson, L. F., Auro, M. E., & Gagnon, A. C. (2010). Environmental and biological controls on Mg and Li in deep-sea scleractinian corals. *Earth and Planetary Science Letters*, *300*(3), 215–225. https://doi.org/10.1016/j.epsl.2010.09.029

Cobb, K. M., Charles, C. D., Cheng, H., & Edwards, R. L. (2003). El Niño/Southern Oscillation and tropical Pacific climate during the last millennium. *Nature*, *424*(6946), 271–276. https://doi.org/10.1038/nature01779

Cohen, A. L., Owens, K. E., Layne, G. D., & Shimizu, N. (2002). The Effect of Algal Symbionts on the Accuracy of Sr/Ca Paleotemperatures from Coral. *Science*, *296*(5566), 331–333. https://doi.org/10.1126/science.1069330

Cohen, A. L., McCorkle, D. C., Putron, S. de, Gaetani, G. A., & Rose, K. A. (2009). Morphological and compositional changes in the skeletons of new coral recruits reared in acidified seawater: Insights into the biomineralization response to ocean acidification. *Geochemistry, Geophysics, Geosystems*, *10*(7). https://doi.org/10.1029/2009GC002411

Corrège, T. (2006). Sea surface temperature and salinity reconstruction from coral geochemical tracers. *Palaeogeography, Palaeoclimatology, Palaeoecology*, *232*(2), 408–428. https://doi.org/10.1016/j.palaeo.2005.10.014

Cullen, J. T. (2006). On the nonlinear relationship between dissolved cadmium and phosphate in the modern global ocean: Could chronic iron limitation of phytoplankton growth cause the kink? *Limnology and Oceanography*, *51*(3), 1369–1380. https://doi.org/10.4319/lo.2006.51.3.1369

de Baar, H. J. W., Saager, P. M., Nolting, R. F., & van der Meer, J. (1994). Cadmium versus phosphate in the world ocean. *Marine Chemistry*, *46*(3), 261–281. https://doi.org/10.1016/0304-4203(94)90082-5

DeCarlo, T. M., Gaetani, G. A., Cohen, A. L., Foster, G. L., Alpert, A. E., & Stewart, J. A. (2016). Coral Sr-U thermometry. *Paleoceanography*, *31*(6), 626–638. https://doi.org/10.1002/2015PA002908

Dietzel, M., Gussone, N., & Eisenhauer, A. (2004). Co-precipitation of Sr2+ and Ba2+ with aragonite by membrane diffusion of CO2 between 10 and 50 °C. *Chemical Geology*, *203*(1), 139–151. https://doi.org/10.1016/j.chemgeo.2003.09.008

Djogić, R., & Branica, M. (1991). Dissolved uranyl complexed species in artificial seawater. *Marine Chemistry*, *36*(1), 121–135. https://doi.org/10.1016/S0304-4203(09)90058-5

Djogić, R., Sipos, L., & Branica, M. (1986). Characterization of uranium(VI) in seawater1. *Limnology and Oceanography*, *31*(5), 1122–1131. https://doi.org/10.4319/lo.1986.31.5.1122

Elderfield, H., Bertram, C. J., & Erez, J. (1996). A biomineralization model for the incorporation of trace elements into foraminiferal calcium carbonate. *Earth and Planetary Science Letters*, *142*(3), 409–423. https://doi.org/10.1016/0012-821X(96)00105-7

Elderfield, H., Ferretti, P., Greaves, M., Crowhurst, S., McCave, I. N., Hodell, D., & Piotrowski, A. M. (2012). Evolution of Ocean Temperature and Ice Volume Through the Mid-Pleistocene Climate Transition. *Science*, *337*(6095), 704–709. https://doi.org/10.1126/science.1221294

Elderfield, H., Yu, J., Anand, P., Kiefer, T., & Nyland, B. (2006). Calibrations for benthic foraminiferal Mg/Ca paleothermometry and the carbonate ion hypothesis. *Earth and Planetary Science Letters*, *250*(3), 633–649. https://doi.org/10.1016/j.epsl.2006.07.041

Eltgroth, S. F. (2006). Unraveling deep-ocean connections to climate with deep-sea coral records of radiocarbon and Cd/Ca. Dissertation (Ph.D.), California Institute of Technology.http://resolver.caltech.edu/CaltechETD:etd-05262006-110220

Eltgroth, S. F., Adkins, J. F., Robinson, L. F., Southon, J., & Kashgarian, M. (2006). A deep-sea coral record of North Atlantic radiocarbon through the Younger Dryas: Evidence for intermediate water/deepwater reorganization. *Paleoceanography*, *21*(4). https://doi.org/10.1029/2005PA001192

Fairbanks, R. G., & Dodge, R. E. (1979). Annual periodicity of the 18O16O and 13C12C ratios in the coral Montastrea annularis. *Geochimica et Cosmochimica Acta*, *43*(7), 1009–1020. https://doi.org/10.1016/0016-7037(79)90090-5

Farmer, J. R., Hönisch, B., Haynes, L. L., Kroon, D., Jung, S., Ford, H. L., Raymo, M. E., Jaume-Seguí, M., Bell. D. B., Goldstein, S. L., Pena, L. D., Yehudai, M., & Kim, J. (2019). Deep Atlantic Ocean carbon storage and the rise of 100,000-year glacial cycles. *Nature Geoscience*, *12*(5), 355–360. https://doi.org/10.1038/s41561-019-0334-6

Foster, G. L. (2008). Seawater pH, pCO2 and [CO_3^{2-}] variations in the Caribbean Sea over the last 130 kyr: A boron isotope and B/Ca study of planktic foraminifera. *Earth and Planetary Science Letters*, *271*(1), 254–266. https://doi.org/10.1016/j.epsl.2008.04.015

Gabitov, R. I., Gaetani, G. A., Watson, E. B., Cohen, A. L., & Ehrlich, H. L. (2008). Experimental determination of growth rate effect on U6+ and Mg2+ partitioning between aragonite and fluid at elevated U6+ concentration. *Geochimica et Cosmochimica Acta*, *72*(16), 4058–4068. https://doi.org/10.1016/j.gca.2008.05.047

Gaetani, G. A., & Cohen, A. L. (2006). Element partitioning during precipitation of aragonite from seawater: A framework for understanding paleoproxies. *Geochimica et Cosmochimica Acta*, *70*(18), 4617–4634. https://doi.org/10.1016/j.gca.2006.07.008

Gaetani, G. A., Cohen, A. L., Wang, Z., & Crusius, J. (2011). Rayleigh-based, multi-element coral thermometry: A biomineralization approach to developing climate proxies. *Geochimica et Cosmochimica Acta*, *75*(7), 1920–1932. https://doi.org/10.1016/j.gca.2011.01.010

Gagnon, A. C., Adkins, J. F., Fernandez, D. P., & Robinson, L. F. (2007). Sr/Ca and Mg/Ca vital effects correlated with skeletal architecture in a scleractinian deep-sea coral and the role of Rayleigh fractionation. *Earth and Planetary Science Letters*, *261*(1), 280–295. https://doi.org/10.1016/j.epsl.2007.07.013

Gagnon, A. C., Adkins, J. F., Erez, J., Eiler, J. M., & Guan, Y. (2013). Sr/Ca sensitivity to aragonite saturation state in cultured subsamples from a single colony of coral: Mechanism of biomineralization during ocean acidification. *Geochimica et Cosmochimica Acta*, *105*, 240–254. https://doi.org/10.1016/j.gca.2012.11.038

Hasenfratz, A. P., Jaccard, S. L., Martínez-García, A., Sigman, D. M., Hodell, D. A., Vance, D., Bernasconi, S. M., Kleiven, H. F., Haumann, F. A., & Haug, G. H. (2019). The residence time of Southern Ocean surface waters and the 100,000-year ice age cycle. *Science*, *363*(6431), 1080–1084. https://doi.org/10.1126/science.aat7067

Hathorne, E. C., Gagnon, A., Felis, T., Adkins, J., Asami, R., Boer, W., … You, C.-F. (2013). Interlaboratory study for coral Sr/Ca and other element/Ca ratio measurements. *Geochemistry, Geophysics, Geosystems*, *14*(9), 3730–3750. https://doi.org/10.1002/ggge.20230

Hemsing, F., Hsieh, Y.-T., Bridgestock, L., Spooner, P. T., Robinson, L. F., Frank, N., & Henderson, G. M. (2018). Barium isotopes in cold-water corals. *Earth and Planetary Science Letters*, *491*, 183–192. https://doi.org/10.1016/j.epsl.2018.03.040

Hines, S. K. V., Southon, J. R., & Adkins, J. F. (2015). A high-resolution record of Southern Ocean intermediate water radiocarbon over the past 30,000 years. *Earth and Planetary Science Letters*, *432*, 46–58. https://doi.org/10.1016/j.epsl.2015.09.038

Hönisch, B., & Hemming, N. G. (2005). Surface ocean pH response to variations in pCO2 through two full glacial cycles. *Earth and Planetary Science Letters*, *236*(1), 305–314. https://doi.org/10.1016/j.epsl.2005.04.027

Horner, T. J., Rickaby, R. E. M., & Henderson, G. M. (2011). Isotopic fractionation of cadmium into calcite. *Earth and Planetary Science Letters*, *312*(1), 243–253. https://doi.org/10.1016/j.epsl.2011.10.004

Horner, T. J., Lee, R. B. Y., Henderson, G. M., & Rickaby, R. E. M. (2013). Nonspecific uptake and homeostasis drive the oceanic cadmium cycle. *Proceedings of the National Academy of Sciences*, *110*(21), 2500-2505.

Inoue, M., Nohara, M., Okai, T., Suzuki, A., & Kawahata, H. (2004). Concentrations of Trace Elements in Carbonate Reference Materials Coral JCp-1 and Giant Clam JCt-1 by Inductively Coupled Plasma-Mass Spectrometry. *Geostandards and Geoanalytical Research*, *28*(3), 411–416. https://doi.org/10.1111/j.1751-908X.2004.tb00759.x

John, S. G., & Adkins, J. F. (2010). Analysis of dissolved iron isotopes in seawater. *Marine Chemistry*, *119*(1), 65–76. https://doi.org/10.1016/j.marchem.2010.01.001

Key, R. M., Olsen, A. , van Heuven, S., Lauvset, S. K., Velo, A. , Lin, X., Schirnick, C., Kozyr, A., Tanhua, T., Hoppema, M., Jutterström, S., Steinfeldt, R., Jeansson, E., Ishii, M.,

Perez, F. F., & Suzuki, T. (2015). Global Ocean Data Analysis Project, Version 2 (GLODAPv2). doi: 10.3334/CDIAC/OTG. NDP093_GLODAPv2

Kinsman, D. J. J., & Holland, H. D. (1969). The co-precipitation of cations with CaCO3—IV. The co-precipitation of Sr2+ with aragonite between 16° and 96°C. *Geochimica et Cosmochimica Acta*, *33*(1), 1–17. https://doi.org/10.1016/0016-7037(69)90089-1

Lane, T. W., & Morel, F. M. M. (2000). A biological function for cadmium in marine diatoms. *Proceedings of the National Academy of Sciences*, *97*(9), 4627–4631. https://doi.org/10.1073/pnas.090091397

Langmuir, D. (1978). Uranium solution-mineral equilibria at low temperatures with applications to sedimentary ore deposits. *Geochimica et Cosmochimica Acta*, *42*(6, Part A), 547–569. https://doi.org/10.1016/0016-7037(78)90001-7

Lea, D., & Boyle, E. (1989). Barium content of benthic foraminifera controlled by bottom-water composition. *Nature*, *338*(6218), 751–753. https://doi.org/10.1038/338751a0

Lea, D. W. (1993). Constraints on the alkalinity and circulation of glacial circumpolar deep water from benthic foraminiferal barium. *Global Biogeochemical Cycles*, *7*(3), 695–710. https://doi.org/10.1029/93GB01536

Lea, D. W. (1995). A trace metal perspective on the evolution of Antarctic Circumpolar Deep Water chemistry. *Paleoceanography*, *10*(4), 733–747. https://doi.org/10.1029/95PA01546

Lea, D. W., & Martin, P. A. (1996). A rapid mass spectrometric method for the simultaneous analysis of barium, cadmium, and strontium in foraminifera shells. *Geochimica et Cosmochimica Acta*, *60*(16), 3143–3149. https://doi.org/10.1016/0016-7037(96)00184-6

Lea, D. W., Pak, D. K., & Spero, H. J. (2000). Climate Impact of Late Quaternary Equatorial Pacific Sea Surface Temperature Variations. *Science*, *289*(5485), 1719–1724. https://doi.org/10.1126/science.289.5485.1719

Lear, C. H., Mawbey, E. M., & Rosenthal, Y. (2010). Cenozoic benthic foraminiferal Mg/Ca and Li/Ca records: Toward unlocking temperatures and saturation states. *Paleoceanography*, *25*(4). https://doi.org/10.1029/2009PA001880

Lear, C. H., & Rosenthal, Y. (2006). Benthic foraminiferal Li/Ca: Insights into Cenozoic seawater carbonate saturation state. *Geology*, *34*(11), 985–988. https://doi.org/10.1130/G22792A.1

Marchitto, T. M., Bryan, S. P., Doss, W., McCulloch, M. T., & Montagna, P. (2018). A simple biomineralization model to explain Li, Mg, and Sr incorporation into aragonitic foraminifera and corals. *Earth and Planetary Science Letters*, *481*, 20–29. https://doi.org/10.1016/j.epsl.2017.10.022

Marchitto, Thomas M., Curry, W. B., & Oppo, D. W. (2000). Zinc concentrations in benthic foraminifera reflect seawater chemistry. *Paleoceanography*, *15*(3), 299–306. https://doi.org/10.1029/1999PA000420

Martin, P., Goodkin, N. F., Stewart, J. A., Foster, G. L., Sikes, E. L., White, H. K., Hennige, S., & Roberts, J. M. (2016). Deep-sea coral δ13C: A tool to reconstruct the difference between seawater pH and δ11B-derived calcifying fluid pH. *Geophysical Research Letters*, *43*(1), 299–308. https://doi.org/10.1002/2015GL066494

McConnaughey, T. (1989). 13C and 18O isotopic disequilibrium in biological carbonates: I. Patterns. *Geochimica et Cosmochimica Acta*, *53*(1), 151–162. https://doi.org/10.1016/0016-7037(89)90282-2

McCorkle, D. C., Martin, P. A., Lea, D. W., & Klinkhammer, G. P. (1995). Evidence of a dissolution effect on benthic foraminiferal shell chemistry: δ13C, Cd/Ca, Ba/Ca, and Sr/Ca results from the Ontong Java Plateau. *Paleoceanography*, *10*(4), 699–714. https://doi.org/10.1029/95PA01427

McCulloch, M. T., D'Olivo, J. P., Falter, J., Holcomb, M., & Trotter, J. A. (2017). Coral calcification in a changing World and the interactive dynamics of pH and DIC upregulation. *Nature Communications*, *8*, 15686. https://doi.org/10.1038/ncomms15686

Middag, R., van Heuven, S. M. A. C., Bruland, K. W., & de Baar, H. J. W. (2018). The relationship between cadmium and phosphate in the Atlantic Ocean unravelled. *Earth and Planetary Science Letters*, *492*, 79–88. https://doi.org/10.1016/j.epsl.2018.03.046

Montagna, P., McCulloch, M., Douville, E., López Correa, M., Trotter, J., Rodolfo-Metalpa, R., Dissard, D., Ferrier-Pagès, C., Frank, N., Freiwald, A., Goldstein, S., Mazzoli, C., Reynaud, S., Rüggeberg, A., Russo, S., & Taviani, M. (2014). Li/Mg systematics in scleractinian corals: Calibration of the thermometer. *Geochimica et Cosmochimica Acta*, *132*, 288–310. https://doi.org/10.1016/j.gca.2014.02.005

Olsen, A., Key, R. M., Heuven, S. van, Lauvset, S. K., Velo, A., Lin, X., Schirnick, C., Kozyr, A., Tanhua, T., Hoppema, M., Jutterström, S., Steinfeldt, R., Jeansson, E., Ishii, M., Pérez, F. F. & Suzuki, T. (2016). The Global Ocean Data Analysis Project version 2 (GLODAPv2) – an internally consistent data product for the world ocean. *Earth System Science Data*, *8*(2), 297–323. https://doi.org/10.5194/essd-8-297-2016

Penman, D. E., Hönisch, B., Zeebe, R. E., Thomas, E., & Zachos, J. C. (2014). Rapid and sustained surface ocean acidification during the Paleocene-Eocene Thermal Maximum. *Paleoceanography*, *29*(5), 357–369. https://doi.org/10.1002/2014PA002621

Raddatz, J., Liebetrau, V., Rüggeberg, A., Hathorne, E., Krabbenhöft, A., Eisenhauer, A., Böhm, F., Vollstaedt, H., Fietzke, J., López Correa, M., Freiwald, A., & Dullo, W.-C. (2013). Stable Sr-isotope, Sr/Ca, Mg/Ca, Li/Ca and Mg/Li ratios in the scleractinian cold-water coral *Lophelia pertusa*. *Chemical Geology*, *352*, 143–152. https://doi.org/10.1016/j.chemgeo.2013.06.013

Raddatz, J., Rüggeberg, A., Flögel, S., Hathorne, E. C., Liebetrau, V., Eisenhauer, A., & Dullo, W.-C. (2014). The influence of seawater pH on U / Ca ratios in the scleractinian cold-water coral *Lophelia pertusa*. *Biogeosciences*, *11*(7), 1863–1871. https://doi.org/10.5194/bg-11-1863-2014

Rae, J. W. B., Burke, A., Robinson, L. F., Adkins, J. F., Chen, T., Cole, C., Greenop, R., Li, T., Littley, E. F. M., Nita, D. C., Stewart, J. A., & Taylor, B. J. (2018). CO_2 storage and release in the deep Southern Ocean on millennial to centennial timescales. *Nature*, *562*(7728), 569–573. https://doi.org/10.1038/s41586-018-0614-0

Rae, James W. B., Foster, G. L., Schmidt, D. N., & Elliott, T. (2011). Boron isotopes and B/Ca in benthic foraminifera: Proxies for the deep ocean carbonate system. *Earth and Planetary Science Letters*, *302*(3), 403–413. https://doi.org/10.1016/j.epsl.2010.12.034

Raitzsch, M., Kuhnert, H., Hathorne, E. C., Groeneveld, J., & Bickert, T. (2011). U/Ca in benthic foraminifers: A proxy for the deep-sea carbonate saturation. *Geochemistry, Geophysics, Geosystems*, *12*(6). https://doi.org/10.1029/2010GC003344

Reeder, R. J., Nugent, M., Lamble, G. M., Tait, C. D., & Morris, D. E. (2000). Uranyl Incorporation into Calcite and Aragonite: XAFS and Luminescence Studies. *Environmental Science & Technology*, *34*(4), 638–644. https://doi.org/10.1021/es990981j

Reeder, R. J., Nugent, M., Tait, C. D., Morris, D. E., Heald, S. M., Beck, K. M., Hess, W. P., & Lanzirotti, A. (2001). Coprecipitation of Uranium(VI) with Calcite: XAFS, micro-XAS, and luminescence characterization. *Geochimica et Cosmochimica Acta*, *65*(20), 3491–3503. https://doi.org/10.1016/S0016-7037(01)00647-0

Reynaud, S., Ferrier-Pagès, C., Meibom, A., Mostefaoui, S., Mortlock, R., Fairbanks, R., & Allemand, D. (2007). Light and temperature effects on Sr/Ca and Mg/Ca ratios in the scleractinian coral Acropora sp. *Geochimica et Cosmochimica Acta*, *71*(2), 354–362. https://doi.org/10.1016/j.gca.2006.09.009

Robinson, L. F., Adkins, J. F., Keigwin, L. D., Southon, J., Fernandez, D. P., Wang, S.-L., & Scheirer, D. S. (2005). Radiocarbon Variability in the Western North Atlantic During the Last Deglaciation. *Science*, *310*(5753), 1469–1473. https://doi.org/10.1126/science.1114832

Rollion-Bard, C., & Blamart, D. (2015). Possible controls on Li, Na, and Mg incorporation into aragonite coral skeletons. *Chemical Geology*, *396*, 98–111. https://doi.org/10.1016/j.chemgeo.2014.12.011

Rollion-Bard, C., Blamart, D., Cuif, J.-P., & Dauphin, Y. (2010). In situ measurements of oxygen isotopic composition in deep-sea coral, Lophelia pertusa: Re-examination of the current geochemical models of biomineralization. *Geochimica et Cosmochimica Acta*, *74*(4), 1338–1349. https://doi.org/10.1016/j.gca.2009.11.011

Rosenthal, Y., Field, M. P., & Sherrell, R. M. (1999). Precise determination of element/calcium ratios in calcareous samples using sector field inductively coupled plasma mass spectrometry. *Analytical Chemistry*, *71*(15), 3248–3253. https://doi.org/10.1021/ac981410x

Rosenthal, Yair, Lear, C. H., Oppo, D. W., & Linsley, B. K. (2006). Temperature and carbonate ion effects on Mg/Ca and Sr/Ca ratios in benthic foraminifera: Aragonitic species Hoeglundina elegans. *Paleoceanography*, *21*(1). https://doi.org/10.1029/2005PA001158

Rosenthal, Yair, Perron-Cashman, S., Lear, C. H., Bard, E., Barker, S., Billups, K., … Wilson, P. A. (2004). Interlaboratory comparison study of Mg/Ca and Sr/Ca measurements in planktonic foraminifera for paleoceanographic research. *Geochemistry, Geophysics, Geosystems*, *5*(4). https://doi.org/10.1029/2003GC000650

Ross, C. L., Falter, J. L., & McCulloch, M. T. (2017). Active modulation of the calcifying fluid carbonate chemistry (δ 11 B, B/Ca) and seasonally invariant coral calcification at sub-tropical limits. *Scientific Reports*, *7*(1), 13830. https://doi.org/10.1038/s41598-017-14066-9

Russell, A. D., Hönisch, B., Spero, H. J., & Lea, D. W. (2004). Effects of seawater carbonate ion concentration and temperature on shell U, Mg, and Sr in cultured planktonic foraminifera. *Geochimica et Cosmochimica Acta*, *68*(21), 4347–4361. https://doi.org/10.1016/j.gca.2004.03.013

Saenger, C., Affek, H. P., Felis, T., Thiagarajan, N., Lough, J. M., & Holcomb, M. (2012). Carbonate clumped isotope variability in shallow water corals: Temperature dependence and growth-related vital effects. *Geochimica et Cosmochimica Acta*, *99*, 224–242. https://doi.org/10.1016/j.gca.2012.09.035

Schlitzer, R. (2018). Ocean Data View. https://odv.awi.ed

Schlitzer, R., Anderson, R. F., Dodas, E. M., Lohan, M., Geibert, W., Tagliabue, A., … Zurbrick, C. (2018). The GEOTRACES Intermediate Data Product 2017. *Chemical Geology*, *493*, 210–223. https://doi.org/10.1016/j.chemgeo.2018.05.040

Schmidt, G. A. (1999). Forward modeling of carbonate proxy data from planktonic foraminifera using oxygen isotope tracers in a global ocean model. *Paleoceanography*, *14*(4), 482–497. https://doi.org/10.1029/1999PA900025

Schmidt, G.A., Bigg, G. R., and Rohling, E. J. (1999). Global Seawater Oxygen-18 Database - v1.22. https://data.giss.nasa.gov/o18data/

Sinclair, D. J., Kinsley, L. P. J., & McCulloch, M. T. (1998). High resolution analysis of trace elements in corals by laser ablation ICP-MS. *Geochimica et Cosmochimica Acta*, *62*(11), 1889–1901. https://doi.org/10.1016/S0016-7037(98)00112-4

Spooner, P. T., Guo, W., Robinson, L. F., Thiagarajan, N., Hendry, K. R., Rosenheim, B. E., & Leng, M. J. (2016). Clumped isotope composition of cold-water corals: A role for vital effects? *Geochimica et Cosmochimica Acta*, *179*, 123–141. https://doi.org/10.1016/j.gca.2016.01.023

Spooner, P. T., Robinson, L. F., Hemsing, F., Morris, P., & Stewart, J. A. (2018). Extended calibration of cold-water coral Ba/Ca using multiple genera and co-located measurements of dissolved barium concentration. *Chemical Geology*, *499*, 100–110. https://doi.org/10.1016/j.chemgeo.2018.09.012

Stewart, J. A., Anagnostou, E., & Foster, G. L. (2016). An improved boron isotope pH proxy calibration for the deep-sea coral Desmophyllum dianthus through sub-sampling of fibrous aragonite. *Chemical Geology*, *447*, 148–160. https://doi.org/10.1016/j.chemgeo.2016.10.029

Thiagarajan, N., Adkins, J., & Eiler, J. (2011). Carbonate clumped isotope thermometry of deep-sea corals and implications for vital effects. *Geochimica et Cosmochimica Acta*, *75*(16), 4416–4425. https://doi.org/10.1016/j.gca.2011.05.004

Thiagarajan, N., Subhas, A. V., Southon, J. R., Eiler, J. M., & Adkins, J. F. (2014). Abrupt pre-Bølling–Allerød warming and circulation changes in the deep ocean. *Nature*, *511*(7507), 75–78. https://doi.org/10.1038/nature13472

van de Flierdt, T., Robinson, L. F., & Adkins, J. F. (2010). Deep-sea coral aragonite as a recorder for the neodymium isotopic composition of seawater. *Geochimica et Cosmochimica Acta*, *74*(21), 6014–6032. https://doi.org/10.1016/j.gca.2010.08.001

Wall, M., Ragazzola, F., Foster, L. C., Form, A., & Schmidt, D. N. (2015). pH up-regulation as a potential mechanism for the cold-water coral *Lophelia pertusa* to sustain growth in aragonite undersaturated conditions. *Biogeosciences*, *12*(23), 6869–6880. https://doi.org/10.5194/bg-12-6869-2015

Wang, X. T., Prokopenko, M. G., Sigman, D. M., Adkins, J. F., Robinson, L. F., Ren, H., Oleynik, S., Williams, B., & Haug, G. H. (2014). Isotopic composition of carbonate-bound organic nitrogen in deep-sea scleractinian corals: A new window into past biogeochemical change. *Earth and Planetary Science Letters*, *400*, 243–250. https://doi.org/10.1016/j.epsl.2014.05.048

Wang, X. Tony, Sigman, D. M., Prokopenko, M. G., Adkins, J. F., Robinson, L. F., Hines, S. K., Chai, J., Studer, A. S., Martínez-García, A., Chen, T., & Haug, G. H. (2017). Deep-sea coral evidence for lower Southern Ocean surface nitrate concentrations during the last ice age. *Proceedings of the National Academy of Sciences*, *114*(13), 3352–3357. https://doi.org/10.1073/pnas.1615718114

Wang, Z., Gaetani, G., Liu, C., & Cohen, A. (2013). Oxygen isotope fractionation between aragonite and seawater: Developing a novel kinetic oxygen isotope fractionation model.

Geochimica et Cosmochimica Acta, *117*, 232–251. https://doi.org/10.1016/j.gca.2013.04.025

Weber, J. N., & Woodhead, P. M. J. (1972). Temperature dependence of oxygen-18 concentration in reef coral carbonates. *Journal of Geophysical Research (1896-1977)*, *77*(3), 463–473. https://doi.org/10.1029/JC077i003p00463

Xu, Y., Tang, D., Shaked, Y., & Morel, F. M. M. (2007). Zinc, cadmium, and cobalt interreplacement and relative use efficiencies in the coccolithophore Emiliania huxleyi. *Limnology and Oceanography*, *52*(5), 2294–2305. https://doi.org/10.4319/lo.2007.52.5.2294

Yu, J., & Elderfield, H. (2007). Benthic foraminiferal B/Ca ratios reflect deep water carbonate saturation state. *Earth and Planetary Science Letters*, *258*(1), 73–86. https://doi.org/10.1016/j.epsl.2007.03.025

Yu, J., Foster, G. L., Elderfield, H., Broecker, W. S., & Clark, E. (2010). An evaluation of benthic foraminiferal B/Ca and δ11B for deep ocean carbonate ion and pH reconstructions. *Earth and Planetary Science Letters*, *293*(1), 114–120. https://doi.org/10.1016/j.epsl.2010.02.029

Zachos, J., Pagani, M., Sloan, L., Thomas, E., & Billups, K. (2001). Trends, Rhythms, and Aberrations in Global Climate 65 Ma to Present. *Science*, *292*(5517), 686–693. https://doi.org/10.1126/science.1059412

Chapter 6

Antao, S. M., & Hassan, I. (2010). Temperature Dependence of the Structural Parameters in the Transformation of Aragonite to Calcite, as Determined from in Situ Synchrotron Powder X-Ray-Diffraction Data. *The Canadian Mineralogist*, *48*(5), 1225–1236. https://doi.org/10.3749/canmin.48.5.1225

Bischoff, J. L. (1969). Temperature controls on aragonite-calcite transformation in aqueous solution. *American Mineralogist*, 54, 149–155.

Bonifacie, M., Calmels, D., Eiler, J. M., Horita, J., Chaduteau, C., Vasconcelos, C., Agrinier, P., Katz, A., Passey, B.H., Ferry, J.M., & Bourrand, J.-J. (2017). Calibration of the dolomite clumped isotope thermometer from 25 to 350 °C, and implications for a universal calibration for all (Ca, Mg, Fe)CO 3 carbonates. *Geochimica et Cosmochimica Acta*, *200*, 255–279. https://doi.org/10.1016/j.gca.2016.11.028

Brand, W. A., Assonov, S. S., & Coplen, T. B. (2010). Correction for the 17O interference in δ(13C) measurements when analyzing CO2 with stable isotope mass spectrometry (IUPAC Technical Report). *Pure and Applied Chemistry*, *82*, 1719–1733. https://doi.org/10.1351/pac-rep-09-01-05

Brenner, D. C., Passey, B. H., & Stolper, D. A. (2018). Influence of water on clumped-isotope bond reordering kinetics in calcite. Geochimica et Cosmochimica Acta, 224, 42–63. https://doi.org/10.1016/j.gca.2017.12.026

Budd, D. A. (1988). Aragonite-to-calcite transformation during fresh-water diagenesis of carbonates: Insights from pore-water chemistry. *GSA Bulletin*, *100*(8), 1260–1270. https://doi.org/10.1130/0016-7606(1988)100<1260:ATCTDF>2.3.CO;2

Carlson, W. D. (1980). The calcite-aragonite equilibrium: effects of Sr substituion and anion orientational disorder. *American Mineralogist*, 65, 1252–1262.

Cummins, R. C., Finnegan, S., Fike, D. A., Eiler, J. M., & Fischer, W. W. (2014). Carbonate clumped isotope constraints on Silurian ocean temperature and seawater δ18O. Geochimica et Cosmochimica Acta, 140, 241–258. https://doi.org/10.1016/j.gca.2014.05.024

Daëron, M., Blamart, D., Peral, M., & Affek, H. P. (2016). Absolute isotopic abundance ratios and the accuracy of Δ 47 measurements. *Chemical Geology*, *442*, 83–96. https://doi.org/10.1016/j.chemgeo.2016.08.014

Davis B.L., & Adams, L.H. (1965). Kinetics of the calcite ⇌ aragonite transformation. *Journal of Geophysical Research*, *70*(2), 433–441. https://doi.org/10.1029/JZ070i002p00433

Dennis, Kate J., Affek, H. P., Passey, B. H., Schrag, D. P., & Eiler, J. M. (2011). Defining an absolute reference frame for 'clumped' isotope studies of CO2. *Geochimica et Cosmochimica Acta*, *75*(22), 7117–7131. https://doi.org/10.1016/j.gca.2011.09.025

Dennis, Kate J., & Schrag, D. P. (2010). Clumped isotope thermometry of carbonatites as an indicator of diagenetic alteration. *Geochimica et Cosmochimica Acta*, *74*(14), 4110–4122. https://doi.org/10.1016/j.gca.2010.04.005

Dennis, K.J., Cochran, J. K., Landman, N. H., & Schrag, D. P. (2013). The climate of the Late Cretaceous: New insights from the application of the carbonate clumped isotope thermometer to Western Interior Seaway macrofossil. *Earth and Planetary Science Letters*, *362*, 51–65. https://doi.org/10.1016/j.epsl.2012.11.036

Dickinson, S. R., & McGrath, K. M. (2001). Quantitative determination of binary and tertiary calcium carbonate mixtures using powder X-ray diffraction. *The Analyst*, *126*(7), 1118–1121. https://doi.org/10.1039/b103004n

Eiler, J. M. (2007). "Clumped-isotope" geochemistry—The study of naturally-occurring, multiply-substituted isotopologues. *Earth and Planetary Science Letters*, *262*(3), 309–327. https://doi.org/10.1016/j.epsl.2007.08.020

Eiler, J. M. (2011). Paleoclimate reconstruction using carbonate clumped isotope thermometry. *Quaternary Science Reviews*, *30*(25), 3575–3588. https://doi.org/10.1016/j.quascirev.2011.09.001

Ferry, J. M., Passey, B. H., Vasconcelos, C., & Eiler, J. M. (2011). Formation of dolomite at 40–80 °C in the Latemar carbonate buildup, Dolomites, Italy, from clumped isotope thermometry. Geology, 39(6), 571–574. https://doi.org/10.1130/G31845.1

Gallagher, T. M., Sheldon, N. D., Mauk, J. L., Petersen, S. V., Gueneli, N., & Brocks, J. J. (2017). Constraining the thermal history of the North American Midcontinent Rift System using carbonate clumped isotopes and organic thermal maturity indices. Precambrian Research, 294, 53–66. https://doi.org/10.1016/j.precamres.2017.03.022

Ghosh, P., Adkins, J., Affek, H., Balta, B., Guo, W., Schauble, E. A., Schrag, D., & Eiler, J. M. (2006). 13C–18O bonds in carbonate minerals: A new kind of paleothermometer. *Geochimica et Cosmochimica Acta*, *70*(6), 1439–1456. https://doi.org/10.1016/j.gca.2005.11.014

Guo, W., Mosenfelder, J. L., Goddard, W. A., & Eiler, J. M. (2009). Isotopic fractionations associated with phosphoric acid digestion of carbonate minerals: Insights from first-principles theoretical modeling and clumped isotope measurements. *Geochimica et Cosmochimica Acta*, *73*(24), 7203–7225. https://doi.org/10.1016/j.gca.2009.05.071

Henkes, G. A., Passey, B. H., Grossman, E. L., Shenton, B. J., Pérez-Huerta, A., & Yancey, T. E. (2014). Temperature limits for preservation of primary calcite clumped isotope

paleotemperatures. *Geochimica et Cosmochimica Acta*, *139*, 362–382. https://doi.org/10.1016/j.gca.2014.04.040

Henkes, G. A., Passey, B. H., Grossman, E. L., Shenton, B. J., Yancey, T. E., & Pérez-Huerta, A. (2018). Temperature evolution and the oxygen isotope composition of Phanerozoic oceans from carbonate clumped isotope thermometry. *Earth and Planetary Science Letters*, *490*, 40–50. https://doi.org/10.1016/j.epsl.2018.02.001

Huntington, K. W., Eiler, J. M., Affek, H. P., Guo, W., Bonifacie, M., Yeung, L. Y., Thiagarajan, N., Passey, B., Tripati, A., Daëron, M., & Came, R. (2009). Methods and limitations of 'clumped' CO_2 isotope (Δ_{47}) analysis by gas-source isotope ratio mass spectrometry. *Journal of Mass Spectrometry*, *44*(9), 1318–1329. https://doi.org/10.1002/jms.1614

Huntington, Katharine W., Budd, D. A., Wernicke, B. P., & Eiler, J. M. (2011). Use of Clumped-Isotope Thermometry To Constrain the Crystallization Temperature of Diagenetic Calcite. Journal of Sedimentary Research, 81(9–10), 656–669.

Ingalls, M. (2019). Reconstructing carbonate alteration histories in orogenic sedimentary basins: Xigaze forearc, southern Tibet. Geochimica et Cosmochimica Acta. https://doi.org/10.1016/j.gca.2019.02.005

Jamieson, J. C. (1953). Phase Equilibrium in the System Calcite-Aragonite. *The Journal of Chemical Physics*, *21*(8), 1385–1390. https://doi.org/10.1063/1.1699228

Koga, N., Kasahara, D., & Kimura, T. (2013). Aragonite Crystal Growth and Solid-State Aragonite–Calcite Transformation: A Physico–Geometrical Relationship via Thermal Dehydration of Included Water. Crystal Growth & Design, 13(5), 2238–2246. https://doi.org/10.1021/cg400350w

Lacroix, B., & Niemi, N. A. (2019). Investigating the effect of burial histories on the clumped isotope thermometer: An example from the Green River and Washakie Basins, Wyoming. Geochimica et Cosmochimica Acta, 247, 40–58. https://doi.org/10.1016/j.gca.2018.12.016

Lloyd, M. K., Eiler, J. M., & Nabelek, P. I. (2017). Clumped isotope thermometry of calcite and dolomite in a contact metamorphic environment. *Geochimica et Cosmochimica Acta*, *197*, 323–344. https://doi.org/10.1016/j.gca.2016.10.037

Lloyd, M. K., Ryb, U., & Eiler, J. M. (2018). Experimental calibration of clumped isotope reordering in dolomite. *Geochimica et Cosmochimica Acta, 242,* 1–20. https://doi.org/10.1016/j.gca.2018.08.036

Madon, M., & Gillet, P. (1984). A theoretical approach to the kinetics of calcite ⇌ aragonite transition: application to laboratory experiments. *Earth and Planetary Science Letters*, *67*(3), 400–414. https://doi.org/10.1016/0012-821X(84)90178-X

Miyake, A., & Kawano, J. (2010). High-temperature molecular dynamics simulation of aragonite. *Journal of Physics: Condensed Matter*, 22(22), 225402.

Passey, B. H., Levin, N. E., Cerling, T. E., Brown, F. H., & Eiler, J. M. (2010). High-temperature environments of human evolution in East Africa based on bond ordering in paleosol carbonates. *Proceedings of the National Academy of Sciences*, *107*(25), 11245–11249. https://doi.org/10.1073/pnas.1001824107

Passey, B. H., & Henkes, G. A. (2012). Carbonate clumped isotope bond reordering and geospeedometry. *Earth and Planetary Science Letters*, *351–352*, 223–236. https://doi.org/10.1016/j.epsl.2012.07.021

Rodríguez-Sanz, L., Bernasconi, S. M., Marino, G., Heslop, D., Müller, I. A., Fernandez, A., Grant, K., M., & Rohling, E. J. (2017). Penultimate deglacial warming across the Mediterranean Sea revealed by clumped isotopes in foraminifera. *Scientific Reports*, *7*(1), 16572. https://doi.org/10.1038/s41598-017-16528-6

Ryb, U., & Eiler, J. M. (2018). Oxygen isotope composition of the Phanerozoic ocean and a possible solution to the dolomite problem. Proceedings of the National Academy of Sciences, 115(26), 6602–6607. https://doi.org/10.1073/pnas.1719681115

Ryb, U., Lloyd, M. K., Stolper, D. A., & Eiler, J. M. (2017). The clumped-isotope geochemistry of exhumed marbles from Naxos, Greece. *Earth and Planetary Science Letters*, *470*, 1–12. https://doi.org/10.1016/j.epsl.2017.04.026

Schauble, E. A., Ghosh, P., & Eiler, J. M. (2006). Preferential formation of ^{13}C–^{18}O bonds in carbonate minerals, estimated using first-principles lattice dynamics. *Geochimica et Cosmochimica Acta, 70*(10), 2510–2529. https://doi.org/10.1016/j.gca.2006.02.011

Schauer, A. J., Kelson, J., Saenger, C., & Huntington, K. W. (2016). Choice of ^{17}O correction affects clumped isotope (Δ_{47}) values of CO_2 measured with mass spectrometry: ^{17}O correction affects CO_2 clumped isotopes. *Rapid Communications in Mass Spectrometry*, *30*(24), 2607–2616. https://doi.org/10.1002/rcm.7743

Shenton, B. J., Grossman, E. L., Passey, B. H., Henkes, G. A., Becker, T. P., Laya, J. C., Perez-Huerta, A., Becker, S.P., & Lawson, M. (2015). Clumped isotope thermometry in deeply buried sedimentary carbonates: The effects of bond reordering and recrystallization. GSA Bulletin, 127(7–8), 1036–1051. https://doi.org/10.1130/B31169.1

Staudigel, P. T., & Swart, P. K. (2016). Isotopic behavior during the aragonite-calcite transition: Implications for sample preparation and proxy interpretation. *Chemical Geology*, *442*, 130–138. https://doi.org/10.1016/j.chemgeo.2016.09.013

Stolper, D. A., & Eiler, J. M. (2015). The kinetics of solid-state isotope-exchange reactions for clumped isotopes: A study of inorganic calcites and apatites from natural and experimental samples. *American Journal of Science*, *315*(5), 363–411.

Thiagarajan, N., Adkins, J., & Eiler, J. (2011). Carbonate clumped isotope thermometry of deep-sea corals and implications for vital effects. *Geochimica et Cosmochimica Acta*, *75*(16), 4416–4425. https://doi.org/10.1016/j.gca.2011.05.004

Thiagarajan, N., Subhas, A. V., Southon, J. R., Eiler, J. M., & Adkins, J. F. (2014). Abrupt pre-Bølling–Allerød warming and circulation changes in the deep ocean. *Nature*, *511*(7507), 75–78. https://doi.org/10.1038/nature13472

Tripati, A. K., Sahany, S., Pittman, D., Eagle, R. A., Neelin, J. D., Mitchell, J. L., & Beaufort, L. (2014). Modern and glacial tropical snowlines controlled by sea surface temperature and atmospheric mixing. *Nature Geoscience*, *7*, 205.

Wang, Z., Schauble, E. A., & Eiler, J. M. (2004). Equilibrium thermodynamics of multiply substituted isotopologues of molecular gases. *Geochimica et Cosmochimica Acta*, *68*(23), 4779–4797. https://doi.org/10.1016/j.gca.2004.05.039

Winkelstern, I. Z., & Lohmann, K. C. (2016). Shallow burial alteration of dolomite and limestone clumped isotope geochemistry. Geology, 44(6), 467–470. https://doi.org/10.1130/G37809.1

Ye, Y., Smyth, J. R., Boni, P. (2012). Crystal structure and thermal expansion of aragonite-group carbonates by single-crystal X-ray diffraction. *American Mineralogist, 97*, 707-712. http://dx.doi.org/10.2138/am.2012.3923

Zhang, H., Cai, Y., Tan, L., Qin, S., & An, Z. (2014). Stable isotope composition alteration produced by the aragonite-to-calcite transformation in speleothems and implications for paleoclimate reconstructions. *Sedimentary Geology*, *309*, 1–14. https://doi.org/10.1016/j.sedgeo.2014.05.007